Heat and Moisture Migration within a Porous Urea Particle Bed

A Thesis

Submitted to the College of Graduate Studies and Research

in Partial Fulfillment of the Requirements for the Degree of

Doctor of Philosophy

in the Department of Mechanical Engineering

University of Saskatchewan

Saskatoon, Saskatchewan

By

Xiaodong Nie

PERMISSION TO USE

I agree that the Libraries of the University of Saskatchewan may make this thesis freely available for inspection. I further agree that permission for copying of this thesis in any manner, in whole or in part, for scholarly purposes may be granted by my supervisors (Professor R. W. Besant and Professor R.W. Evitts) or, in their absence, by the Head of the Department of Mechanical Engineering, or the Dean of the College of Engineering. It is understood that any copying or publication or use of this thesis or parts thereof for financial gain shall not be allowed without my written permission. It is also understood that due recognition shall be given to me and to the University of Saskatchewan in any scholarly use which may be made of any material in my thesis.

Requests for permission to copy or to make other use of material in this thesis in whole or part should be addressed to:

Head of the Department of Mechanical Engineering

University of Saskatchewan

Saskatoon, Saskatchewan S7N 5A9

ABSTRACT

Urea is an important nitrogen fertilizer for plant nutrition, but is very susceptible to moisture sorption and caking even at low moisture contents, e.g. 0.25% w/w. When urea particles adsorb moisture followed by drying, crystal bridges form between urea particles. For particles in a bed, this process is called caking. Cakes in stored urea cause a degradation of its quality and value. Investigations of the moisture absorption in beds of manufactured urea particles and adsorption on the external and internal surfaces of urea particles are a necessary step if engineers are to recommend procedures to reduce caking and control inventories.

Research on moisture adsorption and cake strength of urea fertilizer has not been sufficiently explored. Only recently have researchers started to devise tests to investigate the crystal bonding between two urea particles. Prior to this research, investigations of the moisture interactions in beds of urea were nearly non-existent. This thesis presents experimental, theoretical and numerical methods to investigate the coupled heat and moisture transfer processes in a bed of urea particles while the bed is exposed to ambient air with changing temperature and humidity.

Urea particles are nearly spherical with uniform particle size distribution. The particle size, its internal pore structure and rough crystalline external surface depend on the manufacturing process. In this thesis, two types of urea products are investigated, i.e. Georgia urea and Terico urea. The rough external surface and internal pore structure of each particle makes the total surface area exposed to water much larger than similar smooth and solid spherical particles. Although Georgia urea has higher external surface area than Terico urea, the latter type has larger total surface area and internal pore volume. For both Terico urea and Georgia, the internal surface area dominates the water sorption process but the external moisture sorption of Georgia urea is more important than that of Terico urea.

All the water vapor interaction experiments were carried out with air flow through a test bed because it shortens the duration of each experiment to a few hours in most cases. A series of experiments with step changes in inlet air temperature and humidity for air flow through a urea bed indicated that the measured outlet air temperature and humidity responses, each at a specific air flow rate, reveals a typical exponential or transient time change that can be

characterized by a time constant. After formulating the theoretical problem for step changes in the inlet properties, the analytical solutions showed that the time constants of outlet response to whether a temperature step change or a humidity step change are functions of the convection coefficient and air velocity. The predicted outlet air temperature is determined by only one time constant for a temperature step change while it is determined by these two time constants for a humidity step change.

A new test cell with sampling test ports was developed to measure the transient moisture uptake of a urea particle bed and its distribution at any time without any interruption of the experiment. A novel particle sampling device, modified from a syringe and pistons, was designed to minimize the particle exposure to ambient air during the moisture content determination using a Karl Fischer titrator. Data from two continuous cyclic step changes in the inlet flow with relative humidities between 4% and 70% at room temperature showed a hysteresis in the isothermal moisture content for only the first cycle. After the second sorption-desorption cycle, the hysteresis disappeared. This implies that the internal pore and particle surface geometry changes are very slow after the first cycle.

A new theoretical porous media model was developed for a coupled heat and moisture transport process when humid air flowed uniformly through a large test bed in two coupled computational domains: internal domain (i.e., the particle phase) and the external domain (i.e., the interstitial air space). The moisture migration in two computational domains included: water vapor diffusion inside each particle, and water vapor convection and diffusion in the interstitial air space in the urea particle bed. For energy transport, the temperature was assumed to be uniform inside each particle, but heat convection and conduction between the urea particles and the interstitial air outside particles occurred throughout the bed. Both heat transfer and mass transfer in internal domain and external domain were coupled by the heat and mass convection at the gas-particle interface. The numerical simulation was compared with the data of moisture uptake and showed good agreement implying that the internal moisture diffusion that dominates the moisture uptake process is a very slow process.

These above experimental, theoretical and numerical research studies provide a set of information on how urea particles adsorb or desorb moisture from or to ambient air on the external and internal pore surface, which offers a useful suggestion for urea caking prevention and is also a first and necessary step to the study of further caking formation and strength.

ACKNOWLEDGEMENTS

My sincere thanks and appreciations are extended to my supervisors Professor emeritus R.W. Besant and Professor R.W. Evitts. Thank you for your guidance and support throughout this research.

Thanks also go to my committee members - Porfessor L. Tabil, Professor C. Simonson and Professor D. Torvi for your suggestions and comments on my thesis.

I am also grateful to Mr. Chris James, Mr. Dave Deutscher, Dr. Ramin Azargohar, Mr. Tom Bonli, Mr. Bill Crerar, Mr. Yang Shuai, Mr. Glyn Kennell, Mr. John Bolster for their help during my experimental work.

Scholarship from the university and the department, and financial assistance from Potash Corporation of Saskatchewan (PCS) and Natural Sciences and Engineering Research Council (NSERC) are also acknowledged and appreciated.

DEDICATION

I dedicate this thesis my husband - Houtian Frank Ge, and my daughter - Athena Qianya Nie. Thank you for your love.

TABLE OF CONTENTS

LIST OF TABLES

LIST OF FIGURES

NOMENCLATURE

ACRONYMS

MC	Moisture Content
RH	Relative Humidity
CRH	Critical relative humidity

ROMAN SYMBOLS

A	Cross section area of the pipe or test container, m^2
A_b	Cross section area of the bed or nominal contact area for particle bed, m^2
A_{fs}	Fluid-gas interstitial area, m^2
A_m	Specific surface area based on mass, m^2/kg or m^2/g
A_p	External area of one particle, m^2
A_v	Specific surface area based on bed volume, m^2/m^3
A_{vs}	Specific surface area based on solid volume, m^2/m^3
$a \sim d$	Coefficients
B	Bias error
b	Side length of one crystal cube on the urea surface
Bi	Biot number
C	Correction coefficient; BET-C value
$C_1 \sim C_3, C_8 \sim C_{13}$	Coefficients
C_f	Shear stress coefficient
Cp	Specific heat capacity at constant pressure, J/(kg.K) or J/(mol.K)
D_c	Internal diameter of the test cell, m
D	Diameter or length, m; Molecular diffusivity, m^2/s
D^d	Dispersion coefficient, m^2/s
D^t	Total diffusivity including molecular diffusivity and dispersion effect, m^2/s
d	Diameter, m or mm
$\overline{d}$	Average diameter, m or mm
dr	Size step, mm or m
dx	Size step, mm or m

dt	Time step, s
e	Surface emissivity, 0~1
f	Friction factor; Ratio; Coefficient;
$f(t)$	Time dependent function
Gr	Grashol number
g	Functions; Gravity, m^2/s
H_{fg}	Heat of water-vapor phase change, J/kg
H_s	Heat of solution, kJ/mol
h	Height of liquid in manometer for pressure measurement, m
$h_{b,c}$	Thermal contact conductance, W/K
h_m	Mass convection coefficient, m/s
h_t	Heat convection coefficient, $W/(m^2.K)$
h_w	Moisture adsorption heat, J/(kg)
$\dot{h}$	Convective heat flux per unit volume, W/m^3
i	Arbitrary integer index
Jh	Chilton-Colburn factor for heat transfer
Jm	Chilton-Colburn factor for mass transfer
K	Thermal conductivity of fluid, W/(m.K); Permeability, m^2/s
K^d	Additional thermal conductivity due to dispersion, W/(m.K);
K^t	Total thermal conductivity of fluid including dispersion effect, W/(m.K);
k	Particle size distribution coefficient
k_B	Boltzman constant, $k_B = 1.381 \times 10^{-23}$ J/K
k_k	Kozeny constant
L	Bed length, m
Le	Lewis number
M	Mass, kg or g
M_A	Molecular weight, g/mole
M_u	The total mass of urea particles in the bed, kg
$\dot{m}_a$	Mass flow rate of air, kg/s
$\dot{m}_w$	Moisture adsorption rate of urea particles, kg/s

$\dot{m}$	Phase change rate of water, kg/(m^3.s)
$\overline{\dot{m}}$	Average phase change rate of water, kg/(m^3.s)
N	Number of samples for statistical analysis; Number of nodes in simulation domains
n	Number of crystal layers on the external surface; Correlation coefficient
N_A	Avogadro constant
N_c	Number of crystal cubes on one urea particle surface
N_s	Number of spherical particles in the bed
Nu	Nusselt number
P	Precision error; Perimeter of the pipe, m; Pressure, Pa
P_o	initial adsorbate gas (N_2 or Kr) absolute saturation pressure at 77 K, Pa
Pe	Peclet number
Pr	Prandtl number
P_u	Vapor pressure of solid urea, Pa
$\dot{Q}_a$	Volumetric air flow rate, Lpm
$\dot{q}$	Heat flux,
R	Radius of a particle, m or mm; gas constant, J/(kg.K); thermal resistance, K/W
Ra	Raleigh number
R_m	Collision radius of the molecule, $\overset{o}{\text{A}}$
R/l	The ratio of curvature to spherical particle diameter
R^2	The coefficient of determination
r	Radial position in a particle, m or mm
Re	Reynolds number
S	Standard error; Source term
SEE	Standard error of estimator
Sc	Schmit number
Sh	Sherwood number
St	Stanton number for heat transfer
St_m	Stanton number for mass transfer
T	Temperature, K or ^oC
$\overline{T}$	Average temperature, K or ^oC
$\hat{T}$	Estimated temperature, K or ^oC

t Time, s or h; Student t; Thickness, $\overset{o}{A}$

t_m Peak time

U Uncertainty; cross-section area average fluid flow velocity, m/s

u_D Darcy velocity, m/s

u_p Pore velocity, m/s

V Volume of the bed, m^3

V_a volume of test gas taken up by sorption or released by desorption at STP, m^3

$V_{M,pore}$ Total adsorption pore volume inside urea particles measured by BET test (cm^3/g)

V_m volume of one complete mono-layer of adsorbed gas at STP, m^3

V_o molar volume of the gas, 0.22414 (m^3/mole)

V_p Volume of one particle, m^3

V_s Volume of solid, m^3

V_u Volume of urea particles in the bed, m^3

W Humidity ratio of air

$\overline{W}$ Average humidity ratio

X Moisture content, g/g or w/w

$\overline{X}$ Average moisture content, g/g or w/w

x Axial position, m

$z_1 \sim z_4$ Variables for substitution

GREEK SYMBOLS

α Coefficient; thermal diffusivity, m^2/s

β Empirical coefficient to account for the non-equilibrium moisture transfer conditions; Expansion coefficient; Equation coefficient

β_s Solution of urea in water, mol/kg

σ The Stefan-Boltzmann Constant, $5.6703\ 10^{-8}$ (W/m^2K^4); Area of surface occupied by a single adsorbed gas molecule, m^2

ε Volume fraction; Porosity

ψ Sphericity

ϕ Relative humidity

$\Delta\phi$ Relative humidity change

φ Arbitrary property

λ Mean free path, $\overset{o}{\text{A}}$

ρ Density, kg/m^3;

$\overline{\rho}$ Average density, kg/m^3

θ Dimensionless property (temperature or relative humidity)

τ Time constant, second; tortuosity

τ_W Shear stress, Pa

Δr Size step, m or mm

ΔT Temperature change

ΔP Pressure drop, Pa

ΔX Bed depth, m or mm

Δx Size step, m or mm

μ Dynamic viscosity, Pa.s

ν Kinetic viscosity, m^2/s; Freedom

SUPERSCRIPTS

0 Initial time; Old time

0^+ Initial time after switching

0^- Initial time before switching

1 Present or new time

c Correction

cc Two times correction

max Maximum

T Temperature

SUBSCRIPTS

a Air; or in air

b Bed

C Interception for source term

c Contact; Conduction; Cold

d_h Hydraulic diameter, $d_h = 4\varepsilon_e / A_{v,e}$, m

ds Dry sample

dw distilled water

E East node

e	External domain; East face
ec	Empty cell
eff	Effective
G	Gravimetric method
g	Gas phase
h	Hydraulic; Hot
I	Inlet
i	Internal domain
ie	From external to internal domain
KF	Karl Fischer titrator
k	General subscript, mean temperature or relative humidity
L	Longitudinal
l	Liquid water
la	Liquid adsorbate
m	liquid used in manometer
N	North node
n	Coefficient; North face
O	Outlet
P	Present node; Slop for source term
p	Solid particle phase; Particle; Particle diameter
pe	From particle to external domain through the area boundary interfaces
r	Radiation
S	South node
s	Surface; Solid; Sample; South face
s'	Other solid
ssu	Saturated solution of urea
T	Temperature, or transverse
t	Total
ϕ	Relative humidity
u	Solid urea
us	Surface of solid urea particles
v	Water vapor
vs	Saturated water vapor

W	West node
w	Moisture; West face
ws	Solid urea particles with adsorbed moisture or wetted sample
X	Average moisture content
0	At initial time, or before initial time
0^+	Initial time after switching
0^-	Initial time before switching
∞	At infinite time, or at quasi-equilibrium state
0~5	Integer index

CHAPTER 1

INTRODUCTION

Terminology:

In this research study, the objective is to investigate the moisture sorption and desorption process within a bed of urea particles. It is unavoidable to frequently use terminology such as sorption, adsorption and absorption and desorption in this thesis. The terminologies used in this thesis are defined and explained below.

Sorption is adsorption or absorption process while desorption is the reverse process of sorption.

Absorption is the process of bonding or phase changing within a bed of solid particles or porous solid or liquid internally without a chemical reaction. For instance, a sponge can absorb water when it is initially dry. Water with an open surface can absorb gases such as CO_2, O_2 and N_2. When humid air enters into a bulk bed of urea particles, the urea particle bed can absorb moisture from humid air. When humid air diffuses into a porous urea particle, which is taken as another porous media, the urea particle absorbs moisture from humid air. Absorption results in a mass gain by the bed, porous solid or liquid, a phase change for the absorbed molecules and a change of internal energy or temperature.

Adsorption is a process of the molecules of a gas or liquid solute accumulating without a chemical reaction on a solid surface, more rarely, a liquid (adsorbent), forming a molecular or atomic film (the adsorbate). When moisture accumulates on the external surface of each urea particle after humid air enters into a bulk bed of urea particles, each urea particle surface adsorbs moisture.

When a bulk bed of urea particles are placed in presence of humid air, moisture absorption by the particle bed and moisture adsorption on the urea particle surface occur simultaneously.

1.1 General

Fertilizers are substances applied to the soil to supply essential plant nutrients. Crop yields are much higher where fertilizers are used than in cases where very little fertilizer is used. In Canada, the highest rates of fertilizer application and highest crop yields are in eastern Canada while the lowest are in the prairies where it is drier and the crop profits per unit area are lower. Among 17 elements essential for plant growth, nitrogen (N), phosphorus (P) and potassium (K) are three of the most important and commonly required nutrient elements while sulfur (S), calcium (Ca), magnesium (Mg), iron (Fe), copper (Cu), manganese (Mn), boron (B), and zinc (Zn) are less commonly required elements (McKenzie, 1998). Manufactured or commercial available fertilizer mixes are sold on the basis of the N, P and K content (expressed as percentages by mass). These usually contain a high proportion of one or more of these elements. For example, urea, a commonly used fertilizer, has the analysis 46-0-0, indicating that it contains 46% N but no P or K content. Maintaining the quality of urea during storage and transport is the main goal of this research.

As Elver and Hawkin (1996) summarized, the manufacturing process and properties of urea are well known. Urea, $(NH_2)_2CO$, is manufactured from ammonia (NH_3) and carbon-dioxide (CO_2). Carbon dioxide is obtained while manufacturing ammonia from coal or from other hydrocarbons such as natural gas and petroleum-derived raw materials. Urea can be manufactured as prills, granules, flakes, pellets, crystals, and in liquid water solutions. Solid urea is produced as prills or granules in the commercial market. The commercial synthesis of urea from ammonia and carbon dioxide is produced in a process called the Bosch-Meiser urea process that includes two principal reactions. The first reaction is a fast exothermic process that combines ammonia and carbon dioxide at high pressure to form ammomium carbamate ($H_2N\text{-}COONH_4$), while the second reaction is a slow endothermic process where the ammomium carbamate is subsequently dehydrated by using heat to form urea and water. The chemical reactions are written as:

$$2NH_3 + CO_2 \leftrightarrow H_2N\text{-}COONH_4 \leftrightarrow (NH_2)_2CO + H_2O \qquad (1\text{-}1)$$

The first reaction will essentially go to completion under typical reaction conditions. The second reaction will not go to completion. The conversion on a CO_2 basis is usually in the order of 50-80%. This conversion increases with an increasing temperature and NH_3/CO_2 ratio and decreases with an increasing H_2O/CO_2 ratio. During the manufacturing process, ammonia

and carbon dioxide are fed to the synthesis reactor operating at around 180-210^{o}C and 15 MPa pressure (Bress and Packbier, 1977). The reaction mixture, containing ammonia, ammonium carbamate and urea, is first stripped of the ammonia and the resultant solution passes through a number of decomposers operating at progressively reduced pressures. Here the unconverted ammomium carbamate is decomposed back to ammonia and carbon dioxide and recycled to the reactor (Bress and Packbier, 1977). The urea solution is concentrated by evaporation or crystallisation, and the crystals are melted to produce urea in the form of prills or granules. Prills are made by spraying molten liquid urea droplets from the top of a high tower where they drop and solidify to form solid prills as they pass through a counter current cool air stream. Granular urea is formed by spraying smaller molten urea droplets into a mixture of dried urea particles and fines such that larger particles are formed by agglomeration process in a rotating drum.

Both prill and granular urea particles are in nearly spherical shape and particle diameters range between 1 and 3 mm, which is similar to many agricultural seed sizes. Figure 1.1 shows the samples of solid urea particles where Figure 1.1 (a) is a small pile of Georgia urea, a prill urea product from PCS (Potash Corporation of Saskatchewan) manufactured in Georgia Island, GA, USA, and Figure 1.1 (b) is a Terico urea pile, a granular urea product manufactured by Agrium Inc. in Calgary, AB, CANADA. The traditional sieving method, used to estimate the weighted average particle size for a bed of particles with wide range of particle size, is not suitable for the measurement of urea particle sizes.

(a) Prill Georgia urea pile (b) Granular Terico urea pile

Figure 1.1 Samples of urea particles.

Although urea particles are in nearly spherical shape, variance in the shape is visible especially when an image system is used to acquire 2-D images of urea particles. Blob analysis can be used to search an object and produce information about its 2-D image as shown in Figure 1.2. During blob analysis, a series of processing operations are required, including the setup of background criteria. A blob, also called binary large object, is an area of touching pixels with the same logical color state. All non-zero pixels in a binary image are in a foreground state while all other zero pixels are in a background state. A pile of Terico urea particles and a pile of Georgia urea particles (about one hundred particles respectively) were randomly selected from the storage bag to have blob analysis for particle size determination. Figure 1.2 shows typical 2-D images of urea particles. It is clear that both the prill urea and granular urea particles are nearly spherical in shape, and are of similar sizes. Using blob analysis, the average particle size of prill Georgia urea were measured to be 1.82±0.06 mm while the granular Terico urea particles were measured to be 2.21±0.06 mm both at 95% confidence level. Prill urea particles in Figure 1.2(a) are more spherical compared to granular urea particles in Figure 1.2(b). The sphericity (see definition in section B.3 of Appendix B) of urea particles was estimated to be 0.68~0.92. 2-D binary image of urea particles, shown in Figure 1.2, implies that the sphericity of Georgia urea particle is higher than Terico urea particles.

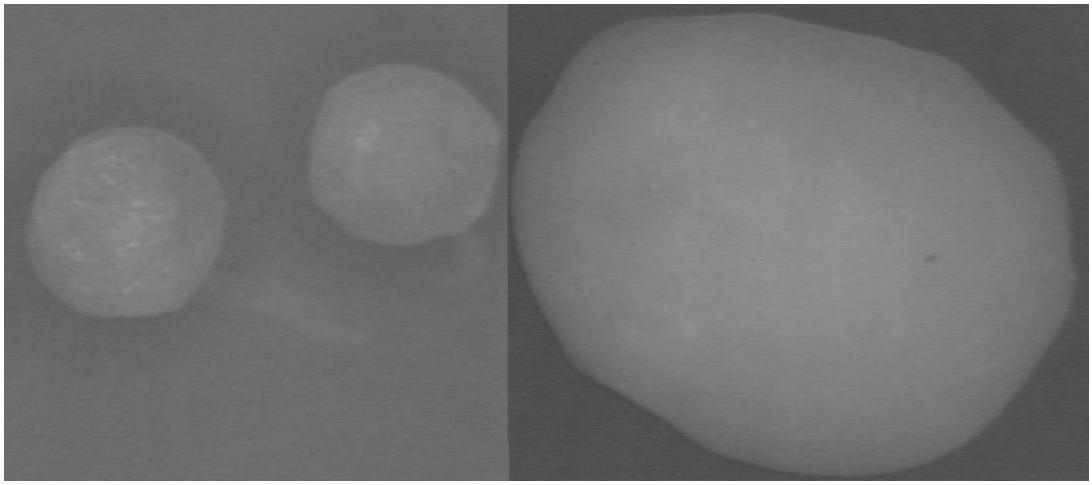

(a) Two Georgia urea particles, $\overline{d}_p = 1.82 \pm 0.06$ mm

(b) A Terico urea particle, $\overline{d}_p = 2.21 \pm 0.06$ mm

Figure 1.2 2-D binary images of urea particles.

Like most fertilizer products, urea particles adsorb moisture from the environmental atmosphere. Urea particles are very susceptible to moisture adsorption, decomposition, and caking even at moisture contents as low as 0.25% w/w during transportation and storage processes. The moisture absorption of the urea bed and adsorption on the urea surface is the main focus of this thesis. Moisture sorption and desorption performance of urea particles are determined by exposing the bed to a humid air environment.

1.2 Characteristics of urea particles

1.2.1 Porous structure

Porous structure inside each type of urea particle is produced during the solidification process of molten urea droplets at high temperature. For prill urea, the solidification rate of molten urea droplets passing through the cooling air flow in the cooling tower is not uniform radially in each droplet. For granular urea, a mixture of dried urea seed particles and slightly molten or sticky particles and fines are combined in a rotating drum where the seeds gather or agglomerate the sticky urea droplets. Both production methods result in internal pores in each particle.

A JEOL 840A scanning electron microscope (also called SEM, manufactured by JEOL Ltd. in Tokyo, Japan) was used to investigate typical urea particle external and fracture surface topography of urea. Before scanning, urea particle samples, external surface and sliced fracture surface, were coated with a thin film of gold under vacuum conditions to increase the electrical conductivity of the surfaces. A high-energy beam of electrons was used to sputter the surface of urea particles. The sputtered electrons interacted with the gold atoms coated on the urea surface or fracture surface which resulted in signals containing information about the surface topography.

Figure 1.3 is a collection of the SEM pictures of external surface and fracture surface of dry Georgia and Terico urea particles. It can be seen clearly that urea crystals with characteristic lengths of a few μm gather on the external particle surface and the internal fracture surface, forming a rough external surface and tortorous interconnected air paths inside each particle.

The crystals on the outer surface of the Terico urea appear to be several times larger than those on the Georgia urea. Compared with Georgia urea particles, Terico urea particles have bigger pores and higher internal porosity.

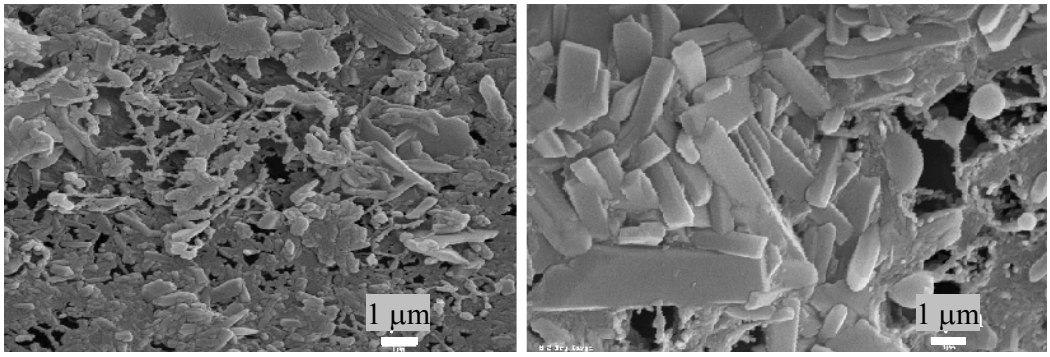

(a) External surface of Georgia urea particle (b) External surface of Terico urea particle

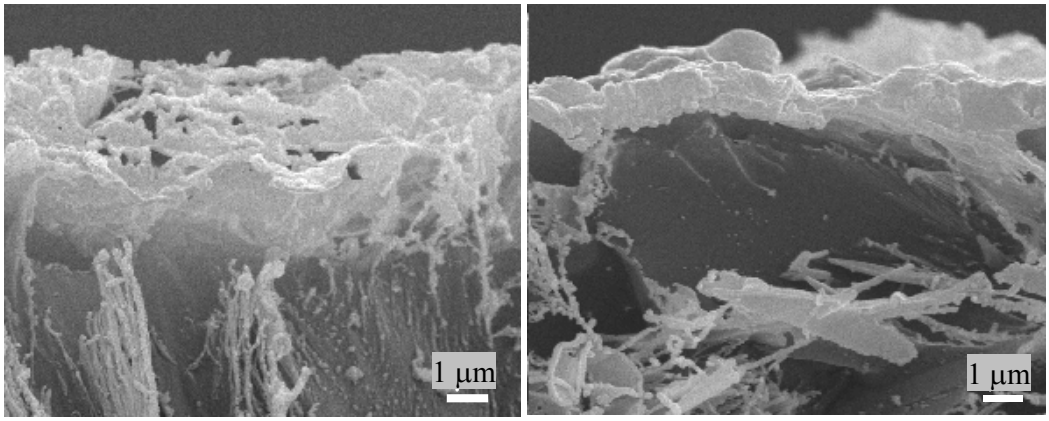

(c) Internal fracture of Georgia urea particle (d) Internal fracture of Terico urea particle

Figure 1.3 SEM pictures of urea particles.

1.2.2 Thermodynamic physical properties

Pure urea is white and odorless at room temperature. Its physical properties are dependent on the temperature. The melting point of urea is 132.6^{o}C. In the temperature range of 133 to 150^{o}C, i.e. above the melting point, both density and dynamic viscosity of urea melt decrease with an increase in temperature. For urea in the solid phase, the density, molar heat capacity

and vapor pressure of solid phase are functions of temperature as shown in the following equations.

The density of solid phase is temperature dependent (Elvers and Hawkin, 1996).

$$\rho_u = 1396.0 - 0.208 \times T \ \ (\text{kg/m}^3) \tag{1-2}$$

where T is temperature in K. The molar heat capacity of solid phase in temperature 240-400 K is calculated by (Elver and Hawkin, 1996)

$$Cp_u = 38.43 + 4.98 \times 10^{-2} T + 7.05 \times 10^{-4} T^2 - 8.61 \times 10^{-7} T^3 \ \ (\text{J/(K.mol)} \tag{1-3}$$

where T has the units of K.

The vapor pressure of the solid phase in the temperature range of 56 to 130^{o}C is a function of temperature (Elver and Hawkin, 1996).

$$\ln P_u = 32.472 - 11755 / T \tag{1-4}$$

where P_u is in Pa and T is temperature in K.

The water vapor pressure of a saturated solution of urea in a temperature 10-80^{o}C can be calculated as following equation (1-5) (Elver and Hawkin, 1996).

$$\ln P_{v.ssu} = 175.766 - 11552 / T - 22.679 \ln T \tag{1-5}$$

where the units in equation (1-5) are the same as equation (1-4).

The critical relative humidity ratio (CRH) is defined as a threshold relative humidity, below which solid urea can adsorb moisture till a equilibrium state but above which solid urea can adsorb moisture from ambient air continuously until the solid is completely dissolved. CRH is calculated as the ratio of the water vapor pressure of a saturated urea solution, $P_{v,ssu}$, to the saturated water vapor pressure, P_{vs} (Elvers and Hawkin, 1996).

$$\text{CRH} = \frac{P_{v,ssu}}{P_{vs}} \tag{1-6}$$

where P_{vs}, is saturation pressure of water vapor (Pa) which is a function of temperature (ASHRAE 2004).

$$P_{vs} = \exp\left(C_8 / T + C_9 + C_{10}T + C_{11}T^2 + C_{12}T^3 + C_{13}\ln T\right) \quad (1\text{-}7)$$

where T is absolute temperature in K, constants C_8 =-5.8002006e+03, C_9 =1.3914993,

C_{10}=-4.8640239e-02, C_{11}=401764768e-05, C_{12} =-1.4452093e-08 and C_{13}=6.5459673.

Then the CRH can be estimated with equation (1-5), (1-6) and (1-7) as shown in Table 1.1. CRH of urea decreases with increasing temperature.

Table 1.1 Vapor pressure of a saturated urea solution ($P_{v,ssu}$) and critical relative humidity (CRH) of urea at different temperatures (Elver and Hawkin, 1996)

Temperature (°C)	$P_{v,ssu}$ (Pa)	(CRH)
20	1858.1	0.783
25	2451.9	0.770
30	3185.9	0.753
35	4079.7	0.733
40	5152.9	0.710
45	6424.2	0.684
50	7910.8	0.656
55	9628.3	0.627
60	11589.5	0.597

Urea is very soluble in water. This high solubility is caused by its extensive hydrogen bonding with water molecules. Hydrogen bonding is caused by the attractive force between the hydrogen, attached to electronegative atoms of one molecule (e.g. H_2O), and an electronegative atom of a different molecule (e.g. urea). Hydrogen in water molecules has a polarity that is positive while the electronegative atoms that have a negative polarity in urea are nitrogen and oxygen. For urea, this hydrogen bond is a strong fixed dipole-dipole van der

Waals-Keesom force, but it is a weaker bond than covalent, ionic and metallic bonds between atoms of, for example, salt molecules. For interactions between urea and water molecules up to eight hydrogen bonds may form as shown in Figure 1.4 - two from the oxygen atom, one from each hydrogen atoms and one from each nitrogen atom. Solubility of urea particles is dependent on the temperature of the solution. Table 1.2 shows solubility of urea at several temperatures (Meessen, 1996).

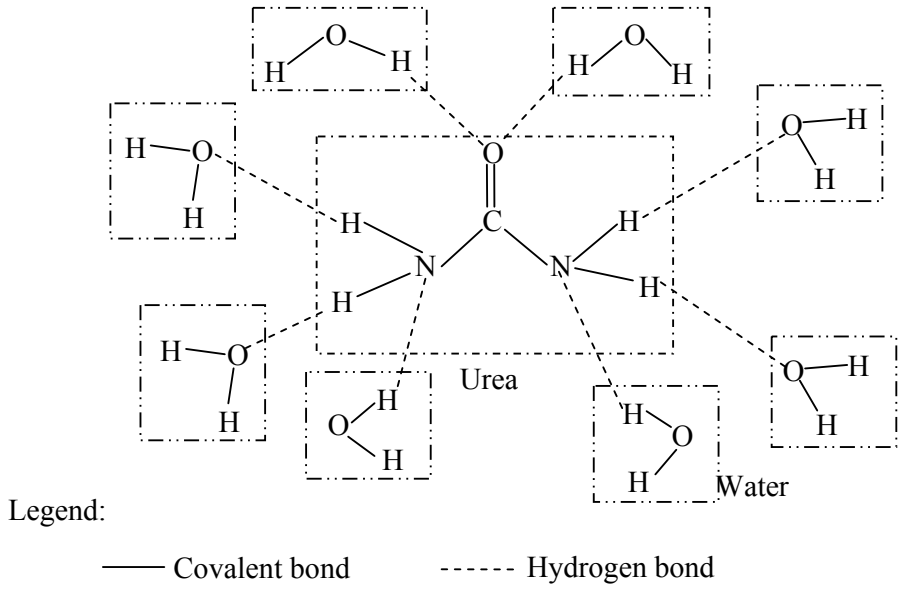

Figure 1.4 2-D schematic diagram showing eight hydrogen bonds of one urea molecule (Jeffrey, 1997)

Table 1.2 Solubility of urea in water at different temperatures (Elver and Hawkin, 1996)

Temperature (^{o}C)	Solubility (g urea /g water)
20	1.08
30	1.34
40	1.65
50	2.05
60	4.54

1.2.3 Chemical properties

Urea can easily hydrolyze back to its manufacturing input chemicals, ammonia and carbon dioxide. Even with a very small amount of moisture, urea can release ammonia. Urea tends to be chemically unstable at high temperatures because it will decompose at temperatures above 70^{o}C. This makes the gravimetric drying method invalid as a method to determine the moisture content of urea particles. Two urea molecules can be combined to release ammonia and form biuret – the most common impurity of urea. Biuret content should be less than 2% by mass of urea because it is not good for plant growth (Elvers and Hawkin, 1996).

1.3 Factors related to fertilizer moisture adsorption and caking

There are many factors that influence the rate and extent of urea's moisture adsorption and caking including: particle size and packing, moisture content, ambient air humidity, bed pressure and temperature.

1.3.1 Particle size and packing

It is the distribution of particle size and how particles are packed that can influence the number of contact points between particles and the total solid-fluid surface area in a bed. In a consolidated bed, the wider the range of particle sizes, the tighter the packing or the smaller the void fraction (i.e., porosity), the more the number of contact points and the larger the contact area per unit volume of bed. Larger solid-fluid surface area means the larger surface area available for one or multi-layer moisture adsorption and more contact points or area means the higher potential cake strength of crystal bridges. The number of contact points between particles in a bed depends on particle shape, particle size and particle packing. A decrease of particle size will cause an increase in number of contact points between particles per unit volume. Since the surface area of a spherical particle is proportional to the square of the diameter while the volume varies with the cube of diameters, the smaller the particle diameter, the larger the specific surface area.

Urea particles are produced in a nearly spherical shape with a diameter of usually 1 to 3 mm. The 2-D image analysis method was used to determine the particle size. Georgia urea particles were measured to be 1.82±0.06 mm, while Terico urea particles were measured to be

2.21±0.06 mm at 95% confidence level. This implies that urea products are not only uniform in shape but also have a very narrow range of particle sizes. Therefore, the effect of particle size and packing on caking strength is negligible for urea particle beds from one manufacturer. For sphere-like urea particles of a similar size, a Georgia urea particle bed with small particle diameters has a large specific surface area and much more contact points or larger contact area compared to a Terico urea particle bed with larger particle diameters. For a randomly packed bed of spherical particles, the bed porosity typically ranges from 0.359 (close random packing) to 0.44 (very loose random packing) (Dullien, 1992).

However, if the bed is filled with urea particles with different particle diameters, or if part of the urea particles in a bed are ground into smaller ones due to the static pressure or other external forces, the bed of urea particles can be packed tighter, causing an increase in contact point numbers and contact areas per unit volume of bed. Increased contact point numbers and contact point areas are expected to increase the cake strength.

1.3.2 Moisture content

Caking only occurs with the presence of moisture. When urea particles adsorb moisture followed by subsequent drying, crystal bridges form between urea particles. If there is no moisture content, no caking occurs. Urea fertilizer is very susceptible to moisture adsorption and caking even at moisture contents of 0.25% w/w. To maintain high quality urea fertilizer, it is important to keep the moisture content of the finished urea products during manufacturing process as low as possible. During shipping and storage processes, some effective methods or precautions are taken to prevent or reduce urea fertilizer moisture penetration, such as the use of sealed water-proof shipping and storage bags, dry and cool ambient air storage conditions away from heat or moisture sources.

1.3.3 Relative humidity

Relative humidity of the adjacent air is another key factor as important as moisture content for caking, because water vapor, which can be adsorbed by urea particles, is determined by the relative humidity at a known temperature. When a dry urea sample is exposed to humid air with a relative humidity lower than the critical relative humidity (saturation point), urea will adsorb some water vapor by means of van der Waals forces and a monolayer or multi-layers of adsorbed water may exist on the surface. The equilibrium moisture content below the

critical relative humidity is finite. However, when the relative humidity exceeds the critical relative humidity, urea particles will adsorb moisture continuously and completely dissolve if the relative humidity in the adjacent air remains above the critical value. During storage and transport processes, the urea particle piles or beds could experience a wide range of change in air relative humidity due to environmental temperature and humidity fluctuations. Even when urea is shipped and stored in sealed polyethylene bags, some moisture can diffuse through microscopic pores of each bag to cause adsorption, decomposition and caking over long storage times. Under frequent diurnal changes in relative humidity, urea fertilizer will be subject to a series of cycles of adsorption, desorption, partial dissolution and evaporation without reaching a steady state.

1.3.4 Pressure

Pressure, whether hydrostatic pressure or external pressure, is a common factor causing caking in piles of urea fertilizer. Hydrostatic pressure at a certain position in a urea pile is proportional to the urea density and height of urea particles above this specific position of the urea bed. An increase of pressure means tight packing, an increase in number of the contact points between particles and an increase in total contact area in the urea piles. At the same condition of moisture content, high pressure provides the condition for high cake strength. In other words, caking can be reduced by controlling the height of urea piles.

1.3.5 Temperature

Temperature is another very important factor in the caking process because the moisture migration and accumulation in urea particle beds is highly coupled with heat transfer and temperature redistribution. Firstly, environmental air properties including both humidity and temperature have diurnal and seasonal variations. Secondly, the heat released during adsorption, condensation and dissolution will change the temperature of both the urea particles and the interstitial air between urea particles. Thirdly, the isothermal moisture adsorption / desorption characteristic with respect to environmental relative humidity decreases with an increase in air temperature, or increases with a decrease in temperature. Finally, when the ambient air temperature is changed but the absolute humidity of air remains constant, the relative humidity of the air will increase when the temperature drops and decreases when the air temperature increases. If urea particles undergo a wide range of

temperature variations, for example heating to a high temperature, especially after moisture adsorption, caking or growth of crystal bridges between particles will be a serious problem.

1.4 Literature review

Many papers and reports have been published concerning heat or moisture transport within porous media with experimental and theoretical/numerical methods in a variety of fields: new building materials (e.g. insulations and membranes), food, soil and even agricultural fertilizer such as potash. For fertilizers, cake strength measurement and caking prevention has attracted the interest of researchers and industry for over 30 years. Researchers have recently started the investigation on organic urea fertilizer including moisture uptake and transfer and caking.

In this thesis, investigations on heat and moisture transfer in solid particle beds are reviewed in section 1.4.1. Research studies on beds of particles with internal pore structure and rough surfaces are reviewed in section 1.4.2. Research studies on determination of convection coefficients and dispersion within particle beds are reviewed in section 1.4.3. Recent research works on inorganic fertilizer caking are reviewed in section 1.4.4. Research studies related to urea fertilizer's moisture adsorption and caking are reviewed in section 1.4.5.

1.4.1 Heat and moisture migration in solid particle beds

Kaviany (1995) reviewed theories developed for flow through porous media, including momentum, energy and mass transport equations. For heat transfer in porous media, local thermal equilibrium was assumed when local temperature differences between different phases was negligible. However, if heat generation existed in the solid or fluid phases, or when solid and fluid had significant different heat capacities and thermal capacities, thermal non-equilibrium theory between fluid and solid phases was used instead of local thermal equilibrium.

Peng et al. (1999) modeled the chemical thermodynamic state of potash with a mixture of three different salts of KCl, NaCl and $MgCl_2$. In their analysis, the Pitzer (ion-interaction) model for these four ions was used to predict the isothermal adsorption and dissolution characteristics of potash fertilizer, i.e. the equilibrium moisture content of potash particle bed versus the adjacent air or solid surface relative humidity at different temperatures. Peng et al.

(2000) introduced this moisture adsorption and dissolution model of potash particles to the experimental and simulation of the coupled heat and mass transfer within a potash bed while it was subjected to humid air flow. An experimental test rig was designed to measure the air temperature and humidity at both the inlet and outlet, and mass gain of a potash bed subject to a step change in air flow through the bed. A theoretical model for the porous medium was set up and solved by numerical simulation with the finite difference method (FDM). The agreement between the experimental data and numerical simulation showed that non-equilibrium moisture and temperature distribution between the particle surface and interstitial space air existed along the bed length. The relatively high moisture dissolution ability of potash at relative humidity higher than 52%, due to a small fraction of $MgCl_2$ on the potash particle surfaces, caused a significant temperature rise for both solid and air phase along the bed and an outlet air humidity response delay.

Zhou (2000) measured the physical properties of each of six different types of potash products and measured the moisture accumulation in a test bed of two potash fertilizer products, standard and granular. A one-dimensional transient numerical model was developed to simulate coupled heat conduction and moisture diffusion in a test bed using local volume average (LVA) technique for adsorption/dissolution and condensation curve developed by Peng et al. (1999). Experimental data were compared to the numerical simulations for a variety of operating conditions and showed a good agreement.

Zili and Nasrallah (1999) presented a theoretical formulation for a forced convective drying process of granular products considering flow, heat and mass transfer for three different cases – piston flow, non-Darcian 1-D flow, and non-Darcian intermittent flow. Their model, solved numerically by the finite volume method (FVM), predicted the time-space variations of the fluid and solid temperatures and moisture content. The granular medium drying kinetics and the convective heat flux exchange with the exterior are investigated in the model. Comparison between three different cases indicated that intermittent flow had the best drying effect.

Chen et al. (2004) modeled the water film movement and accumulation in a potash bed governed by the effects of capillarity and gravity as well as vapor diffusion through the interstitial air space in a granular potash bed. An irreducible saturation was introduced to distinguish two totally different moisture migration mechanisms. If the local moisture saturation level was larger than irreducible saturation, capillarity and gravity dominated the liquid film movement in this wet region. If the local moisture saturation level was lower than

this irreducible saturation, water vapor diffusion dominated the moisture movement in this comparatively dry region of the bed. The average moisture content spatial distribution in three layers for different particle sizes under different initial moisture content was measured using a test facility to compare data with numerical simulations. The irreducible saturation was inversely determined by comparing simulations and data to be a function dependent on particle size – such that the irreducible saturation ratio decreased with the increase of particle size.

Li and Fan (2007) reported the transient heat and moisture transfer behaviour in clothing insulation made of fibrous battings and covering fabrics using numerical method. A dynamic moisture adsorption process and moisture bulk movement were combined with liquid condensation movement. The finite volume method was used to obtain the numerical simulation in which both the effect of condensate on porosity and permeability of fibrous battings were taken into account. The numerical analysis provided guidance on how to select comfort clothing fibers for cold weather conditions – inner fiber of clothing with a high emissivity, high air permeability, low dispersion coefficient of surface water, low moisture adsorption was preferred in winter for less condensation and moisture adsorption. In addition, the covering fabrics influenced the moisture content of the fibrous batting.

All the above research investigations were based on the porous medium of solid particles or fibres, but these particles were solid without any porous structure inside. This meant that all moisture accumulation only happened on the external surface of each particle and a very thin layer of liquid film may form, especially near contact points.

1.4.2 Beds of particles with internal pore structure

In the past, silica gel (SiO_2), a well-known granular desiccant, was investigated in the removal of moisture from confined spaces in energy wheel. The very large internal surface area inside each silica gel particle provided a large capacity of moisture storage. Pesaran et al. (1987a and b) simulated heat and mass transfer of airborne moisture into a thin bed of silica gel particles using a model which accounted for the different internal particle diffusion properties. It was indicated that surface diffusion was dominant for macro-porous silica gel while both surface diffusion and Knudsen diffusion were important for micro-porous silica gel.

Whitaker (1988) developed a method to derive porous particle effective diffusivity that could

not be determined by direct experimental methods. His theoretical analysis based on diffusion process in two regions was developed to derive the overall effective diffusivity for packed beds of porous particles which was found to be dependent on the bed porosity and diffusivity ratio of two regions. Therefore the particle effective diffusivity, which is the effective diffusivity within an individual porous particle with internal pores, could be inversely extracted from the comparison of experimental and theoretical overall effective diffusivity for packed beds. Subsequently, the internal tortuosity of the particle bed was calculated based on the determined particle bed effective diffusivity.

Grathwohl (1998) summarized the internal diffusion-controlled sorption process of a pure liquid or gas inside natural porous media such as soil. The apparent diffusion coefficient used for the transient diffusion process consisted of pore diffusion and surface diffusion. It was difficult to distinguish these two kinds of diffusion modes because they occurred simultaneously. Surface diffusion in one adsorption layer on the pore wall resulted in an additional mass transfer in the direction opposite to the increase of surface concentration. When the attractive force from the surface decreased with the multi-molecular adsorption layers compared to just mono-molecule layer, the contribution of surface diffusion increased.

Sun and Besant (2005) investigated the convection of moist air through a bed of silica gel numerically and experimentally and showed good agreement. A separated theoretical model for mass diffusion within a spherical particle was developed to derive an analytical result indicating that the apparent internal diffusion coefficient inside silica gel particles was much smaller than the diffusion coefficient in the interstitial air between the particles. However, internal moisture diffusion within each particle was not embedded into the moisture migration along the silica gel bed.

Chen et al. (2006 and 2007) investigated the moisture adsorption characteristics of a thin bed of porous polycrystalline potash pellets or granules. A polycrystalline potash pellet consisted of a solid core with the outer porous layer comprised of much smaller particles. The pore structure in the outer layer of a polycrystalline potash pellet caused a delay in the moisture adsorption process compared with the solid potash particles with no pores. The sorption experiments of potash granules were carried out in a series of sealed jars each of which contained a saturated salt solution that provided an air environment with constant relative humidity. This experimental transient adsorption curve of a few particles was curve fitted and

then directly introduced into the simulation to account for the delay in moisture adsorption caused by the porous structure.

It seems there is a need for a new theoretical model to account for moisture movements in two separated domains - interstitial air space or external region of particles in a bed and internal pore space or internal void region inside each particle and its outer surface including any accumulated absorbed water. These two domains are coupled because the interstitial air has a convective boundary interface on each particle which is coupled with its internal void space.

1.4.3 Convection coefficients using the analogies of momentum, heat and mass transfer

Shah and London (1978) proposed that the Nusselt number should only depend on Reynolds number, Prandtl number and the geometry of the air flow passages They also showed a fixed constant ratio between the Nusselt number and the product of the laminar flow friction factor and Reynolds number for flow in channels or cylinders.

Both Arpaci and Larsen (1984) and Bejan (2004) reviewed and listed the effect of flow cross-sectional shape, such as circular, square, equilateral triangle, rectangular, infinite parallel plate, on friction and Nusselt number for fully developed duct flow. It was shown that for fully developed laminar flow where Reynolds number was less than 2000 in a duct with specified cross-section shape, the product of friction factor and Reynolds number was a constant and Nusselt number was another constant. Thus, the convection coefficients depended only on the viscous velocity field of the fully developed flow. Due to the analogy of momentum and heat to mass transfer, the Sherwood number was a constant too when the moisture content of the interstitial air was low.

These analogies of momentum and heat and mass transfer are valid when extended to porous media such as spherical particle beds. Ergun (1952) suggested a general correlation for any flow conditions within particle beds based on experimental data covering a wide range of size and particle shapes and indicated that for fully laminar flow (i.e., $Re < 10$) the product of friction factor and Reynolds number in a spherical particle bed is almost a constant while for transition or turbulent flow the product of friction factor and Reynolds number increases with an increase in Reynolds number (i.e., $Re > 10$). As well, the correlation for non-spherical particle beds was extended. Macdonald et al. (1979) considered the cases for both smooth

particle beds and very rough particle beds and indicated that roughness of particle surface apparently increased the friction.

Kumar et al. (1977) measured and calculated the mass convection data at Reynolds number range of 0.01 to 600 based on the dissolution process of packed bed of cylindrical pellets of benzoic acid in water and 60% aqueous propylene glycol solution. Correlations of Reynolds number, Schmidt number and Sherwood numbers were presented to help determine the mass convection coefficients. At very low Reynolds number that natural convection dominated over forced convection, an asymptotic correlation was developed for both spherical and non-spherical packed beds. When Reynolds number approached zero, the Sherwood number was constant. This correlation of mass transfer should be valid for the heat transfer also because heat and mass transfer were analogous.

Theories have been developed for hydrodynamic dispersion, also called "mechanically convective diffusion", within porous media using statistical methods. Saffman (1959 and 1960) analyzed random walk in an assemblage of randomly straight pores and assumed that the marked elements moved along the path in a sequence of statistically independent steps which meant that movement direction and duration in each step proceeded in a specified random manner. Both longitudinal and lateral dispersion coefficient value was calculated based on the probability density function for movement of each single marked element. At low Peclet number ($Pe<<1$) where convection was negligible, the ratio of the dispersion coefficient to the molecular diffusivity or diffusion coefficient was a constant with a magnitude around 2/3, which agreed well with the experimental data. The ratio of the transverse dispersion coefficient to the molecular diffusion coefficient, for this same range of Peclet numbers, depended on whether the particle positions were random or geometrically cyclic in the bed. If the particle positions were cyclic, the transverse dispersion depended only on the molecular diffusion coefficient with a value close to 2/3, but if they were random this value was 1/3. At high Peclet number ($Pe>>1$), Saffman (1959) over predicted the transverse dispersion by a considerable amount compared to the experimental data but showed parallel trend lines with increasing Reynolds number. Saffman (1960) suspected that a statistical correlation of successive porosity considering the lateral displacement of streamline could account for this discrepancy. These theoretical studies implied another analogy among each ratio of dispersion coefficient to molecular diffusion coefficient, the product of Reynolds number and friction coefficient, Nusselt number and Sherwood number.

Wakao and Funazkri (1978) used a series of reported experimental data, mostly in transient evaporation, sublimation and dissolution processes but considered as steady processes, and pointed that without consideration of axial dispersion, the estimated mass diffusion coefficient or Sherwood number was low. It was proposed that the axial fluid effective dispersion coefficient was a function of Schmidt number, Reynolds number and molecular diffusivity. For Reynolds number range in 3 to 10,000, mass convection coefficient should be corrected based on an empirically determined axial effective dispersion coefficient, $Sh=2+1.1Sc^{1/3}Re^{0.6}$. When Reynolds number was less than three, natural convection could take effects. Wakao et al. (1979) proposed the corrected correlation of Nusselt number in the range of Reynolds number from 15 to 8,500 after considering the axial dispersion $Nu=2+1.1\ Pr^{1/3}Re^{0.6}$.

Wakao and Kaguei (1982) presented three correlations based on two-medium, fluid and solid, treatment of single-phase flow for transient heat transfer within packed beds of spherical particles to find the interfacial convective heat transfer coefficients for one dimensional Darcian flow. The simplified Schumann model (Wakao and Kaguei, 1982) ignored the transient effects and the axial heat conduction in both solid and fluid phases. Their continuous-solid model took into account the axial heat conduction of fluid and solid separately (i.e. decoupled from the fluid flow), but dispersion was not considered. The dispersion-particle-based model improved the continuous-solid model by including the dispersion effect and temperature gradient within each particle, but not the transient effects; however, the thermal capacitance effects and heat conduction along particle layers caused by particle contact were both ignored.

Koch and Brady (1985) examined the dispersion in fixed beds such as spherical particle beds. Three different types of dispersion at high Peclet number were investigated: (1) Pure mechanical dispersion, neglecting the flow near and inside particles, was proportional to velocity, U, and independent of molecular diffusion. (2) Hold-up dispersion, occurring in the trapped region, for example, interior of the solid and region of stagnant or re-circulating fluid, increases with square velocity, U^2; but for impermeable particle, hold-up dispersion is absent. (3) Boundary layer dispersion, occurring near solid surfaces where convection and molecular diffusion took effect, increases with $U\times\ln(U)$. The theoretically predicted values of effective diffusivity in transverse and longitudinal direction were compared with the previously reported experimental data and showed good agreement. Koch et al. (1989) investigated the effect of spatial periodicity in grain structure on the dispersion at low and high Peclet number,

respectively. It was shown that at low Peclet number, the dispersion was similar in ordered and disordered porous media. However, at high Peclet number, dispersion owing to fluid motion in a disordered porous media existed and this macroscopic transport was caused by the microscale mechanical process where particle velocity disturbance was uncorrelated with initial position of particles when the fluid particle was convected through the random microstructure. For ordered media at high Peclet number, the dispersion owing to fluid motion was absent because microstructure was spatially periodic.

Rexwinkel et al. (1997) presented a model that combined the effects of axial dispersion and the bias of flow channeling near the wall of the test cell to explain that the Sherwood number was much lower than the minimum value when the Peclet number was lower than 100 for undiluted beds. However for diluted beds in which not all particles were active in mass transfer process, the apparent drop in mass transfer rate might have originated from misinterpretation of the experimental results. It showed both experimentally and theoretically that low Sherwood numbers could be obtained when large differences existed between the local concentrations but the radial concentration profile was neglected. These models were based on stationary mass balance equations in which transient effects of mass storage were ignored.

1.4.4 Caking of inorganic fertilizers

Thompson (1972) proposed that there were four main mechanisms by which caking of product can occur: mechanical caking (caused by the interlocking or bird-nesting for fibrous and plate-shape particles, but not for spherical particles), plastic flow caking (for amorphous materials with high viscosity), chemical reactions (most common for products during recrystallization or dehydration process, such as the manufacturing of urea particles), and electrostatic attraction (for fine or powder). Urea fertilizer caking caused by humidity during the storage is crystal bridges at the contact point or contact area between particles if drying process follows, which can be considered as the results of continuing chemical reaction such as recrystallization or dehydration due to heat. A comprehensive review of caking in typical granular fertilizer products was presented. Some key factors, such as moisture content, pressure and temperature, were thought to be very important for the caking of granular fertilizers stored in plastic bags. It was concluded that crystal bridging was not a major cause of caking because stress was more important as it altered the solubility of salts and the pore pressure of thin aqueous films.

Wang et al. (2007) developed a centrifugal loading method to determine cake strength of particles packed into a sample ring of potash fertilizer in which the area-average tensile stress was determined at the speed of the centrifuge when each specimen fractured. A series of the cake strength measurement tests with different initial moisture contents, drying times, particle size and chemical composition showed that that the cake strength increased linearly with greater initial moisture content, but decreased with an increase in particle size. For a test ring of potash particles, higher magnesium content and slower drying process provided a stronger cake.

Wang et al. (2008a and b) developed a theoretical/numerical model to simulate crystal growth near one contact point between two potash (only considering KCl) particles during a typical drying process based on ion diffusion in a saturated or super-saturated liquid film near a contact point. The results showed that the mass of crystal deposition near particle-to-particle contact points increased with increased initial moisture content and decreased evaporation or drying rate. This prediction was consistent with the trend of experimental data for the cake strength measurements.

1.4.5 Caking of urea particles

Some research studies have been done on urea particles' manufacturing process, dissolution process in water (Petrescu et al., 1997) or urea crystal (Grdadolnik and Marechal, 2002). However, little research has been published on the moisture uptake and caking of urea. Recently some research groups started to focus on storage problem of granular or prill urea particles.

Brockel et al. (2008) designed a new experimental setup to investigate the bridge formation between two discrete particles at a few specific temperatures and humidities. Caking increased with an increase in either humidity or temperature. A state of matter diagram for urea particles showed the critical caking conditions of relative humidity, when urea particles started to cake or to dissolve during the moisture adsorption process at different air temperature.

Wahl et al. (2006) used a double-particle-system (DPS) stored in a climatic chamber to investigate the formation and growth of solid bridges between urea particles. The effects of load, temperature, humidity, storage time were considered while investigating the geometrical changes in the contact region between two discrete particles and therefore the strength of the

resulting inter-particle bridge. It indicated that after a short storage time a hollow bridge with a low tensile strength was formed while for long storage times, a persistent solid bridge was formed because the tensile strength of bridges increased with decreases of hollow spaces in the bridge. And an increase of temperature and humidity led to a greater bridge diameter, but only a slight increase of the tensile strength due to the hollow bridges.

1.5 Research objectives

The influence factors of caking strength and literature review mentioned above indicates the importance of developing a theoretical / numerical model of moisture migration within a urea particle bed while humid air flows through the bed. The physical process occurring in the urea test beds includes four steps: (1) air and water vapor moves through the urea bed by convection and pore diffusion in the interstitial space; (2) water vapor diffuses from the airflow in the interstitial space within the bed to the interstitial pore space on the urea particle surface by external convection; (3) water vapor diffuses radially within the internal pores inside particles; and (4) moisture sorption or desorption occurs on the external surface area and internal pore surfaces of each particle, and adsorbed or desorbed moisture from or to the environmental water vapor condenses or evaporates immediately on the surface. This liquid moisture moves through the external and the internal surfaces by surface diffusion. The proposed model which considers the physical transport process of moisture for both external and internal surface areas of each particle in a bed is expected to provide an improved prediction for urea storage under varying environmental humidity and temperature conditions.

The objectives established for this study are:

(1) to determine the fundamental physical properties of urea particles and particle beds and their uncertainties that are necessary for theoretical formulation and numerical simulation of the physical processes;

(2) to set up a theoretical model for the heat and mass transfer processes within the urea particle bed while humid air at low Reynolds number flows uniformly and steadily through the bed during a moisture transport process;

(3) to numerically predict the heat and moisture migration and accumulation process within a

urea bed while humid air flows through the bed at low Reynolds number, and compare the simulations with the experimental results; and specify the uncertainty of numerical predictions; and

(4) to obtain experimental data for inlet and outlet air humidity and temperature, and moisture content of a urea particle bed with humid air flow at low Reynolds number through the porous urea bed; and specify the uncertainty of the experimental data.

To achieve the above-mentioned objectives, the following procedural steps are required to implement the urea particle properties measurements for the moisture uptake experiments and the theoretical model development. These include:

(1) to experimentally determine the fundamental physical properties of urea particles or particle beds required to formulate moisture migration in porous urea particle beds, including particle size, permeability, internal and external porosity, internal and external specific surface area, isothermal moisture sorption / desorption characteristics etc. And specify their uncertainties;

(2) to determine effective way to handle urea particles to minimize the uncontrolled moisture-urea particles interactions while determining the moisture content of urea particles, and specifying the uncertainty of moisture content measurement;

(3) to design and construct an experimental test rig, which can be used to conduct a series of transient experiments on moisture accumulation process within a bed of urea particles so that the moisture distribution can be accurately measured at specified time without any interruption of experiments;

(4) using the test rig designed in (3), to directly obtain experimental data of the moisture uptake and transport in a bed of urea particles while humid air at low Reynolds number flows through; and specify the uncertainty of the experimental data;

(5) to develop a theoretical model for the moisture uptake and transport in a bed of urea particles that couples internal moisture diffusion inside each particle with the external moisture diffusion on the particle external surface area in the whole bed;

(6) to predict numerically the moisture uptake and transport in a bed of urea particles while humid air at low Reynolds number flows through, and compare them with the experimental results; and specify the uncertainty of numerical predictions;

(7) to determine the convective heat transfer coefficient within simple smooth and spherical particle beds (lead, glass, steel) which are subject to a pure temperature step change at the inlet based on the transient energy storage of particle beds, and compare the results with the literature;

(8) to conduct experiments on transient outlet air temperature response of a urea particle bed subject to a pure temperature step change at the inlet, investigate the relationship between the time constant and the convective heat transfer coefficient; and compare the results with (7);

(9) to conduct experiments on transient outlet air humidity response of a urea particle bed subject to a pure humidity step change at the inlet; and investigate a simple prediction method of transient moisture uptake of a urea particle bed without long period moisture content measurement .

1.6 Overview of thesis

Chapter 2 presents the details of a series of experiments to determine the outlet air temperature/ humidity of a urea particle bed subject to a temperature/ humidity step change at the inlet while air flows through the bed at different velocities. The experimental data, i.e., the outlet air temperature or outlet air humidity after a urea particle bed, shows typical exponential growth curve. Experimental time constants are obtained by curve fitting the data in exponential form. Measurement uncertainty, regression uncertainty and standard error of estimated time constant are included in this chapter.

Chapter 3 presents a simplified theoretical method to predict the outlet air temperature or outlet air humidity for thin test beds when the urea particle bed is subject to a temperature step change or humidity step change at the inlet. The theoretical results show that both the outlet air temperature for temperature step change and outlet air humidity for humidity step change can be correlated using an exponential equation. The predicted time constant of outlet air temperature for temperature step change is a function of convective heat transfer coefficient

and air velocity while the time constant of outlet air humidity for humidity step change is a function of mass convection coefficient, air velocity, and internal sorption / desorption property of urea particles. The predicted outlet air temperature for humidity step change is determined by these two time constants due to heat release of moisture sorption. The comparison of the predicted time constant and measured one gives the interstitial convection coefficient for heat and mass convection. Measurement uncertainty propagated by the equation, and regression uncertainty are included in this chapter.

Chapter 4 shows the experimental measurement of moisture uptake and transport in a thick bed of urea. A test cell with test ports is used for particle sampling for moisture content determination without interruption of the experiment. A sampling device modified from a syringe and pistons is designed for sampling with minimum sample exposure and moisture change. Both the isothermal moisture sorption / desorption characteristics at room temperature and transient moisture sorption / desorption of urea particle bed with time are presented with measurement and regression uncertainty.

Chapter 5 shows the theoretical formulation and numerical simulation of moisture uptake and transport in a bed of urea particles in which the numerical prediction of the theoretical model is compared with the measured experimental data. Coupled heat and moisture transport equations are used to predict one dimensional temperature and moisture content distributions in a bed of bulk granular urea particles when humid air flows uniformly through the bed. The moisture sorption and transport processes consider two computational domains – water vapor diffusion inside each particle, and water vapor convection and diffusion in the interstitial air space in the urea particle bed. For energy transport, the temperature is assumed to be uniform inside each particle, but convective heat transfer and conduction between the urea particles and the interstitial air outside particles occur throughout the bed.

Chapter 6 gives the summary and conclusions of this research and proposes suggestions for urea particle storage and caking prevention. Also future research steps are given in Chapter 6.

The Appendices include: (A) Moisture content measurement using Karl Fischer titrator and its uncertainty analysis. (B) Measurement of physical properties and uncertainty analysis, including permeability, porosity, specific surface area and hydraulic diameter. (C) Determination of internal properties by BET and uncertainty. (D) Discretization of governing equations and boundary conditions with finite volume method. (E) Determination of the

convective heat transfer coefficients in spherical particle beds. (F) Sensitivity study. (G) Properties used in the numerical simulations. (H) Experimental data not listed in the main body.

CHAPTER 2

EXPERIMENTS OF TRANSIENT RESPONSE OF A THIN UREA PARTICLE BED TO AIRFLOW WITH LOW REYNOLDS NUMBER

2.1 Introduction

The main research objective is to investigate the uptake of moisture by test beds of urea from the ambient environment by means of experimental, theoretical and numerical methods. This is a coupled heat and mass transfer process in a urea bed in most cases because the ambient air temperature and relative humidity change with time and the urea particles are hygroscopic. Among many physical properties of urea particles and beds required to formulate the coupled heat and mass transfer process within urea particle beds, only a few fundamental properties, namely, density, porosity, conductivity, permeability and surface area can be measured directly while others, like tortuosity, internal particle diffusion coefficient, interstitial convection coefficient, etc., cannot be determined directly. As well, the complex internal pore structure and crystalline surface of urea particles (as shown in Figure 1.2) make the measurement of the specific surface area difficult and subject to large uncertainties. With large uncertainties in these properties, the prediction of the combined heat and mass transfer may also be subject to large uncertainties. Nie et al. (2008 a & b) presented a mathematically inverse method to determine convective heat and mass transfer coefficients in which experimental data were compared with numerical simulation of moisture uptake within a bed of urea particle bed. However, both experimental data and numerical simulation indicated that the moisture uptake of urea particle beds was not significantly sensitive to the external convection coefficients. This implied that the determination of convection coefficient using this inverse method was not accurate. For the case in which temperature changes are decoupled from the moisture changes, the convective heat transfer coefficient between air flow and urea particles can be determined by measurements or indirectly using volume average method. It is noted that, with forced convection of air through urea particle beds, experiments can be completed after a few hours of testing; however, without forced convection the diffusions processes may go on for days, especially if the test beds are thick.

From a theoretical point of view, the dimensionless heat convection coefficient (i.e., Nusselt number) should only depend on the geometry of the air flow passages in the bed, Reynolds number and Prandtl number (Shah & London, 1978). Travkin and Catton (2001) reviewed a series of research studies that used direct measurement and indirect volume averaging analysis to find the internal heat or mass transfer coefficients between interstitial fluid flow and a bed of particles for different types of porous media. They found that there were large discrepancies between the predictions from various research groups who used the volume average method (VAM). Most often, an uncertainty analysis was incomplete or missing. Discrepancies in the correlations and deficiencies in the uncertainty analysis imply that there is a need to determine the convective heat and mass transfer coefficients with forced flow through particle beds and to clearly state the correlation uncertainties.

Based on the Anzelius-Schumann transient mathematical model for an input at the inlet of a porous bed of particles under steady forced convection, analysis and data for the determination of heat and mass transfer coefficients have been presented by several researchers. Baclic et al. (1986) presented a theoretical analysis to evaluate heat transfer coefficients for single blow experiments and indicated that, except for very thin beds, errors made in the determination of heat transfer coefficients in packed beds due to replacing the most common exponential temperature at the inlet with an ideal step change would increase directly with the time constant delay in the outlet temperature, convective heat transfer coefficient and bed length. Bulck and Klein (1990) used a single-blow technique where air inlet properties were changed by a large air flow damper to determine the convective heat and mass transfer coefficients for flow through the parallel flow tubes of regenerative wheels. In this analysis the partial differential equations in a stationary coordinate system were transformed to an ordinary differential equation using a moving coordinate system that moved with the mean speed of the temperature wave. The technique used a rapid change but not an ideal step change for the inlet temperature.

Using a specifically designed apparatus to create an ideal step change, Wang et al. (2007a and b) and Abe et al. (2006) investigated a very rapid transient step change technique for measuring the transient response of stationary regenerative energy wheels that were used to exchange heat and water vapor between supply and exhaust air flows. In their analysis of the data, the transient response of the wheel alone was decoupled from the sensor plus wheel response by the use of Duhamel's equation. Recently, Shang and Besant (2008 and 2009a &

2009b) theoretically developed a relationship between the temperature and humidity time constants of energy wheels knowing the wheel flow channel properties and air flow properties. These predicted and measured time constants were used to derive explicit equations for the effectiveness of an energy wheel which was a function of the rotational wheel speed, air inlet velocity and the properties of the wheel when it was used to exchange heat and water vapor between supply and exhaust airstreams.

In this chapter, an experimental setup was designed for transient response of a urea particle bed with a height of 9 am subject to a pure temperature step change or a pure humidity step change at the inlet while air flows steadily through the bed.

2.2 Experimental apparatus and procedures

2.2.1 Apparatus

Figure 2.1 is a schematic diagram of the test cell used to measure the transient response of a thin urea particle bed subject to a step change in the inlet air temperature or humidity while an air flows through at different flow rates. For this test cell, there are two airflow cylindrical tubes each with an inner diameter of 50.8 mm that allow air to pass through the switch rotation plate, the top clamping plate, each test cell and the bottom clamping plate in sequence. Two clamping plates and supporting clamps are used to hold the two test cells. These two identical test cells, each with the same size air flow passage and a very thin stainless screen on the bottom, are made of Styrofoam insulation lined with aluminum foil to make the test cell adiabatic and impermeable. The test cell on the left side is filled with urea particles while the test cell on the right side is kept empty for by-passing one of the air flows. A rotation plate is connected to the top clamping plate by a pin that allows the rotation plate to rotate freely between two stops. For a temperature step change at the inlet ($\phi_{0^+} = \phi_{0^-}, T_{0^+} \neq T_{0^-}$), cooled dry air with respect to room temperature or heated dry air can be switched from passing through the urea particle bed on the left side to passing through the empty bed on the right side or vice versa.

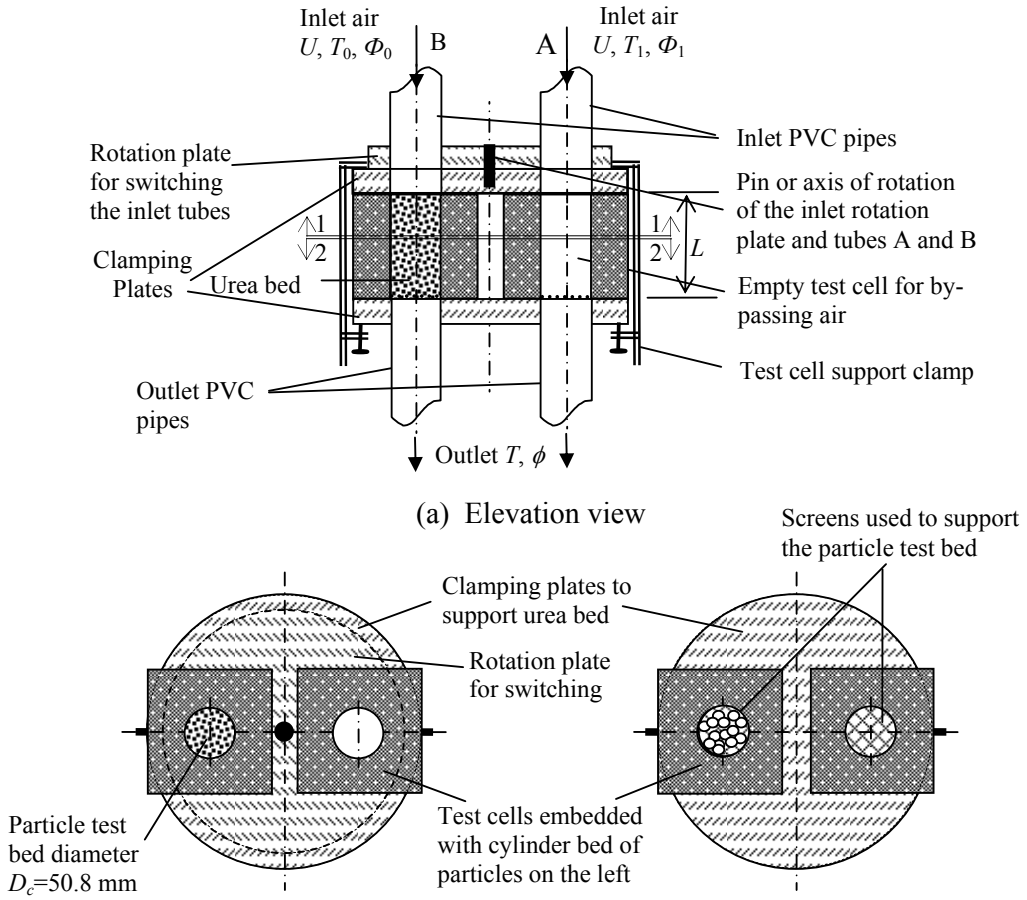

Legend:

L – Length of Urea Bed (90 mm); U – Air velocity (m/s);

T – Air temperature (^{o}C); ϕ – Air relative humidity.

Figure 2.1 Schematic diagram of the test cell to test the transient response of a thin urea particle bed subject to a step change of air temperature or air humidity at the inlet.

For a humidity step change at the inlet ($T^{0^+} = T^{0^-}, \phi^{O^+} \neq \phi^{0^-}$), dry air at room temperature or humid air at room temperature can be switched from passing through the urea particle bed to passing through the empty cell or vice versa. The switching time required to rotate the plates and interchange the two inlet flows was measured to be less than one second. Four thermocouples were placed respectively at the inlet and outlet of both the urea particle bed and the empty cell for air temperature measurement for the pure temperature step change

experiments. Four humidity sensors were placed at the inlet and outlet of both the urea particle bed and the empty bed for relative humidity measurement in humidity step change experiments. Either air temperature or relative humidity data were gathered using a data acquisition system. Experiments on temperature or humidity transient responses of thin urea particle beds were performed separately. The outlet air temperature or humidity downstream of a urea particle bed and an empty test cell cylinder were measured while the bed underwent a sudden change of temperature or humidity at the inlet.

2.2.2 Sample preparation

Both granular Terico and Prill Georgia urea particles were used in the experiments, for which the measured or calculated properties are listed in Table 2.1.

Table 2.1 Properties of Terico and Georgia urea particle and particle beds

Properties	Terico	Georgia	Data sources
Particle diameter, d_p (mm)	2.21±0.06	1.82±0.06	Image analysis measurement
Solid density, ρ_s (kg/m^3)	1323	1323	CRC handbook (Lide, 2006)
Heat capacity of urea, C_p (J/(mol.K))	92.4	92.4	(Elver and Hawkin, 1996)
External specific surface area per unit bed volume, $A_{v,e}$ (m^2/m^3)	1204±240	1992±400	Carmen (1938 and 1939) equation in Section 3.1 in Appendix B
External specific surface area per unit mass, $A_{m,e}$ (m^2/g)	0.192±0.016	0.072±0.171	BET method (Webb, 1997)
Solid particle volume fraction of bed, ε_p	0.64±0.01	0.64±0.01	Mass measurement
Internal porosity, $\varepsilon_{s,i}$	0.9988±0.0009	0.9988~1.0	BET method (Webb, 1997)
Hydraulic diameter, d_h (mm)	1.2±0.2	0.7±0.1	Section B.3 in Appendix B
Bed length, L (m)	0.090±0.001		Design and measurement

It is noted that, for heat transfer only, the external solid volume fraction, ε_p, is important. However for water vapor transfer, the external volume fraction or porosity of interstitial air,

$\varepsilon_{g,e}$, is important for the convective mass transfer coefficient, while the internal volume fraction of void space within the particles, $\varepsilon_{g,i}$, and the internal specific area $A_{v,i}$ are important to account for the internal water diffusion inside individual particles.

Before each experiment, urea particles were dried in the oven at $70^{o}\,C$ for about 48 hours. The oven temperature and drying time was carefully chosen to make sure the measured moisture content of urea particles with Karl Fischer titrator did not change any more. After drying process, urea particles were then double sealed in plastic bags and allowed to cool down to room temperature over a period of 12 hours. The weight of the empty test cell was measured before each experiment. One cylindrical test cell on the left side was filled and packed with dry urea particles as shown in Figure 2.1 while the other cylindrical cell on the right side was empty. The weight of the left test cell was measured again so that the weight difference gave the mass of urea particles in the test cell and allowed the calculation of the bed porosity knowing the urea and particle density.

2.2.3 Inlet air conditioning

Figure 2.2 shows a schematic diagram of the inlet air conditioning processes for the test cell to test the transient temperature / humidity response of a thin urea particle bed. Two different cases are considered: one is for pure heat transfer using dry air that is (i) cooled below and (ii) heated above room temperature, and the other is for water vapor sorption using (i) dry air at room temperature and (ii) humid air also at room temperature. The dry air flow, from the air compressor and the dryer, is divided into two branches. These two branches of air flow are preset by the mass flow controllers (manufactured by MKS Instruments, Inc., Andover, Massachusetts in USA) to have equal volume flow rates which were for both supply air tubes A and B shown in Figure 2.1.

In Figure 2.2 (a), the dry air flow, A, at room temperature passes through an air-hot-water heat exchanger and is heated to $35 \pm 0.1^{o}\,C$ at the test cell inlet. Dry air flow, B, also at room temperature, passes through another air-cold-water heat exchanger and is cooled to $15 \pm 0.1^{o}\,C$ at the test cell inlet. A temperature difference of $20 \pm 0.1^{o}\,C$ is obtained between two dry air flows passing through the empty bed and urea particle bed of the test cell shown in Figure 2.1. In Figure 2.2(b), dry air flow, A, at room temperature passes partly through the adjustable by-pass flow humidifier in order to set the inlet air relative humidity at 65±0.1%.

The other dry air flow, B, also at room temperature, passes through the test cell directly at a relative humidity of 4±0.1% so that a relative humidity difference of 61±0.1% can be obtained between two room temperature air flows passing through the empty cell and urea particle bed.

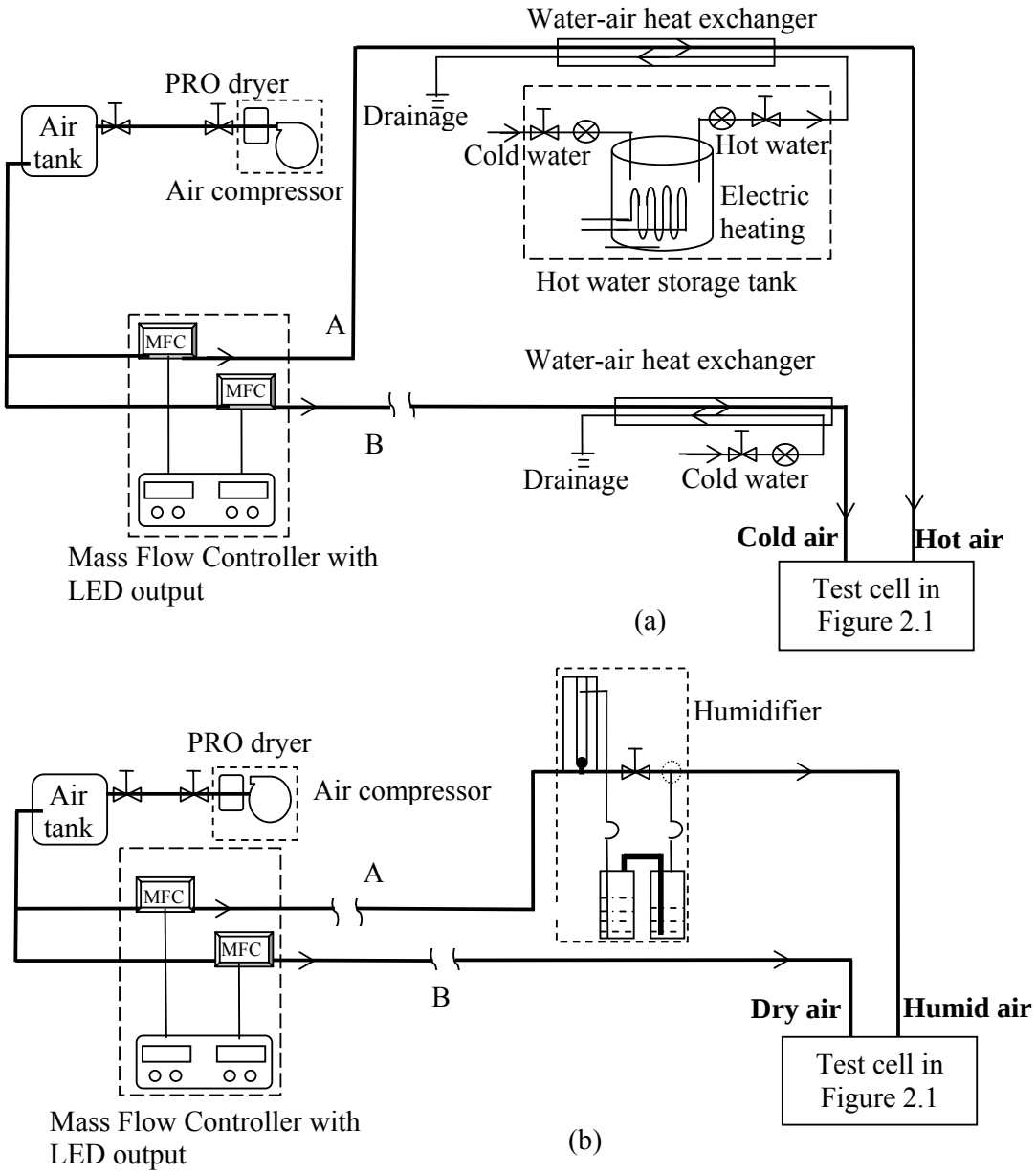

Figure 2.2 Schematic diagrams of the conditioning processes for the inlet air to determine the characteristic time constants for processes with a step change in the inlet air for (a) cold and hot dry air and (b) dry and humid air at room temperature.

The experiments on transient response of a thin urea particle bed, subject to a step change of inlet air temperature or relative humidity, undergo air flow with six different air flow rates, i.e. 160/80/40/20/10/5 Lpm, (or corresponding Darcy velocity of air flow 1.316/0.658/0.329/ 0.164/0.082/0.041 m/s). The air flow rate was measured by a mass flow controller with an uncertainty equal to 1% of the maximum mass flow rate. Table 2.2 shows the inlet air test conditions investigated.

Table 2.2 Inlet air conditions for urea particle beds to determine the heat & mass transfer convection coefficients

	Volumetric air flow rates $\dot{Q}_a$ (Lpm)	Darcy velocity u_D (m/s)
Dry air flow at 22 °C	160±2	1.316
	80±2	0.658
	40±1	0.329
	20±1	0.164
	10.0±0.5	0.082
	5.0±0.5	0.041
Inlet temperature step change (°C), $\Delta T \neq 0, \Delta\phi = 0$		20.0±0.1 °C
Inlet humidity step change, $\Delta T = 0, \Delta\phi \neq 0$		61% ±1%

The uncertainty of mass flow rate will cause uncertainty in the Darcy velocity and Reynolds number based on the equation for error propagation. The uncertainty analysis followed is based on the ASME standard (ASME, 1990).

The Darcy velocity or the average velocity of the cross-section area is defined as $u_D = \frac{4\dot{Q}_a}{\pi D_c^2}$, therefore, the uncertainty of Darcy velocity is

$$\left[\frac{U(u_D)}{u_D}\right]^2 = \left[\frac{U(\dot{Q}_a)}{\dot{Q}_a}\right]^2 + \left[2\frac{U(D_c)}{D_c}\right]^2 \tag{2-1}$$

For air flow rate, the uncertainty was ±1% of the maximum mass flow rate of the mass flow controller as shown in Table 2.2; for the inner diameter of the test cell, the uncertainty is ±0.1 mm. Thus the relative uncertainty of Darcy velocity in Table 2.3, is dominated by the relative uncertainty of the air flow rate.

Reynolds number based on the hydraulic diameter is defined as

$$\mathrm{Re}_{d_h} = \frac{u_p d_h}{\nu} \tag{2-2}$$

where $u_p = \frac{u_D}{\varepsilon}$ is pore velocity, $d_h = \frac{4\varepsilon}{A_{v,e}}$ is hydraulic diameter of the urea particle bed. And Darcy velocity or the average velocity of the cross-section area is $u_D = \frac{4\dot{Q}_a}{\pi D_c^2}$, therefore

$$\mathrm{Re}_{d_h} = \frac{16\dot{Q}_a}{\pi D_c^2 A_{v,e}} \tag{2-3}$$

Uncertainty of Reynolds number is calculated as

$$U\left(\mathrm{Re}_{d_h}\right) = \left\{ \left[\frac{\partial \mathrm{Re}_{d_h}}{\partial \dot{Q}_a} U\left(\dot{Q}_a\right) \right]^2 + \left[\frac{\partial \mathrm{Re}_{d_h}}{\partial D_c} U\left(D_c\right) \right]^2 + \left[\frac{\partial \mathrm{Re}_{d_h}}{\partial A_{v,e}} U\left(A_{v,e}\right) \right]^2 \right\}^{1/2} \tag{2-4}$$

where the partial differentials of Reynolds number with respect to air flow rate, inner diameter of the test cell and specific surface area per unit volume are calculated as followed equations

$$\frac{\partial \mathrm{Re}_{d_h}}{\partial \dot{Q}_a} = \frac{16}{\pi D_c^2 A_{v,e}} = \frac{\mathrm{Re}_{d_h}}{\dot{Q}_a} \tag{2-5}$$

$$\frac{\partial \mathrm{Re}_{d_h}}{\partial D_c} = -2\frac{16\dot{q}_a}{\pi D_c^3 A_{v,e}} = \frac{-2\,\mathrm{Re}_{d_h}}{D_c} \tag{2-6}$$

$$\frac{\partial \mathrm{Re}_{d_h}}{\partial A_{v,e}} = -\frac{16\dot{Q}_a}{\pi D_c^2 A_{v,e}^2} = \frac{-\mathrm{Re}_{d_h}}{A_{v,e}} \tag{2-7}$$

Substituting equations (2-5), (2-6) and (2-7) into equation (2-4), one gets the relative uncertainty of Reynolds number as

$$\left[\frac{U\left(\mathrm{Re}_{d_h}\right)}{\mathrm{Re}_{d_h}}\right]^2 = \left[\frac{U\left(\dot{Q}_a\right)}{\dot{Q}_a}\right]^2 + \left[2\frac{U\left(D_c\right)}{D_c}\right]^2 + \left[\frac{U\left(A_{v,e}\right)}{A_{v,e}}\right]^2 \tag{2-8}$$

For the specific surface area per unit bed volume determined using the Carmen equation for a spherical particle bed, the relative uncertainty is ±20% (Chen, 2004) which is much larger than the relative uncertainty of air flow rate and inner diameter. Therefore the relative uncertainty of Reynolds number, listed in Table 2.3, is dominated by the relative uncertainty of the specific surface area.

Table 2.3 Darcy velocity, Reynolds numbers and their uncertainty determination for both Terico and Georgia urea particle beds subject to inlet temperature or humidity step changes at different air flow rates.

Volumetric flow rate, $\dot{Q}_a$ (Lpm)	Darcity velocity u_D (m/s)	Type of Urea	Reynolds number Re_{d_h}	Relative uncertainty of Re_{d_h}, $U\left(\mathrm{Re}_{d_h}\right)/\mathrm{Re}_{d_h}$
160	1.316±0.016	Terico	284	±20.0%
		Georgia	172	±20.0%
80	0.658±0.016	Terico	142	±20.2%
		Georgia	86	±20.2%
40	0.329±0.008	Terico	71	±20.2%
		Georgia	43	±20.2%
20	0.164±0.008	Terico	36	±20.6%
		Georgia	22	±20.6%
10	0.082±0.004	Terico	18	±20.6%
		Georgia	11	±20.6%
5	0.041±0.004	Georgia	5	±22.4%

2.2.4 Experimental procedure

For the experiments with a urea bed subject to a step change in temperature, before the test cell is filled with dry urea particles double sealed in plastic bags at room temperature and embedded into the air flow passage, air flow is conditioned as shown in Figure 2.2(a). To condition the urea test bed, the cold dry air, B, initially passes through the urea particle bed while hot dry air, A, passes through the empty cell. This cold dry air passes through the bed until the equilibrium condition is achieved. This means that the inlet air temperature of both urea particle bed and empty bed are stable and the cold dry outlet air temperature is equal to the inlet temperature, indicating that urea particle bed is at the same temperature as the cold dry air.

To initiate the step change, the top inlet switch plate of the test cell is quickly rotated 180^{o} to switch the two inlet air flow pipes. In this way, the hot dry air will start to pass through cold dry urea particle bed on the left side in Figure 2.1 while the right empty cell will be used to bypass the cold dry air. Once the outlet air temperature after urea particle bed reaches the inlet hot dry air temperature, the top plate is rotated to its original position so that the cold dry air will start to pass through the heated dry urea particle bed while the hot dry air will be bypassed through the empty cell. Experiments on humidity step changes were completed following similar steps as described above.

2.3 Experimental data and analysis

Dry urea particles at room temperature, if exposed to a flow of dry air with a high temperature, will acquire sensible energy from hot air such that the temperature of urea particles will increase until a new thermal equilibrium between urea particles and the flowing air has been reached. Dry urea particles at room temperature, if exposed to a flow of humid air at room temperature, will adsorb moisture from humid air and the moisture content of the urea particles will increase until the isothermal adsorption equilibrium has been reached. In the meanwhile, the temperature of urea particles will increase for a while due to water phase change during adsorption process. That is to say, when a dry urea particle bed is subject to a steady flow of air with a step change in the inlet temperature or relative humidity, the outlet air temperature or relative humidity (or vapor density) will show a time delay before reaching

the same temperature or humidity as the inlet condition. Weighted exponential time delay equations can be fitted to the outlet temperature or humidity data for both the sensor itself and the sensor plus urea bed. The Duhamel method (Wang et al., 2005) was used to decouple the sensor response from the sensor plus urea bed response such that the time constant of only the urea particle bed is determined. For a small test cell and a very rapid step change at the inlet, this time delay phenomenon can be characterized by a single time constant.

Typical experimental data (air flow of 160 Lpm through Terico urea particle bed) for the normalized temperature and relative humidity versus time are shown in Figure 2.3 and 2.4. Both experimental data of transient temperature response of urea particle beds and transient humidity response of urea particle show a trend of exponential growth in a form of $\theta = 1 - e^{-t/\tau_{a,k}}$ where the time constant subscript, *k,* means temperature, T, or humidity, ϕ. These curve fits are used to determine the time constants of each step change process. For air flow rate of 160 Lpm in Figure 2.3 and 2.4, there are less than 0.5% changes in θ beyond 250 seconds; but for lower flow rates, longer periods of data collection are required. For pure temperature step changes, the time constant decreases with the increase of air flow rate, or Reynolds number. A theoretical analysis of water vapor mass or heat energy balance for air flow through the control volume of the urea particle bed in Chapter 3, shows that outlet air time constant of temperature or humidity downstream of the urea particle bed are functions of the urea bed properties and air properties. The convective heat or mass transfer coefficients for air flow through the particle bed are then determined by comparing the experimental data with the theoretical results.

The transient response of outlet air temperature after urea particle bed when a temperature step change occurred at the inlet air flow with flow rate of 160 Lpm, 80 Lpm, 40 Lpm, 20 Lpm, 10 Lpm and 5 Lpm, showed similar exponential growth forms as shown in Figure 2.3 and 2.4. Similar phenomenon occurred for the outlet air humidity response after urea particle beds when the bed was subject to a humidity step change at the inlet. However, the time constants varied in accordance to the air flow rates and urea particle types, that is to say, the Reynolds number. The time constants of temperature step change or humidity change for experimental data at different air flow rates are summarized in Table 2.4.

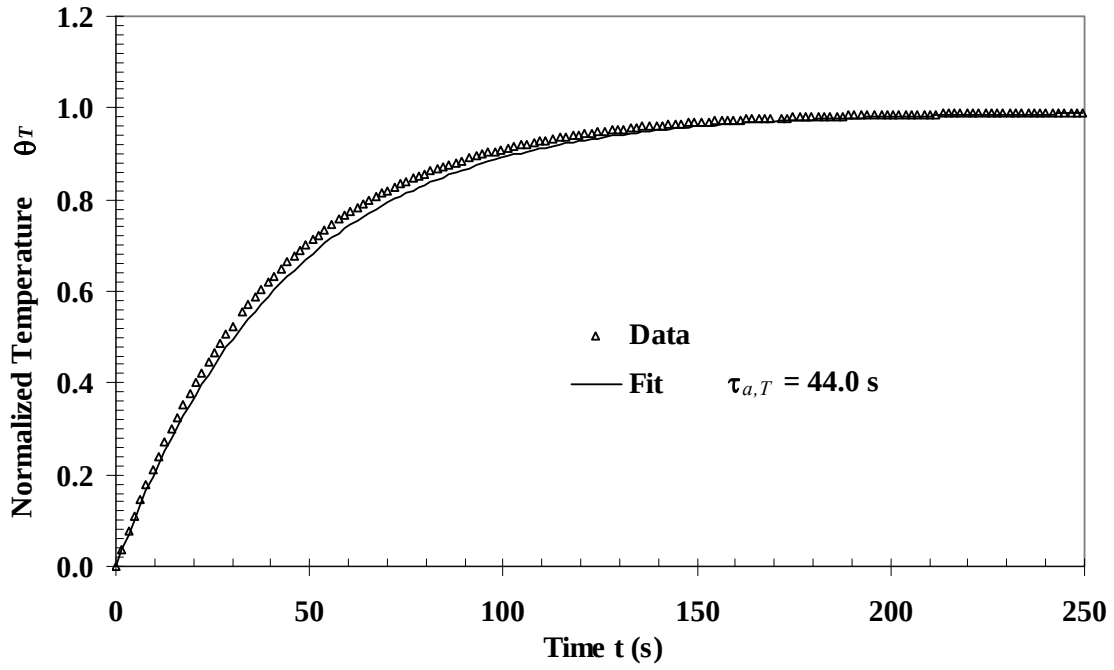

Figure 2.3 Transient data of temperature step change for Terico urea particles with an air flow rate of 160 Lpm ($\mathrm{Re}_{d_h} = 284$) and its curve fit.

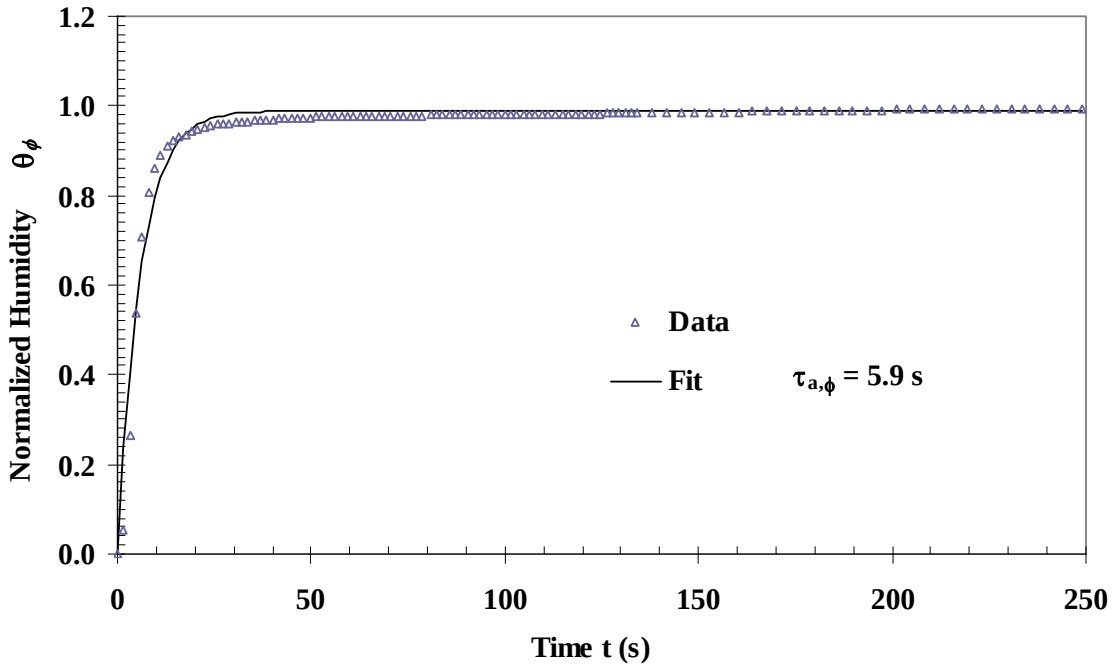

Figure 2.4 Transient data of humidity step change for Terico urea particles with an air flow rate of 160 Lpm ($\mathrm{Re}_{d_h} = 284$) and its curve fit.

For the temperature step change, the normalized temperature is defined as

$$\theta_T = \frac{T - T^{0^-}}{T_\infty - T^{0^-}} \tag{2-9}$$

The experimental data of transient temperature response of the urea particle bed presented a trend of exponential growth. The software of Table Curve in the 5th version (developed by Systat Software Inc. in San Jose, California, USA.) was used to curve fit the data in the equation form of

$$\theta_T = 1 - e^{-t/\tau_{a,T}} \tag{2-10}$$

The R^2 of the correlation and the Standard error of estimation for the parameter $\tau_{a,T}$ were given by Table Curve.

Similarly, for the humidity step change, the normalized humidity is defined as

$$\theta_\phi = \frac{\phi - \phi^{0^-}}{\phi_\infty - \phi^{0^-}} \tag{2-11}$$

The experimental data of transient response of the urea particle bed presented a trend of exponential growth. . The software of Table Curve in the 5th version (developed by Systat Software Inc. in San Jose, California, USA.) was used to curve fit the data in the equation form of

$$\theta_\phi = 1 - e^{-t/\tau_{a,W}} \tag{2-12}$$

The coefficient of determination, R^2, of the correlation and the standard error of estimation for the parameter $\tau_{a,T}$ were calculated by Table Curve as well. Table 2.4 shows the curve fitted time constants of outlet air temperature and outlet air humidity and their uncertainties (standard error of estimation) derived from the experimental data at different air flow rates for both Terico urea particle beds and Georgia urea particle beds.

Table 2.4 Curve-fitted time constant of outlet air temperature and outlet air humidity and their uncertainty determination for Terico and Georgia urea particle beds subject to inlet temperature or humidity step changes at different air flow rates.

Volumetric flow rate $\dot{Q}_a$ (Lpm)	Darcy velocity u_D (m/s)	Type of Urea	Time constant of temperature response		
			Coefficient of determination, R^2	Time constant, $\tau_{a,T}$ (s)	Standard error of estimation, *SEE*
160	1.316	Terico	0.9952	43.5	±0.26
		Georgia	0.9944	35.8	±0.23
80	0.658	Terico	0.9970	84.7	±0.44
		Georgia	0.9955	63.7	±0.38
40	0.329	Terico	0.9979	147.6	±0.28
		Georgia	0.9941	117.6	±0.37
20	0.164	Terico	0.9979	146.1	±0.27
		Georgia	0.9987	421.3	±0.56
10	0.082	Terico	0.9993	289.9	±0.41
		Georgia	0.9993	628.7	±0.73
5	0.041	Georgia	0.9996	1289.1	±0.58
Volumetric flow rate $\dot{Q}_a$ (Lpm)	Darcy velocity u_D (m/s)	Type of Urea	Time constant of humidity response		
			Coefficient of determination, R^2	Time constant, $\tau_{a,\phi}$ (s)	Standard error of estimation, *SEE*
160	1.316	Terico	0.9694	5.8	±0.18
		Georgia	0.9624	4.9	±0.22
80	0.658	Terico	0.9830	8.6	±0.17
		Georgia	0.9788	6.1	±0.13
40	0.329	Terico	0.9745	13.8	±0.33
		Georgia	0.9653	10.7	±0.31
20	0.164	Terico	0.9793	18.0	±0.38
		Georgia	0.9780	12.7	±0.27
10	0.082	Terico	0.9811	14.9	±0.31
		Georgia	0.9808	15.3	±0.31
5	0.041	Georgia	0.9788	23.7	±0.52

2.4 Summary and conclusion

Experimental data of both outlet air temperature after urea particle beds for temperature step change and outlet air humidity after urea particle beds for humidity step change increase with time, showing nearly exponential growth forms. From the data at different air flow rate for Terico urea and Georgia urea, it can be found that the time constant of outlet air temperature is much larger than the one of outlet air humidity at the same airflow rate for same urea type. In addition, both time constants of outlet air temperature and those of outlet air humidity decrease with an increase in Reynolds number.

CHAPTER 3

THEORETICAL METHOD TO DETERMINE THE INTERSTITIAL PARTICLE CONVECTIVE HEAT AND MASS TRANSFER COEFFICIENTS WITHIN UREA BEDS AND SHOW THE ANALOGY AMONG MOMENTUM, HEAT, MASS AND DISPERSION CORRELATIONS

3.1 Problem statement

As shown in Chapter 2, experimental data of transient temperature or humidity responses of a thin urea particle bed subject to a steady of air flow and an ideal step change of air inlet temperature or humidity indicated that the outlet air temperature or humidity show an exponential increase in outlet properties after a step increase for the inlet properties. The time constants of these curves increase with a decrease in air flow rates. Wang et al. (2005) and Abe et al. (2006) investigated a new very rapid transient step change technique for measuring the transient response of stationary regenerative energy wheels that were used to exchange heat and water vapor between supply and exhaust airstreams. It was suggested that the transient responses of the energy wheel, i.e., the time constant, were influenced by the heat or mass convection coefficient, the flow channel geometry, and the inlet air velocity. Shang and Besant (2008 and 2009a & b) proposed a theoretical method to express the effectiveness of an energy wheel and found that the effectiveness of energy wheel is a function of time constants, the energy wheel properties, rotation speed of wheel and air velocity

The objectives of this chapter are (1) to present a theoretical model to predict the transient response of outlet air temperature or outlet air humidity for thin test beds when the urea particle bed is subject to a temperature step change or a humidity step change at the inlet; (2) to develop a mathematical relationship between time constants, Reynolds number and the heat and mass convection coefficient (Nie, et al., 2009a); and (3) to compare with experimental data and determine the internal heat and mass convection coefficients within porous beds.

3.2 Assumptions and theoretical formulations

3.2.1 Assumptions and verifications

A.1) With the known diameter of the test cell bed, $D_c = 50.8$ mm, Terico urea particle diameter, $d_p = 2.21$ mm, and the height of the bed, $L = 90$ mm, the effect of both entrance length and wall effect can be calculated. For the Carmen-Kozeny type media, the entrance length is about one particle diameter (Kaviany, 1995). The air flow length ratio for the entrance (exit) length, with respect to the complete cell height is estimated as $d_p / L = 0.0245 << 1$. Therefore, the entrance/exist effect can be ignored. For spherical particle beds, the wall effect is about half a particle diameter (Ismail, et al., 2002). The air flow area ratio for this wall area with respect to the whole cell cross-section area is estimated as $\pi D_c (0.5 d_p) / (\pi D_c^2 / 4) = 2 d_p / D_c = 0.087 << 1$. According to Nield and Bejan (1992), non-uniformities in the cross-section area due to the effects of flow channelling near the wall or elsewhere due to bed length can be ignored when these ratios are small. In this way, the axial and radial bed properties and air flow variations are expected to be negligible.

A.2) Heat conduction for both air and urea particle phases are negligible compared with convection term. (This has been verified in Appendix D.)

A.3) The Biot number for air flow through the particles in the bed is small (i.e. $\mathrm{Bi}_{d_p} = h_t (d_p / 6) / k_u << 0.1$), which means that the thermal resistance due to heat conduction within the particles is negligible compared to the thermal resistance due to convection, and the temperature variation within the particles is negligible at any time. For Terico urea particles with a diameter of $d_p = 2.2 \times 10^{-3}$ m, $K_u \approx 0.33 >> 0.21$ W/$(\mathrm{K} \cdot \mathrm{m})$ (Nie et al., 2008b), $h_t = 1.13$ W/$(\mathrm{K} \cdot \mathrm{m}^2)$ at the highest Reynolds number 284 and therefore the highest Biot number based on particle diameter is $\mathrm{Bi}_{d_p} = 0.13$; but for other cases, Biot number is less than 0.1.

A.4) Because any temperature sensor within a bed will be in contact with both the air and the particles, it is not possible to arrange for the accurate measurement of either and only the air temperature or urea particle temperature inside the urea particle bed. Linear air temperature distribution within the bed is assumed at any time. The transverse time for air through the

complete bed length ($L = 90$ mm) is $t_T = \varepsilon \cdot L / u_D$, such that the shortest transverse time is 0.025 s at the highest air flow rate of 160 Lpm while the longest transverse time is 0.788 s at the lowest air flow rate of 5 Lpm. Compared with the corresponding outlet air temperature response delay time constant, this transverse time is only 0.06%-0.1% of the outlet air temperature time constant. This ratio shows that the bed length has a negligible influence on the outlet air response delay. Using the theory of Baclic et al. (1986), the dimensionless bed length (proportional to the bed length) is 0.04; therefore the error caused by the ideal step change instead of single blow inlet is negligible. The results using the linear temperature assumption will be corrected based on comparing data with somewhat different theoretical energy analysis where bed temperatures for other solid particles are measured in appendix D.

3.2.2 Temperature step change

Dry urea particles in a bed initially at a cold temperature, if exposed to a flow of dry air at a higher temperature, will acquire sensible energy from the warmer air such that the urea particles will increase in temperature until a new thermal equilibrium between urea particles and the flowing air is reached. The Schumann method developed by Wakao and Kaguei (1982) excluded the transient thermal energy storage in the bed and the heat conduction through the solid and fluid domains of the bed. In the model developed below, the sensible energy change rate of the urea particles in the test cell is balanced by the convective heat transfer rate from the surrounding air in the interstitial air spaces of the bed.

$$(\rho Cp\varepsilon)_u \frac{\partial T_u}{\partial t} = A_{v,e} h_t \left(T_a - T_u\right) \tag{3-1}$$

The partial differential equation for air flowing uniformly through a bed is written as

$$(\rho Cp\varepsilon)_a \frac{\partial T_a}{\partial t} + (\rho Cp)_a u_D \frac{\partial T_a}{\partial x} = A_{v,e} h_t \left(T_u - T_a\right) \tag{3-2}$$

When the thermal capacity of the interstitial air is much smaller relative to the thermal capacity of the urea particles in the bed, i.e., $V\left(\rho_a \cdot Cp_a\right) \cdot \varepsilon / \left(M_u Cp_u\right) << 1$, and the traverse time of the air flow, $L \cdot \varepsilon / u_D$, is much smaller than the time constant for the solid particles in the bed, the energy balance of the air in the interstitial space, equation (3-2) can be written as

$$(\rho Cp)_a u_D \frac{\partial T_a}{\partial x} = A_{v,e} h_t \left(T_u - T_a\right) \tag{3-3}$$

The spatial average, i.e., integration of equations (3-1) and (3-3) with the operator $\int_0^L dx / L$, give the corresponding ordinary differential equation and algebraic equation:

$$M_u Cp_u \frac{d\overline{T}_u}{dt} = V \cdot A_{v,e} h_t \left(\overline{T}_a - \overline{T}_u\right) \tag{3-4}$$

$$\dot{m}_a Cp_a \left(T_{a,O} - T_{a,I}\right) = V \cdot A_{v,e} h_t \left(\overline{T}_u - \overline{T}_a\right) \tag{3-5}$$

where h_t is the volume average convective heat transfer coefficient, and

$$\overline{T}_u = \int_0^L T_u dx / L \tag{3-6}$$

is the average temperature of the urea particles in the test cell at any time, *t*, and

$$\overline{T}_a = \int_0^L T_a dx / L \tag{3-7}$$

is average temperature of the air in the test cell also at time *t*, and

$$M_u = \rho_u V \varepsilon_u = \rho_u A_b L \varepsilon_u \tag{3-8}$$

is the total mass of urea particles in the bed, and

$$\dot{m}_a = \rho_a \dot{Q}_a = \left(\rho_a u_D\right) \cdot A_b \tag{3-9}$$

is air mass flow rate. As mentioned in A.4, it is assumed that the air temperature is linearly distributed, then

$$\overline{T}_a = \frac{T_{a,I} + T_{a,O}}{2} \tag{3-10}$$

Substituting equation (3-10) into (3-5), one gets

$$\overline{T}_u = \left(\frac{\dot{m}_a Cp_a}{V \cdot A_{v,e} h_t} + \frac{1}{2}\right) T_{a,O} - \left(\frac{\dot{m}_a Cp_a}{V \cdot A_{v,e} h_t} - \frac{1}{2}\right) T_{a,I} \tag{3-11}$$

Combining equations (3-4) and (3-5) gives

$$M_u Cp_u \frac{d\overline{T}_u}{dt} = \dot{m}_a Cp_a \left(T_{a,I} - T_{a,O}\right) \tag{3-12}$$

Substituting equation (3-11) into (3-12) results in

$$\frac{M_u Cp_u}{\dot{m}_a Cp_a} \frac{d}{dt}\left[\left(\frac{\dot{m}_a Cp_a}{VA_{ve}h_t} + \frac{1}{2}\right)T_{a,O} - \left(\frac{\dot{m}_a Cp_a}{VA_{ve}h_t} - \frac{1}{2}\right)T_{a,I}\right] + T_{a,O} = T_{a,I} \tag{3-13}$$

Since inlet air temperature is a constant, $\frac{dT_{a,I}}{dt} = 0$, therefore equation (3-13) becomes

$$\frac{M_u Cp_u}{\dot{m}_a Cp_a}\left(\frac{1}{2} + \frac{\dot{m}_a Cp_a}{V \cdot A_{v,e} h_t}\right)\frac{dT_{a,O}}{dt} + T_{a,O} = T_{a,I} \tag{3-14}$$

Introducing a normalized outlet air temperature

$$\theta_{aT,O} = \frac{T_{a,O} - T_{a,I}^{0-}}{T_{a,I} - T_{a,I}^{0-}} \tag{3-15}$$

and substituting equation (3-15) into (3-14), one gets

$$\frac{M_u Cp_u}{\dot{m}_a Cp_a}\left(\frac{1}{2} + \frac{\dot{m}_a Cp_a}{V \cdot A_{v,e} h_t}\right)\frac{d\theta_{aT,O}}{dt} + \theta_{aT,O} = 1 \tag{3-16}$$

with initial condition $\theta_{aT,O} = 0$ at $t = 0$ and $\theta_{aT,O} = 1$ at $t = \infty$. The analytical solutions for the normalized outlet air temperature are

$$\theta_{aT,O} = 1 - e^{-t/\tau_{a,T}} \tag{3-17}$$

where

$$\tau_{a,T} = \frac{M_u Cp_u}{\dot{m}_a Cp_a}\left(\frac{1}{2} + \frac{\dot{m}_a Cp_a}{V \cdot A_{v,e} h_t}\right) = \frac{(\rho \cdot Cp)_u \varepsilon_u L}{(\rho \cdot Cp)_a u_D}\left[\frac{1}{2} + \frac{(\rho \cdot Cp)_a u_D}{A_{v,e} h_t L}\right] \tag{3-18}$$

is defined as the time constant of the normalized outlet air temperature. Substituting equations (3-8) and (3-9) into (3-18) give

$$\tau_{a,T} = \frac{(\rho \cdot Cp)_u \varepsilon_u}{A_{v,e} h_t} + \frac{1}{2} \frac{(\rho \cdot Cp)_u \varepsilon_u}{(\rho \cdot Cp)_a \varepsilon} \left(\frac{L \cdot \varepsilon}{u_D} \right) \tag{3-19}$$

From equation (3-19), it can be seen that:

(1) The time constant of the transient outlet air temperature includes two parts: one is related to the heat convection, the other is related to the transverse time of the air flow through the bed. In other words, the time constant is much greater than the air flow transverse time, i.e. $\tau_{a,T} >> \frac{L \cdot \varepsilon}{u_D}$.

(2) With known urea particle properties and air properties, the time constants of the outlet air temperature, $\tau_{a,T}$, are functions of the Darcy velocity of air flow, u_D, and convective heat transfer coefficient, h_t, both of which are directly related to the Reynolds number.

(3) With an increase in Reynolds number (Re_{d_h}) or Darcy velocity (u_D), the convective heat transfer coefficient, h_t, increases, while the air flow transverse time $L \cdot \varepsilon / u_D$ decreases.

To summarize this theoretical treatment, the characteristic heat transfer time constants obtained from the experimental data are assumed to be equal to the theoretical time constants defined by equations (3-18) or (3-19). In other words, it implies that, with known properties of the urea particle bed and air, including bed length, measured air flow rate, density, specific heat capacity and volume fraction, together with known time constants from curve fits of the experimental data, the convective heat transfer coefficient h_t can be determined. This convective heat transfer coefficient depends on the interstitial airflow pattern in the bed as well as the air conductivity. Since the air flow pattern through a particle bed is as inherently complex as implied by the flow passage-ways, it will be essentially laminar for low Reynolds numbers, i.e. $\mathrm{Re}_{d_h} < 10$ (Kaviany, 1995) but will become more and more complex as Reynolds number increases. Transition to fully developed turbulent flow may not occur until the velocity or Reynolds number become very high. There is little or no measured data available for turbulent flow in a packed particle bed. Most particle bed flows will correspond to the flow in the laminar and transition range of Reynolds numbers. For complex laminar

flows, the molecular diffusion process for heat transfer is directly related to the diffusion process for water vapor mass transfer in air, thus the convective mass transfer coefficient can be directly determined from the convective heat transfer coefficient, i.e., $\mathrm{Sh}_{d_h} = \mathrm{Nu}_{d_h}$ (Incropera et al., 2002), implying that

$$h_m = h_t \frac{D_{v,a}}{k_a} = \frac{h_t}{\rho_a C_{p\,a} \mathrm{Le}} \tag{3-20}$$

where Le is the Lewis number for air. With increasing flow rate beyond the transition Reynolds number, this relationship applies, implying that the flow pattern changes are similar for heat and mass transfer.

3.2.3 Humidity step change

When exposed to a flow of humid air at room temperature, dry urea particles at room temperature will adsorb moisture from humid air and the moisture content of the urea particles will increase until the isothermal adsorption equilibrium is reached. In the meanwhile, the temperature of urea particles will increase due to water phase change during adsorption process. That is to say, a bed of urea particles subject to only a step change in humidity at the inlet, while air flows through the bed, is a coupled heat and mass transfer process. The moisture transfer and heat transfer for the urea particle bed will be developed separately because the internal void spaces inside the urea particles cause the internal particle water vapor adsorption process to be different than the external particle surface adsorption.

3.2.3.1 Moisture sorption process

For the moisture adsorption process in the test cell bed of urea particles, the mass of moisture adsorbed by urea particles is balanced by the convective mass transfer rate from the surrounding air. This balance is written in the similar form as equation (3-4), i.e.

$$M_u \beta \frac{d\overline{X}_u}{dt} = V \cdot A_{v,e} h_m \left(\overline{\rho}_{v,a} - \overline{\rho}_{v,us} \right) \tag{3-21}$$

An empirical coefficient, β, is introduced in equation (3-21) to account for the diffusion process that is not at equilibrium within the particles. This internal diffusion of water vapor is unlike the heat transfer process inside each particle where the temperature will be uniform.

That is, the Biot number for water vapor transfer within the particles are not small because the internal diffusion coefficient is small..

The convective mass transfer rate is balanced by the net moisture of air entering and leaving the porous bed.

$$\dot{m}_a\left(W_O - W_I\right) = V \cdot A_{v,e} h_m \left(\overline{\rho}_{v,us} - \overline{\rho}_{v,a}\right) \tag{3-22}$$

Here, a linear distribution of water vapor density in the interstitial space between particles is assumed, then

$$\overline{\rho}_{v,a} = \frac{\rho_{v,aI} + \rho_{v,aO}}{2} \tag{3-23}$$

$$W_O = \frac{\rho_{v,aO}}{\rho_a} \tag{3-24}$$

$$W_I = \frac{\rho_{v,aI}}{\rho_a} \tag{3-25}$$

Substituting equations (3-23) (3-24) (3-25) into (3-22) gives

$$\overline{\rho}_{v,us} = \left(\frac{\dot{m}_a}{V \cdot A_{v,e} h_m} + \frac{\rho_a}{2}\right) W_O - \left(\frac{\dot{m}_a}{V \cdot A_{v,e} h_m} - \frac{\rho_a}{2}\right) W_I \tag{3-26}$$

Combining equation (3-21) with (3-22) yields,

$$M_u \beta \frac{d\overline{X}_u}{dt} = -\dot{m}_a \left(W_O - W_I\right) \tag{3-27}$$

At equilibrium in a particle bed, $\overline{X}_u = \overline{X}_u\left(\phi, T\right)$, $\phi = \dfrac{\rho_v}{\rho_{vs}}$ and $W = \dfrac{\rho_v}{\rho_a}$, therefore

$$\left(\frac{\partial \overline{X}_u}{\partial t}\right)_T = \left(\frac{\partial \overline{X}_u}{\partial \phi}\right)_T \left(\frac{d\phi}{dW}\right)_T \frac{dW}{dt} = \frac{\rho_a}{\rho_{vs}} \left(\frac{\partial \overline{X}_u}{\partial \phi}\right)_T \frac{dW}{dt} \tag{3-28}$$

During the pure adsorption or desorption process without an external heat source or sink, temperature variations due to water phase change occur but it will not significantly alter the moisture transfer, so that equation (3-27) can be rewritten as:

$$M_u \beta \frac{\rho_a}{\rho_{vs}} \left(\frac{\partial \overline{X}_u}{\partial \phi} \right)_T \frac{d\overline{W}}{dt} = -\dot{m}_a \left(W_O - W_I \right) \tag{3-29}$$

where from equations (3-23), (3-24) and (3-25) that the average humidity ratio of air in the test cell bed is

$$\overline{W} = \frac{W_I + W_O}{2} \tag{3-30}$$

Substituting equation (3-30) into (3-29) and assuming that the inlet humidity ratio of air W_I is a constant, one get

$$\frac{1}{2} \frac{M_u \beta}{\dot{m}_a} \frac{\rho_a}{\rho_{vs}} \left(\frac{\partial \overline{X}_u}{\partial \phi} \right)_T \frac{dW_O}{dt} + W_O = W_I \tag{3-31}$$

After introducing the normalized air humidity ratio

$$\theta_{a\phi,O} = \frac{W_O - W_I^{0^-}}{W_I - W_I^{0^-}} \tag{3-32}$$

where $\theta_{a\phi,O} = 0$ at $t = 0$ and $\theta_{a\phi,O} = 1$ at $t = \infty$. Substituting equation (3-32) into (3-31) give

$$\frac{1}{2} \frac{M_u \beta}{\dot{m}_a} \frac{\rho_a}{\rho_{vs}} \left(\frac{\partial \overline{X}_u}{\partial \phi} \right)_T \frac{d\theta_{a\phi,O}}{dt} + \theta_{a\phi,O} = 1 \tag{3-33}$$

An analytical solution for this normalized outlet air humidity is

$$\theta_{a\phi,O} = 1 - e^{-t/\tau_{a,\phi}} \tag{3-34}$$

where

$$\tau_{a,\phi} = \frac{1}{2} \frac{M_u \beta}{\dot{m}_a} \frac{\rho_a}{\rho_{vs}} \left(\frac{\partial \overline{X}_u}{\partial \phi} \right)_T = \frac{1}{2} \left(\frac{1-\varepsilon}{\varepsilon} \frac{\rho_u}{\rho_{vs}} \right) \beta \left(\frac{\partial \overline{X}_u}{\partial \phi} \right)_T \left(\frac{\varepsilon \cdot L}{u_D} \right) \tag{3-35}$$

is the time constant for the normalized outlet air humid ratio.

3.2.3.2 Heat transfer process

When urea particles adsorbed the moisture from the humid air, the particle temperature will increase due to the moisture adsorption heat caused by the water vapor condensation. Then heat convection will happen simultaneously between the interstitial air and urea particles.

$$M_u Cp_u \frac{d\overline{T}_u}{dt} = V \cdot A_{v,e} h_t \left(\overline{T}_a - \overline{T}_u\right) + \dot{m}_w h_w \tag{3-4a}$$

where $\dot{m}_w$ is the moisture adsorption rate of urea particles and h_w is the moisture adsorption heat.

$$\frac{M_u Cp_u}{\dot{m}_a Cp_a}\left(\frac{1}{2} + \frac{\dot{m}_a Cp_a}{V \cdot A_{v,e} h_t}\right)\frac{dT_{a,O}}{dt} + T_{a,O} = T_{a,I} + \frac{\dot{m}_w h_w}{\dot{m}_a c_{p,a}} \tag{3-14a}$$

Introducing the normalized outlet air temperature

$$\theta_{a,O} = \frac{T_{a,O} - T_{a,I}}{T_{a,O}^{\max} - T_{a,I}} \tag{3-15a}$$

and substituting equation (3-15a) into (3-14a) give

$$\frac{M_u Cp_u}{\dot{m}_a Cp_a}\left(\frac{1}{2} + \frac{\dot{m}_a Cp_a}{V \cdot A_{v,e} h_t}\right)\frac{d\theta_{a,O}}{dt} + \theta_{a,O} = f(t) \tag{3-16a}$$

where $f(t)$ is the variable part contributed to the outlet air temperature changes. It is dependent on the moisture adsorption rate determined by equation (3-21) and can be expressed in an exponential form as

$$f(t) = \frac{1}{\left(T_{a,O}^{\max} - T_{a,I}\right)}\frac{\dot{m}_w h_w}{\dot{m}_a c_{p,a}} = C_1 \cdot e^{-t/\tau_{a,T2}} \tag{3-36}$$

Therefore the analytical solution for equation (3-16a) for a step change in the initial conditions is

$$\theta_{a,O} = C_2 \cdot e^{-t/\tau_{a,T1}} + \frac{C_1.\tau_{a,T2}}{\tau_{a,T2} - \tau_{a,T1}} e^{-t/\tau_{a,T2}} \tag{3-37}$$

where

$$\tau_{a,T1} = \frac{M_u Cp_u}{\dot{m}_a Cp_a}\left(\frac{1}{2} + \frac{\dot{m}_a Cp_a}{V \cdot A_{v,e} h_t}\right) = \frac{(\rho \cdot Cp)_u \varepsilon_u}{A_{v,e} h_t} + \frac{1}{2}\frac{(\rho \cdot Cp)_u \varepsilon_u}{(\rho \cdot Cp)_a \varepsilon}\left(\frac{L \cdot \varepsilon}{u_D}\right) \tag{3-38}$$

is defined as the first time constant for the normalized outlet air temperature, while the second time constant is

$$\tau_{a,T2} = \tau_{a,\phi} \tag{3-39}$$

Special defined time conditions for equation (3-37), i.e., $\theta_{a,O} = 0$ at $t = 0$, $\theta_{a,O} = 0$ at $t = \infty$ but $\theta_{a,O} = 1$ and $\frac{\partial \theta_{a,O}}{\partial t} = 0$ at $t = t_m$ give the initial condition

$$\theta_{a,O}(t = 0) = C_2 + C_1 \frac{\tau_{a,T2}}{\tau_{a,T2} - \tau_{a,T1}} = 0 \tag{3-40}$$

and the peak dimensionless temperature condition

$$\frac{\partial \theta_{a,O}}{\partial t}(t = t_m) = -\frac{C_2}{\tau_{a,T1}} e^{-t_m/\tau_{a,T1}} - \frac{C_1}{(\tau_{a,T2} - \tau_{a,T1})} e^{-t_m/\tau_{a,T2}} = 0 \tag{3-41}$$

$$\theta_{a,O}(t = t_m) = C_2 \cdot e^{-t_m/\tau_{a,T1}} + \frac{C_1.\tau_{a,T2}}{\tau_{a,T2} - \tau_{a,T1}} e^{-t_m/\tau_{a,T2}} = 1 \tag{3-42}$$

The set of equations (3-40) (3-41) and (3-41) result in the solution set as follows

$$t_m = \frac{\tau_{a,T1} \cdot \tau_{a,T2} \cdot \ln(\tau_{a,T2}/\tau_{a,T1})}{\tau_{a,T2} - \tau_{a,T1}} \tag{3-43}$$

$$C_1 = \frac{(\tau_{a,T1} - \tau_{a,T2})/\tau_{a,T2}}{e^{-\frac{t_m}{\tau_{a,T1}}} - e^{-\frac{t_m}{\tau_{a,T2}}}} \tag{3-44}$$

$$C_2 = \frac{1}{e^{-\frac{t_m}{\tau_{a,T1}}} - e^{-\frac{t_m}{\tau_{a,T2}}}} \tag{3-45}$$

3.2.4 Theoretical solutions

In section 3.2.2 theoretical formulation for transient response of a thin urea particle bed subject to a pure air temperature step change at the inlet was developed to explore the analytical time constant for outlet air temperature after a urea particle bed. Comparison of the experimental time constant and the analytical one was used to determine the heat convection coefficient, h_t. Subsequently, in section 3.2.3.1 the mass convection coefficient h_m was determined based on the heat and mass transfer analogy as indicated by equation (3-20). In section 3.2.3.2 a theoretical formulation of moisture transfer for transient response of a thin urea particle bed subject to an air humidity step change at the inlet was developed to explore the analytical time constant for the outlet air humidity after a urea particle bed. In a similar way, the experimental time constant and analytical one can be compared to provide the information of the empirical factor β using equation (3-35). This factor accounts for the non-equilibrium internal diffusion within the urea particles in the test cell. It can have a different value for each test condition (i.e., Reynolds number and humidity step change size). In addition, the theoretical analysis of heat transfer caused by the heat of adsorption for the urea particle bed subject to a humidity step change was investigated and it was found that the temperature temporal profile of outlet air temperature is determined by two time constants – one is the time constant for the outlet air temperature for the pure temperature step change, the other is the time constant for the outlet air humidity for the humidity step change.

3.3 Results and conclusions

3.3.1 Comparison of experimental data and theoretical predictions

Experimental data of outlet temperature or humidity response when a Terico urea particle bed was subjected to a pure temperature or humidity step change with an air flow rate of 160 Lpm were presented in chapter 2. Figure 3.1 shows the modeled/analytical data of outlet air temperature and comparison with experimental data when the Terico urea particle bed is subjected to a pure temperature step change with an air flow rate equal to 160 Lpm. Figures

3.2 shows the experimental and modeled/analytical data of outlet air humidity respectively when the Terico urea particle bed is subjected to a humidity step changes with an air flow rate equal to 160 Lpm. Figure 3.3 shows the comparison of the experimental and predicted data of the outlet air temperature when the Terico urea particle bed is subject to a pure humidity step changes at the inlet with an air flow rate equal to 160 Lpm.

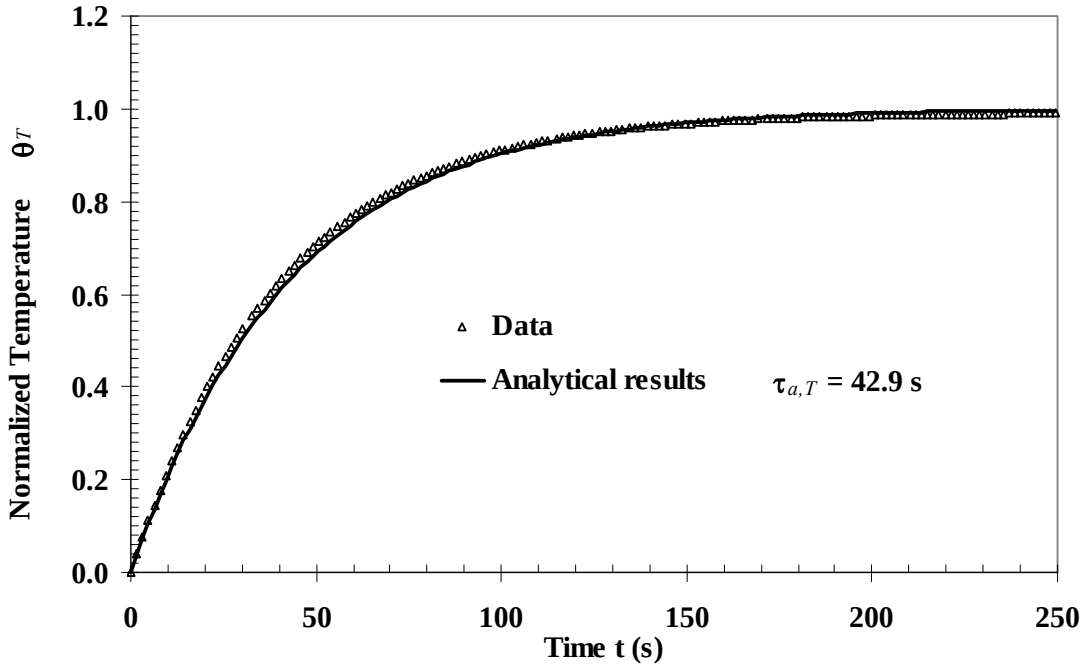

Figure 3.1 Comparison of transient data of temperature step change for the Terico urea particles with an air flow rate of 160 Lpm ($\mathrm{Re}_{d_h} = 284$ **) with the analytical results.**

For a pure temperature step change in Figure 3.1, the analytical results of the normalized outlet air temperature versus time fit the experimental data very well, which shows that the pure temperature response can be characterised by the time constant for outlet air temperature $\tau_{a,T} = 42.9$ s for Terico urea bed at 160 Lpm. For a pure humidity step change, the analytical results of normalized outlet air humidity versus time fit the experimental data very well in Figure 3.2, which shows that the pure humidity response can be characterised by the time constant for outlet air humidity $\tau_{a,\phi} = 5.8$ s for Terico urea bed at 160 Lpm. For the pure

humidity response of Terico urea bed at 160 Lpm, the analytical solution of the normalized outlet air temperature, determined by the two time constants – time constant of outlet air temperature with pure temperature step change, $\tau_{a,T}$, and time constant of outlet air humidity with pure humidity step change, $\tau_{a,\phi}$, as shown in equations (3-37), (3-38) and (3-39), is in general agreement with the experimental data. These comparisons imply that the analysis method described in section 3.2 can be used together with the measured data for the determination of the convective heat and mass transfer coefficients.

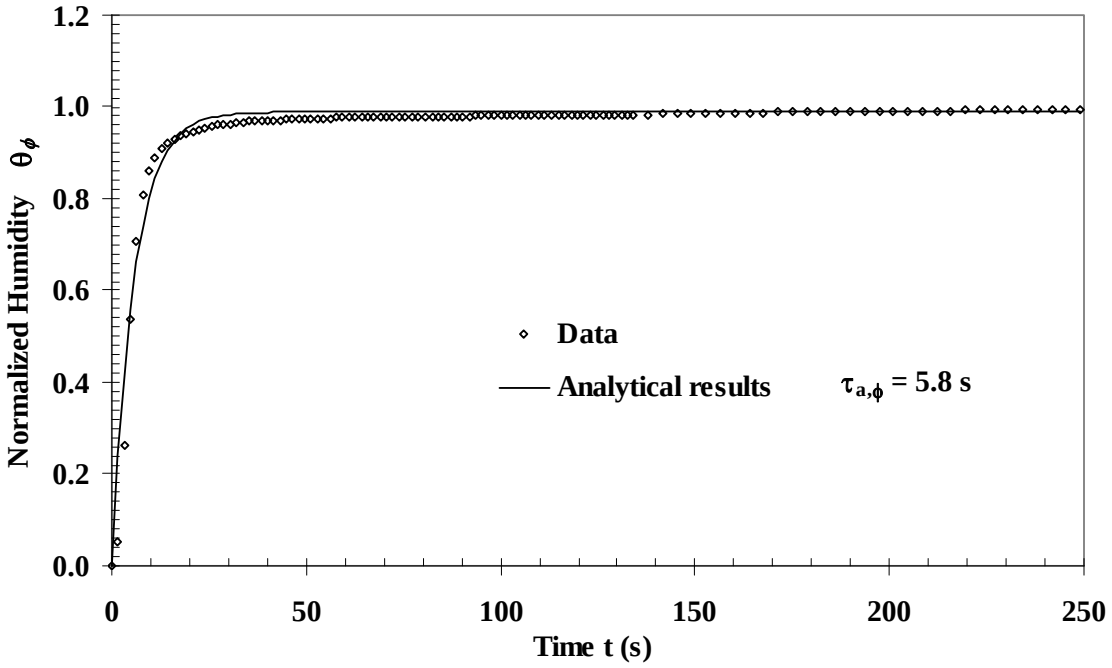

Figure 3.2 Comparison of transient data of humidity step change for the Terico urea particles with an air flow rate of 160 Lpm ($\mathrm{Re}_{d_h} = 284$ **) with the analytical results.**

In Figure 3.3, although the data of outlet air temperature and the analytical results are in general agreement, but there is an obvious deviation in the first 20 seconds where the experimental data increases faster than the analytical solution. Some possible reasons causing this deviation are as follows:

(1) The justified Schumann method was introduced to model the process of heat and /or mass transfer within this urea particle bed and to investigate the response of the bed to the pure temperature or humidity step change. This model ignored the axial heat conduction or mass diffusivity and dispersion due to the fluid flow. For the heat/mass transfer in porous media with velocity/temperature/vapor density gradients, dispersion means the internal thermal energy spreading considered separately from the effective molecular conduction/diffusivity. As a matter of fact, temperature/vapor density gradient and velocity gradient within the pores always exists at any cross-section at any time. However, because of the volume averaging over the pore space, this dispersion contribution is not considered in the Darcian convection but it is included in the total effective thermal/mass diffusivity coefficient (Kaviany, 1995). The total effective diffusivity including dispersion was not included in equation (3-2), so the outlet air temperature response was underestimated.

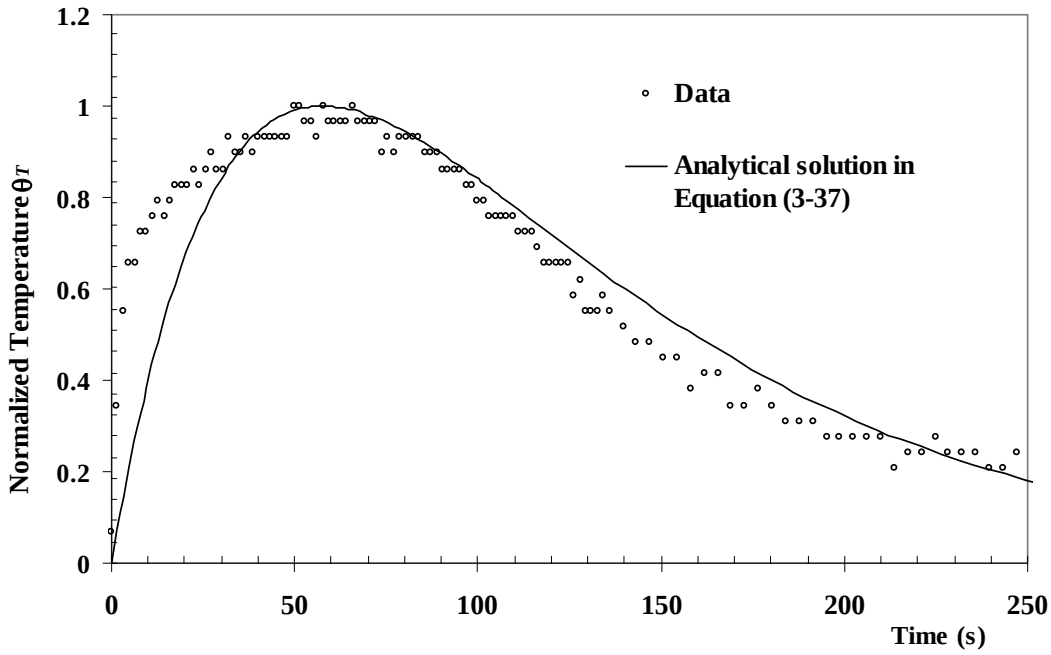

Figure 3.3 Comparison of outlet air temperature of a Terico urea particle bed with the analytical prediction for the bed which is subject to a humidity step change for an air flow rate of 160 Lpm ($\mathrm{Re}_{d_h} = 284$ **)**

(2) Although channelling effects near the wall are estimated to be negligible, non-uniformity packing and non-uniform porosity distribution within the urea particle bed may cause air flow in some pore paths to be faster than the average air flow. The outlet temperature response will be faster if the sensor was located in the path of the faster air flow.

Since in the case of pure temperature step change, the axial heat conduction is shown to be negligible for the solid domain energy equation and the analytical results of the outlet air temperature fit the experimental data very well, it can be concluded that ignoring the axial heat conduction has negligible effect. But generally ignoring dispersion within porous media will underestimate the transient response of the outlet air temperature, i.e., the deviation in the early period in Figure 3.3. Besides, compared with the case of pure temperature step change, the energy equation for the case of pure humidity step change is more complex because the latter includes both the mass transfer and the heat transfer due to the moisture adsorption, condensation or dissolution process. To simply consider the whole urea particle bed as a uniformly moisture adsorption system can cause the deviation.

3.3.2 Determination of h_t and β

Using equations (3-18) or (3-19) and (3-20), the convective heat and mass transfer coefficients can be obtained for both the Terico and Georgia urea particle test cell beds at each air flow rate.

For convenience, the following terms are defined.

$$z_1 = (\rho \cdot Cp)_u \varepsilon_u \tag{3-46}$$

$$z_2 = (\rho \cdot Cp)_a \tag{3-47}$$

$$z_3 = \frac{L}{u_D} = \frac{L \cdot \pi D_c^2}{4\dot{q}_a} \tag{3-48}$$

$$z_4 = \frac{1}{2}\frac{z_1 z_3}{z_2} \tag{3-49}$$

Then equation (3-19) for the calculation of the heat convection coefficient is replaced with

$$\tau_{a,T} = \frac{1}{2}\frac{z_1 z_3}{z_2} + \frac{z_1}{A_{v,e} h_t} \tag{3-50}$$

Also, h_t can be expressed as

$$h_t = \frac{z_1}{A_{v,e}\left(\tau_{a,T} - z_4\right)} \tag{3-51}$$

Combining equation (3-50), equation (3-20) with experimental data provides the convective heat and mass transfer coefficients for both the Terico and Georgia urea particle test cell beds at each air flow rate. The uncertainty of h_t was derived from the equation propagation.

The uncertainties for the terms, z_1, z_2, z_3 are easily derived as follows.

$$U\left(z_1\right) = z_1\left\{\left[\frac{U\left(\rho_u\right)}{\rho_u}\right]^2 + \left[\frac{U\left(Cp_u\right)}{Cp_u}\right]^2 + \left[\frac{U\left(\varepsilon_u\right)}{\varepsilon_u}\right]^2\right\}^{1/2} \tag{3-52}$$

$$U\left(z_2\right) = z_2\left\{\left[\frac{U\left(\rho_a\right)}{\rho_a}\right]^2 + \left[\frac{U\left(Cp_a\right)}{Cp_a}\right]^2\right\}^{1/2} \tag{3-53}$$

$$U\left(z_3\right) = z_3\left\{\left[\frac{U\left(L\right)}{L}\right]^2 + \left[2\frac{U\left(b\right)}{b}\right]^2 + \left[\frac{U\left(\dot{q}_a\right)}{\dot{q}_a}\right]^2\right\}^{1/2} \tag{3-54}$$

Then the uncertainty of h_t is calculated using

$$U\left(h_t\right) = \sqrt{\begin{aligned}&\left[\frac{\partial h_t}{\partial z_1}U\left(z_1\right)\right]^2 + \left[\frac{\partial h_t}{\partial A_{v,e}}U\left(A_{v,e}\right)\right]^2 + \left[\frac{\partial h_t}{\partial \tau_{a,T}}U\left(\tau_{a,T}\right)\right]^2 \\ &+ \left[\frac{\partial h_t}{\partial z_2}U\left(z_2\right)\right]^2 + \left[\frac{\partial h_t}{\partial z_3}U\left(z_3\right)\right]^2\end{aligned}} \tag{3-55}$$

where

$$\frac{\partial h_t}{\partial A_{v,e}} = -\frac{z_1}{A_{v,e}^2\left(\tau_{a,T} - z_4\right)} = -\frac{h_t}{A_{v,e}} \tag{3-56}$$

$$\frac{\partial h_t}{\partial \tau_{a,T}} = -\frac{z_1}{A_{v,e}\left(\tau_{a,T} - z_4\right)^2} = -\frac{h_t}{\left(\tau_{a,T} - z_4\right)} \tag{3-57}$$

$$\frac{\partial h_t}{\partial z_1} = \frac{1}{A_{v,e}(\tau_{a,T} - z_4)}\left(1 + \frac{z_4}{\tau_{a,T} - z_4}\right) = h_t \frac{1}{z_1(1 - z_4/\tau_{a,T})} \tag{3-58}$$

$$\frac{\partial h_t}{\partial z_2} = -\frac{z_1}{A_{v,e}(\tau_{a,T} - z_4)^2} \cdot \frac{z_1 z_3}{2 \cdot z_2^2} = \frac{h_t}{(1 - \tau_{a,T}/z_4) z_2} \tag{3-59}$$

$$\frac{\partial h_t}{\partial z_3} = -\frac{z_1}{A_{v,e}(\tau_{a,T} - z_4)^2} \cdot \left(-\frac{z_1}{2 \cdot z_2}\right) = \frac{h_t}{(\tau_{a,T}/z_4 - 1) z_3} \tag{3-60}$$

therefore,

$$\frac{U(h_t)}{h_t} = \sqrt{\left[\frac{U(z_1)}{z_1\left(1 - z_4/\tau_{a,T}\right)}\right]^2 + \left[\frac{U(A_{v,e})}{A_{v,e}}\right]^2 + \left[\frac{U(\tau_{a,T})}{\left(\tau_{a,T} - z_4\right)}\right]^2 + \left[\frac{U(z_2)}{\left(\tau_{a,T}/z_4 - 1\right) z_2}\right]^2 + \left[\frac{U(z_3)}{\left(\tau_{a,T}/z_4 - 1\right) z_3}\right]^2} \tag{3-61}$$

Calculated results show that the uncertainty of $A_{v,e}$ contribute most to the uncertainty of h_t, and the relative uncertainty of h_t, for each case, is approximated as $U(h_t)/h_t = 20\%$.

Good agreement between experimental data and theoretical solution shown in Figure 3.1, Figure 3.2 and Figure 3.3 implied that the theoretical formulation could be used to predict the outlet air response during the time period when assumptions were generally satisfied, e.g. temperature distribution along the urea bed was assumed to be linear at any time. Based on this assumption, the dimensionless outlet air temperature response presented an exponential growth form. In other words, the exponential growth form was applied to the chosen time period starting from any specific time through the equilibrium state because it was suppose that the temperature distribution was closer to linear during this time period than in the early period. It was found that the assumption of linear temperature distribution could predict the outlet air response during some chosen time period but cause a systematic error in correlation determination (Nie, et al., 2009a). To solve this problem, Nie et al. (2009b) indicated that (a) this linear assumption is only valid for a specific time (called linear time); (b) even though the outlet response is not exponential, the time required for the dimensionless outlet air temperature to reach 63.2% (=1-e^{-1}) is close to the time constant with the assumption of linear temperature distribution at any time. With these findings, the time required to reach 63.2% were used instead of the time constant in exponential growth form to calculate the heat convection coefficients h_t using equations (3-18) or (3-19) and (3-20). Uncertainty of the heat

convection coefficients h_t was also determined following equations (3-52) to (3-61). Table 3.1 shows the determination of the heat and mass convection coefficients and their uncertainty at each air flow rate. Table 3.2 lists one set of uncertainty calculation of h_t for both Terico and 2 urea particle bed while an air with flow rate 160 Lpm flows through.

Table 3.1 Convective heat and mass transfer coefficients of Terico and Georgia urea particle beds at different air flow rates (see uncertainty calculations in Table 3.2)

Volumetric flow rate $\dot{Q}_a$ (Lpm) / Darcy velocity u_D (m/s)	Type of Urea	Reynolds number, Re_{d_h}		Heat convection coefficient, h_t ($\mathrm{W/(m^2 \cdot K)}$)		Mass convection coefficient, h_m (m/s)	
		Value	$\frac{U(\mathrm{Re}_{d_h})}{\mathrm{Re}_{d_h}}$	Value	$\frac{U(h_t)}{h_t}$	Value	$\frac{U(h_m)}{h_m}$
160 / 1.316	Terico	284	20.0%	13.33	±20.2%	1.22×10^{-2}	±20.2%
	Georgia	172		19.47		1.78×10^{-2}	
80 / 0.658	Terico	142	20.2%	14.27		1.30×10^{-2}	
	Georgia	86		14.97		1.37×10^{-2}	
40 / 0.329	Terico	71	20.2%	8.45		7.73×10^{-3}	
	Georgia	43		4.13		3.78×10^{-3}	
20 / 0.164	Terico	36	20.6%	22.81		2.09×10^{-2}	
	Georgia	22		1.033		9.45×10^{-4}	
10 / 0.082	Terico	18	20.6%	---		---	
	Georgia	11		0.838		7.66×10^{-4}	
5 / 0.041	Georgia	5	22.4%	0.857		7.84×10^{-4}	

Table 3.2 A sample of heat convection coefficient, h_t, uncertainty calculation (160 Lpm)

Property and	Unit	Value	Uncertainty
air density, ρ_a	kg/m^3	1.184	0.01
Specific heat capacity of air, Cp_a	J/(kg·K)	1007	10
Bed length, L	m	0.090	0.001
Darcy velocity, u_D	m/s	1.316	0.016
Internal diameter of test cell, D_c	m	0.0508	0.0001
urea density, ρ_u	kg/m^3	1320	13
Specific heat capacity of urea, Cp_u	J/(mol.K)	92.4	0.1
Substitute coefficient, $z_1 = (\rho \cdot Cp)_u \varepsilon_u$	---	429.2	0.57
Substitute coefficient, $z_2 = (\rho \cdot Cp)_a$	---	68175	1070
Substitute coefficient, $z_3 = \dfrac{L}{u_D} = \dfrac{L \cdot \pi D_c^2}{4\dot{Q}_a}$	---	0.0684	0.0012
Terico			
Time constant of temperature response, $\tau_{v,T}$	s	81.1	1.0
Heat convection coefficient, h_t	W/(K·m^2)	13.33	2.7
Georgia			
Time constant of temperature response, $\tau_{v,T}$	s	33.6	1.0
Heat convection coefficient, h_t	W/(K·m^2)	19.47	3.9

The convective heat or mass transfer coefficients increases with increasing air flow rates as shown in Table 3.1. The data for water vapor transient response in Figure 3.2 does not fit the simple theoretical model for mass transfer nearly as well as the temperature response in Figure 3.1. The reason for this is that the water diffusion and adsorption inside each particle is significantly slower than heat diffusion through the particles. To account for this delay in reaching mass distribution equilibrium inside the urea particles, the empirical coefficient, β, is introduced. This coefficient is a ratio of moisture sorption to that for the new equilibrium state. The calculated values of β are presented in Table 3.3. A larger value of β implies a rapid approach of the bed towards a new equilibrium conditions for moisture transfer inside the urea particles. A small value implied the bed is closer to previous equilibrium. The

empirical coefficient, β, either for Terico or Georgia urea particles behaves in the same manner – it increases as the Reynolds number increases.

Table 3.3 Empirical coefficient, β, to account for non-equilibrium moisture sorption at different Reynolds numbers for both Terico and Georgia urea particles

Volumetric air flow rate $\dot{Q}_a$ (Lpm) / Darcy velocity u_D (m/s)	Urea Type	Reynolds number, Re_{d_h}	Empirical coefficient for non-equilibrium moisture sorption, β
160 / 1.316	Terico	284	0.69
	Georgia	172	0.49
80 / 0.658	Terico	142	0.57
	Georgia	86	0.36
40 / 0.329	Terico	71	0.41
	Georgia	43	0.32
20 / 0.164	Terico	36	0.27
	Georgia	22	0.19
10 / 0.082	Terico	18	0.14
	Georgia	11	0.11
5 / 0.041	Georgia	5	0.10

3.3.3 Comparison of correlations

Only dimensionless correlations that correspond to the experimental range of testing in this thesis are discussed. Travkin and Catton (2001) reviewed and compared research results of internal effective heat transfer coefficients in porous media deduced using the Volume Averaging Theory (VAT). Parameters considered include types of media material, Reynolds number and porosity range. Kar and Dybbs (1982) developed a correlation for laminar flow in sintered powder metal specimens. Kays and London (1984) presented experimental data and empirical correlations for gas flow through a randomly packed spherical particle bed with

porosity range of 0.37 to 0.39 and a Reynolds number range of $10 \le \mathrm{Re}_{d_h} \le 5000$. The uncertainties of these correlations were not presented explicitly. A Chilton-Colburn factor versus Reynolds number correlation was determined by Nie et al. (2008a and b) for a numerical simulation of heat and mass transport through porous urea particle beds with average particle size of 1.82 or 2.21 mm, porosity of 0.36 and Reynolds number less than 20. Peng et al. (2000) did the same for a granular potash particle bed. Large differences exist among all these correlations, suggesting significant bias errors in the various test methods. In the laminar flow regime where Reynolds numbers is less than 5, it is expected that the Nusselt numbers will be constant (details will be discussed in section 3.3.4); however, the trend of constant Nusselt number in low Reynolds number range did not appear in the correlations of Nie et al. (2008b) and Peng et al. (2000). These two correlations were both inversely deduced from numerical simulations which were compared to the experimental data. Nie et al. (2008b) indicated that the moisture uptake is not sensitive to the change of convection coefficients. This implies that the inverse test method using VAT may lead to large uncertainties in h_t.

Nie et al. (2009a) used the theoretical method mentioned in section 3.2 to propose a correlation of dimensionless Chilton-Colburn factor for heat transfer as a function of Reynolds number ($5 < \mathrm{Re}_{d_h} < 300$), which presented a large deviation from other correlations. The following reasons were listed to explain the discrepancy.

(1) Firstly, the linear temperature distribution was assumed to apply along the urea bed at any time. However, Nie et al. (2009b) indicated that this linear assumption is only valid very near a specific time and proposed a new technique to derive the convection coefficients within verified linear time period. In appendix D, it was indicated that even though the outlet responses of solid particles of different types are not exponential, the time required for the dimensionless outlet air temperature response to reach 63.2% is close to the time constant with the assumption of linear temperature distribution at any time. Table 3.1 showed the corrected convection coefficients used to reduce the systematic error caused by the assumption of linear temperature distribution.

(2) Secondly, the assumption of no temperature gradient within each urea particles was based on the calculation of Biot number ($\mathrm{Bi}=h_t d_p/6/k_s$) before h_t was determined. However, Biot numbers can be greater than 0.1 for high Reynolds number if the correlation of Nie et al. (2009b) is used. For example, $\mathrm{Bi}_{d_p} = 0.13 > 0.1$ for a Terico urea particle bed when

$Re_{d_h} = 284$. It implied that the assumption of a low Biot number (at high Reynolds number) caused the underestimate of convective heat transfer coefficients h_t.

(3) Thirdly, a temperature step change at the inlet of the dry urea particle bed was assumed to have no moisture sorption or related phase change energy. However, according to Figure 4.5 in Chapter 4, the equilibrium moisture content of the urea at the same dry condition (e.g. RH=4%) could be different. In addition, equilibrium moisture content at the same relative humidity was negatively related to the temperature. Dry urea particles were prepared before experiments and assumed to remain dry during the experiments for a temperature step change. However, the complete isolation of urea particles from the environmental air (not the dry air flow) was impossible especially when particles were packed to fill the test cell. When an initially dry urea particle bed, through which a cool and dry air flow at 15^{o}C passed, was suddenly subjected to a high temperature (35^{o}C) airflow, moisture evaporation occurring on the external surface or tiny urea powders (produced during packing process) consumed some thermal energy causing the outlet air temperature response delay. Thus, the delay of the temperature response caused the errors in determining the convective heat transfer coefficients h_t.

(4) Finally, the complicated properties of urea particles, such as its complex pore geometry and fragile structural characteristics could be a problem. While preparing the urea particle beds, tight packing could produce some urea powder. These tiny urea powders filled in the void space of the bed very near the urea particle surface could change the interaction between flowing air and urea surface. As Koch and Brandy (1985) indicated that the regime of convective dispersion very near the surface of particles was different from the void space. Ignoring dispersion in the porous media would cause the estimated convective heat transfer coefficient to be inaccurate. This will be presented in details in section 3.3.4.3.

For these above reasons (1) to (4), a new research study on determination of convection coefficients within simple spherical particle beds has been investigated in appendix D. In this new research, all the above reasons for bias have been eliminated (e.g., reason (1) (2) (4) or alleviated (e.g., reason (3)).

The new correlation of the dimensionless Nusselt number versus Reynolds number ($5 < Re_{d_h} < 300$) with non-linear justification mentioned above is proposed in the form

$$\mathrm{Nu}_{d_h} = a\,\mathrm{Re}_{d_h}^{b}, \qquad 5 < \mathrm{Re}_{d_h} < 300 \tag{3-62}$$

where a=0.0076±0.0186, b=0.8633±0.5046. The uncertainty of the correlation $t \times SEE$=±0.2278 at the 95% confidence limits. The coefficient of determination, R^2, between the dependent variable (Nu_{d_h}) and data used to obtain the correlation equation (3-62) is 0.8855. With the relationship $\mathrm{Jh}_{d_h} = \mathrm{St} \cdot \mathrm{Pr}^{2/3}$ and $\mathrm{St} = \mathrm{Nu}_{d_h} / \mathrm{Re}_{d_h} \mathrm{Pr}$, the correlation of Chilton-Colburn factor as a function of Reynolds number can be derived from equation (3-62). All the dimensionless properties are based on hydraulic diameter, d_h , as the characteristic length. Correlations of Chilton-Colburn factor are plotted in Figure 3.4 while the correlations of Nusselt numbers are plotted against the logarithm of the Reynolds number in Figure 3.5. For Re<5, the flow in the bed is expected to be laminar so the above correlation is expected to change. From Figure 3.4, it can be seen that the correlation (3-62) for Jh_{d_h} or Jm_{d_h} decreases somewhat as Re_{d_h} goes to 5. As Re_{d_h} become large Jh_{d_h} or Jm_{d_h} become nearly constant. Except for Kar and Dybbs (1982), other research results do not show this trend. In Figure 3.5, the Nusselt number increases with an increase in Reynolds number when Re<5 while Nusselt number could be a constant at low Reynolds number.

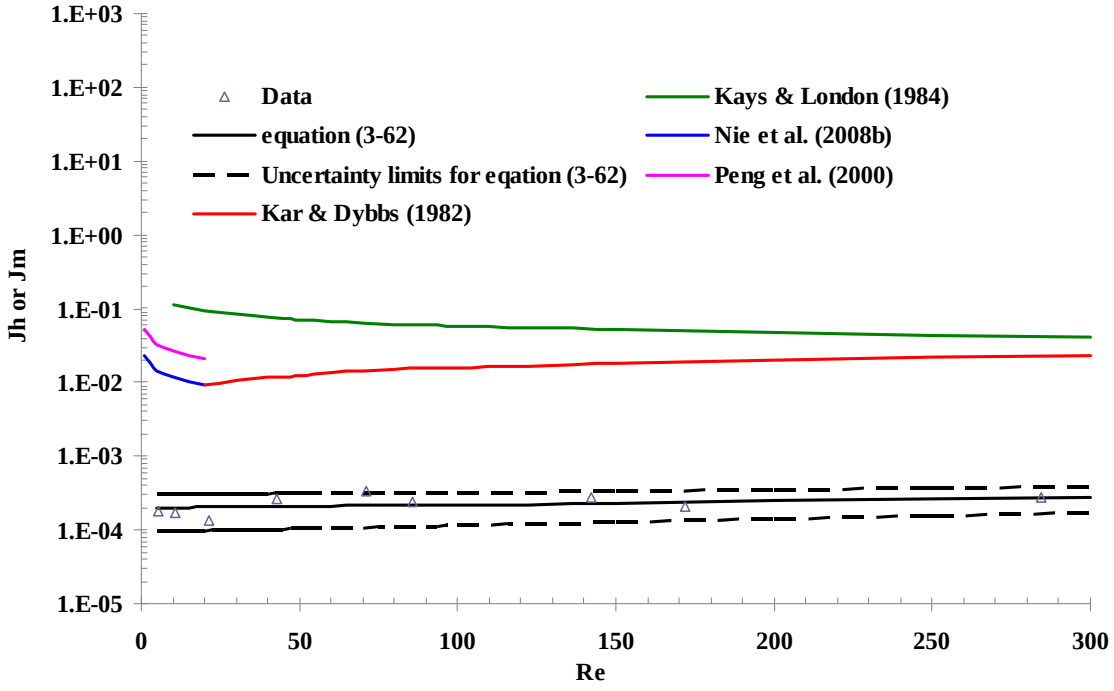

Figure 3.4 Dimensionless Chilton-Colburn factors versus Reynolds number.

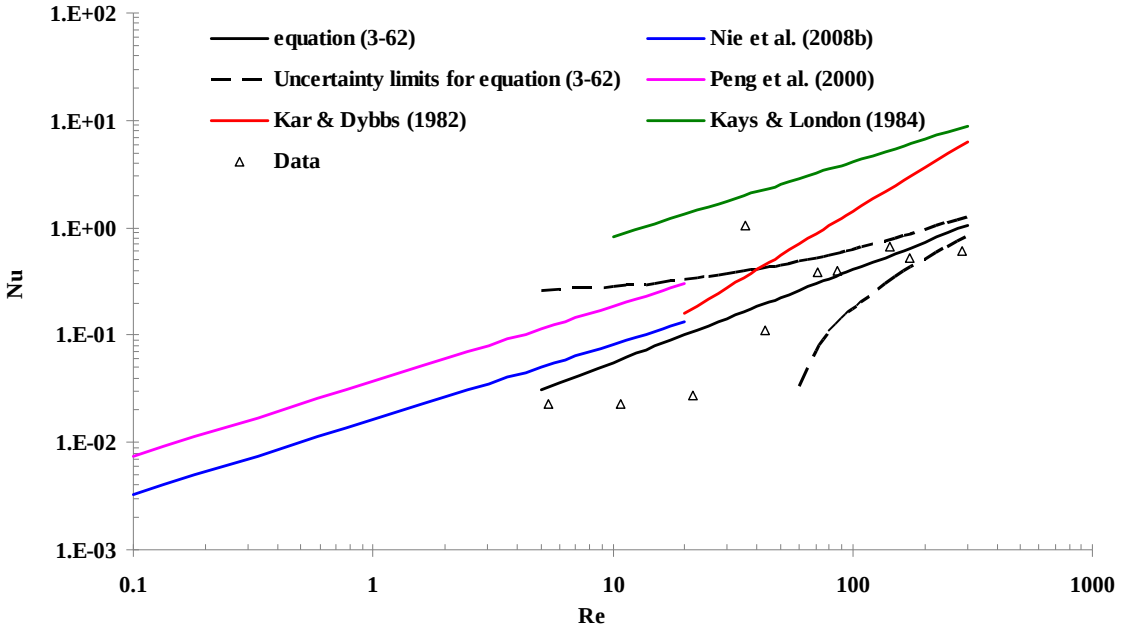

Figure 3.5 Dimensionless Nusselt number versus Reynold number.

In Figures 3.4 and 3.5, differences of up to one order of magnitude, exist among correlations from different researchers. Kar and Dybbs (1982) showed that even for the same porous material with same packing method the correlations can vary by two orders of magnitude. The reasons for this large variation are complicated: a) the assumption of steady or quasi-steady one-dimensional heat transfer process along the porous bed may not be well maintained during experiments; b) the measurement of temperature within the porous particle beds can represent the particle temperature or gas temperature or both; and c) using one Reynolds number to characterize the flow through porous media cannot characterize the local flow regimes, e.g., attached laminar flow or separated laminar flow (Kaviany, 1995). These correlations ignore the actual velocity variation or non-uniformities of velocity distribution across any cross-sectional area of porous media. In this chapter, a new theoretical method was developed assuming an ideal step change at the inlet. Using the transient single-blow method, Baclic et al. (1986) showed that the errors due to transient delays in ideal step change at the inlet and large Reynolds number could lead to large errors. In this chapter, at $\mathrm{Re}_{d_h} = 284$, the

dimensionless time constant is less than 0.26 and the dimensionless bed length is 0.04; while at $\mathrm{Re}_{d_h} = 5$, the dimensionless time constant is less than 0.01 and the dimensionless bed length is 0.04. According to Baclic et al. (1986), the error caused by considering the ideal step change input instead of the single-blow input is negligible or very small over this range of Reynolds number. Nie et al. (2008 a & b) indicated that the numerical simulation of moisture uptake is not sensitive to the convection coefficients. This chapter proposed a correlation within urea particle beds that had a systematic error caused by linear temperature distribution assumption. Equation (3-62) eliminated this systematic error mentioned in reason (1). But the underestimation caused by reasons (2) (3) (4) were not eliminated. In addition, it was observed that (a) one data point at 10<Re<40 are beyond the correlation limits of equation (3-62), implying that experimental data was not sufficient enough to have good repeatability; (b) one data point when Reynolds number is close to 300 is below the uncertainty bound, implying the assumption of a low Biot number at high Reynolds number was not valid. The discrepancy between correlations implies the necessary of an accurate method to determine the convection coefficient within porous bed. Therefore, there is a need to propose a new method that can eliminate or alleviate reasons (1) (2) (3) (4), which will be presented in appendix D.

The empirical coefficient, β, a measure of the mass deposition of moisture inside each individual urea particle compared to the average adsorption at the equilibrium state, is a function of Reynolds number, Re_{d_h}.

$$\beta = a \times \mathrm{Re}_{d_h}^{b}, \qquad 5 < \mathrm{Re}_{d_h} < 300 \tag{3-63}$$

where $a = 0.0451 \pm 0.0201$, $b = 0.48 \pm 0.0402$, $t \times SEE = 0.0952$ at 95% confidence level. The coefficient of determination, R^2, between the dependent variable (β) and equation (3-63) is 0.958, indicating a very good fit of the equation to the data.

Figure 3.6 shows a comparison of the data with the predictions of equation (3-63). As shown in Figure 3.6, β approaches zero when Re_{d_h} is zero. It indicates that at this limit, the urea particles were in previous equilibrium state both internally and externally and the vapor density was the same within the particles as in the interstitial air. Increasing Re_{d_h} (i.e., increasing the air flow rate), increases the convective mass transfer coefficients between the

particles and air flow independent of internal mass diffusion coefficient inside each particle. During this process, the internal water diffusion process inside each particle become stronger due to the higher water vapor density gradient near the external surface caused by the stronger mass convection at higher Reynolds number. Although Terico and Georgia urea particles are from two different manufacturers which means different manufacturing processes and physical properties such as the particle diameter, internal porosity and internal geometry, the relationship between β and Reynolds shows the same behaviour. This is because that the differences of physical properties between Terico and Georgia urea particles are not big enough to cause the evident difference in β. For example, differences on particle or hydraulic pore size (integrated into Reynolds number), internal and external porosity as shown in Table 2.1, are not large enough to show a significant difference in internal particle water accumulation behaviour.

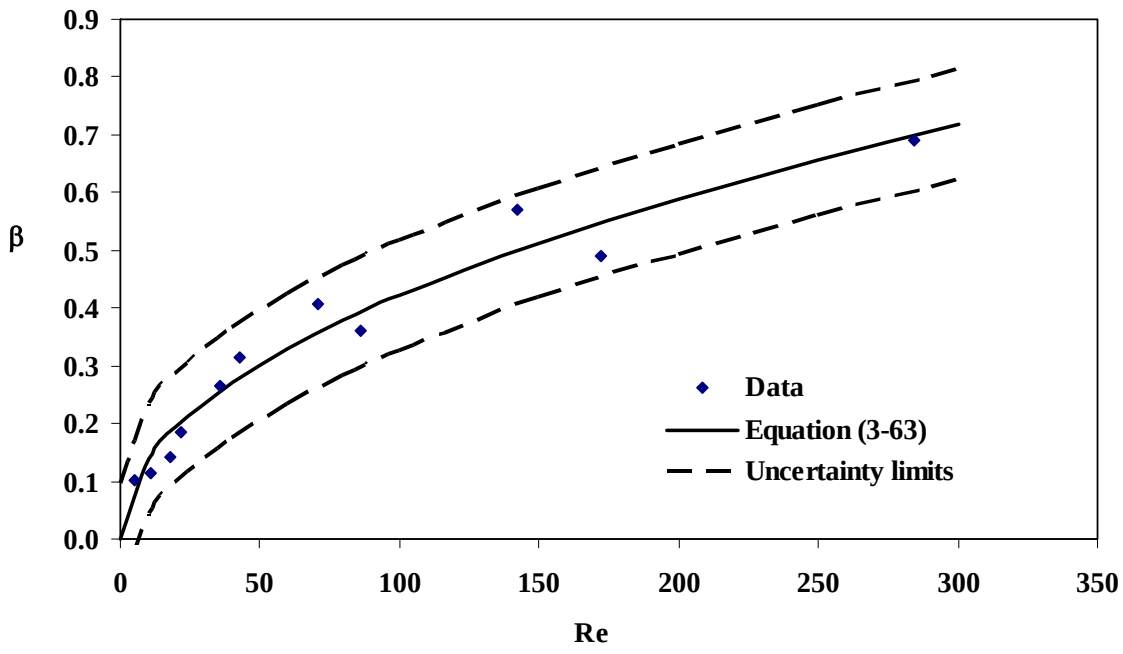

Figure 3.6 Relationship of β versus Reynolds number.

3.3.4 Analogy of momentum, heat or mass convection, convective dispersion

Osborne Reynolds was the first researcher who noticed the similarity between momentum and heat transfer. He presented in 1883 a quantitative analogy between these two transport phenomenon based on study of frictional resistance to fluid flow in conduits. But two restrictions - (1) Pr = 1 and (2) no form drag, i.e., viscous flow - are required for this Reynolds analogy. A complete Chilton-Colburn analogy, also called modified Reynolds analogy, extending the use of this momentum-convection analogy over a wide range of Prandtl number $0.6 < \mathrm{Pr} < 60$ and Schmidt number $0.6 < \mathrm{Sc} < 3000$, is given in form of

$$\frac{C_f}{2} = \mathrm{Jh} = \mathrm{Jm} \tag{3-64}$$

where $\mathrm{Jh} = \mathrm{StPr}^{2/3}$, $\mathrm{St} = \mathrm{Nu}/(\mathrm{Re}\,\mathrm{Pr})$, $\mathrm{Jm} = \mathrm{St_m Sc}^{2/3}$, $\mathrm{St_m} = \mathrm{Sh}/(\mathrm{Re}\,\mathrm{Sc})$. Therefore, equation (3-64) can be rewritten in another form showing that the product of shear stress coefficient, C_f, and Reynolds number, Re, is a constant determined by Nusselt number or Sherwood number as follows.

$$\frac{C_f}{2}\mathrm{Re} = \frac{\mathrm{Nu}}{\mathrm{Pr}^{1/3}} = \frac{\mathrm{Sh}}{\mathrm{Sc}^{1/3}} \tag{3-65}$$

For a fully developed laminar flow in a duct with length, L, hydraulic diameter, d_h, and cross-section area average fluid flow velocity, U, Arpaci and Larsen (1984) and Bejan (2004) reviewed and listed the effect of cross-sectional shape on friction factor and Nusselt number as shown in Table 3.4.

Table 3.4 Friction factor Reynolds number product, $f \cdot \mathrm{Re}_{d_h}$, and Nusselt number, Nu_{d_h} (constant heat flux), for fully developed duct flow with different cross-sectional shapes.

Shape of cross-section	Hydraulic diameter, d_h	Friction factor Reynolds number product, $f \cdot \mathrm{Re}_{d_h}$	Nusselt number, Nu_{d_h}
Circular pipe, diameter D	$d_h = D$	$f \cdot \mathrm{Re}_{d_h} = 16$	$\mathrm{Nu}_{d_h} = 4.36$
Square, side length D	$d_h = D$	$f \cdot \mathrm{Re}_{d_h} = 14.2$	$\mathrm{Nu}_{d_h} = 3.63$
Equilateral triangle, side length D	$d_h = D/\sqrt{3}$	$f \cdot \mathrm{Re}_{d_h} = 13.3$	$\mathrm{Nu}_{d_h} = 3$
Rectangular, side length $D \times 4D$	$d_h = 8D/5$	$f \cdot \mathrm{Re}_{d_h} = 18.3$	$\mathrm{Nu}_{d_h} = 5.35$
Infinite parallel plates, one side length D	$d_h = 2D$	$f \cdot \mathrm{Re}_{d_h} = 24$	$\mathrm{Nu}_{d_h} = 8.24$

where $d_h = \frac{4 \cdot A}{P}$, $f = \frac{\tau_W}{\frac{1}{2}\rho U^2}$, $\Delta P = f \frac{4L}{d_h}\left(\frac{1}{2}\rho U^2\right)$, $\mathrm{Re}_{d_h} = \frac{\rho \cdot U \cdot d_h}{\mu}$, $\mathrm{Nu}_{d_h} = \frac{h_t \cdot d_h}{k}$. These relationships between friction factor and Reynolds number or Nusselt number are valid for fully developed laminar flow in ducts, where $\mathrm{Re}_{d_h} < 2000$.

3.3.4.1 Friction factor *f* within spherical particle beds

It is expected that a similar result can be valid for spherical particle beds when the Reynolds number is small (e.g. less than 5.0). Below the threshold Reynolds number, the friction factor and Reynolds number product will be a constant while above this threshold Reynolds number, the product will likely increase with Reynolds number. Dullien (1992) reviewed the phenomenological flow model used for porous media consisting of packed beds of particles or fibres. Ergune (1952), Carmen (1937) and Kozeny (1927) found that, for a flow through a packed bed at low Reynolds number, the product of friction factor and Reynolds number is a constant if the bed porosity is known. That is to say, the friction factor is only a function of Reynolds number and porosity. For low Reynolds number flow, porosity effects were investigated by many researchers. Dullien (1992) presented their porosity functional

relationship that was also proposed by Rumpf and Gupte (1971) in equation (3-66) which is in agreement with their experimental data.

$$f_p \cdot \mathrm{Re}_p = k \cdot 5.6\varepsilon_e^{-5.5} \tag{3-66}$$

where k=1.00 for urea particle bed's narrow size distribution, $f_p = \frac{\Delta \mathrm{P} \cdot d_p}{L\left(\rho\, u_D^{\,2}\right)}$, $\mathrm{Re}_p = \frac{\rho \cdot u_D \cdot d_p}{\mu}$, $u_D = \frac{\dot{Q}_a}{A} = \varepsilon_e \cdot u_p$. While the air flow through the spherical particle bed, it is common to use hydraulic diameter d_h where $\frac{d_h}{d_p} = \frac{2\varepsilon_e}{3(1-\varepsilon_e)}$. Therefore, equation (3-66) can be transformed to

$$f_{d_h} \cdot \mathrm{Re}_{d_h} = 5.6\varepsilon_e^{-5.5}\left[\frac{2\varepsilon_e^{\,3}}{9(1-\varepsilon_e)^2}\right] = \frac{1.24}{\varepsilon_e^{\,2.5}(1-\varepsilon_e)^2} \tag{3-66a}$$

where

$$\mathrm{Re}_{d_h} = \frac{\rho \cdot u_p \cdot d_h}{\mu} \tag{3-67}$$

$$f_{d_h} = \frac{\Delta p \cdot d_h}{4L\left(\frac{1}{2}\rho \cdot \mathrm{u}_\mathrm{p}^2\right)} \tag{3-68}$$

For a packed urea particle bed with porosity ε_e=0.36~0.44, the pressure drops through the spherical particle bed at low Reynolds number $\mathrm{Re}_{d_h} \le 10$ can be predicted as shown in Table 3.5.

Table 3.5 Product of friction factor and Reynolds number for packed spherical particle beds

Porosity, ε_e	Product of friction factor and Reynolds number $f_{d_h} \cdot \mathrm{Re}_{d_h}$
0.36	38.9
0.38	36.2
0.40	34.0
0.42	32.2
0.44	30.8

For flow rates outside of Darcy law, Macdonald et al. (1979) used extensive experimental data to examine the Ergun equation, and found that the following correlation fits the data very well.

$$f_p \frac{\varepsilon_e^{\,3}}{1-\varepsilon_e} = \frac{180(1-\varepsilon_e)}{\mathrm{Re}_P} + 1.8 \tag{3-69}$$

is for a packed bed of smooth spherical particles. And

$$f_p \frac{\varepsilon_e^{\,3}}{1-\varepsilon} = \frac{180(1-\varepsilon_e)}{\mathrm{Re}_P} + 4.0 \tag{3-70}$$

is for a packed bed of roughest spherical particles. Similarly, these equations can be transformed to

$$f_{d_h} \mathrm{Re}_{d_h} = 40 + C_3 \cdot \mathrm{Re}_{d_h} \tag{3-71}$$

for high Reynolds number $\mathrm{Re}_{d_h} > 10$. C_3 is a constant between 1.8 and 4.0 related to the surface roughness. Figure 3.7 shows the friction factor for flow through spherical particle beds at different Reynolds number.

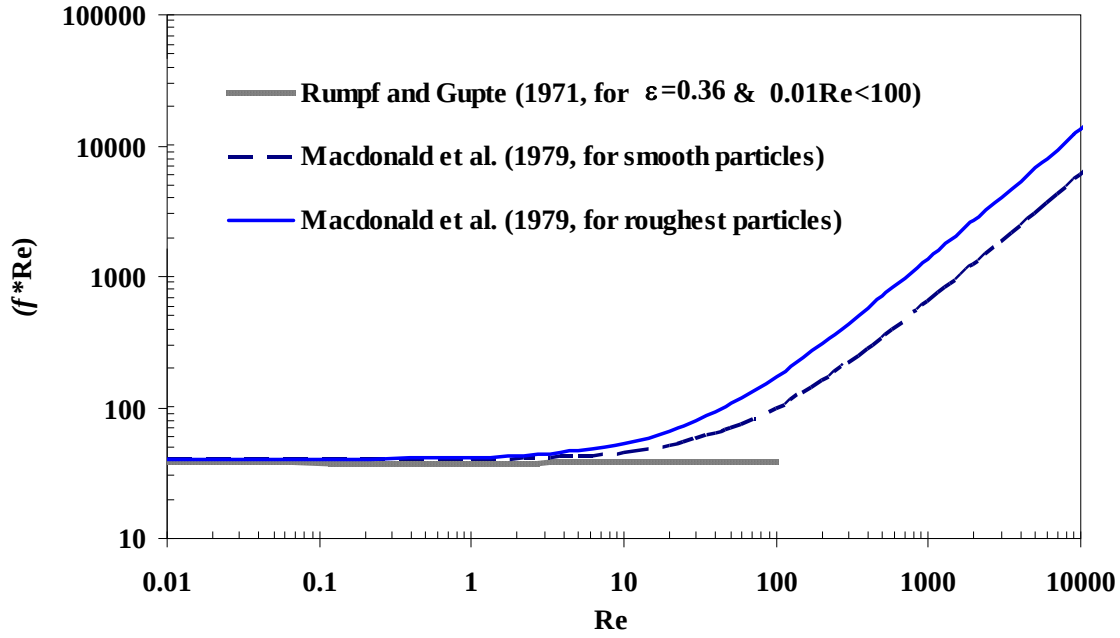

Figure 3.7 Friction factor Reynolds number (based on hydraulic diameter) product for flow through spherical particle beds (ε_e = 0.36).

From Figure 3.7, it can be seen that, (1) For a packed spherical particle bed with a fixed measured porosity for Darcian flow and fully developed laminar flow where $\mathrm{Re}_{d_h} < 5$, the friction factor Reynolds number product, based on hydraulic diameter, is nearly a constant. It was because that in laminar flow, pressure gradient was not dependent on the fluid energy; it increases linearly with the fluid momentum divided by its viscosity, i.e., Reynolds number. (2) For a packed spherical particle bed for higher Reynolds numbers, the friction factor Reynolds number product is independent of bed porosity, and increases linearly with an increase in Reynolds number. This is because, for complex fully developed laminar or transition flows, the pressure gradient is dependent on the energy of the fluid motion, i.e., fluid velocity squared or Reynolds number squared as shown in Figure 3.7 for Re > 100.

3.3.4.2 Correlation of Nusselt number and Sherwood number in packed spherical particle beds

Kumar et al. (1977) investigated mass transfer coefficient from dumped, packed beds of cylindrical pellets of benzoic acid to water and 60% aqueous propylene glycol solution for Reynolds number range 0.01-600, Schmidt number range 767-42400 and bed void fraction range 0.336-0.456. Convectional correlations of Sherwood number were developed with

respect to Reynolds number, Schmidt number and Grashof number, which considers both natural convection and forced convection. The dimensionless mass convection coefficients were developed for Reynolds numbers higher than 0.01. For $\mathrm{Re} < 10$, $123 < \mathrm{Sc} < 42000$,

$$\mathrm{Sh} = \left[2.985 \times 10^{-6} (\mathrm{GrSc})^{1.5} + 1.340 (\mathrm{ScRe})^{2}\right]^{1/6} / \varepsilon \tag{3-72}$$

For $0.001 < \mathrm{Re} < 1, 42000 < \mathrm{Sc} < 706000$ and also for $1 < \mathrm{Re} < 2500$, $123 < \mathrm{Sc} < 706000$,

$$\mathrm{Sh} = \left[0.0209\,\mathrm{Re}^{3.36} + 1.340\,\mathrm{Re}^{2}\right]^{1/6} \mathrm{Sc}^{1/3} / \varepsilon \tag{3-73}$$

The correlation showed that natural convection is dominant for Reynolds number ranging from 0.01 to 0.1 and the Sherwood number is almost a constant. However, for Reynolds number higher than 0.1, the Sherwood number increases with an increase in Reynolds number. It is expected that the same or similar phenomenon occurred within a spherical particle bed while gas flows. For a packed bed with porosity of 0.36, the relationship between $\varepsilon \cdot \mathrm{Sh} \cdot \mathrm{Sc}^{-1/3}$ and Re is plotted in Figure 3.8.

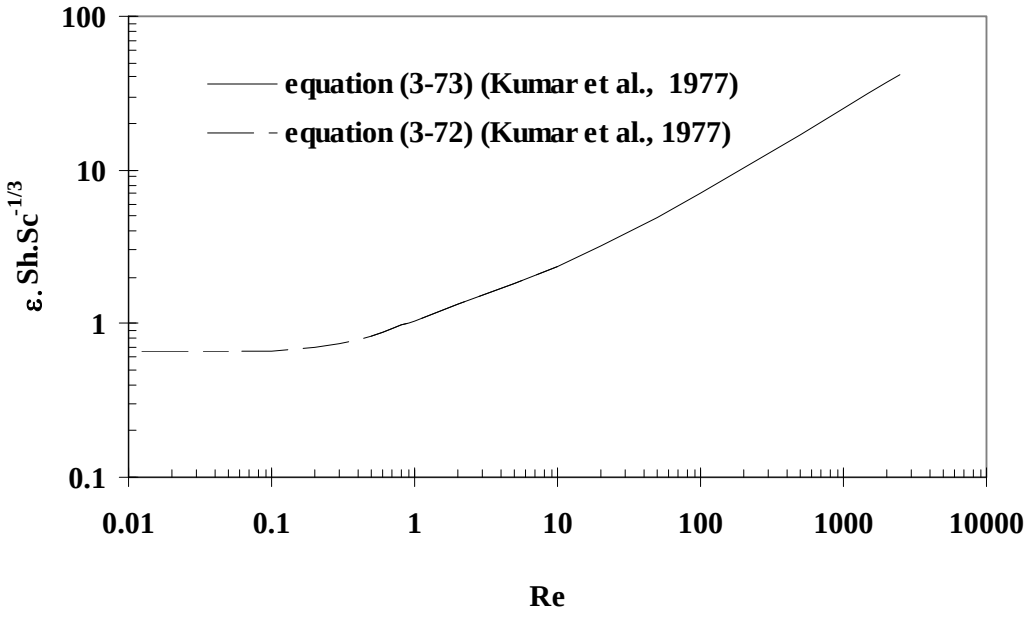

Figure 3.8 Correlation of mass transfer in packed cylinder particle beds (ε = 0.36) with $\varepsilon \cdot \mathrm{Sh} \cdot \mathrm{Sc}^{-1/3}$ vs. Re plot.

Kumar et al. (1977) compared the correlations with experimental data at Reynolds number range from 0.01 to 2500. Good agreement between these correlations and the experimental data implied the validity of the mass convection correlation. From Figure 3.8, it can be seen that, in the range of Reynolds number higher than 1, the dimensionless mass convection coefficients increases with an increase in Reynolds number, but keeps almost a constant at low Reynolds number less than 1.

Wakao and Funazkri (1978) reviewed some research on the mass or heat transfer coefficient determination based on a series of reported experimental data by other researchers, including the work of Kumar et al. (1977). It was found that most transient experimental processes, such as evaporation, sublimation and dissolution etc., were considered as steady processes and that axial dispersion was not considered. Wakao et al. (1978 and 1979) proposed that the axial fluid effective dispersion coefficient was a function of Schmidt number, Reynolds number and molecular diffusivity, and pointed out that without the consideration of axial dispersion, the mass diffusion coefficient or Sherwood number would be underestimated. Their new correlations for these Nusselt number and Sherwood number are corrected to be

$$\mathrm{Nu}_d = 2 + 1.1\,\mathrm{Pr}^{1/3}\,\mathrm{Re}_d{}^{0.6} \tag{3-74}$$

for $\mathrm{Re}_{d_h} > 15$ and

$$\mathrm{Sh}_d = 2 + 1.1\mathrm{Sc}^{1/3}\,\mathrm{Re}_d{}^{0.6} \tag{3-75}$$

for $\mathrm{Re}_{d_h} > 3$, where $\mathrm{Nu}_d = \dfrac{h_t d}{k_a}$, $\mathrm{Re}_d = \dfrac{\varepsilon_e u_p d}{\upsilon_a}$, $d = \dfrac{6V_s}{A_{fs}} = d_p = \dfrac{1.5(1-\varepsilon_e)}{\varepsilon_e} d_h$. For convenience, these correlations are transformed based on hydraulic diameter for a packed spherical particle bed with porosity at ε_e=0.36 as follows.

$$\mathrm{Nu}_{d_h} = \frac{2 + 1.1\,\mathrm{Pr}^{1/3}\left[\mathrm{Re}_{d_h} 1.5(1-\varepsilon_e)/\varepsilon_e\right]^{0.6}}{1.5(1-\varepsilon_e)/\varepsilon_e} = 0.75 + 0.743\,\mathrm{Pr}^{1/3}\,\mathrm{Re}_{d_h}^{0.6} \tag{3-76}$$

$$\mathrm{Sh}_{d_h} = \frac{2 + 1.1\mathrm{Sc}^{1/3}\left[\mathrm{Re}_{d_h} 1.5(1-\varepsilon_e)/\varepsilon_e\right]^{0.6}}{1.5(1-\varepsilon_e)/\varepsilon_e} = 0.75 + 0.743 Sc^{1/3}\,\mathrm{Re}_{d_h}^{0.6} \tag{3-77}$$

However, Wakao et al. (1978 and 1979) did not consider convection at very low Reynolds numbers. The experimental data at very low Reynolds numbers (<3) was not easy to obtain due to the limitations of their tests. But based on the observation of Kumar et al. (1977), and analogy of heat/mass transfer to momentum transportation, it is expected that the Sherwood numbers or Nusselt numbers at low Reynolds numbers (<3) are almost a constant.

Figure 3.9 plots a comparison of correlations between Sherwood or Nusselt number and Reynolds number at constant Prandtl number or Schmidt number derived by Wakao et al. (1978 &1979), Nie et al. (2009b), Kar & Dybbs (1982) and equation (3-62) using different methods and different materials. The trends of Sherwood number or Nusselt number with Reynolds number are similar to the trend of friction factor Reynolds number product with Reynolds number. This implies that the analogy exists between heat / mass convection and momentum for these bed flows. Kar and Dybbs (1982) presented a correlation between Nusselt number and Reynolds number for Darcian type laminar regime using sintered powder metal (stainless steel, nickel and copper) specimens with a porosity range from 0.26 to 0.653. Wakao et al. (1978 & 1979) proposed the correlation without uncertainty information. Nie et al. (2009b), also presented in Appendix D, used the same bed but different material such as steel, lead and glass spherical beads to derive the convection coefficients, but carefully justified the period of linear temperature distribution within the beds. Good agreements between the new correlation from these three different spherical beads with experimental data and other correlations using similar materials indicated its validity (see Appendix D). Careful observation showed that (1) at Reynolds numbers less than 50, the uncertainty bounds of Nie et al. (2009b) tended to expand and overlap with the uncertainty bounds of equation (3-62), which implied that relative uncertainty of convection coefficient was large due to difficulty in obtaining experimental data with good repeatability at low Reynolds number; (2) The reasons of large deviation of equation (3-62) from other correlations at high Reynolds number were investigated in section 3.3.3. Kar and Dybbs (1992) mentioned the difference between different research results using different materials but they did not explore further its cause.

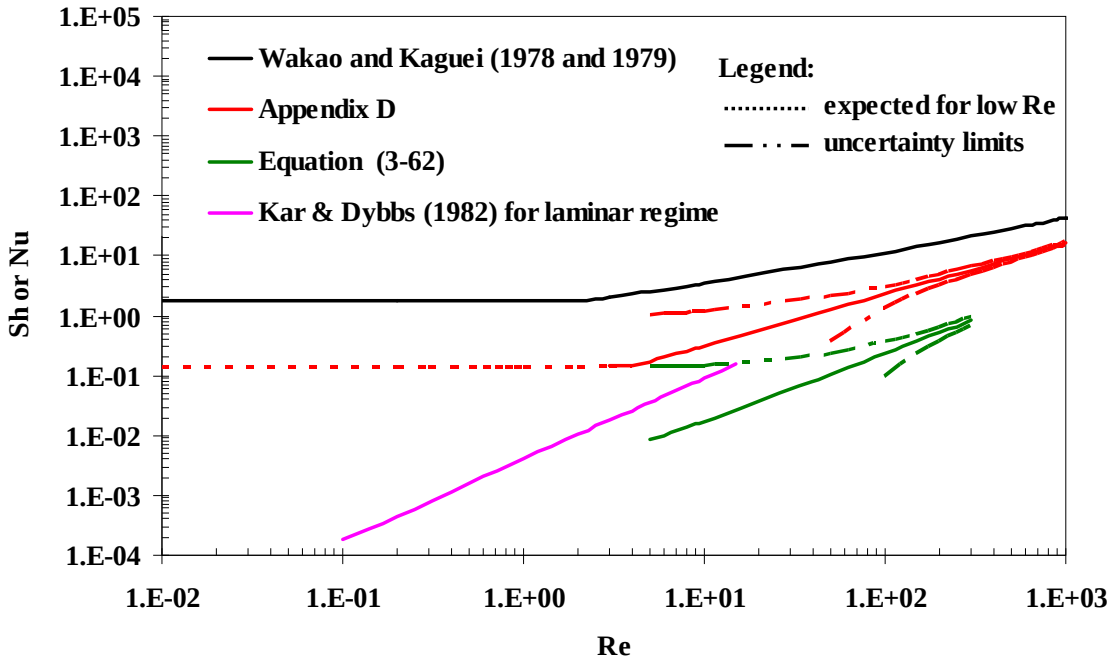

Figure 3.9 Correlation of Sherwood or Nusselt number versus Reynolds number for flow through spherical particle beds (ε_e = 0.36 and Pr = 0.707).

3.3.4.3 Correlation of dispersion in packed spherical particle beds

Saffman (1959 and 1960) modeled the microstructure as a network of capillary tubes with random orientation within a porous media and presented a statistical method to and derive the dispersion in packed spherical particle beds. It was assumed that each marked element follows a random walk in this assemblage of randomly straight pores and the movement direction and duration in each step was in a specified random manner. Therefore the probability density function calculation for movement of each single marked element gave the dispersion value. The derived dispersion coefficient within the packed spherical particle bed was for both the longitudinal and transverse directions respectively. For $\mathrm{Pe} << 1$, the ratio of longitudinal and transverse dispersion to diffusion are derived as

$$\frac{D_L}{D} = \frac{2}{3} + \frac{\mathrm{Pe}^2}{15} \tag{3-78}$$

$$\frac{D_T}{D} = \frac{2}{3} + \frac{\mathrm{Pe}^2}{40} \tag{3-79}$$

For $\mathrm{Pe} >> 1$, longitudinal and transverse dispersion are derived as

$$\frac{D_L}{D} = \frac{10}{9} + \mathrm{Pe} \cdot \ln\left(\frac{3}{2}\mathrm{Pe}\right) - \frac{17}{132}\mathrm{Pe} - \frac{1}{48}\left(\frac{R}{l}\right)^2 \mathrm{Pe}^2 \tag{3-80}$$

$$\frac{D_T}{D} = \frac{1}{3} + \frac{3}{16}\mathrm{Pe} + \frac{1}{40}\left(\frac{R}{l}\right)^2 \mathrm{Pe}^2 \tag{3-81}$$

where l is assumed by the author to be spherical particle diameter d_p, R is radius of curvature, Peclet number is $\mathrm{Pe_m} = \frac{u_p d_p}{D}$.

Koch and Brady (1985) examined three different types of dispersion at high Peclet number in fixed beds such as spherical particle beds: (1) Purely mechanical dispersion, (2) Hold-up dispersion (3) Boundary layer dispersion. The theoretically predicted values of effective diffusivity in the transverse and longitudinal directions were compared with the previously reported experimental data and showed good agreement. Theoretical solutions for the longitudinal and the transverse dispersion are listed as following equations at full range of Peclet number for impermeable particle in which the hold-up dispersion is absent.

For $\mathrm{Pe} > 1$,

$$\frac{D_L}{D} = 1 + \frac{3}{4}\mathrm{Pe} + \frac{\pi^2}{6}\varepsilon \cdot \mathrm{Pe} \cdot \ln(\mathrm{Pe}) \tag{3-82}$$

$$\frac{D_T}{D} = 1 + \frac{63\sqrt{2}}{320}\varepsilon^{1/2}\mathrm{Pe} \tag{3-83}$$

Koch and Brady (1985) also proposed the effective diffusivity for the case of $\mathrm{Pe} < 1$ and showed that the effective diffusivity in both directions is influenced by the Brinkman screening length and the slope of longitudinal effective diffusivity versus Peclet number changed evidently at $\mathrm{Pe} = 1$.

As mentioned in section 3.3.1, dispersion, for the heat/mass transfer in porous media, meant the heat/mass spreading which is considered separately from the convection and effective molecular conduction/diffusivity. The hydrodynamic dispersion in two directions D_T or D_L,

combined the effective mutual molecular diffusion and mechanical dispersion. Molecular diffusion was only due to concentration gradients and the random motion of molecules and was independent of advective fluid velocity. But mechanical dispersion due to the advective diffusion was linearly dependent on the fluid velocity, or Peclet number. Figure 3.10 indicates the trend of longitudinal and transverse hydrodynamic dispersion with the increase of Peclet number investigated by Saffman (1959 & 1960) and Koch & Brady (1985) for spherical particle bed with porosity of 0.36. It is noted that at high Peclet number, effective diffusivity in longitudinal and transverse direction is functions of Peclet number. It was complicated at $\mathrm{Pe} < 1$, but according to the analogy among heat/mass convection and dispersion, the effective diffusivity can be simply taken as a constant (or near a constant).

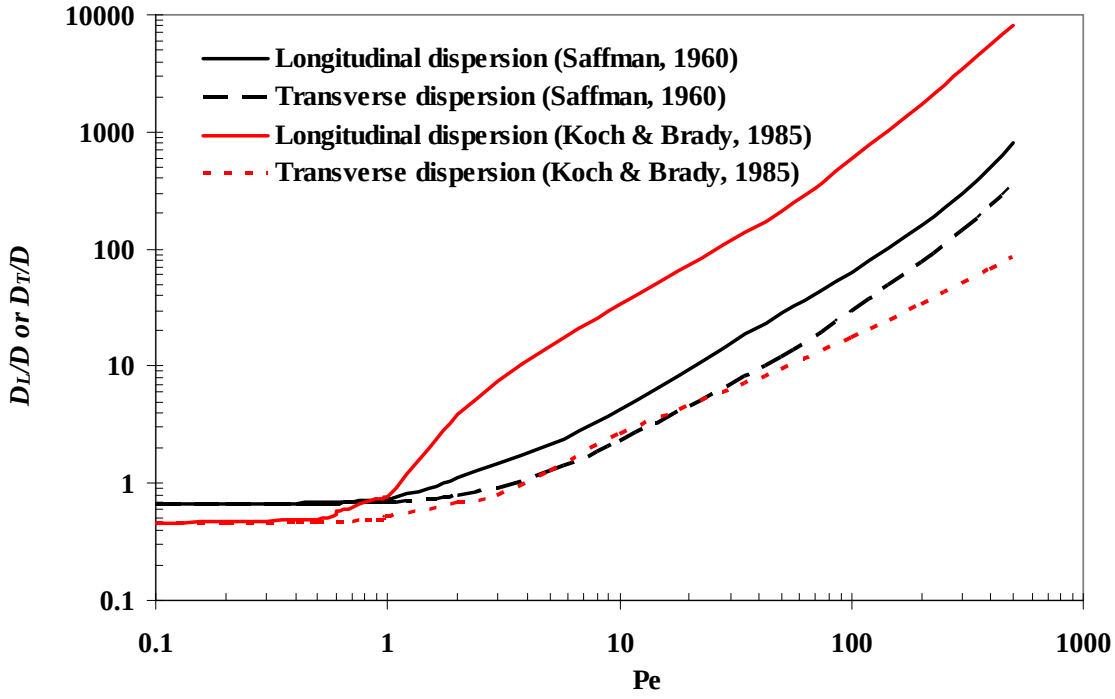

Figure 3.10 The ratio of longitudinal or transverse dispersion to mutual diffusion versus Reynolds number within spherical particle beds with void fraction ε=0.36.

According to Saffman (1959 & 1960), at low Peclet number (Pe<<1), the ratio of dispersion to the mutual diffusion is a constant around 2/3 (the ratio of the bed effective mutual molecular diffusion to mutual molecular diffusion). That is to say, at very low fluid velocity, the mechanically convective dispersion disappears while the mutual molecular diffusion due to only concentration gradient dominates. However, at high Peclet number (Pe>>1), both longitudinal and transverse hydrodynamic dispersion increases with an increase in Peclet number because mechanical dispersion is defined as the product of average fluid velocity and dynamic dispersivity such that mechanical dispersion dominates. For the transition region, both mechanical dispersion and molecular diffusion take effect. Koch & Brady (1985) proposed an asymptotic analysis to demonstrate the diversity of physical processes which could cause diffusion in porous media. At high Peclet number, bulk motion is important while molecular diffusion plays no role. For the region where velocity is zero (hold up region), molecular diffusion is the only mechanism that takes effect no matter how strong the bulk motion. The region where velocity is very close to zero, that is to say, near the surface region where the no-slip boundary condition is applied, is influenced by both convection and molecular diffusion.

The comparison of Figure 3.7, 3.8, 3.9 and 3.10 show a surprising similarity between pressure drop (momentum), heat / mass convection and dispersion processes. Table 3.6 lists the summary of momentum, heat and mass convection, dispersion processes and their causes. It can be seen that convection or advection and dispersion process or phenomena are related to fluid movement. The similarity among momentum, heat and mass transfer can be extended to dispersion, for example, the correlation of heat convection can be applied to mass convection. Whether friction factor Reynolds number product, heat / mass convection or hydrodynamic dispersion, are divided into three zones where Reynolds number or Peclet number being one is the boundary line. Less than one means independent of flow velocity (Reynolds number or Peclet number). Much greater than one means linear increase with an increase in Reynolds number or Peclet number. While for the transition zone where Reynolds number or Peclet number ranged from 1 to 10, these properties are related through a smooth transition zone.

Table 3.6 Summary of analogy among momentum heat and mass convection dispersion processes and causes

Processes	Types	Correlation forms	Causes
Momentum transport	Stress	$f \cdot \mathrm{Re} = g_1(\mathrm{Re})$	Viscous force and pressure gradient
Heat/mass transport	Forced convection	$\mathrm{Nu} = g_2(\mathrm{Re}, \mathrm{Pr})$ $\mathrm{Sh} = g_3(\mathrm{Re}, \mathrm{Sc})$	Due to fluid flow in which heat/mass are convected.
	Natural convection	$\mathrm{Nu} = g_4(\mathrm{Gr}, \mathrm{Pr})$	Due to buoyancy from fluid density differences.
	Conduction /Diffusion	---	Due to temperature / concentration gradients, independent on fluid flow.
	Mechanical dispersion	$D = g_5(\mathrm{Re}, \mathrm{Pr})$	Velocity variation within pores, or pore path length difference due to size, tortuosity, and path network.

3.4 Summary and conclusions

In this chapter, a new theoretical model was develop to predict the transient response of urea particle beds while beds were subjected to an ideal temperature or a humidity step change at the inlet. For a temperature step change, the temperature response of outlet air after a urea particle bed presents an exponential growth form with one characteristic time constant. However, for a humidity step change, the humidity response of outlet air after a urea particle bed presents in an exponential form with one time constant but the temperature response of outlet air can be characterized by two time constants.

A new correlation of Nusselt number versus Reynolds number for porous particle beds, that was inversely determined from the comparison between theoretical prediction and experimental data, were compared with other correlations. This comparison showed great discrepancies. After exploring the reasons why the correlation was so different, the best correlation, presented in appendix D (or Nie, et al., 2009b) was selected. In addition, the analogy of momentum, heat / mass transfer and dispersion was applied to obtain the convection coefficients at low Reynolds number range.

CHAPTER 4

MEASUREMENT OF MOISTURE UPTAKE AND TRANSPORT IN A BED OF UREA PARTICLES

4.1 Introduction

Urea, $(NH_2)_2CO$, is an important nitrogen fertilizer but very susceptible to moisture adsorption and caking even at moisture contents as low as 0.25% w/w. As well, urea can be chemically unstable as it tends to decompose at temperatures above 70 ^oC. Peng et al. (2000) and Sun and Besant (2005) investigated moisture adsorption processes in beds of initially dry potash and silicon gel subject to the flow of humid air. Experiments with urea particles and particle beds are needed to quantify these internal properties and their influence on the response of a bed to humid or dry air flow through a bed. Using these properties, moisture redistribution within urea particle piles can be predicted under known changes in the ambient air.

This chapter presents the experimental method of moisture uptake and transport within a bed of urea particles with a height of 200 mm. Spatial and temporal distribution of urea particle moisture content were determined during the transient moisture sorption process without interruption of the experiment using a new test cell with test sampling ports. A new sampling device modified from a syringe and pistons was used for sampling to minimize sample exposure to moisture changes. In addition to the transient moisture sorption/desorption process, the isothermal moisture characteristics at room temperature of urea particles were presented.

4.2 Experimental Apparatus and Procedures

4.2.1 Test rig for moisture sorption and measurement arrangement

Urea particle bed experiments were designed to obtain experimental data on transient moisture adsorption/desorption and isothermal sorption characteristics at equilibrium. Figure 4.1 presented a schematic of the test facility used for the urea bed experiments. Compressed dry air, produced from an air compressor (manufactured by DeVilbiss Air Power Company in Jackson, TN) with a ITW PRO dryer (manufactured by DeVilbiss Air Power Company in Jackson, TN) downstream, passed through a compressed air tank and then through a mass flow controller (manufactured by MKS Instruments, Inc., Andover, Massachusetts in USA). The mass flow controller can preset a flow rate of dry air at known pressure and temperature with an uncertainty of ±1% of the full range (e.g. 50 Lpm, 100 Lpm, 200 Lpm). A flow adjustment valve was used to divert a selected fraction of dry air flow through the humidifier. The humid air was recombined with the dry air to provide the desired mixed air humidity. This mixed flow passed into the urea bed through the inlet pipe.

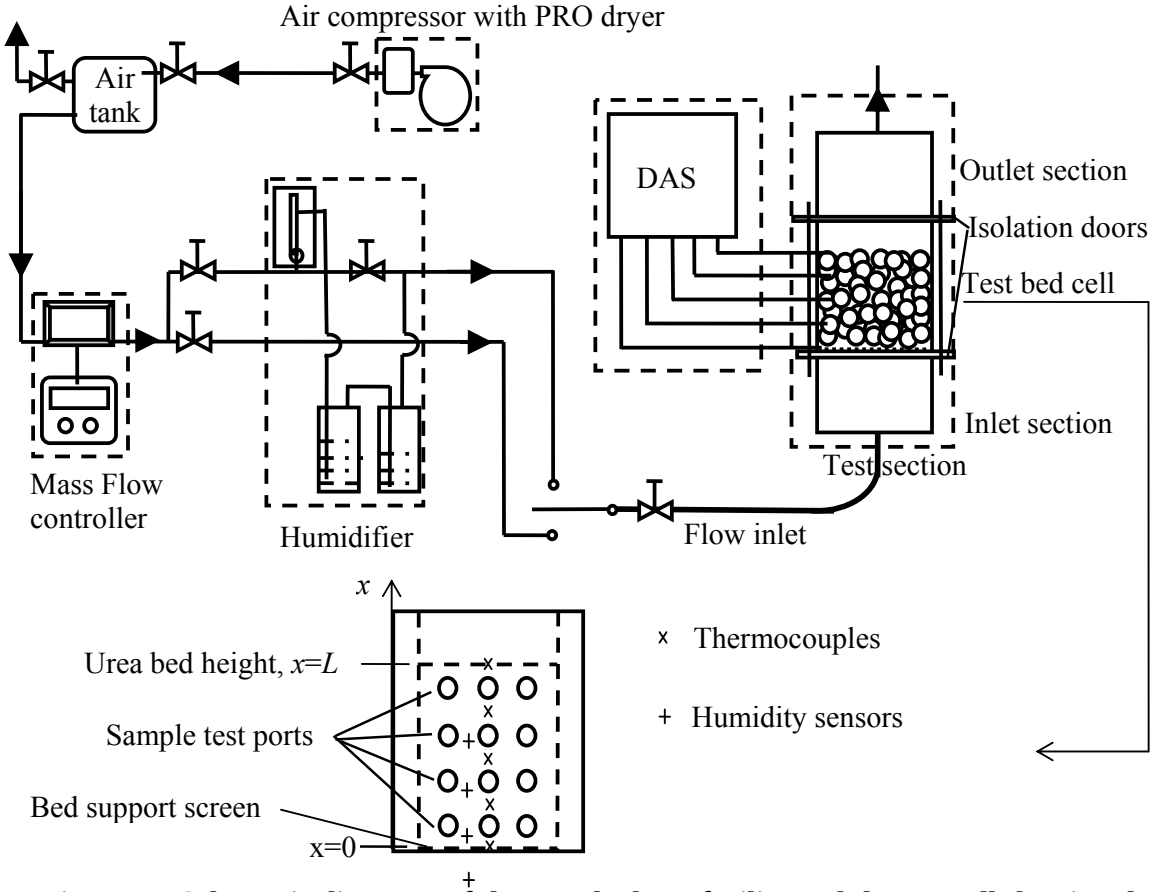

Figure 4.1 Schematic diagrams of the urea bed test facility and the test cell showing the measurement arrangement

The test section is made of polystyrene boards with a thickness of 20 mm, and has a 170 mm by 170 mm square cross-section air flow path. The inner walls of the duct are covered by an aluminum foil layer to ensure an impermeable and adiabatic boundary. The test section includes three parts: an inlet section, a test bed cell and an outlet section. The air flow pipe is connected to the bottom end of the inlet section (100 mm long), which provides an air flow expansion section before the air flow enters into the bottom of the urea bed. The packed urea particle bed is supported by a thin stainless steel screen at the bottom of the test section. This packed bed can have any selected depth up to 250 mm, but depths less than 160 mm are not used. Two sliding doors located at the inlet and outlet of the test section, are used to isolate the urea bed from air before the start of each experiment. Air flow then passes through the packed urea bed and exits the outlet section of the bed which is 100 mm long. During the experiments, the bed height was selected to be 200 mm.

For each experiment, the air flow rate was preset using a calibrated mass flow controller which has a measurement uncertainty of ±1% of full range. Compressed dry air was partially diverted to pass through a humidifier to obtain a selected humid supply air with a constant relative humidity before it enters the test cell. Calibrated humidity and temperature transmitters were placed before and after the test cell, to measure the temperature (uncertainty ±0.1 ^{o}C) and relative humidity (uncertainty ±1 %) of the supply air entering and leaving the urea test cell. To measure the transient adsorption/desorption response of the packed urea bed, T type thermocouples, were placed in the bed at five relative positions (x/L=0, 0.25, 0.5, 0.75 and 1), and humidity sensors were located at x/L=0.125, 0.375, 0.625 and 0.875. All temperature and relative humidity data were automatically recorded by a data acquisition system every second. Both the humidity sensor and thermocouple response was about 2~4 seconds, which can be neglected compared to the outlet air temperature or humidity response at low Reynolds number less than 25.

Three sample test ports for moisture content sampling were arranged uniformly on each layer of each side wall of the urea test bed. Four sample port layers, located at x/L=0.125, 0.375, 0.625 and 0.875, provided x-direction data of urea particle moisture content. A novel but simple particle sampling device was used to extract moistened samples of urea from the test cell. This sampling device was comprised of a syringe tube and two opposing pistons to seal in each urea sample. With each of these particle sampling devices, one urea particle sample can be taken out from one test port and isolated from the ambient air after removal using the

opposing piston to seal the syringe. Test cell design is presented in section 4.2.2 while the particle sampling device is described in detail in section 4.2.3.

4.2.2 Test cell design

Figure 4.2 shows the detailed design of the test cell. This test cell, made of polystyrene boards, is 298 mm high and has a straight square cross-section air flow path of 170 mm by 170 mm. The top and bottom parts with the same height of 39 mm have the thickness of 50 mm while the middle part has a thickness of 20 mm. The top and bottom sliding doors were located at the inlet and outlet of the test cell to isolate the flowing air from the urea particle bed before and after experiments. The stainless screen was located on the interface between the bottom and the middle part to support the packed urea particle bed with a height of 160~250 mm.

Based on the urea particle bed height, L, of 200 mm, four layers of sample test ports along the air flow direction were arranged at the position x/L=0.125, 0.375, 0.625 and 0.875, and each test port was a cylindrical channel through the wall thickness with a diameter of 11 mm. There were 4×4×3 test ports in the test cell, which means that four layers, each layer with three test ports, were arranged on each of the four side views. The three test ports of each layer on each side face were located in the middle, 36 mm left to the middle and 36 mm right to the middle. Before each experiment, the cylindrical test ports were sealed using the black rubber stoppers.

4.2.3 Particle sampling device for moisture content measurement

While measuring the moisture content, it is very important to prevent urea particles from exposure to the air because either moisture gain or loss from a sample will introduce error. Common syringes were modified and used to minimize the exposure of the urea particles to air when samples were taken. Figure 4.3 presents one syringe with two pistons, which was used to take the sample particles out from the test port.

Figure 4.4 presents the detailed procedure described as follows.

(1) Seal one side of the straight pipe with one piston shown in Figure 4.4 (a).
(2) Pull out the rubber stopper on the test port, and put the syringe tube with one piston into the test port as shown in Figure 4.4 (b).

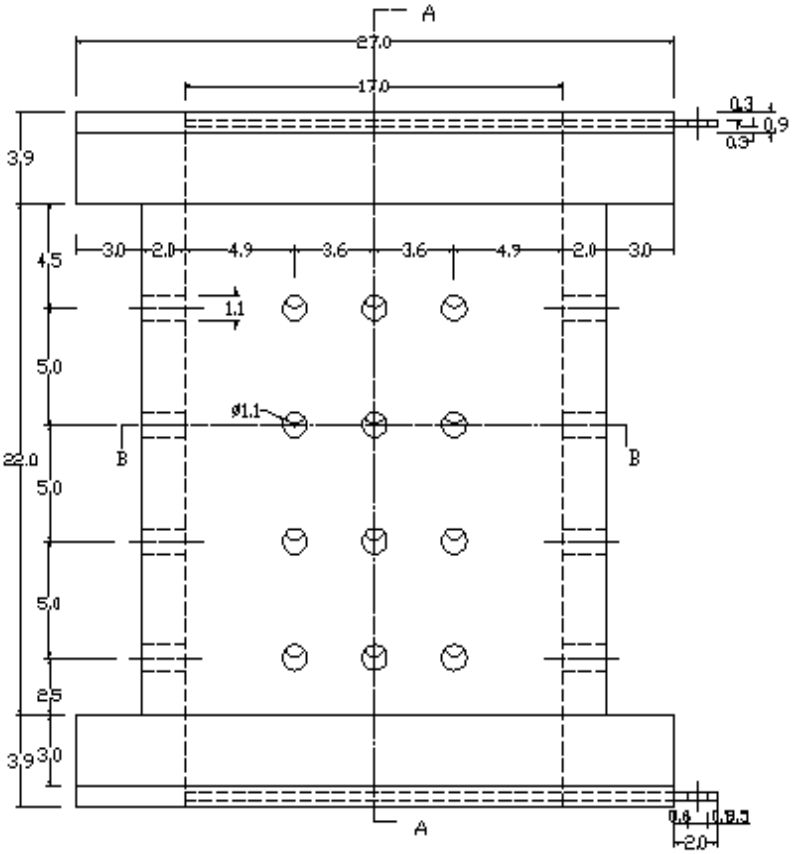

(a) Elevation view of the test cell (units: cm)

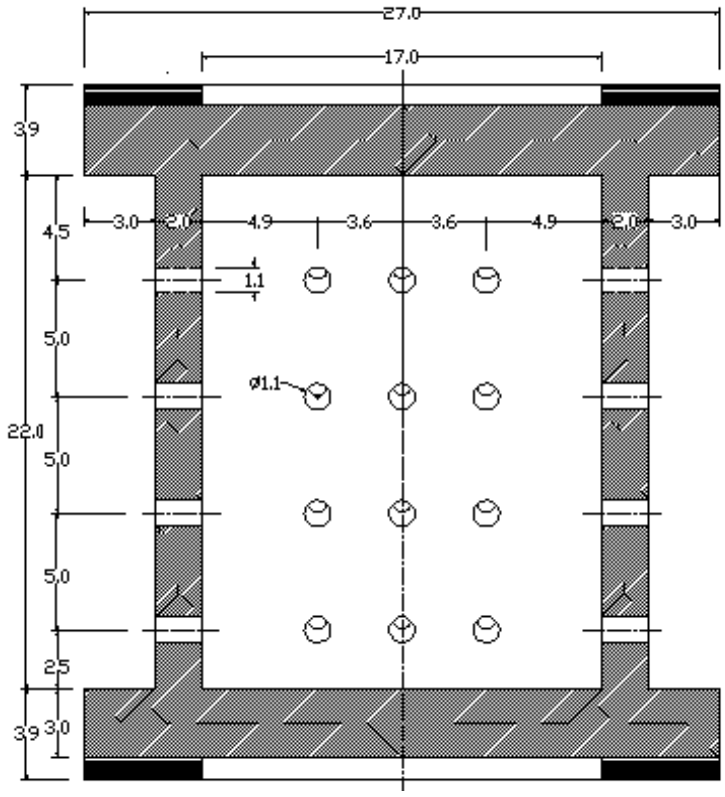

(b) A-A section view of the test cell (units: cm)

Figure 4.2 Design of test cell

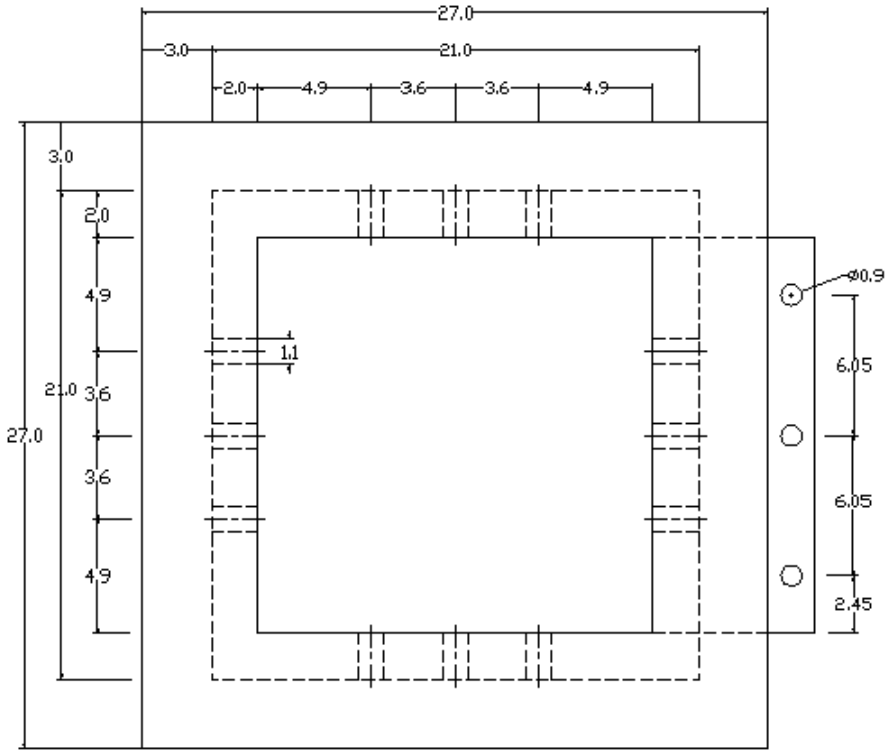

(c)

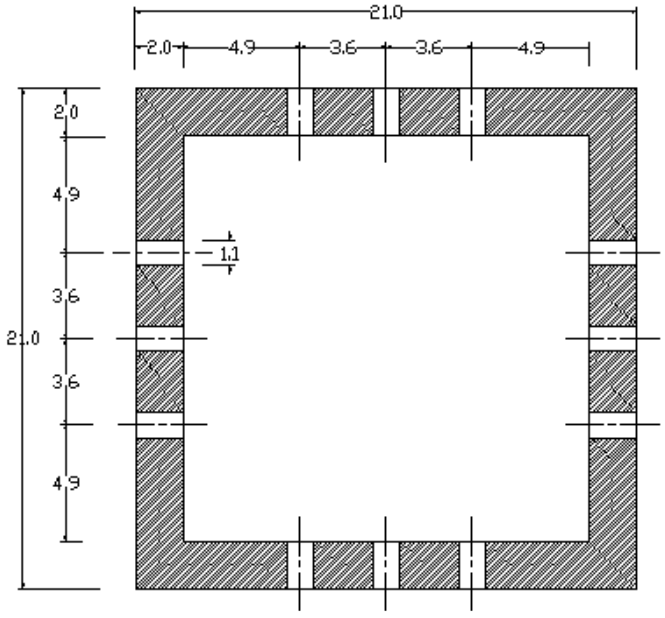

(d)

Figure 4.2 Design of test cell (continued) (c) Top view of the test cell (units: cm) (d) B-B section view of the test cell (units: cm)

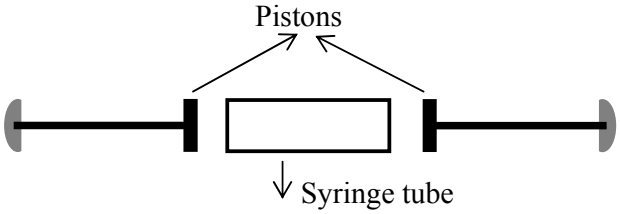

Figure 4.3 Modified syringes used to take the urea particles

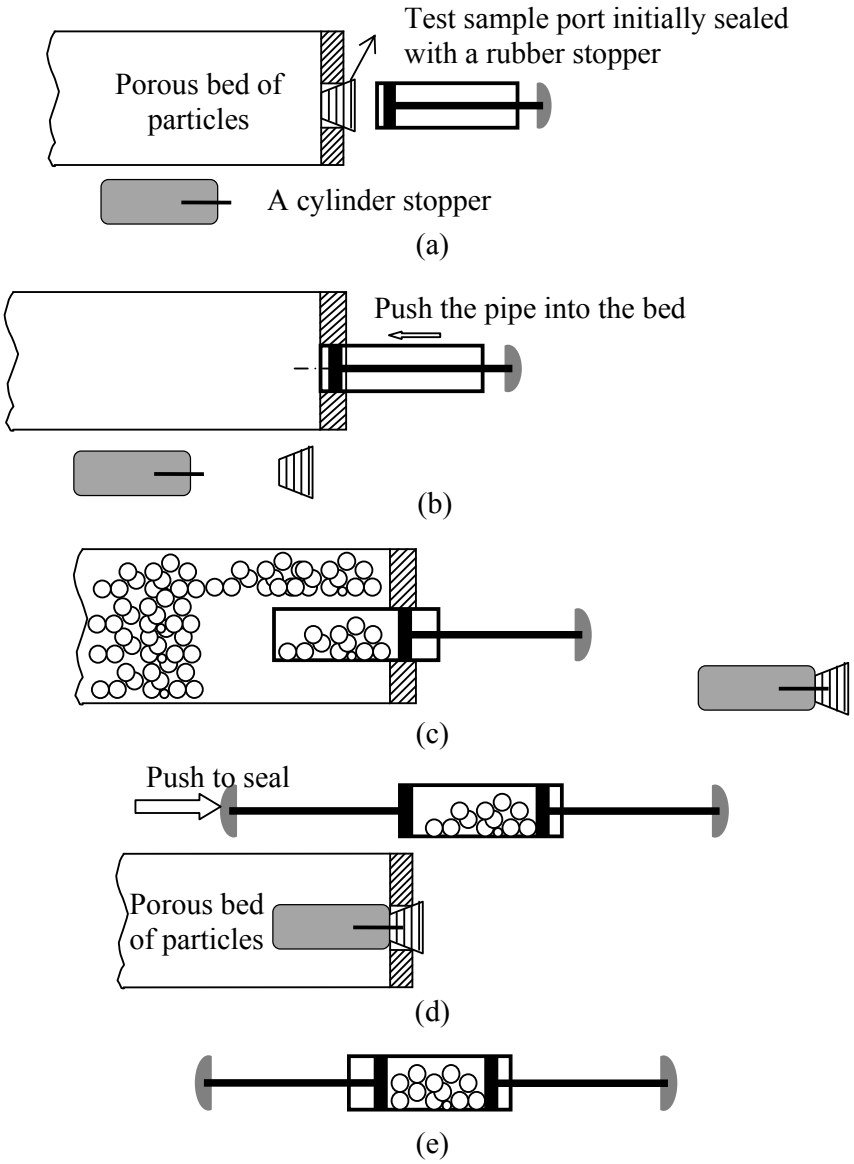

Figure 4.4 Process of handling the urea particles

(3) Keep the piston fixed and push the syringe tube into the bed till the tube can not go further as shown in Figure 4.4 (c). Meanwhile, connect the cylinder stopper to the rubber stopper.
(4) Take the syringe with particles out and seal the other side of the syringe tube, as well seal the test port with the lengthened stopper as shown in Figure 4.4 (d).
(5) Then the sealed sample of urea particles are ready for weighing and measuring the moisture content along with all the others as shown in Figure 4.4 (e).

Before removing the urea particle sample with sampling devices in step (3), the stoppers was lengthened by being connected with a cylinder. The lengthened stoppers were used to take the place of the urea particle samples to avoid the collapsing of the urea particle bed after the urea sample was removed. Therefore, the bed of particles was only disturbed near the sample port from which the sample was taken.

Gravimetric methods, used to measure moisture content for common solid particles such as potash or silicon gel, cannot be used to determine accurately the moisture content of urea samples because urea is chemically unstable above 70^{o}C. The Karl Fischer method was used instead to determine the moisture content of each urea particle sample by measuring the total volume of the chemical reagent consumed to react with the water present in each syringe sample. The method of a preset end point is applied to do each titration until the predetermined voltage is reached. The uncertainty of this moisture content measurement using ORION 950 Ross FASTQC titrator (manufactured by Thermo Fisher Scientific Inc., Waltham, MA) is ±0.08% w/w. Determination of moisture content of urea particles using Karl Fischer titrator and its measurement uncertainty is described in Appendix A.

4.2.4 Experimental Procedure

Urea fertilizer used in the experiment contained 46% nitrogen and usually has moisture content in the range of 0.1%~0.3% w/w when it is delivered from a processing plant in a sealed bag. There are several types of urea particles which have properties that depend on the manufacturing process. Each urea particle has a nearly spherical shape and the size distribution in a bed is quite uniform. For example, Terico urea particles (manufactured by Agrium Inc., Calgary, AB in Canada) have a diameter of 2.21±0.06 mm, while Potash Corporation of Saskatchewan (PCS) produces Georgia urea with a diameter of 1.82±0.06 mm. Each urea test bed sample was prepared by drying the urea samples in the oven at 70 ^{o}C for 48

h, then keeping the dried urea particle sample inside double sealed bags for 24 hours at room temperature (21-24^{o}C).

Before each test, the test cell was filled with a dried and cooled urea sample, which was packed into the test cell using a one-touch vortex shaker (manufactured by Madell Technology Corp. in California, USA) to obtain a uniform consolidated urea bed density at the selected height inside the test cell. The two sliding isolation doors on the top and the bottom of the test bed cell were closed before the start of each test to minimize the influence of ambient air prior to the test. Before starting each experiment, a syringe sample was taken out of the test bed with the particle sampling device and the initial moisture content was determined using the Karl Fischer titrator. After placing the test cell with packed urea particle bed into the test facility shown in Figure 4.1, the adsorption experiment was started by opening the top sliding isolation door and then the bottom one. At scheduled times during the 48-hour test duration (t=0 h, t=2 h, t=5 or 6 h, t=12 h, t=24 h, t=24 h), urea samples were taken from different sampling test ports and taken away to determine the moisture content.

After the 48-hour adsorption experiment, the adsorption process was stopped by closing the sliding doors on the bottom and on top of the test cell. Then the inlet air flow was switched from humid air supply to a dry one. The 48-hour desorption test was then started by following the same procedure as outlined above for the adsorption process. The initial starting condition for desorption of the urea particles was assumed to be the end condition of the adsorption experiment.

4.3 Experimental Data and Analysis

4.3.1 Internal Properties

To understand well the moisture sorption / desorption process and caking of urea particles in humid air environment, it is important to determine the internal properties inside urea particles, such as pore volume and internal specific surface area. The BET test with krypton gas analysis can accurately determine the specific surface area for urea particle samples when the specific surface area is less than 10 m^2/g. By means of calibrated BET equipment, two different types of dry and wet urea samples were measured with Kr gas (see Appendix C). The measured specific surface area from BET analysis gave the total specific surface area

including internal specific surface area and external specific area of the sample particles. The Carmen correlation (Carmen, 1938 and 1939) was used to determine the external specific surface area of packed bed of nearly spherical particles which have smooth surfaces.

However, the SEM images of urea particles, shown in Figure 1.3, clearly indicate that the external surfaces of urea particles are rough. Layers of tiny urea crystals on the external surface cause a surface roughness which increase the external surface area greatly compared to a smooth surface. In Appendix B and C, it is assumed that two to four layers of urea crystals on the external surface of urea particle magnify the external surface area by a factor of 11-23 compared to a smooth spherical particle of the same diameter. Then the allocation of internal and external specific surface area within urea particles can be determined.

Table 4.1 shows the internal and external specific surface area and porosity information of granular Terico and prill Georgia urea particle beds with BET technique (see details and uncertainty information in Appendix B and C). It indicates that, for both granular Terico and prill Georgia urea particles, the internal particle porosity (ε_i) is much smaller than the external bed porosity (ε_e) while the internal surface area ($A_{m,i}$) is comparable to, or larger than, the external surface area ($A_{m,e}$). For the surface area, granular Terico and prill Georgia urea particles behaves totally different. Compared with prill Georgia urea particles, Granular Terico urea particles have smaller external surface area under the same packing and roughness condition because Granular Terico urea particles have larger diameter, but Granular Terico urea particles have much larger total specific surface area because Granular Terico urea particles have more and larger pores inside particles which is verified by their SEM pictures shown in Figure 1.3. For Granular Terico urea particles, internal specific surface area dominates the total specific surface area, or the external specific surface area is much smaller than the internal one. However for prill Georgia urea particles, the roughness of the external surface has an important effect on determination of internal and external surface areas. That is to say, both internal and external surface areas are important information for the moisture adsorption and desorption.

The total surface area of granular Terico urea particles decrease a little from 0.1922 to 0.1770 m^2/g after wetting. But the difference is negligible considering the measurement uncertainty. The total surface area of prill Georgia urea particles does not have any change after wetting.

Table 4.1 Properties of granular Terico and prill Georgia urea particles with BET method

Urea type		Granular Terico	Prill Georgia
External bed porosity ε_e (m^2/ m^3)		0.36	0.36
Smooth external specific surface area $\left(A_{m,e}\right)_{smooth}$ (m^2/g)		0.0014	0.0024
Estimated rough external specific surface area $\left(A_{m,e}\right)_{rough}$ (m^2/g)		0.0156~0.0327	0.0259~0.0541
Measured total specific surface area of urea particles, A_m (m^2/g)	dry	0.1922	0.0719
	wet	0.1770	0.0720
Calculated internal specific surface area $A_{m,i}$ (m^2/g)		0.1766~0.1595	0.0460~0.0178
Internal to total surface area ratio $A_{m,i} / A_m$		0.92~0.83	0.64~0.25
Internal pore diameter, d_{pore} (Å or 10^{-10}m)		100~125	---
Internal porosity ε_i (m^2/ m^3)		0.0012	<0.0012

4.3.2 Isothermal sorption properties at room temperature (21-24^{o}C)

Urea particles adsorb or desorb moisture depending on the local relative humidity. The equilibrium moisture content of urea particles increases with the ambient air relative humidity at room temperature (21-24^{o}C). To measure this equilibrium moisture content of urea urea particles during two cyclic adsorption and desorption process, air with a series of preset constant relative humidity of 4%→26%→49%→60→67%→61%→51%→26%→4%→26% →49%→60→67%→61%→51%→26%→4% at Reynolds number around 10 was forced to flow through a bed of initially dried urea particles. And for each relative humidity set point, the moisture contents of the bed were measured using the Karl Fischer method one time every 12 hours after 24 hours. Each time four samples of urea particles were drawn from the sample ports of the test cell to reduce the measurement uncertainty of moisture content determined by Karl Fischer titrator. At each relative humidity, the moisture sorption/desoprtion process lasted 5-7 days until the equilibrium state when there was no change in moisture content for 24 hours within measurement uncertainty. Corresponding constant relative humidity for each case was the average relative humidity during the experiments. The data of equilibrium

moisture content of urea particles at different relative humidity during the cyclic adsorption and desorption process and their uncertainties are shown in Table 4.2 and Figure 4.5. Also, the correlation for equilibrium moisture content for cyclic adsorption and desorption process at room temperature (21-24^{o}C) are given in equations below and in Figure 4.5. The experimental data showed that both granular Terico and prill Georgia urea particle bed have the same isothermal moisture adsorption and desorption characteristics.

Equation (4-1) gives a correlation of equilibrium moisture content with relative humidity after an adsorption process in the first cycle at room temperature. This correlation is obtained by curve fitting the experimental data.

$$X\left(T = 23^o C, \phi\right) = 0.01 \times \exp\left[a + b \cdot \phi / \ln(\phi)\right] \qquad (\phi \le 0.67) \tag{4-1}$$

where parameters $a = -3.59 \pm 0.12$, $b = -1.43 \pm 0.08$, and the correlation uncertainty limits $t \times SEE = \pm 0.000092$ at the 95% confidence limits. The coefficient of determination, R^2, between the dependent variable moisture content X and equation (4-1) is 0.9995.

For desorption in the first cycle, the correlation is given by equation (4-2).

$$X\left(T = 23^o C, \phi\right) = \frac{0.01}{c + d \cdot \phi / \ln(\phi)} \times g(T) \qquad (\phi \le 0.67) \tag{4-2}$$

where parameters $c = 6.27 \pm 0.04$, $d = 1.77 \pm 0.03$, and the correlation uncertainty limits $t \times SEE = \pm 0.000019$ at the 95% confidence limits. The coefficient of determination, R^2, between the dependent variable moisture content X and equation (4-2) is 0.9999.

Table 4.2 and Figure 4.5 presented the isothermal moisture sorption and desorption characteristics of urea particles at room temperature, i.e. 21-24^{o}C. However, the isothermal moisture sorption and desorption depend on not only the relative humidity but also the temperature. Theoretically, the isothermal moisture sorption curve of urea particles moves down with an increase in temperature, and goes up with a decrease in temperature. The experimental data of isothermal sorption and desorption of urea particles were not completed on the temperature effect due to the following reasons: (1) The isothermal sorption and desorption process of urea particles will take about 85-120 days. (2) The difference of moisture sorption capacities due to a small temperature change (5-10^{o}C) is much lower than the uncertainty of moisture content determination. It is expected that an isothermal moisture

sorption-desorption curve can be obtained under a winter condition (-40—20^{o}C) in the future, offering good suggestion for the urea manufactories in Canada.

Table 4.2 Data and uncertainties of isothermal moisture contents at different relative humidities during cyclic adsorption and desorption processes at room temperature (21~24^{o}C)

No.	Relative humidity, ϕ	Moisture content, X (‰ w/w)	Uncertainty, U(X) (‰ w/w).	Notes
1	4.0%	0.3034	0.2090	
2	26.5%	0.3962	0.0729	
3	49.0%	0.7035	0.0997	
4	59.6%	1.4244	0.1611	The 1st
5	67.0%	3.0189	0.2582	cycle
6	61.0%	2.4480	0.1666	
7	51.1%	2.0300	0.2448	
8	25.5%	1.6790	0.1335	
9	4.2%	1.6070	0.2089	
10	26.0%	1.8129	0.1900	
11	51.0%	2.0950	0.1300	
12	60.0%	2.4430	0.1820	
13	67.3%	3.2520	0.2650	The 2nd
14	59.5%	2.5930	0.2620	cycle
15	48.9%	2.0700	0.1400	
16	25.0%	1.8190	0.1820	
17	4.0%	1.9090	0.2800	

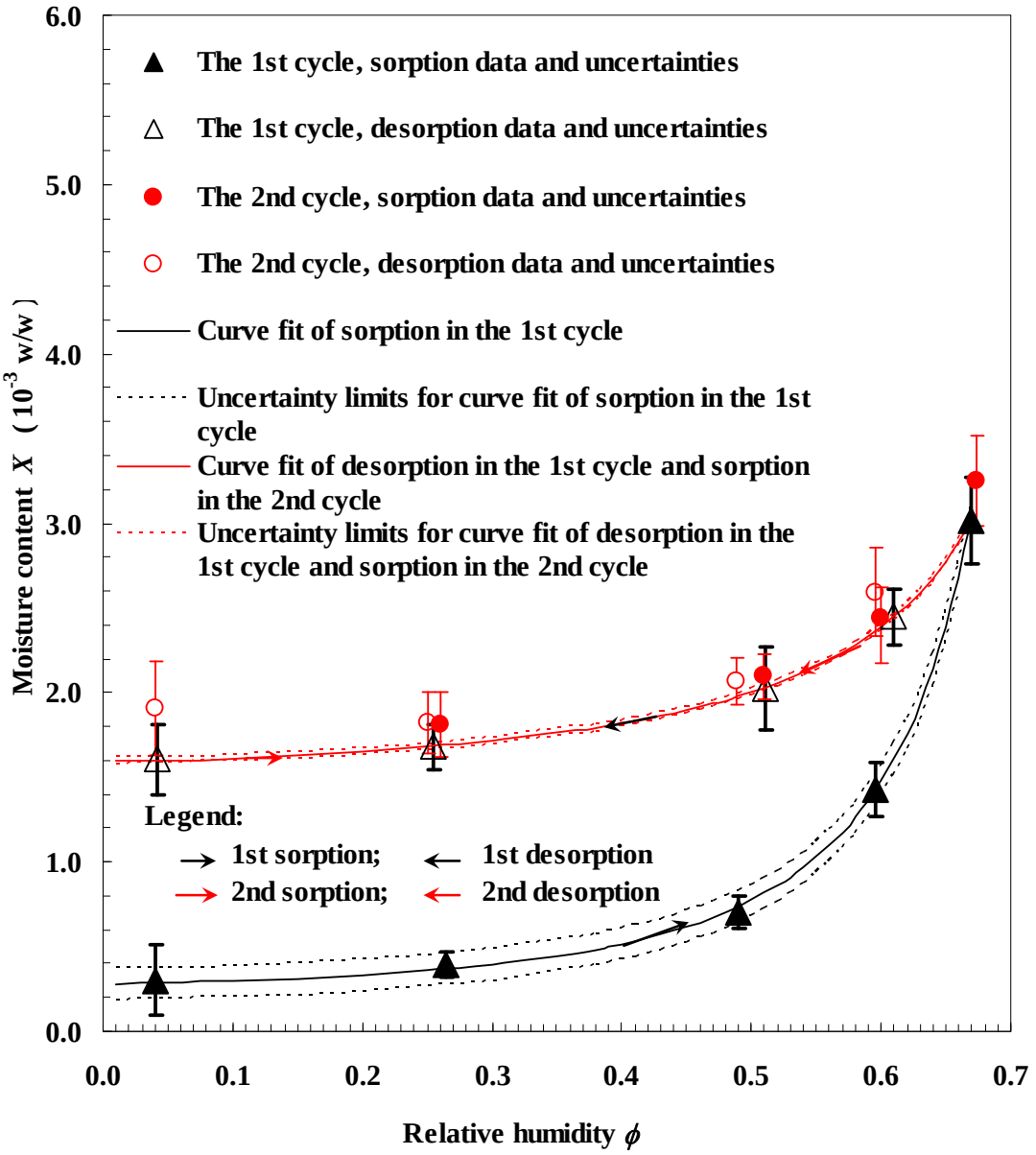

Figure 4.5 Isothermal moisture adsorption and desorption curve of urea particles at room temperature (21~24°C).

It can be seen in Table 4.2 and Figure 4.5 that in the first cyclic sorption process, the isothermal adsorption curve is lower than the isothermal desorption curve. The isothermal equilibrium moisture content during adsorption process started from the dry condition with equilibrium moisture content $X = 0.3\times10^{-3}$ w/w at relative humidity $\phi = 0.04$, continued to

absorb moisture from humid air at a series of relative humidity set points and reached equilibrium moisture content $X = 3.0 \times 10^{-3}$ w/w at relative humidity $\phi = 0.67$; however after moisture desorption at a series of decreasing relative humidity, the urea particle bed still had equilibrium moisture content of $X = 1.6 \times 10^{-3}$ w/w at the same dry condition $\phi = 0.04$. The final equilibrium moisture content after a series of desorption process is significantly higher than initial moisture content. This phenomenon, called hysteresis, was thought to be caused by urea particles' internal structural changes which occurred during the first adsorption process.

Kapsalis (1986) studied the influence of hysteresis and temperature on moisture sorption isotherms. It was indicated that (1) the hysteresis always occurs during the moisture sorption and deorption process; (2) the hysteresis decreases with increasing relative humidity of the atmosphere; (3) the hysteresis is related to the material polarity; (4) temperature change will change the isothermal moisture sorption and desorption curve. Gregg and Sing (1982) proposed that the hysteresis is the evidence of mesopores for physical sorption. It was proposed that the hysteresis is linked to differences in the nucleation and evaporation mechanisms inside pores. And cavitation and pore blocking arising during the desorption may cause the evaporation mechanism to change and then cause the hysteresis. The specific causes of hysteresis still require research.

However, in the second adsorption-desorption cycle, both the isothermal adsorption and desorption data were generally consistent with the first desorption curve. The measured experimental data of moisture content with uncertainty bars overlapped with the first desorption curve and its uncertainty limits. The hysteresis phenomenon occurred in the first adsorption-desorption cycle disappeared in the followed adsorption-desorption second cycle. This implies that the internal pore and particle surface geometry changes are very slow after the first cycle.

4.3.3 Transient sorption and desorption tests

The isothermal sorption curve in Figure 4.5 gives the maximum moisture adsorption capacity information of urea particle bed at equilibrium state for each relative humidity. However, for any change from one point to the other point along the isothermal sorption curve, it took a long time to reach the quasi-equilibrium state. Table 4.3 shows the inlet air test conditions investigated in the transient moisture adsorption / desorption tests. The air flow rate was measured by a mass flow controller with a precision error equal to 1% of the maximum mass

flow rate. Before and after the test bed of urea particles, thermocouples and humidity sensors were arranged for the inlet and outlet air temperature and humidity measurement. In addition, thermocouples were arranged at *x/L*=0, 0.25, 0.5, 0.75 and 1, and humidity sensors were located at *x/L*=0.125, 0.375, 0.625 and 0.875.

Table 4.3 Inlet air conditions for urea particle beds

Volumetric air flow rate $\dot{Q}_a$ (Lpm)	Darcy velocity u_D (m/s)	Reynolds number Re_{d_h}		Temperature	Humidity	
		Terico	Georgia			
200±2	0.1154	24.9	---	*21~24 °C $\pm 0.1^{o}C$	* a constant between 60 ~ 70% ±1% for sorption	* a constant between 4 ~ 10% ±1% for desorption
160±2	0.0923	19.9	---			
100±1	0.0577	12.5	---			
75±1	0.0433	9.3	5.7			
50±1	0.0288	6.2	3.8			
25±1	0.0144	3.1	1.9			
17.5±0.5	0.0101	1.5	1.3			
10.0±0.5	0.0058	1.2	0.8			

* Note: inlet air temperature and humidity may vary due to air environment change.

In this chapter, only one case of moisture sorption and desorption of Terico urea particle bed subject to air flow through at 17.5 Lpm (Reynolds number based on hydraulic diameter was $\mathrm{Re}_{d_h} = 1.5$, see Table 4.3) is presented, but one set of experimental data, including relative humidity, temperature and moisture content of the urea particle bed, are given. The inlet air relative humidity shown in Figure 4.6 and 4.9 and inlet air temperature in Figure 4.7 and 4.10 varies with time due to some variation in the upstream air properties but the air flow rate is held constant at 17.5 Lpm. It can be seen from these data that these inlet property variations cause variations in the bed and outlet properties but they have little or no effect on the bed moisture content.

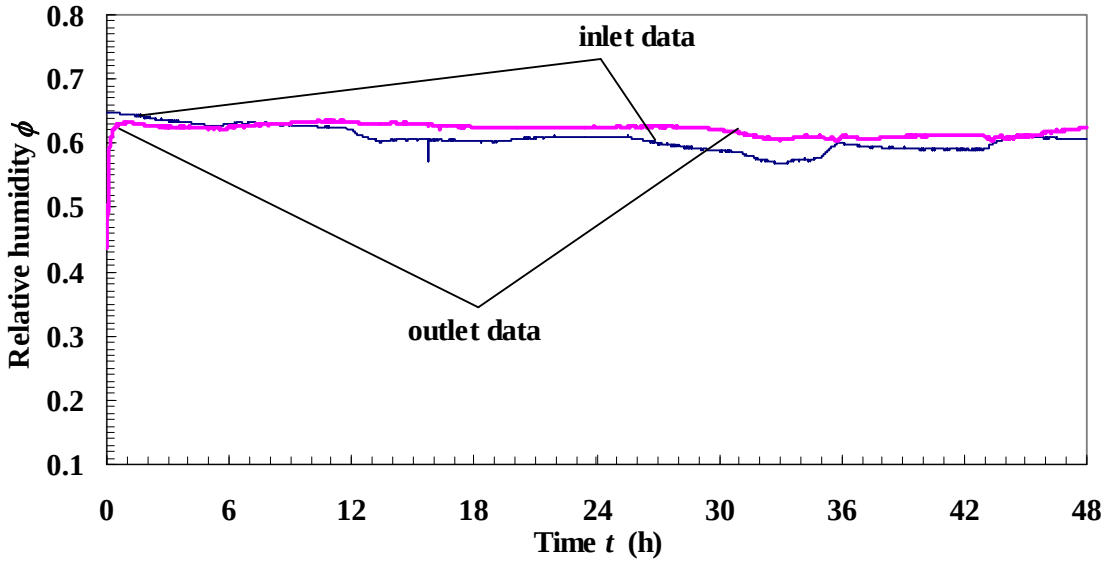

Figure 4.6 Relative humidity of inlet and outlet air in transient response experiment of a dry urea particle bed to humid air flow through the test bed, $\mathrm{Re}_{d_h} = 1.5$ **and inlet** $T = 23^{o}C$**.**

The air flow is selected so that only 6 s are required for the air to pass through the bed at $u_D = 10$ mm/s, but it takes a very much longer time for outlet relative humidity to approach the inlet relative humidity. The response of outlet relative humidity is delayed due to the slow sorption and later the desorption processes of the urea particle bed. In Figures 4.6 and 4.9, the outlet relative humidity does not equal the inlet relative humidity even after 48 h. Considering the measurement uncertainty of relative humidity $\pm 1\%$, the difference between inlet and outlet humidity is about 2~4%. This difference is mainly caused by the measurement uncertainty and that the quasi-equilibrium state is reached at 48 hours. In Figures 4.7 and 4.10, the data implies that temperature change caused by the water vapor phase change in sorption and dissolution is small.

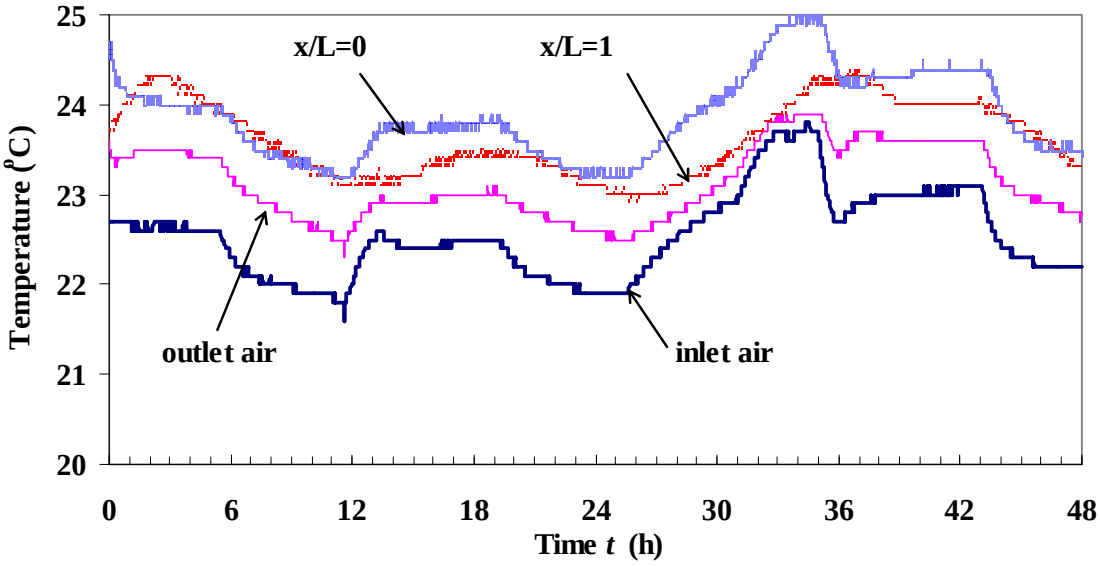

Figure 4.7 Temperature of inlet and outlet air, at two positions along the bed in transient response experiment of a dry urea particle bed to humid air flow through the test bed, $\mathrm{Re}_{d_h} = 1.5$ **and inlet** $T = 23^{o}C$**.**

Figure 4.8 shows the transient sorption/ moisture content at different positions in the dried urea bed subject to moist air flow while Figure 4.11 shows the transient desorption moisture content at different positions in the wetted urea bed subject to dry air flow. Both sorption and desorption process are slow and the equilibrium state can not be ensured even at 48 hours. Adsorption process starts from the dry condition with moisture content $X = 1.0\times10^{-3}$ w/w and reaches $X = 3.0\times10^{-3}$ w/w after 48 hours; however after desorption duration of 48 hours of testing, the moisture content is still $X = 1.8\times10^{-3}$ w/w which is significantly higher than initial moisture content. This phenomenon is thought to be caused by urea particles' internal structural changes which occur during the first adsorption process.

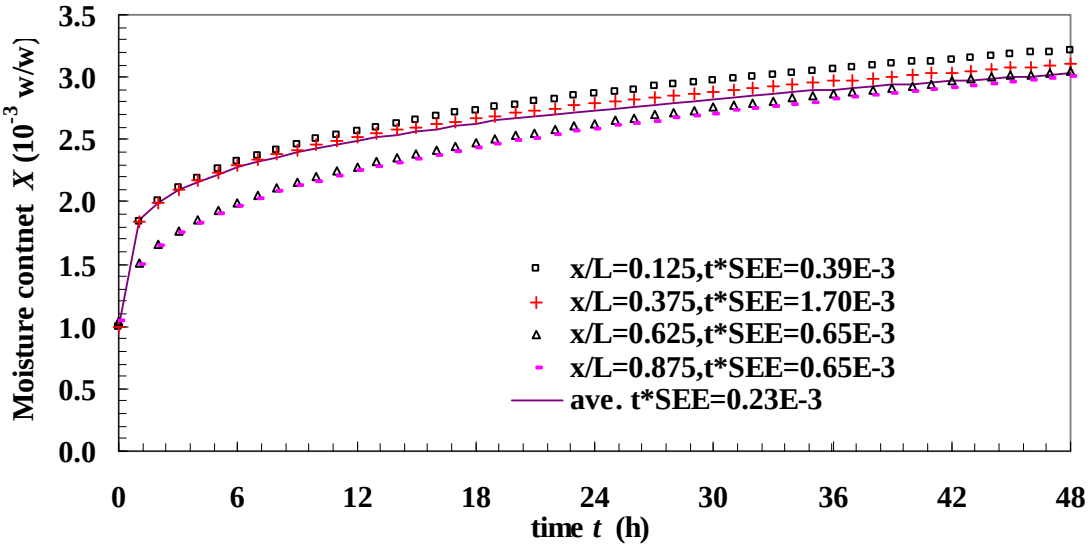

Figure 4.8 Curve fit of the experimental data of moisture content versus time at different positions within the urea particle bed in the transient response experiment of a dry urea particle bed to humid air flow through the test bed, $\mathrm{Re}_{d_h} = 1.5$ **and inlet** $T = 23^o C$**.**

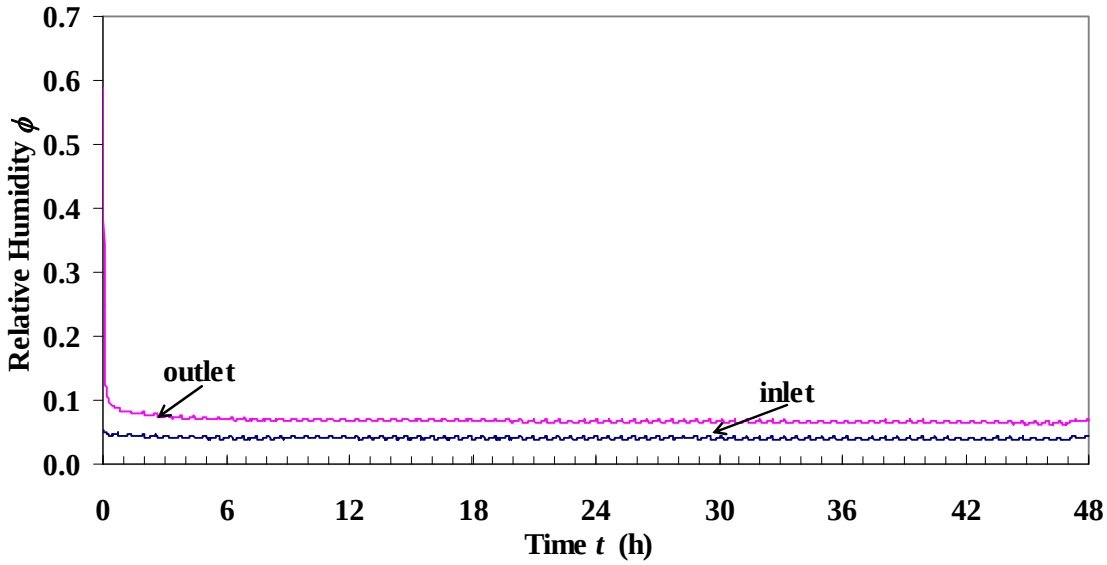

Figure 4.9 Relative humidity of inlet and outlet air in the transient response experiment of a wetted urea particle bed to dry air flow through the test bed, $\mathrm{Re}_{d_h} = 1.5$ **and inlet** $T = 23^o C$**.**

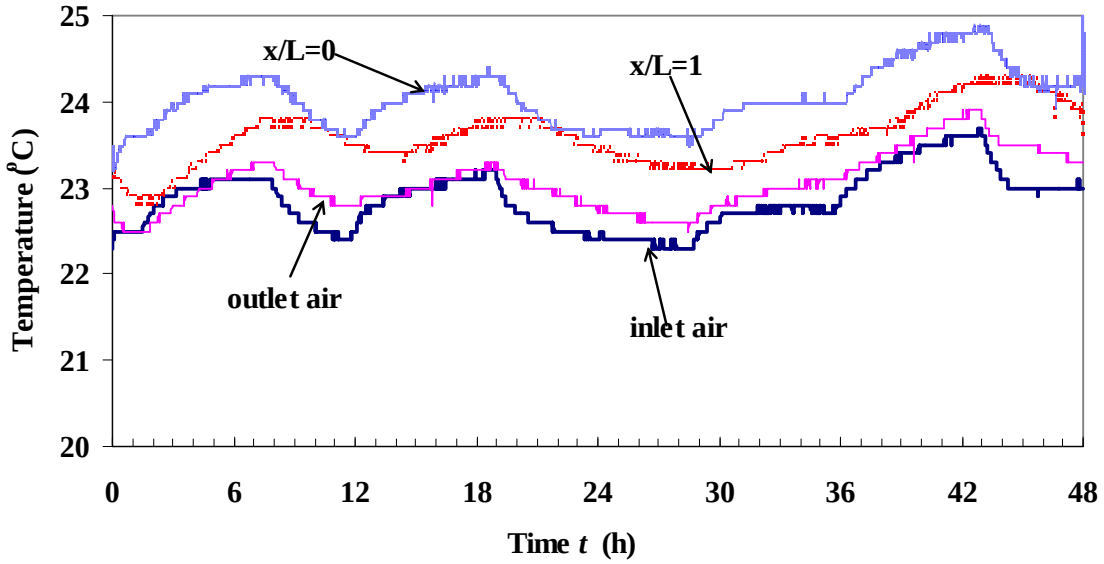

Figure 4.10 Temperature of inlet and outlet air, at two positions along the bed in the transient response experiment of a wetted urea particle bed subject to dry air flow through the test bed, $\mathrm{Re}_{d_h} = 1.5$ **and inlet** $T = 23^{o}C$**.**

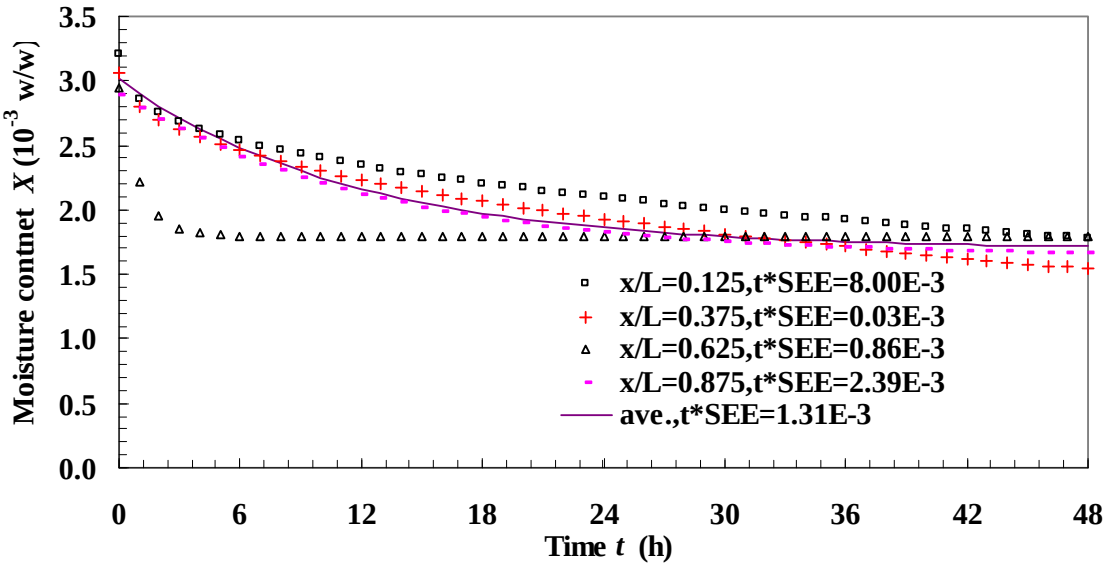

Figure 4.11 Curve fit of the experimental data of moisture content versus time at different positions within the urea particle bed in the transient response experiment of urea particle bed to dry air flow through the test bed, $\mathrm{Re}_{d_h} = 1.5$ **and inlet** $T = 23^{o}C$**.**

4.4 Summary

This chapter presented experimental measurement of moisture uptake and transfer within urea particle beds. A test cell with test ports and a supplementary sampling device were designed for both particle sampling with the least sample exposure to surrounding air and for moisture content determination without interruption of the transient experiment. The transient moisture sorption and desorpton processes within urea particle beds were measured to show that the moisture uptake by urea particles is a slow process because the slow internal diffusion of moisture within each urea particle dominates and moisture was mostly sorbed on or desorbed from the internal surface area inside each individual particle. The experiments of isothermal moisture sorption / desorption data at room temperature further verified that the moisture sorption /desorption processes are slow and hysteresis phenomena occurs during the first cycle of sorption / desorption process.

CHAPTER 5

NUMERICAL SIMULATION OF MOISTURE UPTAKE AND TRANSPORT IN A UREA PARTICLE BED

5.1 Problem statement

Urea fertilizer is comprised of particles which typically are spherical in shape having a particle diameter of 1.0 mm to 3.0 mm. When bulk granular fertilizers such as urea are stored and transported they are often exposed to humid air. Urea particles readily adsorb moisture on their external and internal surfaces when the ambient air relative humidity is higher than 60 percent, and subsequent drying of these particles will cause crystal growth on both surfaces. Subsequently, crystal bridges form between the particles. The formation of crystal bridges between particles is often a fertilizer handling problem because it can lead to the formation of large clumps or cakes.

Many research studies have been done on urea particle manufacturing processes, dissolution processes in water (Petrescu et al., 1997), and urea crystal growth (Grdadolnik and Marechal, 2002), etc. However, little research has been published on the moisture uptake and caking of urea particles in beds. Urea is very susceptible to product degradation due to moisture adsorption, crystal growth and caking, even at moisture contents as low as 0.25% (w/w). Urea particles have a porous internal structure. Scanning electron microscopic (SEM) images and BET measurements show that urea particles, which are nearly spherical in shape, are quite porous with a large internal surface area compared to their external surface area.

While humid air flows through a urea particle bed, some moisture may be adsorbed onto the outer surface of the particles and penetrate into the internal surfaces of each particle. Water transport by vapor diffusion through the internal air spaces within each urea particle and surface diffusion on the internal surfaces is different than water transport via convection and diffusion through the external interstitial air space in a bed of particles. Unlike the effective thermal conductivity of the potash particle bed that increases with an increase in moisture

content, the effective thermal conductivity of a urea particle bed is insensitive to small variations in moisture content because moisture has penetrated into the internal pores.

This chapter presents a new theoretical model for coupled heat and mass transport within a bed of porous urea particles. For the energy transfer process, the temperature gradient is assumed to be negligible inside each particle, but heat conduction in both the particle phase and air phase as well as heat convection between the urea particles and the interstitial air outside particles throughout the bed are considered. The moisture sorption processes were considered in two computational domains, i.e. two different porous media – one is each individual particle, and the other is the urea particle bed. Theoretical formulation is solved by numerical simulation and compared with the experimental data (Nie, et al., 2008a and 2008b).

5.2 Theoretical model

5.2.1 Assumptions and development

Figure 5.1 shows a packed bed of urea particles with a flow length or depth of 160 mm and a cross-section area of 170 × 170 mm^2 at known initial moisture content and temperature that is subject to a step change of air flow rate, temperature and relative humidity at the inlet. To aid in the physical modeling, the following assumptions were used to develop the theoretical model.

(1) Both entrance/exit effect and wall effect can be neglected. For this spherical urea particle bed, the entrance (or exit) length is about one particle diameter (Kaviany, 1995). The air flow length ratio for the entrance (exit) length, with respect to the complete cell height is estimated as $d_p / L = 2.21/200 = 0.011 << 1$. Therefore, the entrance/exist effect can be ignored. For spherical particle beds, the wall effect occurs near the wall about half a particle diameter (Ismail, et al., 2002). The air flow area ratio for this wall area with respect to the whole cell cross-section area is estimated as $4d_p \times L / L^2 = 4d_p / L = 0.044 << 1$; therefore, the non-uniformities in the cross-section area due to the effects of flow channelling near the wall (Nield and Bejan, 1992).

(2) It is assumed that the walls of the urea particle test bed are adiabatic and impermeable

such that the urea particle bed only varies in temperature and particle-layer-average moisture content in the axial x direction of air flow. That is to say, only time and axial position in the flow direction are included as the independent variables to determine the average dependent properties of the bed.

(3) The water vapor transport in the interstitial air space through the urea bed is due to an air pressure difference, which causes bulk flow convection, and vapor diffusion. Both cause the airborne transport of water in the x direction.

(4) The gaseous interstitial mixture, including air and water vapor, is assumed to be an ideal gas mixture which can be volume-averaged because it is at a quasi-equilibrium condition at every point in the bed.

(5) It is also assumed that the urea particles are spherical and have homogeneous or uniform structure (internal porosity distribution) inside when urea particle is dry.

(6) Heat diffusion and water vapor diffusion and adsorption / desorption processes are assumed to vary in the radial direction inside each urea particle, but the temperature gradients within the particles are negligible.

(7) The internal surface area is assumed to be larger than external surface area of each particle. (This assumption will be justified by BET results in Appendix C.)

(8) It is assumed that the external particle surface adsorption / desorption processes are much more rapid than the internal diffusion processes.

(9) The gases in the interconnected pore spaces inside each urea particle are assumed to behave as ideal gases and are in equilibrium with the urea particle at any time and radial position but only the radial gradient in water vapor pressure will induce the diffusion of water.

(10) The total local gas pressure inside the internal pore space is constant and equals to the atmosphere pressure.

(11) Air flow inside each particle is only sufficient to result in a constant total gas pressure within the particle.

(12) Heat sources from chemical reactions such as urea decomposition is considered to be

negligible but the heat of dissolution and adsorption/desorption are included.

(13) Inside each urea particle in the internal domain, it is assumed that there is no temperature gradient since the biggest Biot number at highest Reynolds number of 25 for Terico urea beds ($Bi = h_t \cdot (d_p / 6) / k_p << 0.1$) is very small, therefore each particle is considered thermally as a lumped system. Thus, only the temperature gradient in axial air flow direction is considered and the temperature gradient inside each particle is ignored. Step changes in temperature between one particle and another particle at different values of x may exist giving rise to some heat conduction when the particles are in contact. Thus, heat transport in the axial flow direction is considered to be part of the external interstitial air domain.

The computational domain is comprised of two domains: one is the gaseous void space along the particle bed; and the other domain is each individual particle that is embedded into the bed. These two domains are coupled at the surface interface of each particle (dashed circle line in Figure 5.1(b)), which is assumed to have a uniform temperature and external surface water vapor density.

In Figure 5.1 (a) and (b), the two computational domains are schematically illustrated. The external domain (gas phase) labelled "*e*" includes the air with water vapor in the interstitial volume outside of the particles. The interior domain (particle phase) "*i*" includes the solid particles, particle internal pore space and contents, and adsorbed liquid on the internal and external surface of the particles. These two domains are coupled at the air-particle/liquid interface shown in Figure 5.1(b) where convective heat and water vapor mass transfer occur between the domains. Humid air is transported through the bed by diffusion and forced convection; water is adsorbed on the outer particle surfaces before it diffuses inside and deposits on the internal pore surfaces.

Each particle is taken as an individual porous media. Property variables such as temperature and moisture content or water vapor density in the internal domain are dependent on time, t, position of the particle within the bed in the direction of flow, x, and radial position within the particle, r, while the property variables in the external domain only depend on time and position in the bed in the flow direction, x. Mass and energy transport models are developed for each domain using the local volume average (LVA) theory of porous media.

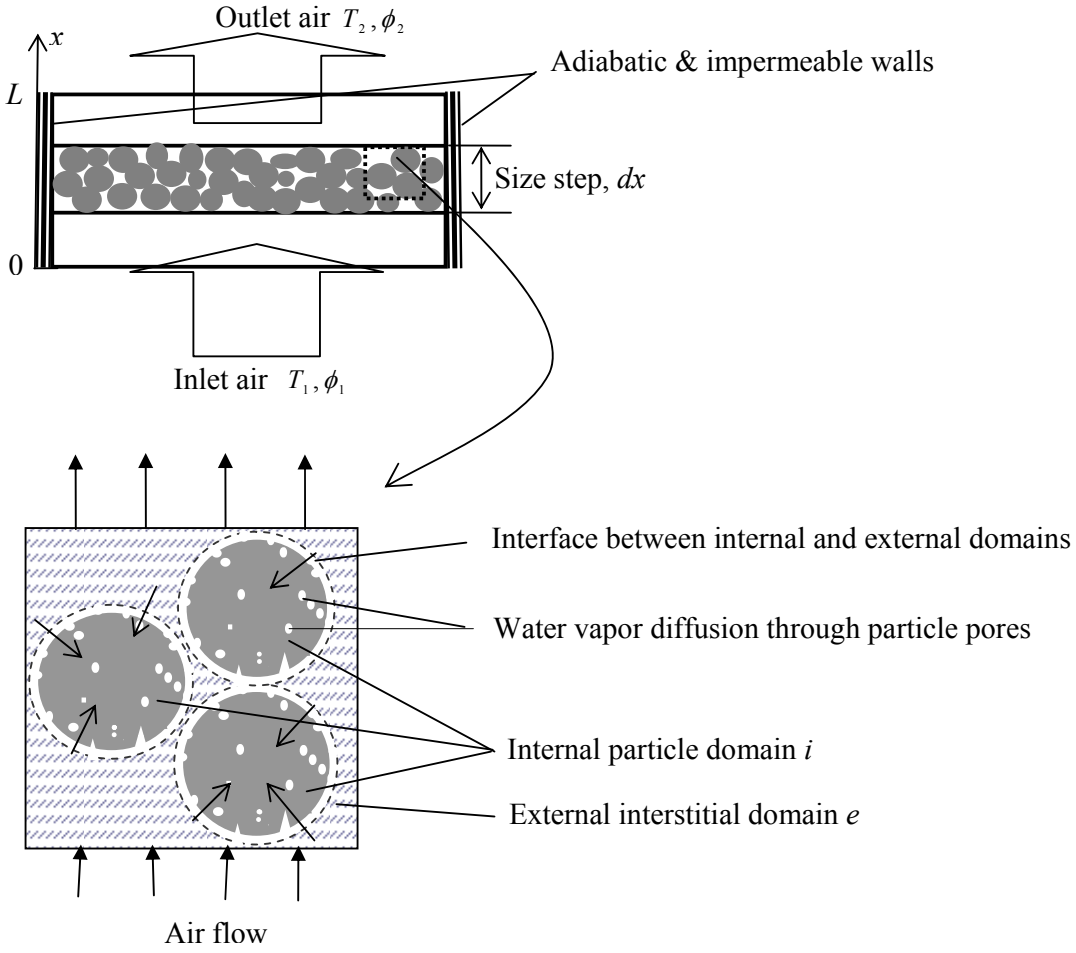

Figure 5.1 Schematic diagram of (a) a urea particle bed with air flow through (b) individual porous particle (internal domain) and gas phase (external domain).

Because the heat generation only occurs in the particle domain, and the differences in the heat capacity and thermal conductivity between the particle and gas phase are not negligible, the local thermal equilibrium cannot be assumed between the two domains (Kaviany, 1995). Instead, the assumption of non-local thermal equilibrium is used to develop the heat transport model between the two domains and it is assumed that each phase is continuous and local phase thermal equilibrium is applicable (Whitaker, 1969).

Since the internal diffusion process is a very slow process, the Biot number based on mass transfer can not be neglected; much larger internal surface area compared with the external

surface area implies that most moisture is sorbed on the internal surface area. Therefore, the internal diffusion of water vapor inside each individual particle must be included in the model. Therefore, the mass transport models are developed separately for the water vapor inside a particle in the internal domain and water vapor in the interstitial particle bed air space of the external domain.

5.2.2 Governing equations

For the coupled mass transport between the internal and external domains, only the behaviour of water vapor is considered. Water vapor in the inlet air passes through the urea particle bed together with the air from the inlet to the outlet in the axial direction. Meanwhile, the convective mass transfer occurs between water vapor in the interstitial air space of the bed and the filled urea particle surface. Due to the porous structure inside each urea particle, the convective water vapor mass flux at the particle surfaces will result in adsorption and condensation or desorption and evaporation on the outer surfaces of urea particles, as well as transfer of water into or out of the internal particle pores by diffusion, where water is adsorbed to form a condensate on the internal pore surfaces of each urea particle.

5.2.2.1 Governing equations of water vapor transport

In the external domain, the transient water vapor transport within the interstitial air space of the particle bed follows the water mass balance equation.

$$\frac{\partial\left(\varepsilon_{g,e}\cdot\rho_{v,e}\right)}{\partial t}+\frac{\partial}{\partial x}\left(u_D\cdot\rho_{v,e}\right)=\frac{\partial}{\partial x}\left(\left(D_{e,eff}+D^d\right)\cdot\frac{\partial\rho_{v,e}}{\partial x}\right)-\dot{m}_e+\dot{m}_{ie} \tag{5-1}$$

where

$$u_D=\frac{\dot{m}_a}{\rho_a A_b}=\frac{\dot{Q}_a}{A_b} \tag{5-2}$$

is the superficial (or Darcy) velocity determined by the constant mass flow rate of dry air, $\dot{m}_a$, at the inlet.

$$D_{e,eff}=\frac{D_{v,a}\cdot\varepsilon_{g,e}}{\tau_e} \tag{5-3}$$

is the external effective diffusion coefficient in the interstitial gaseous phase outside of urea particles. $D_{v,a} = 2.52 \times 10^{-5} \mathrm{m}^2/\mathrm{s}$, is air-vapor molecular diffusivity. D^d considers the dispersion effect in which the ratio of total bed effective diffusivity to air diffusivity $D^t / D_{v,a} = \left(D_{e,eff} + D^d\right) / D_{v,a}$ follows the equations (3-78) to (3-81). The porosity were measured to be $\varepsilon_{g,e} = 0.36$, and τ_e is tortuosity.

$$\dot{m}_e = \rho_l \frac{\partial \varepsilon_{l,e}}{\partial t} \tag{5-4}$$

is the water vapor phase change rate on the external surface of urea particles. In this equation, a positive value implies adsorption and condensation while a negative value means desorption and evaporation.

$$\dot{m}_{ie} = -h_m \left[\rho_{v,e}(x,t) - \rho_{v,i}(x, r = R, t)\right] A_{v,e} \tag{5-5}$$

is the convective mass flux occurring between the water vapor in the interstitial space and the urea particle surface while water vapor passes through the bed.

$\rho_{v,i}(x, r = R, t)$ is the interface vapor density at the liquid-gas interface on each particle and h_m is the mass convection coefficient for water vapor at this same interface. This source/sink term for water vapor flow to or from the external domain is required at every point and any time in the external domain equation (5-1) but is only a boundary condition in the internal domain for equation (5-6). Mass transfer of water vapor between the internal and external domains is coupled at the interface of each particle by equation (5-5) which describes the mass convection of water vapor passing through the area boundary of each particle, $A_{v,e}$.

In the internal domain, water vapor diffusion inside each spherical particle is governed by equation (5-6).

$$\frac{\partial\left(\varepsilon_{g,i} \cdot \rho_{v,i}\right)}{\partial t} = \frac{1}{r^2} \frac{\partial}{\partial r}\left(r^2 \cdot D_{i,eff} \cdot \frac{\partial \rho_{v,i}}{\partial r}\right) - \dot{m}_i \tag{5-6}$$

The effective internal diffusion coefficient, $D_{i,eff}$, is a function of moisture content which varies as the moisture content changes with time as described in section 5.2.5.

$$\dot{m}_i = \rho_l \frac{\partial \varepsilon_{l,i}}{\partial t} \tag{5-7}$$

is the water vapor phase change rate inside the internal domain, i.e., the internal pore surfaces of each particle. Again a positive value for equation (5-7) means adsorption and condensation while a negative value means desorption and evaporation.

5.2.2.2 Governing equations of energy transport

In the gaseous phase, the energy equation in the interstitial air space outside particles is

$$\frac{\partial\left[\varepsilon_{g,e}\cdot(\rho\cdot Cp)_g\cdot T_{g,e}\right]}{\partial t}+\frac{\partial\left[u_D\cdot(\rho\cdot Cp)_g T_{g,e}\right]}{\partial x}=\frac{\partial}{\partial x}\left(\left(K_{e,eff}+K^d\right)\cdot\frac{\partial T_{g,e}}{\partial x}\right)+\dot{h}_{pe} \tag{5-8}$$

The product of density and specific heat capacity for the moist air in the external domain is defined as

$$(\rho\cdot Cp)_g = \rho_v\cdot Cp_v+\rho_a\cdot Cp_a \tag{5-9}$$

The effective thermal conductivity of the gas phase, i.e., moist air in the interstitial space throughout the bed is defined by

$$K_{e,eff} = \varepsilon_{g,e}\cdot\left(K_a + W_e\cdot K_v\right) \tag{5-10}$$

where W_e is the humid ratio of air in the interstitial space. K^d considers the thermal dispersion effect in which the ratio of total bed effective diffusivity to air diffusivity $K^t/K_g = \left(K_{e,eff}+K^d\right)/K_g$ follows the equations (3-78) to (3-81).

The heat transfer rate through the boundary interfaces from the internal domain to the external domain or vice verse, $\dot{h}_{pe}$, is the convective heat flux through the area boundary interfaces, $A_{v,e}$.

$$\dot{h}_{pe} = -h_t\cdot\left(T_{g,e}-T_p\right)\cdot A_{v,e} \tag{5-11}$$

The heat conduction of urea particles in axial direction is governed by

$$\frac{\partial\left\{\left[\varepsilon_p\cdot\left(\rho\cdot c_p\right)_p+\left(\varepsilon_{l,i}\varepsilon_p+\varepsilon_{l,e}\right)\cdot\left(\rho\cdot c_p\right)_l\right]\cdot T_p\right\}}{\partial t}=\frac{\partial}{\partial x}\left(K_{p,eff}\frac{\partial T_p}{\partial x}\right)-\dot{h}_{pe}+\dot{h}_i \tag{5-12}$$

Using the similar weighted average method as for the external domain, the effective thermal conductivity for a particle adsorbed water on the internal and external surface, $K_{p,eff}$, is evaluated by

$$K_{p,eff}=\varepsilon_p\cdot K_p+\left(\varepsilon_{l,i}\varepsilon_p+\varepsilon_{l,e}\right)\cdot K_l \tag{5-13}$$

where K_p is the dry and porous urea particle thermal conductivity.Up to now, there has been no literature that shows the thermal conductivity of pure urea or urea particles. Details will be presented to show how the effective internal conductivity is calculated in section 5.2.4.

5.2.3 Auxiliary equations

5.2.3.1 Volume fraction of solid, liquid and gas

The porous bed volume includes urea particle phase, liquid phase on external particle surface and gas phase in the interstitial air space outside particles.

$$\varepsilon_{l,e}+\varepsilon_{g,e}=1-\varepsilon_p \tag{5-14}$$

where urea particle phase ε_p is a constant. Meanwhile, each urea particle is considered as an individual porous media, including solid, internal liquid and internal gas phases.

$$\varepsilon_{l,i}+\varepsilon_{g,i}=1-\varepsilon_{s,i} \tag{5-15}$$

The volume solid fraction based on bed volume is

$$\varepsilon_s=\varepsilon_p\varepsilon_{s,i} \tag{5-16}$$

The total liquid volume fraction based on bed volume is

$$\varepsilon_l=\varepsilon_p\varepsilon_{l,i}+\varepsilon_{l,e} \tag{5-17}$$

5.2.3.2 Moisture content

Moisture content, the water mass content per unit mass of dry urea particles (g/g, or w/w), includes the moisture adsorbed on the external surface area of urea particles and the moisture penetrated into the internal pore surface inside each urea particles.

$$X = \frac{\varepsilon_l \cdot \rho_l}{\varepsilon_s \cdot \rho_s} = \overline{X}_i + X_e \tag{5-18}$$

where

$$X_e(x,t) = \frac{\varepsilon_{l,e} \cdot \rho_l}{\varepsilon_p \cdot \varepsilon_{s,i} \cdot \rho_s} \tag{5-19}$$

is the partial moisture content on the particle external surface. The particle average internal moisture content is

$$\overline{X}_i(x,t) = \frac{3\int_o^{R=d_p/2} X_i(x,r,t) r^2 dr}{R^3} \tag{5-20}$$

where

$$X_i(x,r,t) = \frac{\varepsilon_{l,i} \cdot \rho_l}{\varepsilon_{s,i} \cdot \rho_s} = \frac{\varepsilon_p \varepsilon_{l,i} \cdot \rho_l}{\varepsilon_p \cdot \varepsilon_{s,i} \cdot \rho_s} \tag{5-21}$$

Isothermal moisture content of urea particles during the 1st sorption process and desorption process follows equations (4-1) and (4-2).

5.2.3.3 Thermodynamic equations

The relative humidity is defined as the ratio of partial water vapor pressure to the saturation water vapor pressure.

$$\phi = \frac{P_v}{P_{vs}} \tag{5-22}$$

where P_{vs} is the partial pressure of water vapor (Pa) and P_{vs}, is saturation pressure of water vapor (Pa) which is a function of temperature (ASHRAE 2004).

$$P_{vs} = \exp\left(C_8 / T + C_9 + C_{10}T + C_{11}T^2 + C_{12}T^3 + C_{13} \ln T\right) \quad (5\text{-}23)$$

where

T = absolute temperature (K)

C_8 = -5.8002006e+03

C_9 = 1.3914993

C_{10} = -4.8640239e-02

C_{11} = 401764768e-05

C_{12} = -1.4452093e-08

C_{13} = 6.5459673

The total air pressure, taken as a constant (see section 5.2.1), is the sum of the partial pressures of dry air and water vapor.

$$P_t = P_a + P_v \quad (5\text{-}24)$$

where both dry air and water vapor, considered as ideal gases (see section 5.2.1), satisfy the thermodynamic status equation.

$$P_a = \rho_a R_a T \quad (5\text{-}25)$$

$$P_v = \rho_v R_v T \quad (5\text{-}26)$$

The humidity ratio of moist air is defined by

$$W = \frac{\rho_v}{\rho_a} = \frac{R_a}{R_v}\frac{P_v}{P_a} \quad (5\text{-}27)$$

5.2.4 Determination of effective heat conductivity

The effective heat conductivity for the whole bed consists of both the effective heat conductivity for the moist air in the external interstitial space and the effective heat conductivity for the packed urea particles.

$$K_{b,eff} = K_{p,eff} + K_{e,eff} \tag{5-28}$$

The value of $K_{p,eff}$ can be determined indirectly from equation (5-10) and (5-28) by measuring the heat flux in a particle bed with a known temperature gradient across the bed. The effective heat conductivity for the whole bed, $K_{b,eff}$, was measured experimentally using a Fox 314 heat flow meter (HFM) without internal air flow. The calculation of Rayleigh number indicated that the buoyancy effects cause by temperature difference is negligible therefore the natural convection can be ignored. For a typical PCS (Georgia) urea particle bed with average particle size of $d_p = 1.8$ mm, $K_{b,eff}$ increased from 0.1856 ± 0.0029 to 0.2407 ± 0.0165 W/(m·K) over a range of moisture content from 0 to 0.8% w/w while for a Terico urea particle bed with average particle size of $d_p = 2.2$ mm, $K_{b,eff}$ increased from 0.2205 ± 0.0044 to 0.2359 ± 0.0067 W/(m.K) over the same range of moisture content from 0 to 0.8% w/w.

The results show that the effective thermal conductivity of Georgia urea particle bed is more sensitive to the moisture content than that of Terico urea particle bed. Georgia urea particle has smaller diameter than Terico urea particle, therefore the external specific surface area of Georgia bed is higher than that of Terico urea bed although the Terico urea bed has much higher total specific surface area than gorgia urea bed. When the terico urea particle bed had the same moisture content as the Georgia urea particle bed, for Terico urea particles most moisture penetrated into the internal pores and were adsorbed on internal surface while for Georgia urea particles much less moisture penetrated inside which caused that Georgia urea particles had much more moisture accumulated at the contact points between particles than Terico urea particles, therefore directly caused the obvious increase in effective thermal conductivity of Georgia urea. Therefore, $K_{p,eff}$ at dry condition was determined to be, for example, 0.1761 W/(m.K) for Georgia urea particle bed while 0.2110 W/(m.K) for Terico urea particle bed since $K_{e,eff}$ was determined from equation (5-10) to be 0.0095 W/(m.K).

Since the Biot number is small for each particle, it can be assumed that the temperature of each particle is uniform at any time and axial position but each particle could have a different temperature at different axial positions. This will induce inter-particle conduction at inter-particle contact points. That is to say, that along the bed length the effective heat conductivity of the packed and contacted particles layers by layers must be modified by a contact conduction term for the bed. In other words, the total thermal resistance must include the contact thermal resistance.

There are many factors that can influence the thermal contact conductance, or inversely the contact thermal resistance. Fletcher (1988) and Madhusudana (1996) indicated that these factors include: (1) Contact pressure is one of the most important factors in determining the contact conductance; the other is moisture content. As contact pressure grows, the contact surface between particles grows which will cause contact conductance to increase while contact resistance decreases. (2) The interstitial material filling the gaps betwwen particles in contact plays an important role in contact conductance. Since the imperfect surfaces at the particle-to-particle contact points reduces the expected smooth surface contact area, the thermal conductivity of the interstitial material and pressure will reduce the contact conductance. That is to say, the smaller the thermal conductance of interstitial material, the larger the contact resistance. (3) Surface roughness, waviness and flatness can influence the contact resistance between particles. (4) Surface deformation is also important to the contact resistance. The deformation between the two particles at a contact point can be plastic or elastic dependent on particle properties and contact pressure. When plastic deformation occurs, contact resistance decreases due to the increase in actual contact area. (5) Particle surface contamination is another factor that may influence the contact resistance. Without knowing the contact area, the measurement of contact conductance is difficult or impossible. Therefore, the contact resistance was measured experimentally instead. Figure 5.2 shows the schematic diagram of the total thermal resistance of the whole urea particle bed, which includes the thermal resistance of individual urea particle, R_p, contact resistance between particles, R_c and the gas phase thermal resistance, R_g.

In Figure 5.2, the total thermal resistance, R_t, includes two paralled thermal resistance – one from the particle phase, $R_{p,t}$, the other from the gas phase, R_g. For the thermal resistance of the particle phase, $R_{p,t}$, it includes the internal particle thermal conductive resistance and the contact resistance. Therefore, the total thermal resistance follows

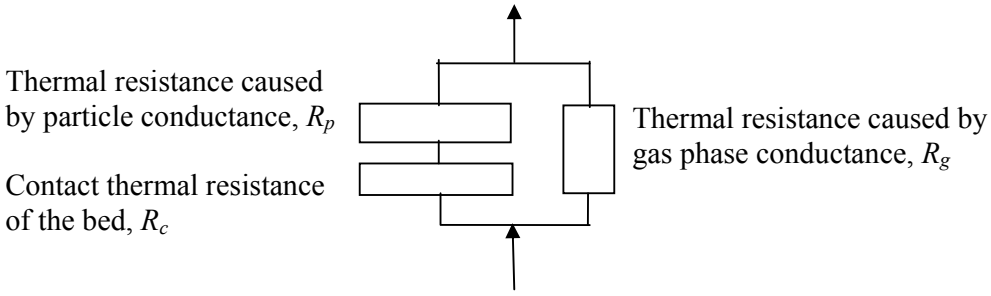

Figure 5.2 Schematic diagram of the total thermal resistance caused by heat conduction of particle, gas and contact conductance.

$$\frac{1}{R_t} = \frac{1}{R_{p,t}} + \frac{1}{R_g} = \frac{1}{R_p + R_c} + \frac{1}{R_g} \tag{5-29}$$

where

$$R_t = \frac{L}{A_b K_{b,eff}} \tag{5-30}$$

is the total thermal resistance of the whole urea particle bed, including particle and gas parts. The thermal resistance of particle part includes particle-particle contact resistance R_p and individual particle thermal resistance R_c as following equation (5-31).

$$R_{p,t} = R_p + R_c = \frac{L}{A_b \cdot K_{p,eff}} + \frac{1}{A_b h_{b,c}} \tag{5-31}$$

where $h_{b,c}$ is thermal contact conductance, or $1/h_{b,c}$ is the contact thermal resistance; $A_{b,c}$ is the nominal contact area, or the cross-section area of the particle bed.

$$R_g = \frac{L}{A_{b,c} K_{e,eff}} \tag{5-32}$$

is the thermal resistance of the gas part. Combining equation (5-30) (5-31) (5-32) with equation (5-29), one gets

$$K_{b,eff} = \frac{h_{b,c} L}{1 + h_{b,c} L / K_{p,eff}} + K_{e,eff} \tag{5-33}$$

If $K_{b,c} / K_{p,eff} = h_{b,c} L / K_{p,eff} << 1$, then

$$K_{b,eff} \cong K_{b,c} + K_{e,eff} \tag{5-34}$$

This indicated that the contact thermal resistance, R_c, or the equivalent thermal conductivity of contact points $K_{b,c}$ can be experimentally determined when the other terms are known.

5.2.5 Effective internal diffusion coefficient

Each individual porous and spherical urea particle is taken as a porous media and moisture penetrates in the radial direction from the particle surface to the center during adsorption process or vice verse. The volume averaged effective internal mass diffusivity within each particle is used to determine both the water vapor diffusion through the pore space and surface diffusion of the liquid film on the pore surfaces. This water movement is mostly governed by the internal structure of the particle and the distribution of internal pores. Pesaran and Mills (1987a and b) suggested that the effective internal diffusivity was a function of moisture content. The sensitivity study of constant effective internal diffusion coefficient was carried out. When using a small constant internal diffusion coefficient, simulated moisture content of urea particles in the first 3 hours fitted the experimental data well but simulation was lower than the data after that and the different between simulation and data increased with time. when using a large constant internal diffusion coefficient, simulated moisture content of urea particles after 10 hours fitted the experimental data well but simulation was higher than the data especially first 3 hours. This implied a variable effective internal diffusion coefficient. The comparison between experimental data and numerical simulation shows that this internal diffusion coefficient increases with moisture content during the adsorption process inside a particle, and the correlation between the effective internal diffusion coefficient and moisture content for X<0.004 was presented by Nie et. al. (2008b) as:

$$D_{i,eff} = D_{i,eff}\Big|_{t=t0} \left(0.905 + 0.085 \cdot e^{10000 \cdot X / 5.3} \right) \tag{5-35}$$

where the internal diffusion coefficient includes pore diffusion and surface diffusion.

$$D_{i,eff}\Big|_{t=t0} = \frac{D_{vi} \cdot \varepsilon_{gi}\Big|_{t=t0}}{\tau_i} + D_s\Big|_{t=t0} \tag{5-36}$$

In contrast, this effective diffusion coefficient is essentially a constant during a desorption process. Nie et al. (2008a) explained the reason why the internal diffusion coefficient increases with moisture content during the adsorption process. It is that the number of pathways increases radially towards the centre of the particles inside the particles. Thus as moisture penetrates into the particle it experiences a greater number of pathways, leading to an increase in the effective diffusion coefficient. Conversely, as the particles dry out, mass transfer is limited due to the lower number of pores closer to the external surface of the particles, and then the effective diffusion coefficient remains constant.

5.2.6 Convection coefficient

Many studies have been done using the indirect volume average technique to find the internal heat transfer coefficient between the interstitial fluid and the particles in different types of porous media. Variations or differences in the predictions of these correlations were up to $\pm 100\%$ and higher for the case of low Reynolds number ($1 \le \mathrm{Re}_{d_h} \le 20$). Theoretically, the dimensionless Nusselt number is only dependent on the Reynolds number, Prandtl number, and the geometry of the air flow path. Nie et al. (2008b) used an inverse mathematical method to deduce the correlation of heat and mass convection coefficient, in which the numerical simulation was compared with the experimental data for the Reynolds number range from 0.5 to 10. Both numerical simulation and experimental measurement indicated that the slow moisture adsorption process was dominated by the internal particle diffusion, and was not very sensitive to the convection coefficient. Nie et al. (2009a) developed a simplified theoretical model to deduce the transient response of the urea particle bed subject to a pure temperature or pure humidity step change which was shown to be a function of Reynolds number and convection coefficient. But the correlation between dimensionless Nusselt number or Sherwood number and Reynolds number was lower than the one using the inverse method at high Reynolds number because the assumptions used were not always valid for each case as mentioned in section 3.3.3. To obtain more accurate data, a new experimental method was carried out to derive a new correlation of the convection coefficient for Reynolds number in the range 5 to 280 using simple spherical particle beds as presented in Appendix D. The new method eliminated or alleviated the deficiency of assumptions used by Nie et al.

(2009a). In addition, the analogy between the momentum transport, heat and mass convection, convection dispersion showed that for air flow through the porous bed, the Nusselt number or Sherwood number could be a constant for Darcy flow regime when Reynolds number was less than 1, but increase linearly with Reynolds number in a log-log plot for Reynolds number higher than 100. In the transition region (e.g. $0.5 < \mathrm{Re}_{d_h} < 10$), the Nusselt number or Sherwood number gradually increases (Nie, et al., 2008a and b). Most correlations of Nusselt number and Reynolds number were developed for forced convection, but natural convection could dominate when Reynolds number is low and the temperature gradient or Rayleigh number are relatively large, for example, $\mathrm{Re}_{d_h} < 3$ (Wakao and Kaguei, 1982). However, for the moisture adsorption or desorption of urea particle bed (chapter 4), the Reynolds number lies between 0.7-25 and experimental data showed that temperature difference within the bed at any time was as about 0.5-1.5^{o}C where Rayleigh number < 3 and the ratio of Rayleigh number to Peclet number << 0.1 such that the natural convection in the porous media was negligible (Nield and Bejan, 1992). It was not easy to develop correlation including both natural convection and forced convection with limited data. But the analogy of relationship between the heat/mass convection, friction Reynolds number product, dispersion and Reynolds number (Peclet number) could be applied here, therefore, the following correlation (Nie, et al., 2009b) was used.

$$\mathrm{Nu}_{d_h} / \mathrm{Pr}^{1/3} = \mathrm{Sh}_{d_h} / \mathrm{Sc}^{1/3} = 0.0491 \times \mathrm{Re}_{d_h}^{\ 0.8572} \qquad \text{for } 3 < \mathrm{Re}_{d_h} < 280 \tag{5-37a}$$

$$\mathrm{Nu}_{d_h} = 0.14 \text{ for } \mathrm{Re}_{d_h} < 3 \tag{5-37b}$$

5.2.7 Thermodynamics of urea dissolution

The heat source term $\dot{h}_i$ in equation (5-12) includes two parts: (1) the enthalpy due to the pure phase change without temperature change $\overline{\dot{m}}_p H_{fg}$, and the energy change $\overline{\dot{m}}_p \cdot Cp_v(T_{ge} - T_P)$ due to temperature change effect; and (2) the heat of solution, $\overline{\dot{m}}_p \beta_s H_s$. The average rate of water adsorbed by a urea particle at different bed position is defined by

$$\overline{\dot{m}}_p(x,t) = \dot{m}_e(x,t) + \varepsilon_p \overline{\dot{m}}_i(x,t) \tag{5-38}$$

where

$$\overline{\dot{m}_i}(x,t) = \frac{\int_0^R \dot{m}_i(x,r,t) 4\pi r^2 dr}{\int_0^R 4\pi r^2 dr} \tag{5-39}$$

It is assumed that urea dissolution takes place everywhere liquid water exists on the particle surface and a saturated solution is formed. Condensation causes the urea temperature to increase while dissolution causes a temperature decrease. Therefore, the sensible energy release rate for each particle is

$$\dot{h}_i = \overline{\dot{m}}_p \cdot \left[H_{fg} + Cp_v (T_{g,e} - T_p) + \beta_s \cdot H_s \right] \tag{5-40}$$

where, at room temperature (e.g., $21-24^{o}\mathrm{C}$), H_{fg}= 2446 kJ/kg (Incropera, 2002), H_s= −13.8 kJ/mol (Keller, 1967) and $\beta_s = 19$ mol/kg (Meessen, 1996).

5.3 Initial and boundary conditions

5.3.1 Initial conditions

It is assumed that water vapor density and temperature are initially constant and uniformly distributed both inside the particles and within the bed.

$$\rho_{v,e}(x, t=0) = \rho_{v,e,0} \tag{5-41}$$

$$T_{g,e}(x, t=0) = T_{g,e,0} \tag{5-42}$$

$$\rho_{v,i}(x, r, t=0) = \rho_{v,i,0} \tag{5-43}$$

$$T_p(x, t=0) = T_{p,0} \tag{5-44}$$

5.3.2 Boundary conditions

In the exterior domain, i.e., within the bed along the direction of air flow outside of the particles, the inlet air water vapor density and temperature are assumed to equal the inlet air vapor density and temperature.

$$\rho_{v,e}(x=0,t)=\rho_{v,e,I} \tag{5-45}$$

$$T_{g,e}(x=0,t)=T_{g,e,I} \tag{5-46}$$

The inlet air temperature and relative humidity were not exactly constant. Due to the environmental air temperature and humidity changed with time during the long experimental time duration, inlet air water vapor density and temperature in equations (5-45) and (5-46) varied with time. Therefore, the data of inlet air temperature and relative humidity were curve fitted to be the inlet boundary conditions.

The gradient of mass and heat transfer at the outlet of the bed is negligible.

$$\frac{\partial \rho_{v,e}}{\partial x}(x=L,t)=0 \tag{5-47}$$

$$\frac{\partial T_{g,e}}{\partial x}(x=L,t)=0 \tag{5-48}$$

It is assumed that there is zero mass flux at the centre of each particle.

$$\frac{\partial \rho_{v,i}}{\partial r}(x,r=0,t)=0 \tag{5-49}$$

At the particle interface surface, the water vapor convected to the surface of particle is diffused into the particle during adsorption. That is to say, the source/sink term for the external domain is the boundary condition for the individual particles.

$$D_{i,eff}\frac{\partial \rho_{v,i}}{\partial r}(x,r=R,t)=h_m\left[\rho_{v,e}(x,t)-\rho_{v,i}(x,r=R,t)\right] \tag{5-50}$$

For particle sensible energy transfer from layer to layer within the bed, it is assumed

$$\frac{\partial T_p}{\partial x}(x=0,t)=0 \tag{5-51}$$

$$\frac{\partial T_p}{\partial x}(x=L,t)=0 \tag{5-52}$$

5.4 Results and conclusions

5.4.1 Numerical simulation

The governing equation of the heat and mass transfer in both internal and external domains, are discretized using the finite volume method (Patanker, 1980) in a fully implicit scheme in Appendix E. The subroutine program for the internal moisture diffusion inside a particle with constant internal diffusion coefficient and constant boundary was validated by the analytical solution. The subroutine program for the internal moisture sorption and desorption within one particle with variable properties in a constant humidity environment was compared with an experimental data and showed good agreement. The 1-D pure mass transfer or the pure heat transfer with constant properties along the bed height without internal diffusion process and source or sink term was validated by the analytical solution. But the numerical simulation of the coupled heat and mass transfer with variable properties in two coupled computational domains can not be validated by analytical solutions. The time step for both domains was set as $dt = 0.01$ s for the early 50 min while $dt = 1$ s after 50 min, and size step dx for the external domain along the bed was the same as a urea particle diameter, i.e., $dx = 2.2$ mm for large particles and $dx = 1.8$ mm for small particles while the size step for the internal domain inside a spherical urea particle is 2.5% of the particle radius. Numerical simulations were carried out over each domain which is coupled at the air-particle/liquid boundary interfaces. An iterative technique is used to solve the coupled equations and obtain solutions for selected initial and boundary conditions. Any property changes with moisture content and temperature are updated to the new value after each time step. Because the internal diffusion process is much slower than the external diffusion and convection process, simulation for each time step starts at the external domain, then the new water vapor density and temperature are used as the convective boundary conditions for the internal domain or particle phase; updated water vapor density at the particle surface and the particle temperature are again imbedded into the simulation for the next time step. Figure 5.3 to Figure 5.10 shows the comparison of numerical simulation and some experimental data for both moisture adsorption and desorption process of a Terico urea particle bed while air flow through the bed at air flow rate 160 Lpm. For the experimental data of a Terico urea particle bed subject to air flow at 17.5 Lpm, simulations using constant inlet condition are given in Appendix H.

Here the numerical results are presented for the actual experimental condition of urea particle bed with $d_p = 2.2$ mm, $\mathrm{Re}_{d_h} = 19.9$ (or air flow rate 160 Lpm), which means that the curve fit of the actual experimental inlet temperature and relative humidity are used as the inlet condition in the numerical simulation during both adsorption and desorption process. For the adsorption process, the actual inlet air relative humidity followed the equation:

$$\phi(x=0,t) = -2.7217\times10^{-8}t^6 + 2.2605\times10^{-6}t^5 - 7.1728\times10^{-6}t^4 + 1.0621\times10^{-3}t^3 - 6.8716\times10^{-3}t^2 + 7.5750\times10^{-3}t + 0.714 \quad (5\text{-}53)$$

where t is the time in hours, the coefficient of determination between humidity and time is R^2 = 0.9422.

For the adsorption process, the actual inlet air temperature followed the curve fit equation:

$$T_g(x=0,t) = -6.3553\times10^{-7}t^6 + 4.3684\times10^{-5}t^5 - 1.1134\times10^{-3}t^4 + 1.2715\times10^{-2}t^3 - 5.1567\times10^{-2}t^2 - 0.1979t + 294.62 \quad (5\text{-}54)$$

where t is the time in hours, T_g is temperature in K, the coefficient of determination between temperature and time is R^2 =0.9873.

For the desorption, the actual inlet air relative humidity for desorption process was

$$\phi(x=0,t) = 3.7421\times10^{-9}t^6 - 2.9859\times10^{-7}t^5 + 9.1803\times10^{-6}t^4 - 1.3675\times10^{-4}t^3 + 1.0291\times10^{-3}t^2 - 3.9501\times10^{-3}t + 0.0934 \quad (5\text{-}55)$$

where t is the time in hours, the , the coefficient of determination between humidity and time is R^2 =0.6871. The actual inlet air temperature for desorption process was

$$T_g(x=0,t\le0.4361) = 1.5277\times10^{3}t^6 - 2.0686\times10^{3}t^5 + 1.0059\times10^{3}t^4 - 1.8361\times10^{2}t^3 - 4.3450t^2 + 5.6038t + 294.05 \quad (5\text{-}56a)$$

where t is the time in hours, T_g is temperature in K, the coefficient of determination between temperature and time is R^2 = 0.9954.

$$T_g(x=0,t>0.4361) = -5.5098\times10^{-8}t^6 + 1.0848\times10^{5}t^5 - 4.4728\times10^{-4}t^4 + 6.3863\times10^{-3}t^3 - 2.6090\times10^{-2}t^2 - 2.2378t + 294.64 \quad (5\text{-}56b)$$

where t is the time in hours, T_g is temperature in K, the coefficient of determination between temperature and time is $R^2 = 0.9364$.

Figures (5.3) and (5.4) compare the numerical predictions of the relative humidity at the inlet and outlet of the bed. In Figure (5.3), which is for an adsorption process, there is some fixed deviation in the outlet predictions after 1 hour. But if taking into account the difference between inlet and outlet air relative humidity at 24 hours due to measurements uncertainty, this fixed deviation in the outlet relative humidity predictions from the experimental data can be neglected. For the desorption process presented in Figure (5.4) there is good agreement after 1 hour.

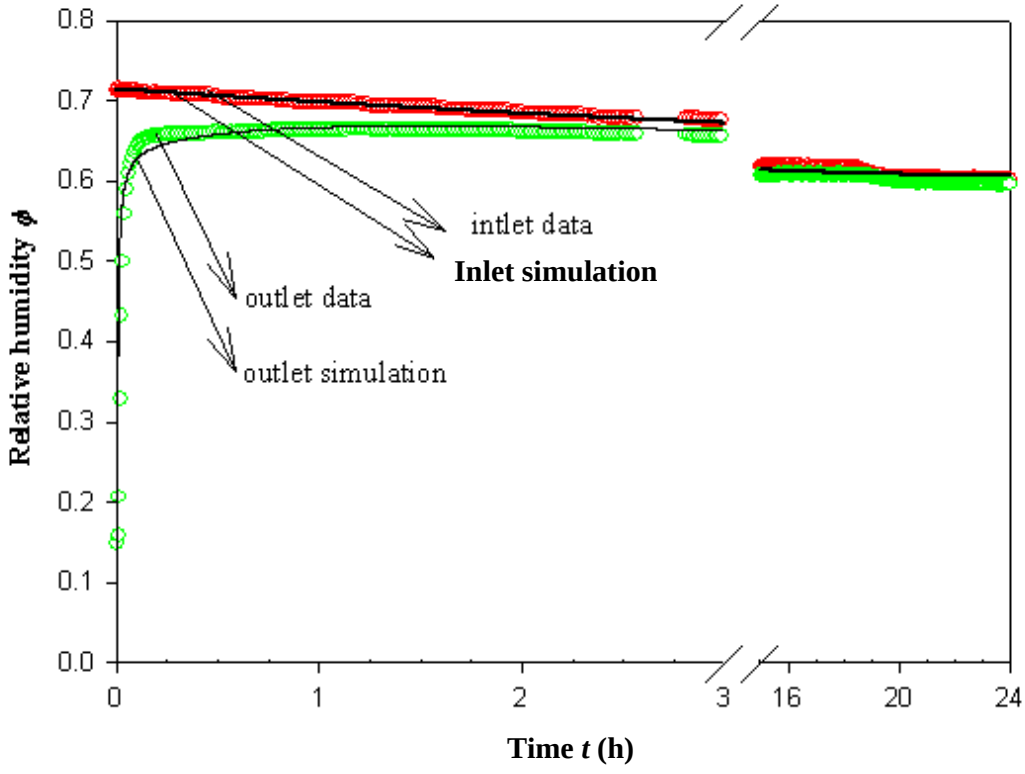

Figure 5.3 Comparison of data and simulations of relative humidity for an adsorption process within a Terico urea particle bed, $\phi_0 = 0.10$, $T_0 = 21.5^{\circ}\mathrm{C}$, $\mathrm{Re}_{d_h} = 19.9$.

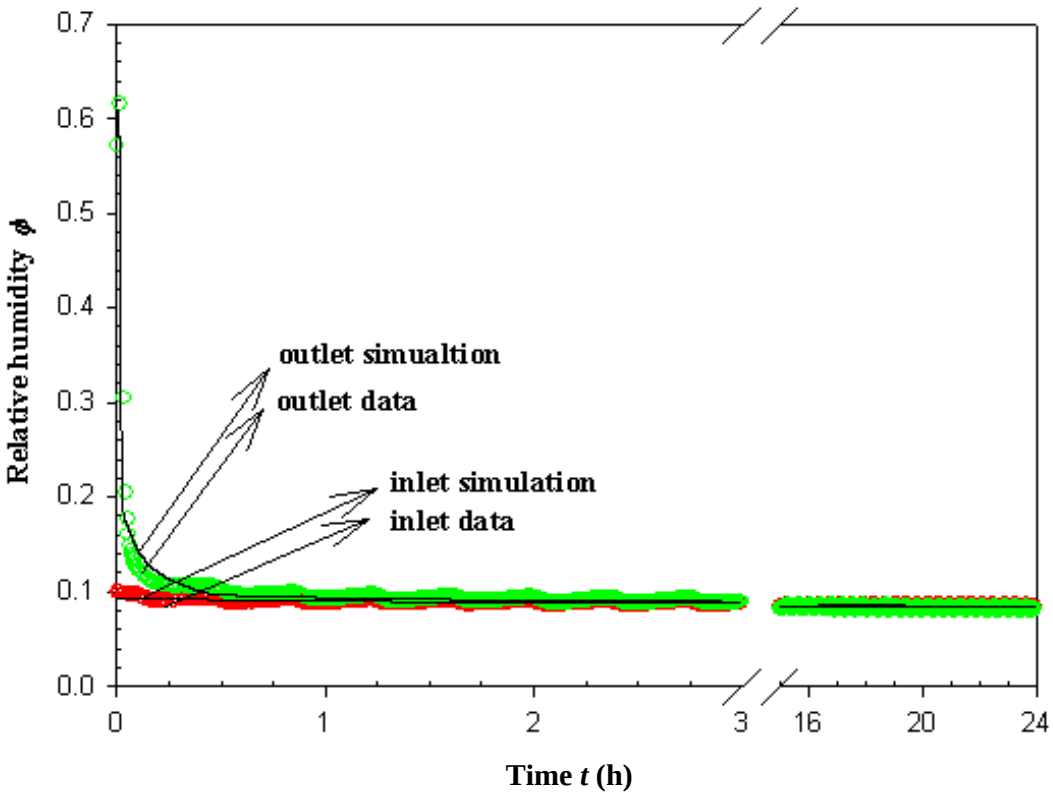

Figure 5.4 Comparison of data and simulations of relative humidity for a desorption process within a Terico urea particle bed, $\phi_0 = 0.61$, $T_0 = 21.0^{\circ}\mathrm{C}$, $\mathrm{Re}_{d_h} = 19.9$.

Figures (5.5), (5.6) and (5.7), (5.8) show the comparison of data and simulated transient air and particle temperature versus time at different positions in the bed during adsorption/desorption processes. In the adsorption process as shown in Figure 5.5, the inlet air temperature was not constant but decreased gradually with time; however, when air flowed through the bed, the air temperature started to increase immediately due to the water vapor phase change or moisture adsorption and dissolution heat release on the urea particle surface until a peak temperature and then dropped to follow after the inlet air temperature. Both experimental data and simulation results of the peak temperature showed that the increase of air temperature occurred firstly in the entrance position of the bed (near $x/L = 0$), then moved forward along the bed till $x/L = 1.0$.

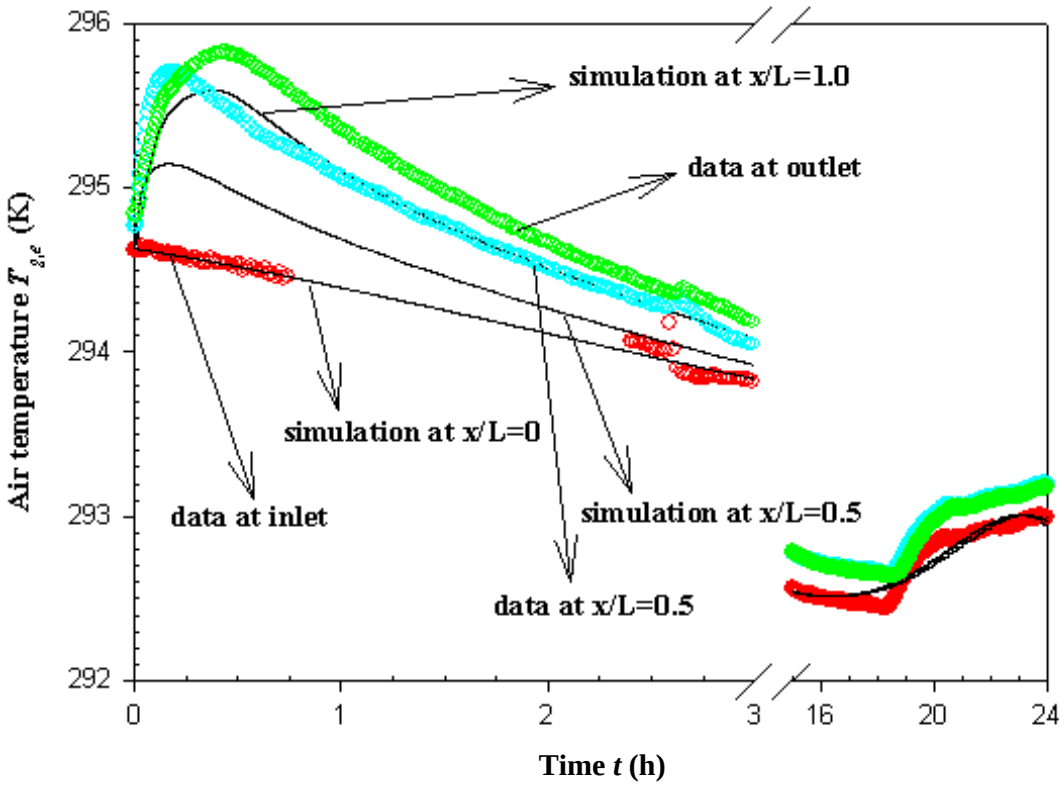

Figure 5.5 Comparison of data and simulated air temperature versus time for an adsorption process at different depths of the Terico urea particle bed, $\phi_0 = 0.10$, $T_0 = 21.5^{\circ}\mathrm{C}$, $\mathrm{Re}_{d_h} = 19.9$.

In the adsorption process as shown in Figure 5.6, when air flowed through the particle bed, particle temperature at the inlet (*x/L* = 0) started to jump a little immediately due to the moisture sorption and continued to increase till a peak temperature and then dropped following after the inlet air temperature by heat convection. With the heat conduction of particle layers along bed direction and the water adsorption from the humid air, particles at any position, *x*, followed the same trend layer by layer.

Usually, the constant inlet condition is not easy to control especially for adsorption process. If the constant inlet air temperature is kept nearly constant, both particle temperature and air temperature along the bed presented a simple trend –just one temperature peak. However, if the inlet air condition is not constant, how the particle temperature varies with time depends on the combination of the convection of the flowing-through cool air that make temperature decrease, with the heat release of moisture condensation, adsorption and dissolution which make temperature increase. The air or particle temperature progress with time will be complicated.

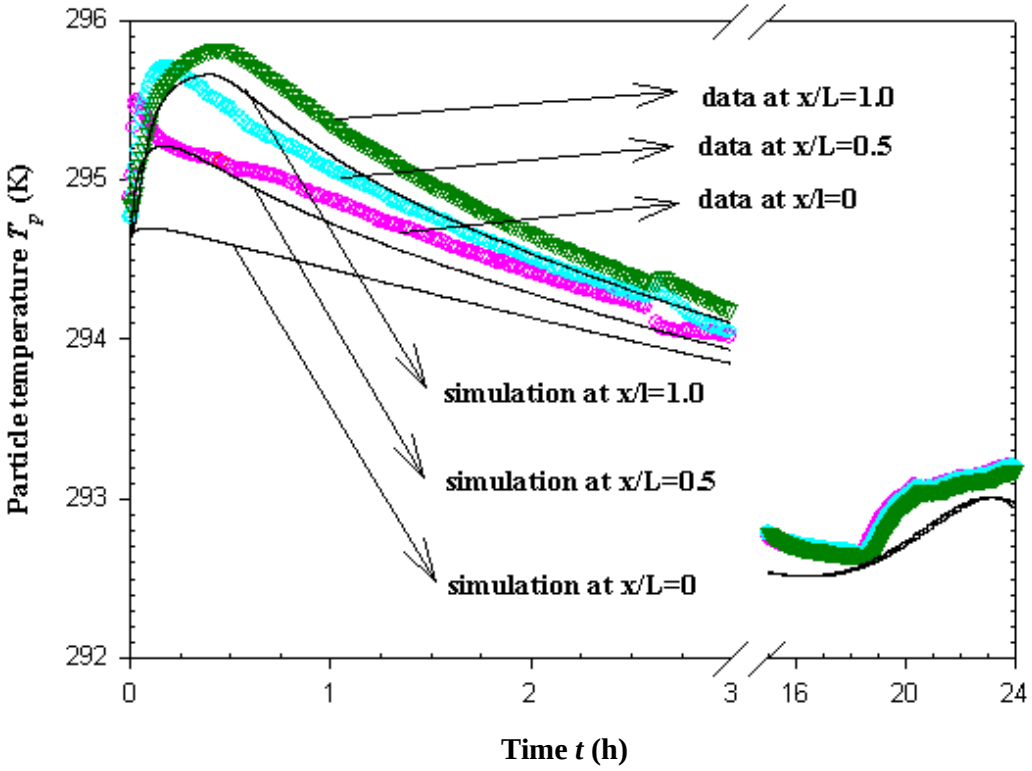

Figure 5.6 Comparison of data and simulated transient particle temperature versus time for an adsorption process at different depths of Terico urea particle bed, $\phi_0 = 0.10$**,** $T_0 = 21.5^{\circ}\mathrm{C}$**,** $\mathrm{Re}_{d_h} = 19.9$**.**

During the desorption process (Figure 5.7 and Figure 5.8), the flowing air temperature decreased as time progressed such that the air temperature decreased quickly and then increased to the inlet temperature. The particle temperature decrease started from the inlet. Then with the heat conduction of particle layers along bed direction and followed water desorption due to the dry air flowing through, particles at any position, x, the bed started to decrease in temperature layer by layer. However, because the inlet air temperature was kept nearly constant, the inlet particle layer was immediately heated by the convection with flowing air, and then the downstream particle layers at positions $x > 0$ heated by convection, conduction.

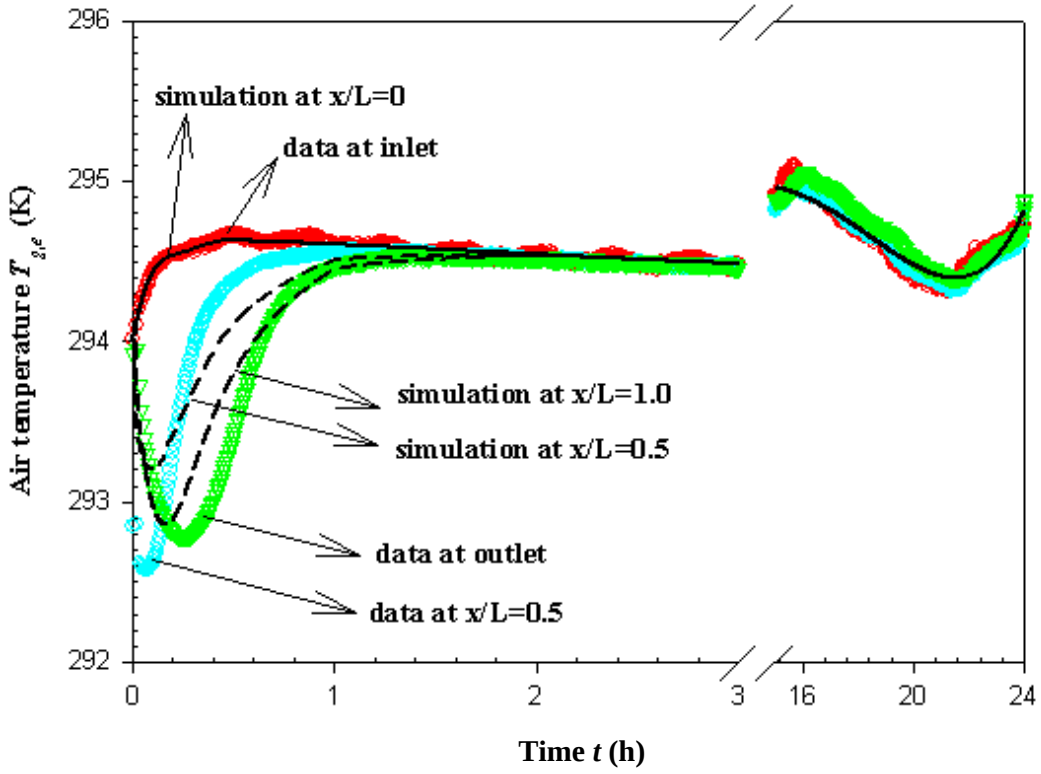

Figure 5.7 Comparison of data and simulated air temperature versus time for a desorption process at different depths of the Terico urea particle bed, $\phi_0 = 0.61$, $T_0 = 21.0^{\circ}\mathrm{C}$, $\mathrm{Re}_{d_h} = 19.9$.

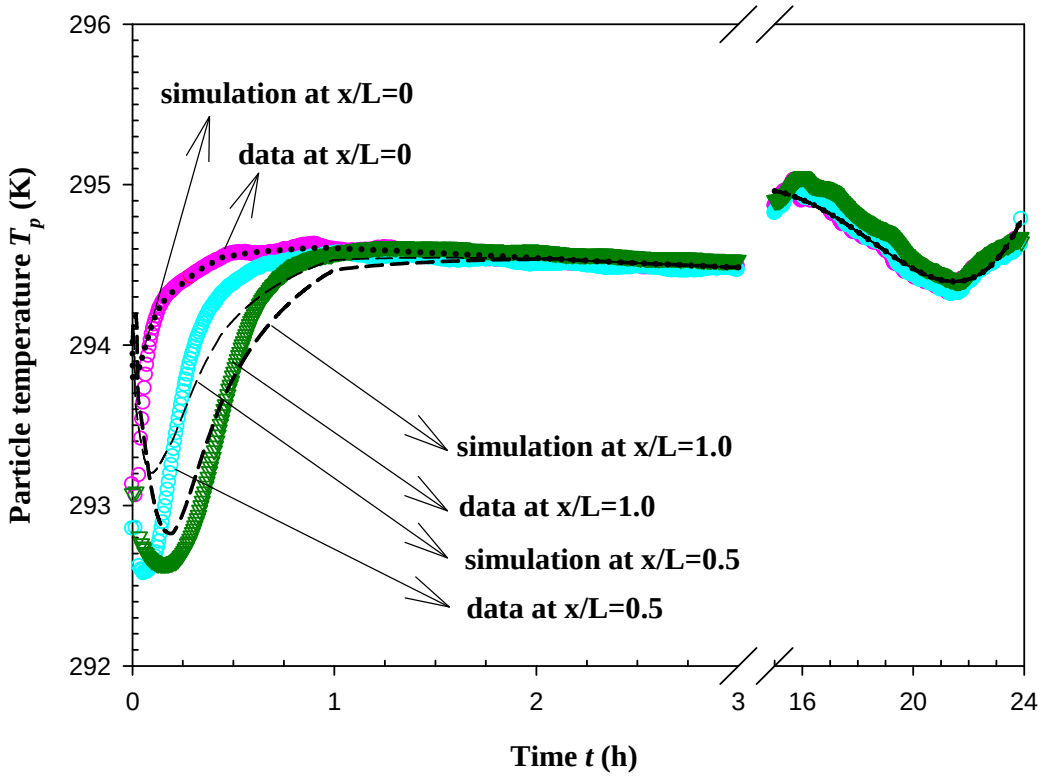

Figure 5.8 Comparison of data and simulated transient particle temperature versus time for a desorption process at different depths of the Terico urea particle bed, $\phi_0 = 0.61$**,** $T_0 = 21.0^{\circ}\mathrm{C}$**,** $\mathrm{Re}_{d_h} = 19.9$**.**

Figures 5.9 and 5.10 shows comparisons of experimental data and simulation results for average moisture content versus time during adsorption/desorption processes. These simulations show agreement with data that are within the uncertainty limits of the data. The model therefore indicates that the internal effective water vapor diffusion coefficient inside each particle is much lower than that for water vapor in air, (i.e., the ratio of between internal and external diffusion coefficient is around 10^{-4} to 10^{-3}). Also, as the internal particle surface area is larger than the external one, internal moisture diffusion processes dominates the moisture adsorption process in the particle bed. Secondly, the model points to the fact that the moisture desorption rate is faster than the moisture adsorption rate, which can be verified with the case of the constant inlet condition (see simulation in appendix H).

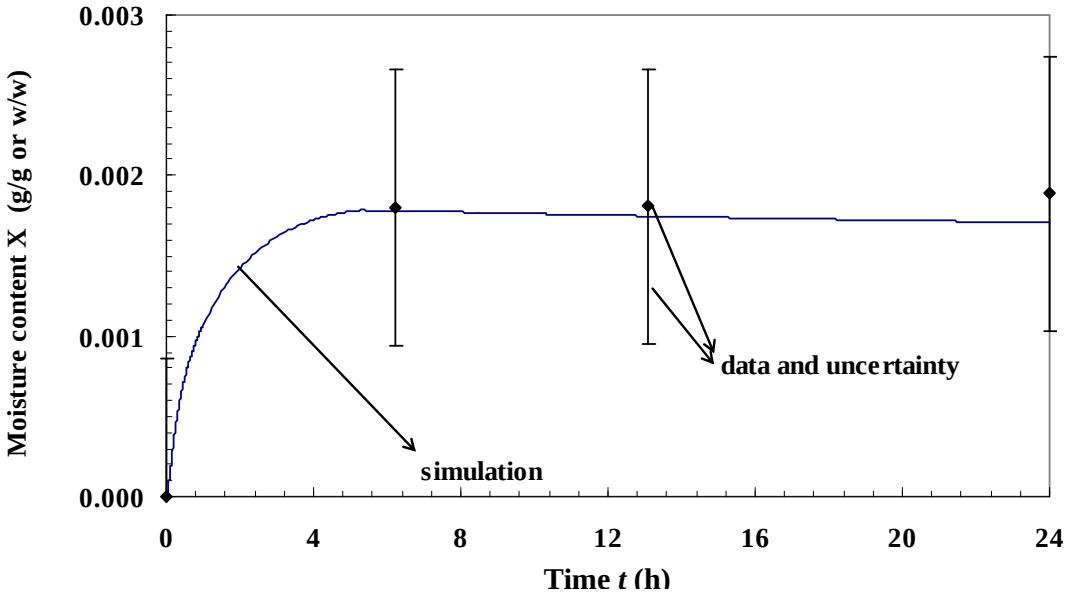

Figure 5.9 A comparison of predicted and experimental data of the transient average moisture content of the Terico urea particle bed during an adsorption process, $\phi_0 = 0.10$, $T_0 = 21.5^{\circ}\mathrm{C}$, $\mathrm{Re}_{d_h} = 19.9$.

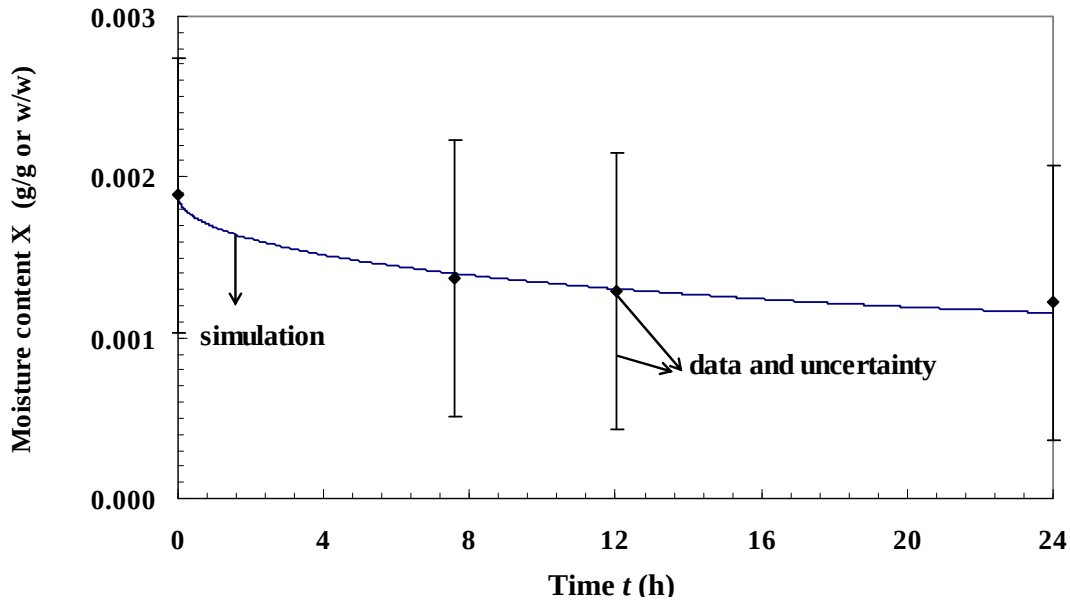

Figure 5.10 A comparison of predicted and experimental data of the transient average moisture content of the Terico urea particle bed during a desorption process, $\phi_0 = 0.61$, $T_0 = 21.0^{\circ}\mathrm{C}$, $\mathrm{Re}_{d_h} = 19.9$.

Sensitivity studies of time step and grid size in two computational domains are shown in Appendix F. Values of important properties of urea particles and particle beds used in numerical simulation are shown in Appendix G. Appendix H gives the numerical simulation results for both adsorption and desorption processes and compares the simulations with data for air flow rate at 17.5 Lpm (data in Chapter 4).

5.4.2 Summary and conclusions

In this chapter, a new model was developed that considered mass and heat transfer in a bed of porous urea particles with air flow through the bed. The model considers two domains; a domain inside each particle and a second domain outside of the particle in the interstitial air space in the bed. These two domains are coupled at the external surface of the particles. The model agrees well with experimental results for moisture adsorption and desorption processes. The following conclusions can be made from this research.

The urea particle bed behaves somewhat similar to a silica gel desiccant bed except that urea has a very small adsorption capacity. Both silica gel desiccants and urea particles have internal pore structure but compared with silica gel, urea particles have much smaller internal porosity and internal surface area available for internal moisture adsorption.

The moisture adsorption process in a bed of urea particles occurred very slowly. This indicates that internal particle transport processes are the rate limiting process since the internal surface is larger than the exterior. The model indicates the effective internal water vapor diffusion coefficient is 10^{-4} to 10^{-3} times smaller than that of water vapor in air. The effective internal diffusion coefficient is also dependent on the moisture content during an adsorption process but is independent of moisture content during moisture desorption.

CHAPTER 6

SUMMARY, CONCLUSIONS AND FUTURE WORK

6.1 Summary

Urea is a very important fertilizer that provides plants with necessary nitrogen nutrition. Moisture adsorption / desorption and caking of the urea particle piles are general phenomena that occur during the process of storage, shipping or transportation. Caking only occurs in the presence of moisture. Air humidity and temperature change continuously with time and this causes the variation in relative humidity of air. The first step for further caking prevention is to investigate a coupled heat and moisture transfer process in a bed of urea particles while the bed is exposed to ambient environment with changing temperature and humidity.

This thesis presented the coupled heat and moisture transfer processes in a bed of urea particles while it was exposed to an ambient environment with a changing temperature and humidity. The first objective of the research was to experimentally determine the physical properties of urea particles and particle beds including: the particle size, shape and internal porosity, the bed porosity and specific surface area, the isothermal moisture adsorption and desorption characteristics. The second objective was to use the well known physical principles of heat and moisture transport through porous granular beds to theoretically formulate and numerically simulate moisture movement within a bed of urea particles, and compare these simulations with measured data for a urea bed subject to a low Reynolds number air flow with a step change in the inlet air temperature or humidity.

Research work can be summarized as followed.

(1) Some fundamental but important properties of urea particles were determined by a eries of experimental measurements. 2-D image analysis was used to determine the particle diameter and the results verified the visual estimation of nearly spherical shape. Scanning electronic microscope (SEM) pictures showed the internal pore structure inside each urea particles and rough surface both internally and externally that changed the moisture sorption process and allocation within urea particle beds. BET technique was introduced to measure the total surface area of urea particles, indicating the importance of internal

moisture diffusion inside each urea particle. Permeability and porosity of urea particle beds were determined by the bed measurement. Karl Fischer titrator was introduced to determine the total moisture content of urea particles.

(2) Internal fluid-solid convection coefficients were determined with three totally different methods. The first one used the mathematically inverse method in which mass transfer of data was compared with the numerical simulation to derive the mass convection coefficient. The second one originated from the observation of outlet air response that the outlet air temperature or humidity showed an exponential growth form. An analytical solution of outlet air temperature and humidity was derived to be a function of heat convection coefficients, time constant and Reynolds number. The third methods used solid spherical particles without any internal pores. The heat energy change of the particle bed was investigated during a specific linear time period based on the experimental data and the heat convection coefficients within the spherical particle beds were derived.

(3) A series of step change experiments were carried out to obtain the outlet property response. (a) Hot and dry air flow with Reynolds number in range of 5~300 were forced to pass through the initial cool and dry urea particle bed to measure the pure temperature response of the urea particle bed. (b) Humid air at room temperature with Reynolds number in range of 5~300 were forced to pass through the initial dry urea particle bed at room temperature to measure the pure humidity response of the urea particle bed. Theoretical solution was also proposed to have a analytical solution.

(4) A new test cell with sampling test ports was designed for experimental measurement of the transient moisture uptake of a urea particle bed and distribution at any time without any interruption of experiment. The novel sampling device modified from a syringe and pistons helped minimize moisture exposure to the air during the moisture determination using Karl Fischer titrator. Isothermal moisture content of urea particles during two cyclic moisture sorption-desorption process were also determined by experimental measurement and presented a hysteresis phenomenon.

(5) A new theoretical model was developed to predict one dimensional temperature and moisture content distributions in a bed of bulk granular urea particles when humid air flowed uniformly through the bed. The moisture sorption and transport processes considered two computational domains – water vapor diffusion inside each particle, and water vapor convection and diffusion in the interstitial air space in the urea particle bed.

(6) Fortran language 90 was used to numerically solve the theoretical model. Comparison of mass transfer within urea particle beds between numerical simulation and experimental data showed good agreement.

6.2 Conclusions

From the complete research set of heat and moisture migration within the porous urea particle bed, the following conclusions can be made.

(1) Urea particles are nearly spherical with uniform size distributions. For two different types urea particles mentioned in the thesis, the granular Terico urea particle has a larger diameter than the prill Georgia urea particle, which causes that the packed Terico urea particle bed has a higher permeability but smaller external specific surface area than the Georgia urea particle bed. Internal pore structure inside each urea particles makes the moisture sorption process within urea particle piles, but to some extent lessens the dependence of urea particle or particle bed property on the moisture content. Because Terico urea particles have higher internal porosity and relatively higher ratio of internal surface area than Georgia urea particles, the effective thermal conductivity of Terico urea particle bed is much less sensitive to the moisture content of urea particle bed that that of Georgia urea particle bed. The caking strength of crystal bridges between urea particles is lessened because most adsorbed moisture has been penetrated into the internal pore and internal surface inside. Moisture sorption is not very sensitive to the fluid-solid convection coefficients in the interstitial air space.

(2) Both experimental data and analytical solution of outlet air temperature/humidity response after the urea particle beds subject to a temperature/humidity showed the dependence of time constants for both temperature and humidity step changes on Reynolds number, that is to say, time constants increases with the decrease in Reynolds number.

(3) A new theoretical method was developed to predict the outlet air temperature or outlet air relative humidity after urea particle beds when the urea particle bed was subject to a pure temperature step change or pure humidity step change at the inlet. The analytical solution of the model showed that the predicted time constant of outlet air temperature for pure temperature step change was a function of connective heat transfer coefficient and air velocity while the time constant of outlet air humidity for pure humidity step change was a function of

mass convection coefficient, air velocity, and internal sorption / desorption property of urea particles and the predicted outlet air temperature for pure humidity step change was determined by these two time constants due to heat release of moisture sorption.

(4) Both granular Terico urea particles and prill Georgia urea particles have the similar isothermal moisture sorption-desorption curve. At a constant temperature, isothermal moisture content of urea particles increases with an increase in relative humidity. The hysteresis of moisture content occurs during the first cyclic sorption-desorption process but greatly is alleviated or almost disappears during the second cyclic sorption-desorption process. The hysteresis of moisture sorption decreases with an increase in relative humidity. The second isothermal sorption/desorption followed the similar curve as the first isothermal desorption curve which implies that the internal pore and particle surface geometry change was a slow process due to the presence of moisture.

(5) Comparison of the simulation and the data of moisture uptake showed agreement implying (a) that the internal moisture diffusion that dominated the moisture uptake process was a very slow process and that the internal air-water vapour diffusion coefficient inside a particle is only 10^{-3}~10^{-4} of vapor-air molecular diffusivity in the air. (b) Internal moisture diffusion coefficient during moisture adsorption process varies with moisture content while internal moisture diffusion coefficient during desorption process is a constant.

6.3 Recommendations for future research

6.3.1 Suggestions

In this thesis, a comprehensive research study has been carried out experimentally, theoretically and numerically to investigate how moisture adsorption and desorption progresses within urea particles or particle beds and as well the determination of important properties for the theoretical and numerical models. During the research job, PCS urea fertilizer from three different manufacturing locations (Georgia, MYS and Trinidad) with high relative humidity and Terico urea from Calgary with low relative humidity were delivered to the lab and stored at room temperature. It was observed that Terico urea particles in sealed bags has low moisture content without caking, that Georgia urea particles in sealed bags has a little caking on the bottom, that Trinad and MYS urea particles in unsealed bags have serious

caking especially the bottom part due to the hydroscopic pressure. From the observation, suggestions for urea fertilizer storage and shipping can be proposed: a) To maintain high quality urea fertilizer, it is important to keep the moisture content of the finished urea products from manufactories below 0.25% w/w. During shipping and storage processes, use sealed water-proof shipping and storage bags to store urea particles and store these bags of urea particles in only dry and cool ambient air environments to avoid heat and moisture gains and subsequent caking. (2) To avoid the hydroscopic pressure on urea piles which will strengthen the caking between urea particles, bags of urea fertilizer should not be piled high.

6.3.2 Future work

Caking only occurs when moisture is present. This research is a good step for the further caking theory and prevention studies on urea fertilizer. More experimental and theoretical/numerical work could be done for the caking process within urea particles or particle beds in the future. Recommendations for future work are as follows:

(1) Include microscopic or X ray images of crystal growth on individual particles while they are exposed to specified humidity and temperature. Caking means the formation of crystal bridges in presence of moisture, which is a transient process. Microscopic images could offer visual evidence for crystal growth.

(2) Measure this crystal growth and change during cyclic step changes of humidity. As mentioned in chapter 4, experimental data showed that equilibrium moisture content of urea particles changed with respect to the relative humidity and temperature. It is expected that this would cause the crystal growth change for different environments.

(3) Measure the fracture cake strength of urea particle sample beds in the centrifuge testing device after these test beds have been subject to specified processes of temperature, humidity and external pressure. This has been done for potash fertilizer (Wang, et al., 2007; Gao, et al., 2009). Urea fertilizer is expected to be even more sensitive to these caking factors.

(4) Measure the water vapor permeability of typical plastic bags used for long term storage of urea if there are no data for this application. Measurement of the vapor permeability of the plastic bags will permit a calculation of moisture gain for the bags stored in a given environment.

(5) Measure the isothermal moisture content of urea particles at different relative humidities in winter conditions, for example, -40 ~ -20 ^{o}C.

REFERENCES

Abe, O O., Wang, Y.H., Simonson, C. J.; Besant, R.W., Shang, W., 2006. Transient Temperature Measurements and Characteristics for Temperature Sensors and Energy Wheels. *ASHRAE Transactions*, **112**(2), pp.76-89.

ASHRAE, 2004. *HVAC Systems and Equipment Handbook*, ASHRAE, Atlanta.

Arpaci, V.S., Larsen P.S., 1984. *Convection Heat Transfer*, Prentice-Hall, N.J.

ASME, 1990. ANSI/ASME PTC 19.1-1985 Part 1. Instruments and Apparatus—Measurement Uncertainty, ASME, New York, NY.

Baclic, B.S., Heggst, P.J., Abou, H.Z.Z., 1986. Differential Fluid Enthalpy Method for Predicting Heating Transfer Coefficients in Packed Beds. *Proceedings of the Eighth International Heat Transfer Conference*, **5**, pp.2617-2622.

Bejan, A., 2004. *Convection Heat Transfer*, Wiley, NewYork.

Bress, D. F. and Packbier, M. W., 1977. The Startup Of Two Major Urea Plants, *Chemical Engineering Progress*.

Brockel U., Kirsch R., Wahl M. and Feise H. J., 2008. Formation and Strength of Solid Bridges in Bulk Solids, *Particulate Science and Technology*, **26**(1), pp.23-32.

Bulck, E.V. and Klein, S.A., 1990. Single-Blow Test Procedure for Compact Heat and Mass Exchangers, *Journal of Heat Transfer, Transactions ASME*, **112**, pp.317-322.

Carman, P.C., 1938. Determination of the Specific Surface of Powders I. *Journal of the Society Chemical Industry*, **57**, pp.225-234.

Carman, P.C., 1939. Determination of the Specific Surface of Powders. II. *Journal of the Society Chemical Industry*, **58**, pp.1-7.

Chen, R.G., Chen, H., Besant, R.W., Evitts R.W, 2004. Properties Required to Determine Moisture Transport by Capillarity, Gravity, and Diffusion in Potash Beds, *Industrial and Engineering Chemistry Research*, **43**(17), pp.5363-5371.

Chen, H., Evitts, R.W., Besant, R.W., 2006. Moisture Adsorption Characteristics of a Thin Bed of Polycrystalline Potash Pellets Part I. Experimental Study, *Powder Technology*, **170**(3), pp.158-166.

Chen, H., Evitts, R.W., Besant, R.W., 2007. Moisture Adsorption Characteristics of a Thin Bed of Polycrystalline Potash Pellets Part II. Numerical Simulation, *Powder Technology*, **171**(1), pp.46-53.

Chen, R.G., 2004. Measurement and Numerical Simulation of Moisture Transport by Capillary, Gravity and Diffusion in Porous Potash Beds, *M.Sc Thesis*, University of Saskatchewan, Saskatoon, SK, Canada.

Dullien, F.A.L., 1992. *Porous Media Fluid Transport and Pore Structure*, 2nd edition, Academic Press, San Diego.

Elvers, B., Hawkin, S., 1996. Urea in, *Ullmann's Encyclopedia of Industrial Chemistry*,VCH, Weinheim, Germany.

Ergun, S., 1952. Fluid flow through Packed Columns, *Chemical Engineering Progress*, **48**, pp.89-94.

Fletcher, L. S., 1988. Recent Developments in Contact Conductance Heat Transfer, *Journal of Heat Transfer*.

Gao, S.Y., Evitts, R.W., Besant, R.W., 2009, Simulation of Potash Cake Strength by Discrete Element Method*, The 6th International Conference for Conveying and Handling of Particulate Solids (CHoPS)*, Brisbane, Australia, the 3rd - 7th August 2009.

Grathwohl, P., 1998. Diffusion in Natural Porous Media: Contaminant Transport, Sorption/Desorption and Dissolution Kinetics, Kluwer Academic Publishers, Boston.

Grdadolnik J., Marechal, Y., 2002. Urea and Urea-water Solutions – an Infrared Study, *Journal of Molecular Structure*, **615**(1-3), pp.177-189.

Gregg, Sing, 1982. *Adsorption, Surface Area, and Porosity* (2nd edition). Academic Press, London.

Incropera, F.P., DeWitt, D.P., Bergman, T.L., Lavine, A.S., 2002. *Fundamentals of Heat and Mass Transfer*, J.Wiley & Sons, New York, pp.347.

Ismail, J., Fairweather, M. and Javed K., 2002. Structural Properties of Beds Packed with Ternary Mixtures of Spherical ParticlesPart I–Global Properties, *Chemical Engineering Research and Design*, 80(6), pp.637-644.

Jeffrey, G.A., 1997. *An Introduction to Hydrogen Bonding (Topics in Physical Chemistry)*. Oxford University Press, New York.

Kapsalis J.G., 1986. Influences of Hysteresis and Temperature on Moisture Sorption Isotherms, *Water Activity: Theory and Applications to Food*, pp.173-214. Springer, New York.

Kar, K.K., and Dybbs, A., 1982. Internal Heat Transfer Coefficients of Porous Metals, *Heat Transfer in Porous Media, ASME*, **22**, pp.81-91.

Kaviany, M., 1995. *Principles of HeatTransfer in Porous Media*, 2nd ed. Springer, New York.

Kays, W.M., and London, A.L., 1984. *Compact Heat Exchangers*, McGraw-Hill, New York.

Keller, RA, 1967. *Basic Tables in Chemistry*, McGraw-Hill, New York.

Kumar, S., Upadhyay, S. N., and Mathur V. K., 1977. Low Reynolds Number Mass Transfer in Packed Beds of Cylindrical Particles, *Ind. Eng. Chem. Process Des. Dev.*, **16** (1), pp.1-8.

Koch, D.L. and Brady, J.F., 1985. Dispersion in Fixed Beds, *Journals of Mechanics*, **54**, pp.399-427.

Li, Y.B., Fan, J.T., 2007. Transient Analysis of Heat and Moisture Transfer with Sorption/Desorption and Phase Change in Fibrous Clothing Insulation, *Numerical Heat Transfer, Part A: Applications*, **51**(7), pp.635-655.

Lide, D.R., (Ed.), 2006. *CRC Handbook of Chemistry and Physics*, CRC Press, Boca Raton (FL), pp. 3–516.

Macdonald, I.F., EI-Sayed, M.S., Mow, K., and Dullien, F.A.L., 1979. Flow through Porous Media – the Ergun Equation Revised, *Industrial and Engineering Chemistry Fundamentals*, **18** (3), pp.199-208.

Madhusudana, C. V., Ling, F. F., 1995. *Thermal Contact Conductance*. Springer.

McKenzie, R., 1998. Crop Nutrition and Fertilizer Requirements, published to the web on January 1, 1998, http://www1.agric.gov.ab.ca/$department/deptdocs.nsf/all/agdex3791.

Meessen, J. H., 1996. Urea in, *Ullmann's Encyclopedia of Industrial Chemistry*, Wiley-VCH, Weinheim.

Nie, X.D., Besant, R.W., and Evitts, R.W., 2008(a). An Experimental Study of Moisture Uptake and Transport in a Bed of Urea Particles, *Granular Matter*, **10**(4), pp.301-308.

Nie, X.D., Evitts, R.W., and Besant, R.W., 2008(b). Simulation of Moisture Uptake and Transport in a Bed of Urea Particles, *Industrial and Engineering Chemistry Research*, **47**, pp.7888-7896.

Nie, X.D., Besant, R.W., Evitts, R.W., 2009(a). Convective Heat and Mass Transfer Coefficient Measurements and Correlations for Particle Beds Using Temperature and Humidity Step Changes with Air Flow through a Test Bed**,** *Chemical Engineering Science*, **64**, pp.3476- 3485.

Nie, X.D., Besant, R.W., Evitts, R.W., 2009(b). A New Technique to Determine Convection Coefficients with Flow through Particle Beds, submitted to *ASME, Heat Transfer Division*.

Nield D.A., and Bejan A., 1992. *Convection in Porous Media*. Springer-Verlag, New York.

Nsofor, E. C., and Adebiyi G. A., 2001. Measurements of the gas-particle convective heat transfer coefficient in a packed bed for high-temperature energy storage, *Experimental Thermal and Fluid Science*, **24**, pp.1-9.

Rumpf and Gupte, 1971. Einflüsse der Porosität und Korngrößenverteilung im Widerstandsgesetz der Porenströmung, *Chemie Ingenieur Technik*, 43(6), pp.367-375.
(related content was cited by Dullien (1992) in the book: *Porous Media Fluid Transport and Pore Structure*).

Patankar, S.V., 1980. *Numerical Heat Transfer and Fluid Flow*. McGraw-Hill: Toronto.

Peng Shi-Wen, Strathdee Graeme and Besant Robert W., 1999. Dissolution Reaction of Potash Fertilizer with Moisture, *The Canadian Journal of Chemical Engineering*, **77**, pp.1127-1134.

Peng Shi-Wen, Besant Robert W. and Strathdee Graeme, 2000. Heat and Mass Transfer in Granular Potash Fertilizer with a Surface Dissolution Reaction, *The Canadian Journal of Chemical Engineering*, **78**, pp.1076-1086.

Pesaran, A.A., Mills, A.F., 1987(a). Moisture Transport in Silica Gel Packed Beds - I. Theoretical Study, *International Journal of Heat and Mass Transfer*, **30**(6), pp.1037-1049.

Pesaran, A.A., Mills, A.F., 1987(b). Moisture Transport in Silica Gel Packed Beds – II. Experimental Study, *International Journal of Heat and Mass Transfer*, **30**(6), pp.1051-1060.

Petrescu, S., Petrescu, J., Lisa, C., 1997. Mass Transfer at Solid Dissolution, *Chemical Engineering Journal*, **66**(1), pp.57-63.

Rexwinkel, G., Heesink, A. B. M., and Swaaij, W. P. M. Van, 1997. Mass Transfer in Packed Beds at low Peclet Numbers - Wrong Experiments or Wrong Interpretations? *Chemical Engineering Science*, **52**, pp3995-4003.

Saffman, P.G., 1959. A Theory of Dispersion in Porous Medium, *Fluid Mechanics*, **6**, pp.321-349.

Saffman, P.G., 1960. On the Effect of Molecular Diffusivity in Turbulent Diffusion, *Fluid Mechanics*, **8**, pp.273-283.

Sanderson, R. T., 1983. Electronegativity and bond energy, *Journal of the American Chemical Society,* **105**(8), pp.2259-2262.

Shah, R.K., and London A.L., 1978. Laminar Flow Forced Convection in Ducts*, Supplement 1 to Advances in Heat Transfer*, Academic Press, NewYork.

Shang, W., Besant, R.W., 2008. Theoretical and Experimental Methods for the Sensible Effectiveness of Air-to-Air Energy Recovery Wheels, *International Journal* of *HVAC & R Research*, **14**, pp.373-396.

Shang, W., Besant, R.W., 2009(a). Effectiveness of Desiccant Coated Regenerative Wheels from Transient Response Characteristics and Flow Channel Properties Part I. Development of Effectiveness Equations from Transient Response Characteristics, *International Journal of HVAC & R Research*, **15**(2), pp.329-345.

Shang, W., Besant, R.W., 2009(b). Effectiveness of Desiccant Coated Regenerative Wheels from Transient Response Characteristics and Flow Channel Properties Part II: Predicting and Comparing the Latent Effectiveness of Dehumidifier and Energy Wheels Using Transient Data and Properties, *International Journal of HVAC & R Research*, **15**(2), pp.346-365.

Sun, J., Besant, R.W., 2005. Heat and Mass Transfer during Silica Gel – Moisture Interactions, *International Journal of Heat and Mass Transfer*, **48**(23-24), pp.4953-4962.

Tanaka, H., Touhara, H., Nakanishi, K. and Watanabe, N., 1984. Computer experiment on aqueous solution. IV. Molecular dynamics calculation on the hydration of urea in an infinitely dilute aqueous solution with a new urea-water pair potential, J. Chem. Phys., **80**(10), pp.5170-5186.

Thompson, D.C., 1972. Fertilizer Caking and Its Prevention, *Proceedings of Fertilizer Society*, **125**, London, UK.

Travkin, V.S., and Catton, I., 2001.Transport Phenomena in Heterogeneous Media Based on Volume Averaging Theory, *Advances in Heat Transfer*, **34**, pp.1-144.

Wahl, M., Kirsch, R., Brockel, U., Trapp, S., Bottlinger, M., 2006. Caking of Urea Prills, *Chem. Eng. Technol*.(in Germany), **29** (6), pp.674-678.
(DOI: 10.1080/02726350701759084, 2008. *Particulate Science and Technology* (English version), **26**, pp.23-32.)

Wakao, N., Funazkri, T., 1978. Effect of Fluid Dispersion Coefficients on Particle-fluid Mass Transfer Coefficients in Packed Beds, *Chemical Engineering Science*, **33**, pp.1375-1384.

Wakao, N., Funazkri, S., 1978. Effective Diffusion Coefficients for Fluid Species Reacting with First Order Kinetics in Packed Bed Reactors and Discussion on Evaluation of Catalyst Effectiveness Factors, *Chemical Engineering Science*, **33**, pp.183-187.

Wakao, N., Kaguei, S., Funazkri, T., 1979. Effect of Fluid Dispersion Coefficients on Particle-to-fluid heat Transfer Coefficients in Packed Beds – Correlation of Nusselt numbers. *Chemical Engineering Science*, **34**(3), pp.325-336.

Wakao, N., Kaguei, S., 1982. *Heat and Mass Transfer in Packed Beds*, Gordon and Breach Science, New York.

Wang, Y., Besant, R. W., Evitts, R.W., Dolovich, A.T., 2007. Measurement of Cake Strength in Potash Using a Centrifuge, *Particle and Particle Systems Characterization*, **23**(5), pp.399-407.

Wang, Y., Evitts, R.W.; Besant, R.W., 2008(a). Modelling Crystal Growth between Potash Particles near Contact Points during Drying Processes. Part I: Problem formulation, *Canadian Journal of Chemical Engineering*, **86**(2), pp.192-198.

Wang, Y., Evitts, R.W.; Besant, R.W., 2008(b). Modelling Crystal Growth between Potash Particles near Contact Points during Drying Processes. Part II: Analysis, results, and comparison with experimental data, *Canadian Journal of Chemical Engineering*, **86**(2), pp.199-206.

Wang, Y.H., Simonson, C.J., Besant, R.W., Shang, W., 2005. Transient Humidity Measurements for Flow through an Energy Wheel, *ASHRAE Transactions,* **111**(2), pp.353-369.

Wang, Y.H., Simonson, C. J., Besant, R.W., Shang, W., 2007(a). Transient Humidity Measurements - Part I: Sensor Calibration and Characteristics, *IEEE Transactions on Instrumentation and Measurement*, **56**(2), pp.1074-1079.

Wang, Y.H., Simonson, C. J., Besant, R.W., Shang, W., 2007(b). Transient Humidity Measurements - Part II: Determination of the Characteristics of an Interactive Device, *IEEE Transactions on Instrumentation and Measurement*, **56**(2), pp.1080-1086.

Weast, R.C., (Ed.), 1977. *CRC Handbook of Chemistry and Physics*, CRC Press, Boca Raton (FL), pp.5–27.

Webb, P.A., Orr, C., 1977. *Analytical Methods in Fine Particle Technology*, 2nd ed. Micromeritics Instruments Corporation, Norcross, MA, USA.

Whitaker, S. 1969. Advances in Theory of Fluid Motion in Porous Media. *Industrial and Engineering Chemistry*, **61**(12), pp.14-28.

Whitaker, S., 1988. Diffusion in packed beds of porous particles, *AIChE Journal* (Chemical Engineering Research and Development), **34**(4), pp.679-687.

Worsham, J. E. , Levy, H.A. AND Peterson S.W., 1957. The Positions of Hydro~,en Atoms in Urea by Neutron Diffraction, Acta Cryst. **10**, pp.319-323.

Zhou, Q, 2000. Measurement and Simulation of Transient Moisture and Heat Diffusion in a Potash Layer, *M.Sc Thesis*, University of Saskatchewan, Saskatoon, SK, Canada.

Zili, L.; Nasrallah, S. B., 1999. Heat and Mass Transfer During Drying in Cylindrical Packed Beds, *Numerical Heat Transfer, Part A: Applications*, 3**6**(2), pp.201-228.

APPENDIX A

MEASUREMENT OF MOISTURE CONTENT AND DETERMINATION OF ITS UNCERTAINTY

Accurate measurement of moisture content is important for the research of investigating how moisture transports within the urea particle storage bulk. Among many instruments and methodologies which have been developed to provide accurate measurement of moisture content, two methods are applied in our research: one is the gravimetric method; the other is the Karl Fischer (KF) titrator.

A.1 Gravimetric method and its measurement uncertainty

The gravimetric method simply depends on measuring a sample weight before and after it is dried. It uses the weight difference to calculate the moisture content of the sample. Many methods of drying, such as oven drying, air drying, vacuum drying and etc., can be used in conjunction with gravimetric methods. These drying methods rely on procedures that are time intensive. In addition, urea will decompose and loss the mass at 70 ^{o}C and above. To avoid these problems, a formula has been derived which allows the determination of moisture content in a more flexible way, whereby the only input needed is the initial moisture content in addition to the sample weight. Before each experiment, dry urea particle sample are prepared by oven drying at 70 ^{o}C for 24 hours, bagged in double sealed bags and cooled down to room temperature for 12 hours. Dried and cooled urea particles packed in the empty cell are used as the base weight of sample. The initial moisture content of the dry urea samples are determined by the KF titrator. The extra moisture content of urea particles by gravimetric method is determined by using the weight difference shown in equation (A-1).

$$X_G = \frac{M_{ec,ws} - M_{ec,ds}}{M_{ec,ds} - M_{ec}} \tag{A-1}$$

where M_{ec} is the weight of the empty cell; $M_{ec,ds}$ is the weight of the cell filled with dry urea particles; $M_{ec,ws}$ is the weight of the cell filled with urea particles adsorbed some moisture; X_G is the moisture content with the gravimetric method.

In terms of the propagation of uncertainty by a function, the uncertainty of moisture content with the gravimetric method can be calculated as

$$\left[\frac{U(X_G)}{X_G}\right]^2 = \left[\frac{U(M_{ec,ws} - M_{ec,ds})}{M_{ec,ws} - M_{ec,ds}}\right]^2 + \left[\frac{U(M_{ec,ds} - M_{ec})}{M_{ec,ds} - M_{ec}}\right]^2 \quad \text{(A-2)}$$

For an electronic balance, uncertainty of mass measurement is known as $U(M)$, then equation (A-2) can be rewritten as

$$[U(X_G)]^2 = 2[U(M)]^2 X_G^2 \left[\frac{1}{(M_{ec,ws} - M_{ec,ds})^2} + \frac{1}{(M_{ec,ds} - M_{ec})^2}\right] \quad \text{(A-3)}$$

Substituting equation (A-1) into (A-3), one gets

$$U(X_G) = \frac{\sqrt{2(1 + X_G^2)}}{(M_{ec,ds} - M_{ec})} U(M) \quad \text{(A-4)}$$

In case that $X_G << 1$, $U(X_G) \approx 1.414 \frac{U(M)}{(M_{ec,ds} - M_{ec})}$.

A.2 Introduction to potentiometric measurement

The KF titrator is a type of automatic potentiometric titrator for water determination. The well known KF equation for alcoholic based reagent is presented as follows:

$$ROH + SO_2 + R'N \leftrightarrow [R'NH]SO_3R \quad \text{(A-5)}$$

$$H_2O + I_2 + [R'NH]SO_3R + 2R'N \rightarrow [R'NH]SO_4R + 2[R'NH]I \quad \text{(A-6)}$$

where ROH is a reactive alcohol and $R^{'}N$ is a suitable base. With the mole ratio of the chemical reaction between water and the reagent (titrant) Iodine, and the calibrated titrant concentration, water mass can be determined by accurately measuring the reagent volume consumed for the reaction with water.

Drops of the reagent (including Iodine) are added continuously into the solution to react with the water in the solution which produces I^{-1} ions till all the water is used up and then no more I^{-1} is produced. The end point of the reaction between water and Iodine can be predicted by the potentiometric equipment which includes a reference electrode, an indicator electrode, and a potential measuring device. With the potentiometric method, the ion concentrations are directly obtained from the potential of an ion selective electrode measured with respect to a reference electrode. There are two ways to determine the end point – one uses preset endpoint and the other uses first derivative. Preset endpoint method assumes that the endpoint occurs at the predetermined potential (mV). Aliquots of the titrant are added until a predetermined potential (mV) is reached as shown in Figure A.1, This technique is useful for analysis without a clearly defined endpoint with industry standards, but it requires the sample and its reaction with the titrant to be well known. The first derivative technique assumes that the endpoint occurs at the greatest change in mV reading per volume of titrant added. Each time aliquots of a titrant are added to the sample, the potential changes are recorded and first derivative analysis is applied to the data such that the endpoint is determined based on the greatest potential change.

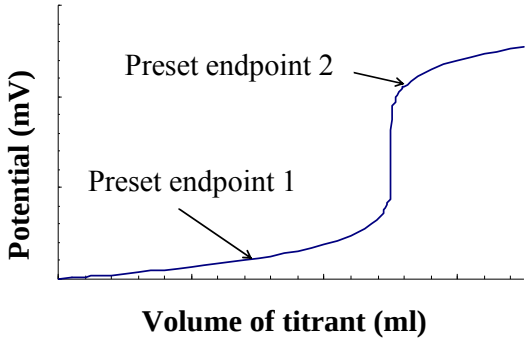

Figure A.1 Schematic diagram of the preset endpoint method

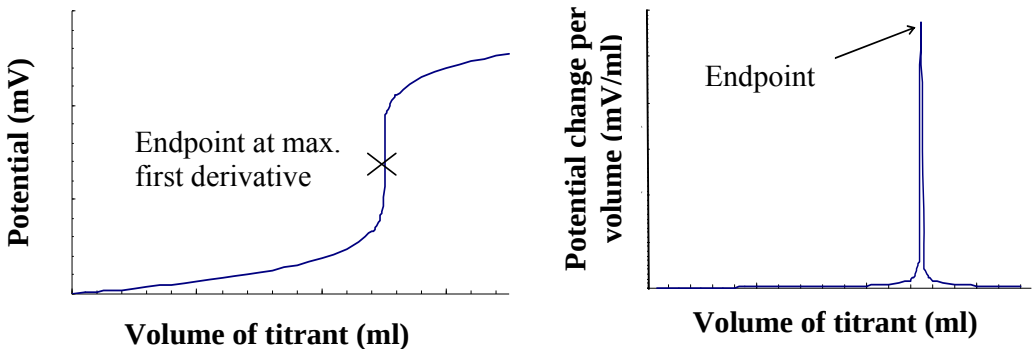

Figure A.2 Schematic diagram of the first derivative method

A.3 Karl Fischer titrator

The ATI ORION 950 Ross FASTQC Titrator, shown in Figure A.3, includes: (1) reagent and dispenser, (2) work solution and the stirrer, (3) electrodes, (4) the control panel for setting-up, data analysis, potential measurement, results output, and (5) a printer.

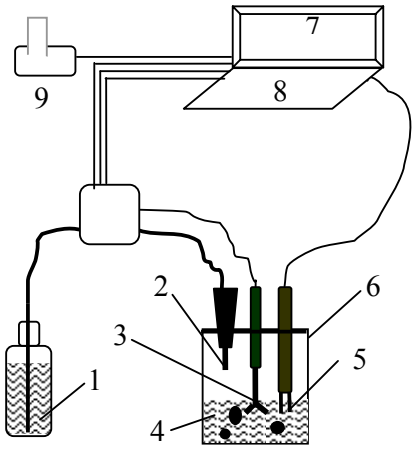

Legend:

1 – Reagent; 3 – Stirrer; 5 – Electrodes; 7 – Display screen; 9 – Printer;

2 – Dispenser; 4 – Solvent; 6 – Sealed vessel; 8 – Control panel;

Figure A.3 Schematic diagram of the Karl Fischer titrator

A.3.1 Reagent (titrant) and dispenser

One-component reagent contains all the substances necessary for KF reaction. Two types of the KF Reagent for moisture determination are shown in Table A.1. The reagent can be automatically dispensed into the sealed vessel for reaction with water in the solvent drop by drop in terms of the preset increment of titrant. This automatic potentiometric titrator cannot give results more accurate than those that could be obtained by manual but very careful potentiometric techniques. However automatic titrators decrease the operator time needed to do titrations, and as well make possible the use of much smaller samples because automatic flow control equipment can introduce the titrant in smaller increments.

Table A.1 Two types of KF reagents for moisture determination

Type	Comp 5	Comp 1
Main composition	Pyridine free	2-Methoxyethoxyethanol free
	2-Methoxyethoxyethanol	2-(2-methoxyethoxy) ethanol
	Imidazole	Imidazole
	Iodine (I_2)	Iodine (I_2)
	Sulfur dioxide (SO_2)	Sulfur dioxide (SO_2)

A.3.2 Working solution (solvent) and stirrer

Methanol (CH_3OH) is commonly used as the standard solvent due to the following reasons. The stoichiometric KF reaction can take place effectively in Methanol. And Methanol dissolves most components and reaction products of the KF reaction so that precipitation does not occur which might otherwise coat the electrodes and interfere with the indication system. And most soluble solid chemicals, such as urea, can dissolve in Methanol. To accelerate the dissolving process of sample especially for solid particles, the stirrer is used to shorten the total titration time and therefore reduce the source error from atmospheric moisture. The relatively good conductivity of a methanol electrolytic solution enables both a sensitive as well as reproducible end-point indication.

In some cases it is advisable to replace methanol by other solvent for its solubility of long-

chain hydro-carbon is as equally unsatisfactory as are some side reactions which take place with certain amines, mineral acids and ketenes. Then other solvents are therefore used in certain circumstance instead of methanol or preferably as mixtures with methanol. For example, a mixture of chloroform is better for fats, while propanol should be used as for aromatics.

For sodium chloride, ammonium chloride, potassium chloride and other alkaline halides crystallize, which has no water of hydration but usually contain included moisture, a mixture of methanol and formamide is suggested as it can improve the solubility of the salts. However, sometimes only the adherent moisture of salt, instead of total water, is to be determined. In this case methanol/choro-form is preferred as the working solution to prevent salt from dissolving.

A.3.3 Others

The electrode bar including a reference electrode and an indicator electrode is connected to the control panel where the relative potential of indicator electrode in terms of the reference one can be measured and displayed. The control panel provides the incorporated software which helps initialize the titration method, for example, mole weight of the determinant, mole ratio of the reaction between titrant and determinant, concentration of titrant, increment of titrant, potentials of preset endpoint, etc.

A.4 Procedures of water determination for samples

Besides the reagent, solvent and the sample, some auxiliary instruments and elements are necessary for water determination: electronic balance, weighing paper, a series of syringes, distilled water, acetone, alcohol, etc.

Before determining the moisture content of samples by titration, pre-titration to blank and standardize the system are routine but important tasks.

A.4.1 Pre-titration to blank the system

Pre-titration with KF reagent is a necessary routine task before experiments take place, and these are done once per day at the start of the experiments. Pre-titration is crucially important

because the methanol is never absolutely moisture-free as it is very hydroscopic. In addition water vapor can penetrate into the titration vessel directly from the surrounding air because the system cannot be isolated totally. After a long idle time, accumulated moisture should be taken into account. In order to eliminate these sources of error, pre-titration prior to the investigation of the sample is performed using a blank sample.

A.4.2 Standardization of the system

Although the titre of the KF reagent is defined by manufacturer (WE=5 mg/ml), determination of the titrant concentration and its correction becomes another important routine task because the following reasons: (1) The titrant concentration itself changes because the system cannot be completely separated from the atmosphere; (2) The atmospheric humidity ranges from 25% to 75%; (3) Self-decomposition of Methanol happens.

Determining the titrant concentration using distilled water is the simplest and most effective way. Before standardization, a pre-titrant concentration is set in the analysis method. Suppose the standardization result with distilled water is 1.08 g/g while as we all know moisture content of distilled water should be 1 g/g. In this case, there are two ways to correct it: 1) One is to rewrite the method, correct the titrant concentration (new concentration = old concentration/1.08) to keep the moisture content of water always at 1 g/g, then the result from the KF titrator does not need any correction. 2) The other is to keep the old titrant concentration, but use 1.08 as the correction coefficient, C, to correct results from the KF titrator, i.e. $X_{KF}^{c} = \frac{X_{KF}}{C} = \frac{X_{KF}}{1.08}$ where X_{KF} is the direct result of moisture content by the KF titrator (g/g), C is the correction coefficient determined by the procedure of system standardization, X_{KF}^{c} is the corrected moisture content by the KF titrator after correction of titrant concentration.

The determination of the titrant concentration, i.e. titration of distilled water, should always be carried out under the same conditions as the intended water determination. The same titration method and the same procedures should be used. The type of the solvent and the volumes involved should be approximately the same. The amount of water used for standardization should be of the same order of magnitude as the amount of water anticipated to be determined.

A.4.3 Working procedures for Titration

Followed are the detailed steps how to investigate the MC of samples which maybe solid or liquid, even distilled water.

A.4.3.1 Pre-titration to dehydrate the system

(1) If it is a continued experiment, proceed to step 2 immediately. Add methanol solvent into the sealed vessel.

(2) Press TITRATE SAMPLE to blank the system. Usually choose either of methods, and just set sample weight as 1.000 g.

A.4.3.2 Standardization of the system

(3) Put the syringe full of water on the balance and set it to zero.

(4) Input several drops of distilled water into the sample testing vessel.

(5) Reweigh the syringe full of water and write down the weight of the distilled water dropped into the sample testing vessel.

(6) Press the key TITRATE SAMPLE to start titrate. Choose a suitable method and enter the known sample weight in step 5.

(7) Get the result of moisture content for distilled water.

(8) Get the correction coefficient, *C*, from the result in step 7.

A.4.3.3 Sample titration

(9) Take some urea particle sample out in the sealed Sampling Device (see Chapter 4).

(10) Put the Sampling Device filled with sample on the electron balance and set the balance to zero.

(11) Pour sample into the vessel.

(12) Reweigh the Sampling Device with the remaining sample and record the net weight of sample which has been poured into the vessel in step 11.

(13) Press STIR and choose suitable stirring speed to accelerate the dissolution as well as moisture extraction from the surface and inside of the urea particles.

(14) When the sample has dissolved almost completely, press TITRATE SAMPLE to start titrate. Choose suitable method and enter the known sample weight in step 12.

(15) Get the result of moisture content for sample, X_{KF} .

(16) Divide the result of moisture content, X_{KF}, by the correction coefficient, C, in step 8, and then get the corrected results, X_{KF}^{c} .

(17) If next sample is ready, repeat step 1-16 while standardization can be exempted. If it is successive titration, just repeat step 9-16.

A.4.4 Successive titration

Successive titrations are a variation of the KF titration. After titrating the first sample, the next sample is immediately added to the same solution. Then the titrated solution acts as the dehydrated working medium for the next determination. The amount of work involved is thus reduced, as the otherwise necessary pre-titration is no longer required. KF reaction is also accelerated due to the accumulation of sulphur dioxide and amine.

However the “successive titration” is largely restricted to alcohol samples because otherwise the proceeding addition of samples would reduce the alcohol concentration to a level which would alter the stoichiometry. Generally the alcohol content in the titration vessel should not fall below 50%. The limit depends on the alcohol used. For methanol, a content of 30% will suffice.

The water content of the sample is calculated from the amount of KF reagent consumed and the titrant concentration entered, and corrected by the correction coefficient from the system standardization.

A.5 Uncertainty of moisture content determination by the KF titrator

The KF titrator outputs the result of moisture content directly using the following equation (A-7) & (A-8). Figure A.4 shows the schematics how to calculate the reagent concentration correction, *C*, with results by the KF titrator.

$$X_{KF} = \frac{M_{w,KF}}{M_{ws}} \tag{A-7}$$

$$X_{KF}^{c} = \frac{X_{KF}}{C} \tag{A-8}$$

where X_{KF} is Direct result of MC by the KF titrator (g/g); $M_{w,KF}$ is moisture mass determined by KF titrator (g); M_{ws} is mass of sample measured by electron balance (g); C is correction coefficient determined by system standardization; X_{KF}^{c} is MC by the KF titrator after correction of titrant concentration (g/g).

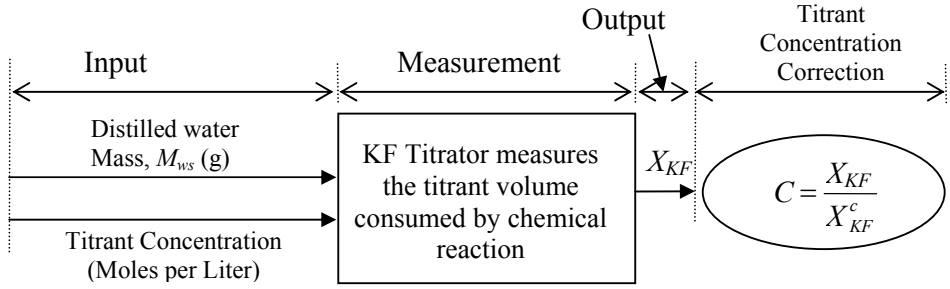

Figure A.4 Getting correction coefficient of titrant concentration, *C*

In fact, the moisture content is defined as the ratio of moisture mass to the dry sample mass.

$$X = \frac{M_w}{M_{ds}} = \frac{M_w}{M_{ws} - M_w} \tag{A-9}$$

where X is true moisture content (g/g); M_w is moisture mass (g); M_s is mass of sample (g); M_{ds} is mass of dry sample (g). Therefore, for the special case of water determination by the KF titrator, the final moisture content needs the second correction as shown in equation (A-10) to correct for moisture content of the mass M_s in equation (A-9).

$$X_{KF}^{cc} = \frac{M_{w,KF}^{c}}{M_{ws} - M_{w,KF}^{c}} = \frac{X_{KF}^{c}}{1 - X_{KF}^{c}} \tag{A-10}$$

For sample with low moisture content $X_{KF}^{c} << 1$, $X_{KF}^{cc} \approx X_{KF}^{c}$, the second correction can be ignored. Figure A.5 shows the schematics how to calculate actual moisture content, X_{KF}^{cc}, with the direct result, X_{KF}, provided by the KF titrator.

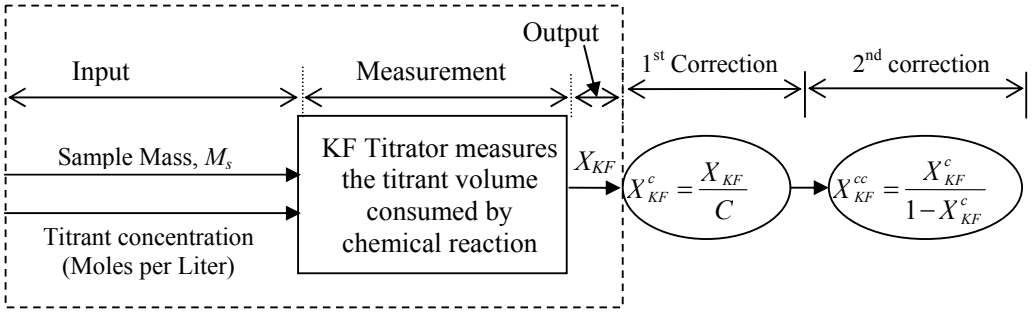

Figure A.5 Procedure of sample MC measurement by the KF titrator

A.5.1 Calibration of the KF titrator using the distilled water

Distilled water is usually used as a standard source to calibrate and establish the uncertainty of the KF titrator. Many experiments using a range of masses of distilled water are used to determine titrator's accuracy.

A.5.1.1 Data and calculations

Table A.2 presents the recorded data (moisture content X_{KF} from the KF titrator and consumed titrant volume), correction coefficient C, corrected KF moisture content X_{KF}^{c} and its deviation from the standard value, ΔX.

Table A.2 Calibration of Karl Fischer titrator

NO.	distilled water mass (g)	X_{KF} (g/g)	Consumed titrant (ml)	$X_{KF}^{c} = \frac{X_{KF}}{C}$ (g/g)	MC Error, $\Delta X = X_{KF}^{c} - 1$
	Group 1: correction coefficient, C =1.147				
---	0.0098	1.147	2.091	---	---
1	0.0048	1.1180	0.998	0.9747	-0.0253
2	0.0047	1.1740	1.026	1.0235	0.0235
3	0.0044	1.0940	0.895	0.9538	-0.0462
4	0.0035	1.0720	0.698	0.9346	-0.0654
5	0.0045	1.1870	0.993	1.0349	0.0349
6	0.0047	1.0960	0.999	0.9555	-0.0445
7	0.0032	1.1700	0.696	1.0201	0.0201
8	0.0245	1.1160	5.087	0.9730	-0.0270
9	0.0033	0.9665	0.593	0.8426	-0.1574
10	0.0055	1.1390	1.166	0.9930	-0.0070
11	0.0052	1.0620	1.028	0.9259	-0.0741
12	0.0094	1.0850	1.897	0.9459	-0.0541
13	0.0047	1.1400	0.996	0.9939	-0.0061
14	0.0034	1.1060	0.996	0.9643	-0.0357
15	0.0233	1.1040	4.788	0.9625	-0.0375
16	0.0299	1.0810	6.016	0.9425	-0.0575
	group 2: correction coefficient =1.123				
---	0.0110	112.3	2.299	---	---
17	0.0087	1.1700	1.894	1.0419	0.0419
18	0.0036	1.1750	0.787	1.0463	0.0463
19	0.0042	1.1450	0.895	1.0196	0.0196
20	0.0080	1.2000	1.786	1.0686	0.0686
21	0.0114	1.1240	2.384	1.0009	0.0009
22	0.0117	1.0960	2.387	0.9760	-0.0240
23	0.0158	1.1180	3.287	0.9955	-0.0045

24	0.0217	1.1110	4.485	0.9893	-0.0107
25	0.0098	1.1210	2.065	0.9982	-0.0018
26	0.0111	1.0130	2.092	0.9020	-0.0980
27	0.0216	1.1230	4.492	1.0000	0
28	0.0108	1.1320	2.275	1.0080	0.0080
	group 3: correction coefficient =1.114				
---	0.0338	111.4	7.009	---	---
29	0.0135	1.0700	2.688	0.9605	-0.0395
30	0.0204	1.1040	4.190	0.9910	-0.0090
31	0.0168	1.1460	3.582	1.0287	0.0287
32	0.0115	1.1160	2.388	1.0018	0.0018
33	0.0112	1.0660	2.222	0.9569	-0.0431
34	0.0256	1.0680	5.088	0.9587	-0.0413
35	0.0125	1.1540	2.685	1.0359	0.0359
36	0.0103	1.0880	2.085	0.9767	-0.0233
37	0.0106	1.0580	2.087	0.9497	-0.0503
38	0.0106	1.1820	2.332	1.0610	0.0610
39	0.0383	1.0940	7.797	0.9820	-0.0180
40	0.0150	1.1770	3.285	1.0566	0.0566
41	0.0182	1.0610	3.594	0.9524	-0.0476
42	0.0153	1.1710	3.334	1.0512	0.0512
43	0.0139	1.0390	3.334	0.9327	-0.0673
44	0.0168	1.1470	3.587	1.0296	0.0296
	group 4: correction coefficient =1.074				
---	0.0255	107.4	missed	---	---
45	0.0203	1.1080	4.186	1.0317	0.0317
46	0.0243	1.0580	4.785	0.9851	-0.0149
47	0.0142	1.0190	2.692	0.9488	-0.0512
48	0.0129	1.1190	2.687	1.0419	0.0419
49	0.0224	1.0710	4.464	0.9972	-0.0028
50	0.0168	1.0510	3.286	0.9786	-0.0214

51	0.0169	1.0450	3.288	0.9730	-0.0270
52	0.0137	1.0550	2.689	0.9823	-0.0177
53	0.0151	1.0630	2.988	0.9898	-0.0102
54	0.0167	1.0580	3.288	0.9851	-0.0149
55	0.0150	1.0680	2.982	0.9944	-0.0056

A.5.1.2 Data analysis

Sample mean moisture content $\overline{X}$, standard deviation S_X, standard deviation of the mean $S_{\overline{X}}$ are calculated as followed with 55 sample tests (N = 55, Degrees of freedom, v = 54).

Sample mean value

$$\overline{X} = \frac{\sum_{i=1}^{55} X_i}{N} = 0.9876 \tag{A-11}$$

where X_i means $X_{KF,i}^{c}$ for convenience.

The sample standard deviation of the 55 readings is given by,

$$S = \left[\frac{\sum (X_i - \overline{X})^2}{\nu} \right]^{1/2} = 0.0425 \tag{A-12}$$

The standard deviation of the sample mean is,

$$S_{\overline{X}} = \left(\frac{S^2}{N} \right)^{1/2} = 0.0057; \tag{A-13}$$

For 55 samples that follow a normal distribution, the interval $\overline{X} + t \cdot S_{\overline{X}}$ will include about 95% of the total scatter of the measurement for the mean value. Student t=2 for 54 degrees of freedom for 55 samples.

Then the precision error P for the mean value is

$$P\left(\overline{X}\right) = t \cdot S_{\overline{X}} = 0.0114 \quad \text{(A-14)}$$

The bias error is

$$B\left(\overline{X}\right) = -0.0124 \quad \text{(A-15)}$$

The total uncertainty of the mean value of moisture content at 95% confidence level is

$$U\left(\overline{X}\right) = \left[B(\overline{X})^2 + P(\overline{X})^2\right]^{1/2} = 0.017 \quad \text{(A-16)}$$

However, for only one MC measurement of the distilled water, the precision error is calculated as

$$P(X) = t \cdot S_X = 2 \times 0.0425 = 0.085 \quad \text{(A-17)}$$

The bias error is given by

$$B(X) = -0.0124 \quad \text{(A-18)}$$

The total uncertainty of the moisture content at 95% confidence level for one measurement of distilled water is

$$U(X) = \left[B(X)^2 + P(X)^2\right]^{1/2} = 0.086 \quad \text{(A-19)}$$

The relative uncertainty is $\frac{U(X)}{X} = 8.6\%$.

A.5.2 Uncertainty of water mass for one measurement, $U\left(M_{w,KF}^{c}\right)$

The calculated uncertainty of one MC measurement was 0.086 g/g for the mass of distilled water lying between 0.0030 g and 0.04g at X=1 g/g when no urea is present. This does not mean that it can be used as the uncertainty of MC measurement for urea particles with any moisture content.

The KF titrator measures the absolute moisture mass $M_{w,KF}$ by directly measuring the titrant volume consumed in the chemical reaction, and then gives X_{KF}^{c} by dividing moisture mass

$M_{w.KF}$ by the sample mass M_s after the first correction of titrant concentration C. For the distilled water, its moisture content is simply defined as

$$X = \frac{M^c_{w,KF}}{M_s} \tag{A-20}$$

Where X is moisture content of distilled water and X=1 g/g, $U(X) = 0.086$ g/g; $M^c_{w,KF}$ is moisture mass measured by KF titrator (g); M_s is mass of distilled water measured by electron balance around 0.0030~0.04g and the uncertainty of the mass measurement are $U(M_s) = 0.0001$ g.

Followed is the theoretical calculation of uncertainty with a Gaussian distribution.

Equation (A-20) can also be written as $M^c_{w,KF} = X \cdot M_s$, which allows to write

$$U\left(M^c_{w,KF}\right) = \left[[X \cdot U(M_{ds})]^2 + [M_s \cdot U(X)]^2\right]^{1/2} \tag{A-21}$$

$$U\left(M^c_{w,KF}\right) = \left[(1 \times 0.0001)^2 + (M_s \times 0.086)^2\right]^{1/2} \tag{A-22}$$

$$U\left(M^c_{w,KF}\right) \approx 0.0003 \sim 0.0035 g \tag{A-23}$$

To be careful, the upper limit is taken as the uncertainty of water mass measured by the KF titrator $U\left(M^c_{w,KF}\right)$= 0.0035 g.

From the analysis mentioned above, it is seen that the calibration of the KF titrator using distilled water tells not the uncertainty of the MC of samples, but the uncertainty of water mass measurement.

A.5.3 Uncertainty of MC measurement for sample particles, $U\left(X^c_{KF}\right)$

Based on the uncertainty analysis of water measurement by the KF titrator, the uncertainty of MC measurement for particle samples can be derived as followed. With equation (A-7) and (A-8), one gets that

$$X_{KF}^{c} = \frac{M_{w,KF}^{c}}{M_s} \tag{A-24}$$

Where X_{KF}^{c} is moisture content of samples measured by the Karl Fischer titrator (g/g); $M_{w,KF}^{c}$ is moisture mass determined by KF titrator (g), $U(M_{w,KF}^{c}) = 0.0035$ g; M_s is mass of sample measured by electron balance (g), $U(M_s) = 0.0001$ g.

Therefore,

$$\left[\frac{U(X_{KF}^{c})}{X_{KF}^{c}}\right]^2 = \left[\frac{U(M_{w,KF}^{c})}{M_{w,KF}^{c}}\right]^2 + \left[\frac{U(M_s)}{M_s}\right]^2 \tag{A-25}$$

$$\left[U\left(X_{KF}^{c}\right)\right]^2 = (X_{KF}^{c})^2 \left\{\left[\frac{U(M_{w,KF}^{c})}{M_{w,KF}^{c}}\right]^2 + \left[\frac{U(M_s)}{M_s}\right]^2\right\} \tag{A-26}$$

$$U\left(X_{KF}^{c}\right) = \frac{1}{M_s} \cdot \left\{\left[U(M_{w,KF}^{c})\right]^2 + \left[X_{KF}^{c} \cdot U(M_s)\right]^2\right\}^{1/2} \tag{A-27}$$

$$U\left(X_{KF}^{c}\right) = \frac{1}{M_s} \cdot \left\{0.0035^2 + (X_{KF}^{c} \times 0.0001)^2\right\}^{1/2} \tag{A-28}$$

Besides, from equation (A-10), one gets that

$$U\left(X_{KF}^{cc}\right) = \frac{U\left(X_{KF}^{c}\right)}{\left(1 - X_{KF}^{c}\right)} \tag{A-29}$$

For the urea particle sample with mass M_b (>2 g) and MC (X_{KF}^{c}) of 0.0005~0.01 g/g,

$$U\left(X_{KF}^{cc}\right) \cong U\left(X_{KF}^{c}\right) = \frac{U(M_{w,KF}^{c})}{M_s} = \frac{0.0035}{M_s} \text{ g/g} \tag{A-31}$$

As well, in equation (A-26), $\frac{U(M_s)}{M_s} << \frac{U(M_{w,KF}^{c})}{M_{w,KF}^{c}}$, that is to say, the contribution of uncertainty in sample mass to uncertainty in MC measurement can be negligible. Table A.3 shows the MC measurement uncertainty of the solid particle sample which is dominated by

the uncertainty of the water mass measured by the KF titrator. Increase in the sample mass helps to reduce the uncertainty of MC measurement for solid particles.

Table A.3 Uncertainty of MC determination for solid sample by KF titrator

Mass of sample, M_s (g)	2	3	4	5
Uncertainty of MC, X_{KF}^{c} (g/g)	0.00175	0.00117	0.00088	0.00070

APPENDIX B

MEASUREMENT AND UNCERTAINTY DETERMINATION OF PHYSICAL PROPERTIES –PERMEABILITY, EXTERNAL POROSITY, EXTERNAL SPECIFIC SURFACE AREA

B.1 Permeability measurement and its uncertainty

B.1.1 Principle of permeability (K) measurement

Permeability, K, is a measure of flow conductance of a porous medium, which appears as a constant proportionality in Darcy momentum equation.

$$u_D = \frac{K}{\mu} \cdot \frac{\Delta P}{L} \tag{B-1}$$

where u_D is Darcy velocity (m/s), $u_D = \frac{\dot{Q}_a}{A} = \frac{4\dot{Q}_a}{\pi \cdot D_c^{\,2}}$; $\dot{Q}_a$ is volume flow rate of air (m^3/s); A is cross-section area of the test container (m^2), $A = \frac{\pi \cdot D_c^{\,2}}{4}$; D_c is internal diameter of the test container (m); K is permeability (m^2); μ is dynamic viscosity of air (Pa·s), $\mu = \rho_a \cdot \nu$; ρ_a is density of air (kg/m^3); ν is kinematic viscosity of air (m^2/s); L is height of urea layer above the screen (m); ΔP is pressure difference across urea layers (Pa), $\Delta P = \rho_m \cdot g \cdot h$; ρ_m is density of liquid used for inclined manometer (kg/m^3); h is vertical height of liquid inclined manometer (m).

The Darcy equation is applicable to flow at low Reynolds number based on particle diameter, i.e. $\mathrm{Re}_{d_p} = \frac{u_D \cdot d_P}{\nu} < 10$, for which the pressure driving force is only balanced by the net viscous forces.

In principle, the Darcy equation is applicable to fluids, either liquids or gases. However, the gas (usually air) flow is preferred to measure permeability because dry air will not dissolve the urea and flow at lower velocity helps to maintain a steady pore structure. Permeability is the property depending on the interconnecting structure of the porous medium while liquid or gas flow at higher velocity, sometimes tends to change the pore structure and cause a rearrangement of particles. Since, urea particles may dissolve when exposed to water, dry air is selected to flow through the urea bed to measure K.

B.1.2 Experimental apparatus

The measurement of permeability is deduced from equation (B-1), that is to say, measuring the pressure difference, air temperature and flow rate using the test facility shown in Figure B.1. The air pump with pro-dryer provides dry air at a flow-rate preset by the mass flow-rate controller (MKS) with LED. Dry air is forced to pass through a large cylindrical test container (D_c = 306 mm) filled with urea particles. The pressure difference between the inlet and the ambient air is measured by an inclined manometer, and the air temperature at the outlet is read by a temperature sensor which measures the temperature of discharge air outside of the urea particle bed.

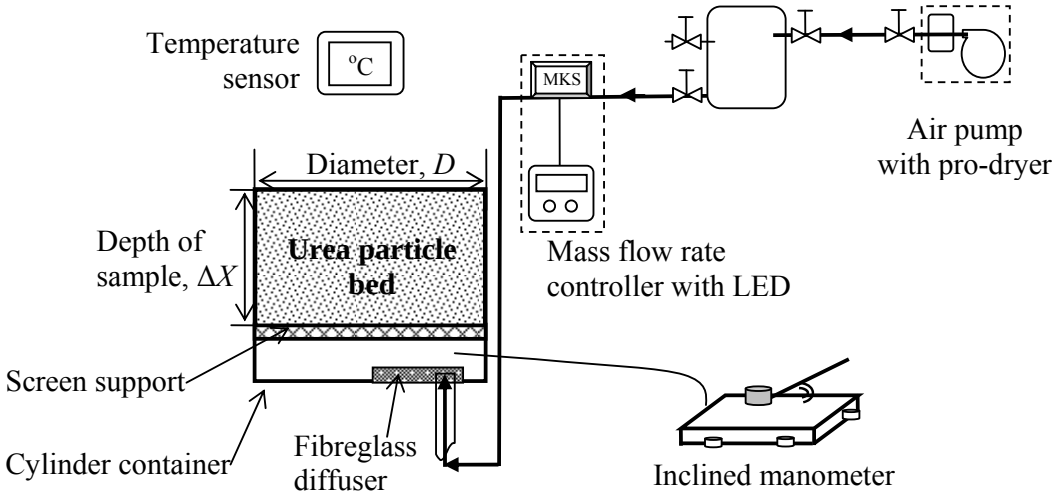

Figure B.1 Schematic diagram of permeability measurement

In order to minimize wall effects and particle alignment effects caused by proximity to the wall, two important geometric parameters namely the diameter of the test container and the depth of test samples are selected to be large enough compared with the particle size. The fibreglass diffuser makes the air supply uniformly distributed over the bottom of the particle bed and minimizing the effects of inlet momentum.

B.1.3 Experimental procedure

The test procedure used to measure permeability, K, is as follows:

1) Measure internal diameter of the cylinder container (D_c) and height of sample (L).

2) Measure the air temperature (T).

3) Adjust and measure the dry air flow rate ($\dot{Q}_a$) through urea particle bed using the calibrated volumetric flow meter.

4) Measure the pressure difference between urea particle bed and ambient air by using an inclined manometer (ΔP).

5) Repeat step 3 and step 4 at different flow rates.

6) Determine viscosity of air in terms of measured air temperature.

7) Calculate the permeability in terms of equation (B-1).

B.1.4 Experimental results

Table B.1 shows the permeability experimental data and measurement for Georgia and Terico urea particle bed with unshaken and shaken packing at different flow rate. As mentioned above, Darcy momentum equation is only valid for flow at low Reynolds number $\mathrm{Re}_{d_p} < 10$. These linear curve-fit equations $K = a + b \cdot u_D$ and the regression uncertainty $t \times SEE$ are listed in Table B.2(a) and (b). The Reynolds number based on hydraulic diameter is $\mathrm{Re}_{d_h} = \dfrac{u_p \cdot d_h}{\nu}$, where the actual air velocity in pore $u_p = \dfrac{u_D}{\varepsilon_e}$, and for nearly spherical

particle bed, $\frac{d_h}{d_p} = \frac{2\varepsilon_e}{3(1-\varepsilon_e)}$, therefore $\mathrm{Re}_{d_h} = \frac{2}{3(1-\varepsilon_e)}\mathrm{Re}_{d_p}$. Table B.2 (a) and (b) also list the external porosity for a packed urea particle bed shown in section B.2 and estimated Reynolds number based on hydraulic diameter.

When $\mathrm{Re}_{d_p} < 10$, permeability is expected to be independent of the Darcy velocity if the Darcy velocity does not change the particle arrangement in the bed. From the statistical analysis in Table B.2, it can be seen that, (1) permeability seems to change slightly with Darcy velocity because air flows have changed the pore structure a little bit. (2) air flow rates have more impact on unshaken beds than shaken one.

B.1.5 Uncertainty of permeability measurement

The permeability, K, defined in equation (B-1), is a function of pressure difference ΔP, volume flow rate, $\dot{Q}_a$, test container diameter, D_c, and test sample height, L. It can be rewritten as

$$K = \frac{1}{\mu} \cdot \frac{L}{\rho_m \cdot g \cdot h} \cdot \frac{4\dot{Q}_a}{\pi D_c{}^2} \tag{B-1a}$$

The uncertainty of permeability K can be calculated as

$$\frac{U(K)}{K} = \left\{ \left[\frac{U(h)}{h}\right]^2 + \left[\frac{U(\dot{Q}_a)}{\dot{Q}_a}\right]^2 + \left[2 \cdot \frac{U(D_c)}{D_c}\right]^2 + \left[\frac{U(L)}{L}\right]^2 \right\}^{1/2} \tag{B-2}$$

With known uncertainty of measured properties, such as inner diameter of test cell, D_c, sample height L, vertical height of liquid in the inclined manometer, h, and volumetric flow rate, $\dot{Q}_a$, as shown in Table B.2, the relative uncertainty of permeability, $U(K)/K$, is determined and listed in Table B.1 (a) & (b). The relative uncertainty of permeability is dominated by the uncertainty of flow rate measurement and then increases with the increase in Darcy velocity.

Table B.1 (a) Permeability measurement and uncertainty and statistical analysis for Terico urea particle bed

D_c=306 mm, L =152 mm, air temperature T_a=23°C, air density ρ_a=1.19 kg/m^3, air viscosity υ=1.54×10^{-5} m^2/s							
$\dot{Q}_a$ (%*)	u_D (m/s)	Re_{d_p}	unshaken				
			ΔP (Pa)	ε_e	Re_{d_h}	K (m^2)	$U(K)/K$
10	0.004533	0.65	1.23	0.46	0.80	1.03×10^{-8}	0.107
20	0.009065	1.30	2.62		1.59	9.65×10^{-9}	0.058
30	0.013598	1.95	4.00		2.39	9.47×10^{-9}	0.041
40	0.018130	2.60	5.23		3.19	9.65×10^{-9}	0.032
50	0.022663	3.25	6.77		3.98	9.32×10^{-9}	0.027
60	0.027195	3.90	8.31		4.78	9.11×10^{-9}	0.023
70	0.031728	4.55	9.85		5.58	8.97×10^{-9}	0.020
80	0.036261	5.20	11.39		6.37	8.87×10^{-9}	0.018
90	0.040793	5.85	12.93		7.17	8.79×10^{-9}	0.017
100	0.045326	6.50	14.78		7.97	8.54×10^{-9}	0.015
Regression line			K = 1.02×$^{-8}$ - 3.62×$^{-8}$×u_D; t×SEE = ± 3.68×10^{-10}				
			shaken				
10	0.004533	0.65	2.06	0.36	0.68	6.12×10^{-9}	0.105
20	0.009065	1.30	4.22		1.36	5.99×10^{-9}	0.055
30	0.013598	1.95	6.37		2.04	5.94×10^{-9}	0.038
40	0.018130	2.60	8.53		2.72	5.92×10^{-9}	0.029
50	0.022663	3.25	10.74		3.40	5.88×10^{-9}	0.024
60	0.027195	3.90	12.99		4.08	5.83×10^{-9}	0.021
70	0.031728	4.55	15.15		4.75	5.84×10^{-9}	0.018
80	0.036261	5.20	17.36		5.43	5.82×10^{-9}	0.016
90	0.040793	5.85	19.92		6.11	5.71×10^{-9}	0.015
100	0.045326	6.50	22.47		6.79	5.62×10^{-9}	0.014
Regression line			K = 6.11×10^{-9}- 9.83 ×10^{-9}×u_D; t×SEE = ± 9.55×10^{-11}				

Note: * means that percentage of the full range of the flow rate (200 Lpm).

Table B.1 (b) Permeability measurement and uncertainty and statistical analysis for Georgia urea particle bed

D_c=306 mm, L =152 mm, air temperature T_a=23 °C, air density ρ_a=1.19kg/m^3, air viscosity υ=1.54×10^{-5} m^2/s							
$\dot{Q}_a$ (%*)	u_D (m/s)	Re_{d_p}	unshaken				
			ΔP (Pa)	ε_e	Re_{d_h}	K (m^2)	$U(K)/K$
10	0.004533	0.54	3.69	0.45	0.66	3.42×10^{-9}	0.103
20	0.009065	1.07	7.39		1.30	3.42×10^{-9}	0.053
30	0.013598	1.61	11.39		1.96	3.33×10^{-9}	0.036
40	0.018130	2.14	15.24		2.60	3.31×10^{-9}	0.027
50	0.022663	2.68	19.24		3.25	3.28×10^{-9}	0.022
60	0.027195	3.21	23.09		3.90	3.28×10^{-9}	0.019
70	0.031728	3.75	26.94		4.55	3.28×10^{-9}	0.017
80	0.036261	4.29	31.24		5.21	3.23×10^{-9}	0.015
90	0.040793	4.82	35.31		5.85	3.22×10^{-9}	0.014
100	0.045326	5.36	39.40		6.51	3.20×10^{-9}	0.013
Regression line			K = 3.43×10^{-9} – 5.31×10^{-9}×u_D; t×SEE = ± 4.80×10^{-11}				
10	0.004533	0.54	5.69	0.36	0.57	2.22×10^{-9}	0.102
20	0.009065	1.07	11.08		1.12	2.28×10^{-9}	0.052
30	0.013598	1.61	16.47		1.69	2.30×10^{-9}	0.035
40	0.018130	2.14	22.32		2.24	2.27×10^{-9}	0.027
50	0.022663	2.68	28.17		2.81	2.24×10^{-9}	0.022
60	0.027195	3.21	33.40		3.36	2.27×10^{-9}	0.019
70	0.031728	3.75	38.79		3.93	2.28×10^{-9}	0.016
80	0.036261	4.29	44.94		4.50	2.25×10^{-9}	0.015
90	0.040793	4.82	51.10		5.05	2.22×10^{-9}	0.014
100	0.045326	5.36	58.03		5.62	2.18×10^{-9}	0.013
Regression line			K = 2.28e-9 – 1.30×10^{-9}×u_D; t×SEE = ± 6.84×10^{-11}				

Note: * means that percentage of the full range of the flow rate (200 Lpm).

The relative change of permeability $\frac{\Delta K}{K}$ over the range of Darcy velocity change, Δu_D, can be calculated as,

$$\left|\frac{\Delta K}{K}\right| = \frac{\Delta u_D}{K} \cdot \left|\frac{\partial K}{\partial u_D}\right| \tag{B-3}$$

Compare ΔK and $U(K)$, one get that

$$\frac{|\Delta K|}{U(K)} = \frac{\left|\frac{\Delta K}{K}\right|}{\frac{U(K)}{K}} \tag{B-4}$$

Table B.3 presents the detailed calculation of permeability change, ΔK, and comparison with $U(K)$ while volumetric flow rate changes from 10% to 100% of full range 200 Lpm.

Form the results in Table B.3, the change in permeability, ΔK, over the Darcy velocity change range from $u_D = 0.004533$ to $u_D = 0.04533$ m/s, has the same or less order of the magnitude as the average uncertainty of permeability $\overline{U}(K)$, i.e. $O(\Delta K) \sim O[\overline{U}(K)]$, which verifies that the permeability is independent of the Darcy velocity.

Table B.2 Uncertainty of measured parameters

Measured properties		Absolute uncertainty	Relative uncertainty
Diameter	$D_c = 306$ mm	$U(D_c) = 1$ mm	$U(D_c)/D_c = 0.33\%$
Sample bed height	$L = 152$ mm	$U(L) = 1$ mm	$U(L)/L = 0.66\%$
Vertical height of the inclined manometer	$h = (9\sim200)/25$ mm	$U(h) = 0.5/25$ mm	$0.25\% \le U(h)/h \le 5.5\%$
Flow rate	$\dot{Q}_a = 20\sim200$ Lpm	$U(\dot{Q}_a) = 2$ Lpm	$1\% \le U(\dot{Q}_a)/\dot{Q}_a \le 10\%$

Table B.3 Comparison between permeability change caused by Reynolds number and their uncertainties

Group	$u_{D,1} = 0.004533$		$u_{D,2} = 0.04533$		ΔK	$\overline{U}(K)$	$\frac{\Delta K}{U(K)}$
	K_1 (m^2)	$\frac{U(K_1)}{K_1}$	K_2 (m^2)	$\frac{U(K_2)}{K_2}$			
Terico/ Unshaken	1.03e-08	0.107	8.54e-09	0.015	1.76e-09	6.15e-10	2.86
Terico / Shaken	6.12e-09	0.105	5.62e-09	0.014	5.00E-10	3.61e-10	1.39
Georgia/ Unshaken	3.42e-09	0.103	3.20e-09	0.013	2.20e-10	1.97e-10	1.12
Georgia/ Shaken	2.22e-09	0.102	2.18e-09	0.013	4.00e-11	1.27e-10	0.314

B.2 Porosity measurement and its uncertainty

As the SEM images of external surface area and cross-section area of urea particles in the Chapter 1, urea particles are not solid but porous, which means that the total porosity, ε, includes internal porosity, ε_i and outer porosity ε_e. The relationship between them is

$$\varepsilon = \varepsilon_e + \varepsilon_i \cdot (1 - \varepsilon_e) \tag{B-5}$$

where ε is the total porosity of the urea bed; ε_e is external porosity, i.e., volume fraction of the bulk volume occupied by the void space outside of urea particles; ε_i is the internal porosity, volume fraction of total urea particle volume occupied by the void space inside the urea particles.

B.2.1 Principle of external porosity (ε_e) measurement

The external porosity, ε_e, is the fraction of the bulk volume of the porous sample that is occupied by pore or void space between urea particles in a bed, that is

$$\varepsilon_e = 1 - \varepsilon_s = 1 - \frac{V_s}{V_{ec}} \tag{B-6}$$

The total internal volume of the container, V_{ec}, can be measured by means of filling the container with the distilled water before porosity measurement. The volume of the solid space in the container occupied by pure urea particles, $V_s = M_s / \rho_s$. Since the air density is much smaller than urea particles, the air mass is negligible compared with urea articles in the bed. Then the porosity can be calculated as

$$\varepsilon_e = 1 - \frac{M_s}{\rho_s} \cdot \frac{\rho_{dw}}{M_{dw}} = 1 - \frac{M_{ec,s} - M_{ec}}{\rho_s} \cdot \frac{\rho_{dw}}{M_{ec,dw} - M_{ec}} \tag{B-6}$$

where ρ_s is the density of pure urea particle; ρ_{dw} is the density of distilled water; M_{ec} is the mass of the dry and empty container; $M_{ec,s}$ is the total mass of the container packed with urea particles; $M_{\mathrm{ec},dw}$ is the total mass of the container full of distilled water.

B.2.2 Experimental apparatus and procedure

Figure B.2 shows the container for packing urea particles on the weigh scale for mass measurement.

The test procedure used to measure porosity, ε_e, is as follows:

(1) Measure the mass of the dry and empty container, M_{ec}.
(2) Measure the total mass of the container full of the distilled water, $M_{ec,dw}$.
(3) According to the room temperature, choose proper water density and then calculate the volume of the container, V_{ec}.
(4) Fill the dry and empty container with packed urea particles, and measure the total mass after packing, $M_{ec,s}$, and then calculate the external porosity.

B.2.3 Experimental results and uncertainty analysis

From equation (B-6), the uncertainty of the external porosity deduced from the equation propagation is

$$\left[\frac{U(\varepsilon_e)}{1-\varepsilon_e}\right]^2 = \left[\frac{U(M_s)}{M_s}\right]^2 + \left[\frac{U(M_{dw})}{M_{dw}}\right]^2 + \left[\frac{U(\rho_s)}{\rho_s}\right]^2 + \left[\frac{U(\rho_{dw})}{\rho_{dw}}\right]^2 \tag{B-7}$$

where $U(M_{ec,s} - M_{ec}) = U(M_{ec,dw} - M_{ec}) = \sqrt{2} \cdot U(M)$.

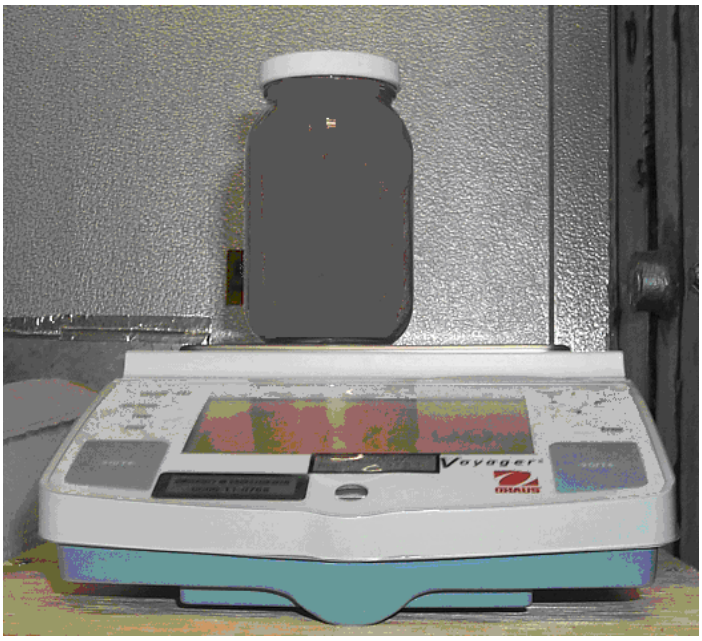

Figure B.2 Experimental apparatus for porosity measurement with gravimetric method

Table B.4 shows the experimental data and measurement uncertainty of external porosity. For consolidated urea particles, porosity lies in a narrow range from 0.361 to 0.364, probably independent of particle size, because two different urea particles, both Terico and Georgia from different manufactories, are in nearly spherical shape and have uniform size distribution and close particle size around 2 mm.

From equation (B-7) and Table B.4, it can be seen that for this cylindrical glass container which can hold either at least 600 g urea particles or nearly 1000 g distilled water, the uncertainty of external porosity, $U(\varepsilon_e)$ is dominated by the property uncertainty, i.e., urea density and distilled water density, while the contribution of the mass measurement uncertainty, for whatever type of electrical weigh scales, is negligible.

Table B.4 Porosity measurement of urea particle bed

ρ_s=1323 kg/m^3		ρ_{dw}=1000 kg/m^3	M_{ec}=482.08 g	$M_{ec,dw}$=1446.19g
$\frac{U(\rho_s)}{\rho_s}$=10%		$\left[\frac{U(\rho_{dw})}{\rho_{dw}}\right]$=10%	$U(M)$=0.01/0.1/1 g depending on the type of scale	
Group		$M_{ec,s}$ (g)	ε_e	$U(\varepsilon_e)$
Terico	Unshaken	1175.48	0.46	0.01
	Shaken	1296.31	0.36	0.01
Georgia	Unshaken	1181.91	0.45	0.01
	Shaken	1293.99	0.36	0.01

B.3 External specific surface area and hydraulic diameter

Specific surface area can be defined as the surface area of pores (interstitial surface area or surface area between solid and fluid) per unit volume (bed volume or solid volume) or per unit mass. Due to urea particles' porous structure, the total specific surface area of the porous urea bed includes two parts – external specific surface area ($A_{v,e}$ or $A_{m,e}$), and internal specific surface area ($A_{v,i}$ or $A_{m,i}$). The relationship between these two kinds of specific surface area is expressed as.

$$A_v = A_{v,e} + (1-\varepsilon_e)\cdot A_{v,i} \tag{B-8a}$$

$$A_{vs} = A_v / (1-\varepsilon) \tag{B-8b}$$

$$A_m = A_{m,e} + A_{m,i} \tag{B-8c}$$

where A_v is specific surface area based on a unit volume of the particle bed; $A_{v,e}$ is the external specific surface area based on the volume; $A_{v,i}$ is the internal specific surface area based on volume; A_{vs} is specific surface area based on solid volume; A_m is specific surface area based on mass; $A_{m,e}$ is external specific surface area based on mass; $A_{m,i}$ is internal

specific surface area based on mass; ε_e is external porosity outside the urea particles in the bed.

In this appendix, only the external specific surface area based on volume is considered. There are several methods to determine specific surface area of particle beds, but only the BET method of measurement has the potential to give accurate results when the internal surface area is large compared to the external surface and or the external surface is rough.

Hydraulic diameter, d_h, defines as four times the ratio of the pore volume to the interstitial solid-fluid area, is

$$d_h = \frac{4\varepsilon_e}{A_{v,e}} \tag{B-9}$$

B.3.1 Calculation using definition for spherical particles

Because urea particles are manufactured in nearly spherical shape, the external surface area of smooth spherical particle bed per unit bed volume, $A_{v,e}$, is defines as the ratio of the interstitial solid-fluid area to the bulk volume. This is,

$$A_{v,e} = \frac{\pi \cdot d_p{}^2}{\left(\frac{1}{6} \cdot \pi \cdot d_p{}^3\right) \Big/ \left(1-\varepsilon_e\right)} = \frac{6\left(1-\varepsilon_e\right)}{d_p} \tag{B-10a}$$

$$A_{vs,e} = \frac{6}{d_p} \tag{B-10b}$$

where d_p is spherical particle diameter; ε_e is the external porosity.

Combine equation (B-9) and (B-10a), the relationship between the hydraulic diameter and particle diameter for spherical particle bed can be obtained as followed (Dullien, 1982).

$$d_h = \frac{2\varepsilon_e}{3\left(1-\varepsilon_e\right)} d_p \tag{B-11}$$

However, urea particles are not in perfect spherical shape. Sphericity of a particle, Ψ, introduced to measure how spherical it is, is the ratio of the surface area of a sphere (with the same volume as the given particle) to the surface area of the particle:

$$\psi = \frac{\pi \cdot d_p^{'2}}{A_p} = \frac{\pi^{1/3}\left(6V_p\right)^{2/3}}{A_p} \tag{B-12}$$

where $V_p = \frac{1}{6} \cdot \pi \cdot d_{p'}^{\ 3}$ is volume of the particle; $d_p^{'}$ is the equivalent spherical diameter that has the same volume as the particle; A_p is the surface area of the particle. Sphericity, $0 < \psi \leq 1$, measures how round the object is. Only for an exact spherical particle, $\psi = 1$.

B.3.2 Calculation of specific surface area using the Carmen correlation

With the assumption that there is no flow inside the urea particles, the correlation equation due to Carmen (1938, 1939) can be used to estimate the external specific surface area of unshaken or shaken granular bed of smooth or nearly smooth particles. The Carmen correlation is expressed as follows.

$$A_{vs,e} = \left[\frac{1}{k_k} \cdot \frac{\left(\varepsilon_e\right)^3}{\left(1-\varepsilon_e\right)^2} \cdot \frac{1}{K}\right]^{1/2} \tag{B-13a}$$

$$A_{v,e} = A_{vs,e} \cdot (1-\varepsilon_e) = \left[\frac{\left(\varepsilon_e\right)^3}{k_k \cdot K}\right]^{1/2} \tag{B-13b}$$

where k_k is Kozeny constant, estimated to be 5 for packed spherical particles; K is permeability of the bed.

The correlation depends on the measurement of ε_e and K. Table B.5 shows the calculated external specific surface area and hydraulic diameter for a urea particle bed.

B.3.3 Experimental data and uncertainty with Carmen equation

The uncertainty of external specific surface are per unit bed volume is propagated from equation (B-13b) as followed.

$$\left[\frac{U(A_{v,e})}{A_{v,e}}\right]^2 = \left[\frac{3}{2}\frac{U(\varepsilon_e)}{\varepsilon_e}\right]^2 + \left[\frac{1}{2}\frac{U(K)}{K}\right]^2 \quad \text{(B-14)}$$

Table B.5 Specific surface area and hydraulic diameter of a urea particle bed

Group		Terico	Georgia
		Shaken	Shaken
ε_e, (m^3/m^3)		0.36	0.36
Spherical particles	d_p, (mm)	2.21	1.82
	$A_{v,e}$, (m^2/m^3) (B-10a)	1738	2110
	d_h, (mm) (B-11)	0.8	0.7
Carmen equation	$A_{v,e}$, (m^2/m^3) (B-13b)	1204	1992
	$A_{vs,e}$, (m^2/m^3) (B-13a)	1881	3113
	$A_{m,e}$, (m^2/kg)	1.42	2.35
	d_h, (mm) (B-9)	1.2	0.73
Sphericity, ψ, (B-12)		0.68~0.92	

As mentioned in section B.1 and B.2, the relative uncertainty of external porosity measurement $\frac{U(\varepsilon_e)}{\varepsilon_e}$ is approximated at 2.5% and the relative uncertainty of permeability $\frac{U(K)}{K}$ is approximated at 5%. Therefore the relative uncertainty of external specific surface area $\frac{U(A_{v,e})}{A_{v,e}}$, caused by the correlation equation propagation is about 4.5%.

Carmen correlation was a good way to calculate the specific surface area for porous media, but the error or uncertainty information was not presented. Chen (2004) used a series of beds

packed with smooth and spherical particles, and compared calculated specific surface area with two different methods in section B.3.1 and B.3.2, and concluded that this Carmen correlation had an uncertainty of about $\pm 20\%$ for smooth nearly spherical particles. Therefore the relative uncertainty of specific surface area and hydraulic diameter determined by Carmen equation is considered as $\pm 20\%$.

B.3.4 External rough surface

The SEM images of urea particles in Chapter 1 show that the external surface of urea particles is not smooth. Rough surfaces increase the external surface area greatly. Since urea in its solid form can exist as a crystalline solid, it can be hypothesized that the external surface of each urea particle is comprised of cubic crystals each of side length b and positioned as shown in Figure B.3.

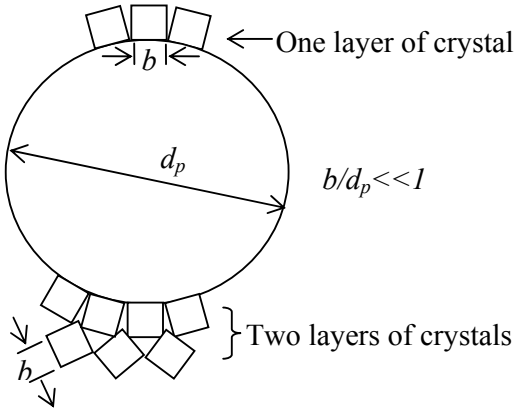

Figure B.3 Schematic diagram of rough surface of urea particles

Figure B.3 is the schematic diagram of rough surface of urea particles indicating how this spherical rough surface is formed. It is supposed that there are n layers of very small cubes, each of volume b^3 that occupy the entire outer surface of each urea particle. In each layer, the number of cubes occupied on the external surface completely covers the surface is given by

$N_c = \frac{\pi \cdot d_p^2}{b^2}$. For n layers of cubes on the surface, total external surface area increases greatly. For b/d_p<<1, the external area amplification ratio can be estimated as followed.

$$\frac{\left(A_{v,e}\right)_{rough}}{A_{v,e}} = \frac{5 \cdot b^2 \cdot N_c + (n-1) \cdot 6 \cdot b^2 \cdot N_c}{\pi \cdot d_p^2} = 6 \cdot n - 1 \qquad \text{(B-15a)}$$

$$\frac{\left(A_{m,e}\right)_{rough}}{A_{m,e}} = 6 \cdot n - 1 \qquad \text{(B-15b)}$$

where $\left(A_{v,e}\right)_{rough}$ or $\left(A_{m,e}\right)_{rough}$ is rough external specific surface area per unit bed volume or mass; $A_{v,e}$ or $A_{m,e}$ is smooth external specific surface area per unit bed volume or mass.

It is not easy to determine how many layers of crystal are accumulating on the external surface area, because the rough external surface is connected with the irregular internal surface by complex pore path. The Figure B.4 showed that the shape of the crystals on the external surface is not cubic but flat, and the length of the crystal is about 1-2 μm. It is supposed that there are two layers of crystal on the external surface, and other pore path or pore surface belongs to the internal domain, than the rough external specific surface area is estimated about 11 times of the smooth external specific surface area.

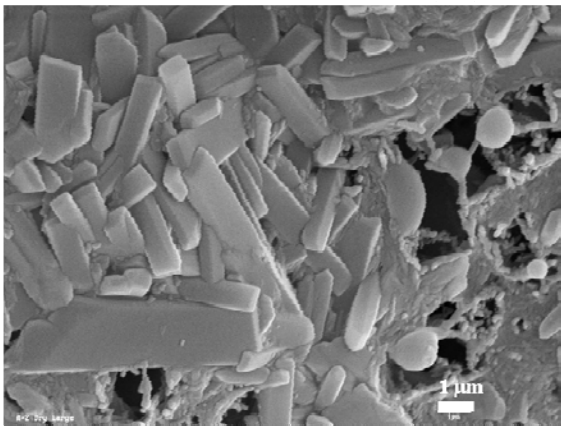

Figure B.4 Rough external surface of a urea particle

APPENDIX C

DETERMINATION OF INTERNAL AND MICROSCOPIC PROPERTIES OF UREA PARTICLES

C.1 BET theory for the determination of specific surface area

C.1.1 Gas sorption

When a gas or vapor is in contact with a solid surface, some gas or vapor molecules become attached or bond to the surface. This is called adsorption when there is no chemical reaction, Gas molecules can also be admitted to internal void spaces of particles or a particle bed, which is called absorption. Absorption and adsorption processes can occur simultaneously in porous particle bed and they may be called sorption processes but when the net effect is to release gas molecules it is usually called desorption.

Gaseous molecules and atoms can attach themselves onto surfaces by either weak or strong molecular forces. In physic-sorption, there is a weak van der Waals attraction force of the adsorbate gaseous molecules to the solid surface molecules. In chemic-sorption, the adsorbate joins the solid by the formation of strong chemical bonds between molecules at exposed surfaces. This chemic-sorption interaction force is much stronger than physic-sorption force, implying larger associated energy gains or losses in the chemical bonds than for physic-sorption. When the chemi-sorption process releases energy which is manifested by a temperature rise, the process is said to be an exothermic process, other wise, it is said to be endothermic. Likewise sorption processes with the formation of weak molecular bonds are usually exothermic and desoprtion is endothermic but the amounts of energy involved are usually orders of magnitude smaller than for chemi-soprion. In general, chemi-sorption has more stringent requirements for the chemical species compatibility of adsorbate molecules and surface site molecules than physic-sorption. The Brunauer, Emmett and Teller (BET) theory of gas sorption is developed for physic-sorption of zero to infinite layers of adsorbate on solid surfaces. The results of this model for sorption and desorption can be used to

determine the total surface area available for both inside and outside porous solid particles such as urea.

Generally the physical sorption of gases by solids increases with the partial pressure of the adsorbate gas and decreases with temperature. While using the BET method to investigate the surface area and pore structure, the sorption or desorption isotherm is determined. Sorption and desorption is expressed as a mass or molar quantity of gas or volume at standard temperature and pressure (STP) per unit mass taken up or released by initially clean, dry and solid surface, at a constant temperature, *T*. This mass or standard volume adsorbed is plotted as a function of the adsorbate gas pressure *P* as shown in Figure C.1. In the BET method, liquid Nitrogen or Krypton at 1 atm and 77 K is usually used as the test gas, resulting in several molecular layers of adsorbate gas molecules physically bonded on the solid particle. Different forms of adsorption isotherms for solid particles depend on the composition of adsorbate gas used as well as pore size and other physical properties. Figure C.1 shows one typical adsorption and desorption isotherm for a porous solid when multiple layers of adsorbed gas exist on the sorption surfaces.

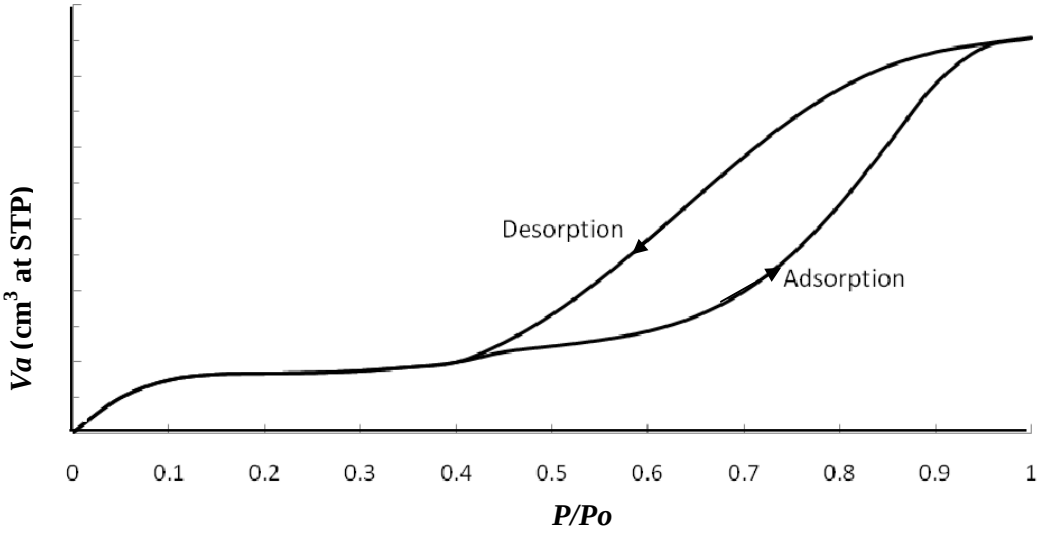

Figure C.1 Adsorption and desorption isotherms for a porous solid

C.1.2 Molecular structure of water and urea bonds

The chemical structure of both the water molecules (H_2O) and urea molecules (CN_2OH_4), as shown in Figure C.2, can be used to help explain how water is adsorbed by urea particles. Figure C.2 (a) shows the water molecule structure and two water molecules weakly joined by Van Der Waals forces. The oxygen atom of one water molecule attracts more than its "fair share" of electrons and this results in a small negative electrical charge near the oxygen atom O^{2-}, and this charge attracts an equal and opposite positive charge on the hydrogen atoms H^{+} on the other H_2O molecule. This bond between water molecules is called self bonding and is readily broken when a small amount of energy is added. Figure C.2 (b) shows the structure of urea molecules and how a urea molecule is wrathfully bonded to adjacent urea molecules and forms the crystalline structure. Figure C.2 (c) indicates the standard coordinate of urea and water molecular. Figure C.3 (d) lists the electro-negativity of H, C, O and N atoms for the urea molecules which cause the existence of electron static polarity for each strong chemical bond such as C-O, C-N, N-H.

When water is in contact with the available urea surface atoms, the polarity of the water molecule allows it to form weak hydrogen bonds with other polar attractive atoms in the urea molecule as shown in Figure 1.4. Electrostatic attraction between any adjacent water molecules results in weak hydrogen bonds, therefore, many layers of water molecules can form as an adsorbate on surfaces. When a thick layer of water is formed on the surface, the outer layer has the characteristics of liquid water which is mobile.

C.1.3 BET theory and equations

Gas adsorption has been investigated using two different models - one is Langmuir theory and the other is Brunauer, Emmett and Teller (BET) theory. Langmuir theory is more properly applicable to chemi-sorption situations than physical adsorption because of the assumption that only one molecular layer of gas forms on a solid surface for chemi-sorption. For the BET theory there can be multi-molecular layers of gas on the surface for adsorption of gaseous molecules. Usually nitrogen is used as the BET analysis gas for solid test specimens with a specific surface area larger than 10 m^2/g, while Krypton can be used for specimens with specific surface areas less than 10 m^2/g.

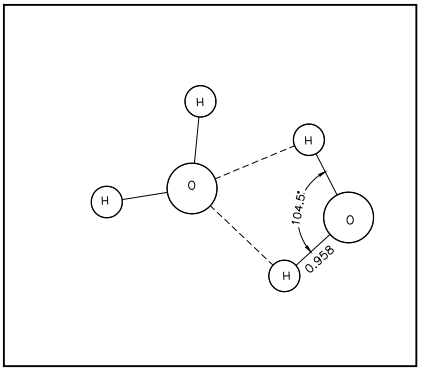

(a) Two water molecules with hydrogen bonds (Jeffrey, 1997);

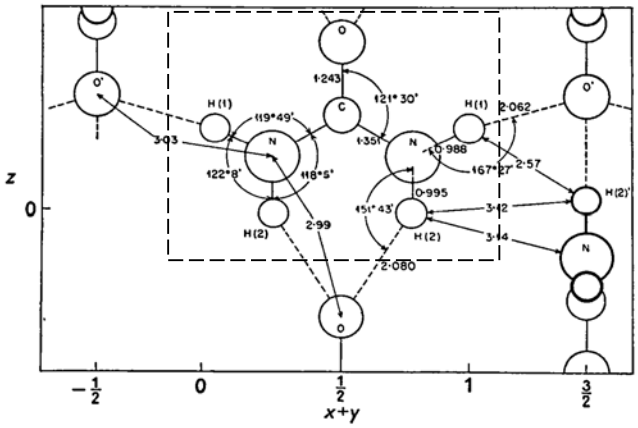

(b) Urea molecule with hydrogen and chemical bonds with adjacent urea molecules (Worsham, et al., 1957)

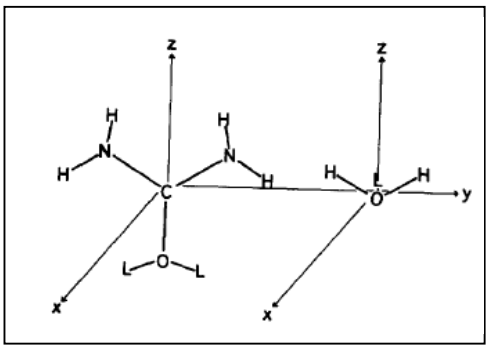

(c) Standard coordinates of urea and water molecular (Tanaka, et al., 1984)

Atom	H	C	N	O
Electro-negativity	2.1	2.5	3.0	3.5

(d) Electro-negativity of atoms (Sanderson, 1983)

Figure C.2 Polarity and structure of urea and water molecules in a 2-D plane

In the BET method of test, an initially degassed and clean solid particle sample (e.g. urea) is suddenly exposed in a test chamber to an analysis gas (e.g. Nitrogen or Krypton) at one initially selected gas pressure. This chamber pressure is continuously monitored while the volume of the test chamber is held constant. When the volume of this chamber is closed by a valve to start the test, the gas pressure will decline as the solid particles adsorb the gas molecules in several layers on all the available surfaces of the test specimen and the gas pressure will, after 10-20 minutes of exposure (the time depends on sample chemical type and mass), come to a new steady state pressure. Measuring this transient pressure change and

temperature allows the experimenter to calculate the quantity of gas adsorbed for each test condition.

The Brunauer-Emmett-Teller (BET) equation (C-1), used to describe multilayer adsorption, gives the relationship between the quantity of adsorbed test gas (V_a at STP) and the pressure of the test gas (or relative pressure, P/P_o). From BET equation, the quantity of a monomolecular layer gas adsorbed on the entire surface, V_m at STP, can be inversely deduced. BET theory assumes that the forces active in the condensation of gases are also responsible for the binding energy in multi-molecular adsorption. It assumes that the adsorbed gas molecules accumulate in layers such that the number of molecules in each layer decreases following a geometric progression equation. By equating the condensation rate of gas molecules onto an already adsorbed layer to the rate of evaporation from that layer, and summing for an infinite number of layers, BET expression (C-1) can be obtained, which relates the gas pressure, P, to the corresponding gas volume, V_a.

$$\frac{P}{V_a \cdot (P_o - P)} = \frac{1}{V_m \cdot C} + \frac{C-1}{V_m \cdot C}\left(\frac{P}{P_o}\right) \tag{C-1}$$

where P is absolute gas pressure (Pa); P_o is absolute saturation pressure of adsorbate gas at the temperature 77 K (Pa); V_a is volume of test gas taken up during sorption or released by desorption (m^3) at STP; C is a constant called BET-C value; V_m is volume of one complete mono-layer of adsorbed gas at STP.

The volume quantity of monolayer molecules of gas adsorption, V_m, is determined by BET equation (C-1). With known mass of solid sample M_s, the specific surface area A_m can be calculated using equation (C-2).

$$A_m = \frac{\sigma}{M_s}\left(V_m \frac{\cdot N_A}{V_o}\right) \tag{C-2}$$

Where A_m is specific surface area (m^2/g); σ is area of surface occupied by a single adsorbed gas molecule, (m^2); M_s is mass of the solid sample, (g); V_m is the volume quantity of gas adsorbed when the entire surface is covered with a monomolecular layer (m^3) at STP; N_A is Avogadro constant, (6.023e23 molecules/mole); V_o is molar volume of the gas, (0.22414 m^3/mole);

The surface area occupied by each gas molecule, σ, in unit of m^2, is calculated with the following correlation.

$$\sigma = (4)(0.866)\left[\frac{M_A}{4(2N_A\rho_{la})^{1/2}}\right]^{2/3} \quad \text{(C-3)}$$

Where M_A is the molecular weight, (g/mole); ρ_{la} is the density of the liquid adsorbate, (kg/ m^3).

Internal porosity is calculated by equation (C-4).

$$\varepsilon_i = \rho_s V_{M,pore} \quad \text{(C-4)}$$

Where ε_i is internal porosity; $V_{M,pore}$ is total adsorption pore volume inside urea particles measured by BET test (cc/g); ρ_s is urea particle density (kg/m^3).

C.2 BET equipment and measurement test procedure

C.2.1 Micromeritics ASAP 2000

Figure C.3 presents a frontal view of the Micromeritics ASAP 2000 which is used to measures physic-sorption surface area and pore size. It includes two parts: one is for degassing and the other is for analysis. The sample degassing stations on the left side helps to clean and dry samples under a vacuum condition. Gases used for analysis, backfill or evacuate space test chamber are connected using stainless steel tubes at the rear of the equipment. The liquid N_2 Dewar flask shown in Figure C.3 can be elevated or lowered to provide a constant temperature (around 77 K) environment at room air pressure for test sample when gas sorption or desorption happens. On the right side of Figure C.3, the analysis port is used to install the sample holder with each degassed sample. The P_o (saturation pressure) tube, located close to analysis port, is used to measure the saturation pressure of the analysis gas and store the analysis gas and purge the analysis gas on the test sample surface prior to each test. When the test is started, both the sample holder and the Po tube are kept in the liquid N_2 in the Dewar vessel (77 K).

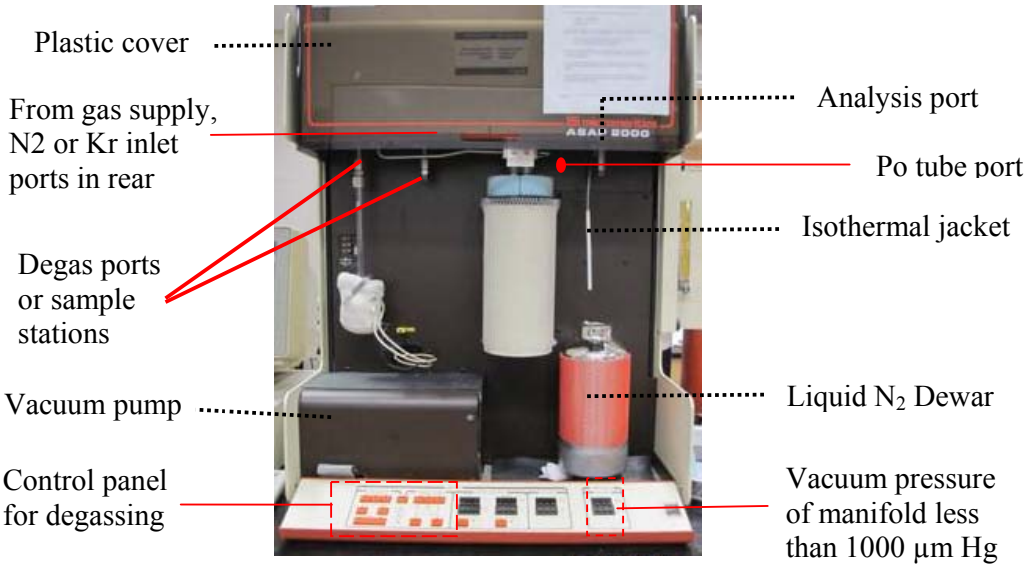

Figure C.3 Micromeritics instrument for BET testing and analysis

Three pressure transducers (in Figure C.4) with different ranges: 0-1000 mm Hg, 0-10 mm Hg and 0-1 mm Hg are arranged to measure the pressure in the manifold. The volume of analysis gas V_a taken up or released by a sample at various absolute gas pressures, P, or various relative pressures (P/P_o) is to be determined. By means of static volumetric methods, adsorption/ desorption is determined using mass balance equations, accurate gas state equations and measured pressures. The volume of gas adsorbed, V_a, is indirectly measured and calculated using equation (C-1) and converted to the standard pressure and temperature (STP) condition so that the absorbed mass can be calculated.

C.2.2 Sample preparation

For BET analysis, two different types of urea (Terico & Georgia) at initially wet and dry conditions are prepared for testing. Dry urea sample is taken directly from the sealed urea fertilizer bag stored at room temperature. The wet sample is obtained by taking the samples from the sealed storage bag and placing urea particles in a cabinet at constant relative humidity for 16 hours and then drying the sample using a vacuum filter. Degassing procedures provide a clean and dried sample in vacuum condition for further BET analysis.

C.2.3 Sample quantity

It is very important to use an appropriate mass of sample. Too much sample surface or mass will increase both the degassing and analysis time. On the other hand, if urea sample is of insufficient mass, its weight measurement will result in a high relative error. Too small a sample mass will result in a very low surface area and uptake of adsorbed gas by the sample so that a very small pressure difference signal occurs in the constant volume system. Then low resolution and unreliable measurements will arise. Buoyancy effects are another important consideration. Because the sample weight is determined by subtracting the weight of the empty sample holder from the combined sample holder and degassed sample. However, the empty sample holder is weighed with air inside while sample holder with degassed sample is backfilled with another gas (He or Kr) after degassing. The density difference between backfilled gas and air will play a significant role in mass measurement if too small a sample mass is used.

C.2.4 Degassing of the sample

Degassing of the samples is necessary before the BET test and analysis. The purpose of degassing is to remove previously adsorbed vapor or gas molecules from all the surfaces and internal pores of each sample. By degassing each sample, adsorptive test gas molecules can enter to interact directly with the urea particles. Sample degassing is carried out under evacuation conditions while heating the sample. For the urea samples, the temperature for degassing is set at $50^{o}C$ because urea will chemically decompose at temperatures over $70^{o}C$. For krypton gas analysis, the vacuum is set at 200 μm Hg (absolute pressure). This pressure brings difficulties in degassing the initially wet samples because the water adsorbed on the particle surfaces should totally evaporate in the vacuum and this kind of evaporation takes a very long time. To accelerate degassing of a wet urea sample, a vacuum pump and a filter were used to partially remove the moisture adsorbed by urea sample before starting the degassing of wet samples.

C.2.5 Analysis gas

Krypton has a much lower saturation pressure than nitrogen (i.e. the saturation pressure of krypton is 2.5 mmHg while saturation pressure of nitrogen is 760 mmHg at 77 K). So compared to nitrogen, there is only 1/300 the number of krypton molecules present in the test

volume at the same relative pressure (P/P_o) in the free space above sample. Since about the same number of krypton and nitrogen molecules are required to form a monolayer on each sorption surface, it means that a much greater mass fraction of the krypton gas will be adsorbed than that for the case of nitrogen. As an inert gas, krypton is better with regard to the solid-surface interaction for a sample with a low specific surface area. On the other hand, krypton analysis cannot offer porosity or pore size data because there is no desorption data.

C.3 Experimental procedure

C.3.1 Preparation for Micromeritics instrument

Because BET analysis test gas was changed from nitrogen to krypton for the first time using BET facility, the gas supply was checked and reconnected to the right cylinder as shown in Table C.1 and Figure C.3. Then the filter for the analysis port was changed (shown in Figure C.3) to 20 μm which is specially designed for krypton analysis.

Table C.1 Gas used for BET analysis

Gas used for	N_2 analysis	Kr analysis
Saturation pressure P_o	N_2	N_2
Free space analysis	He	He
Degas backfill	N_2	Kr
Analysis	N_2	Kr

Before turning on the BET micromeritics instrument, the following settings on the back of the instrument need to be checked: 1) Gas pressure of nitrogen and krypton is at 10 Psig. Initially the inlet valves are open and chemisorption valve is closed. 2) Oil level in vacuum pumps is normal. 3) Install two cold trap glass tubes and filler rods after proper washing and drying. 4) Fill the flask with liquid nitrogen (which provides constant temperature 77 K for the gas adsorption) and place the flask at Condenser port. 5) Check the saturation pressure tube is also installed on its port.

Then start the program and turn on the micromeritics instrument and the vacuum pump. Change the system option and set analysis gas as krypton.

C.3.2 Evacuation system

Before starting the BET test, it is important to remove completely any residual gas remaining in the manifold and the P_o tube. At the beginning all valves are closed. The following detailed steps are used to evacuate the whole system and expel N_2 gas out of manifold, P_o tube in Figure C.4.

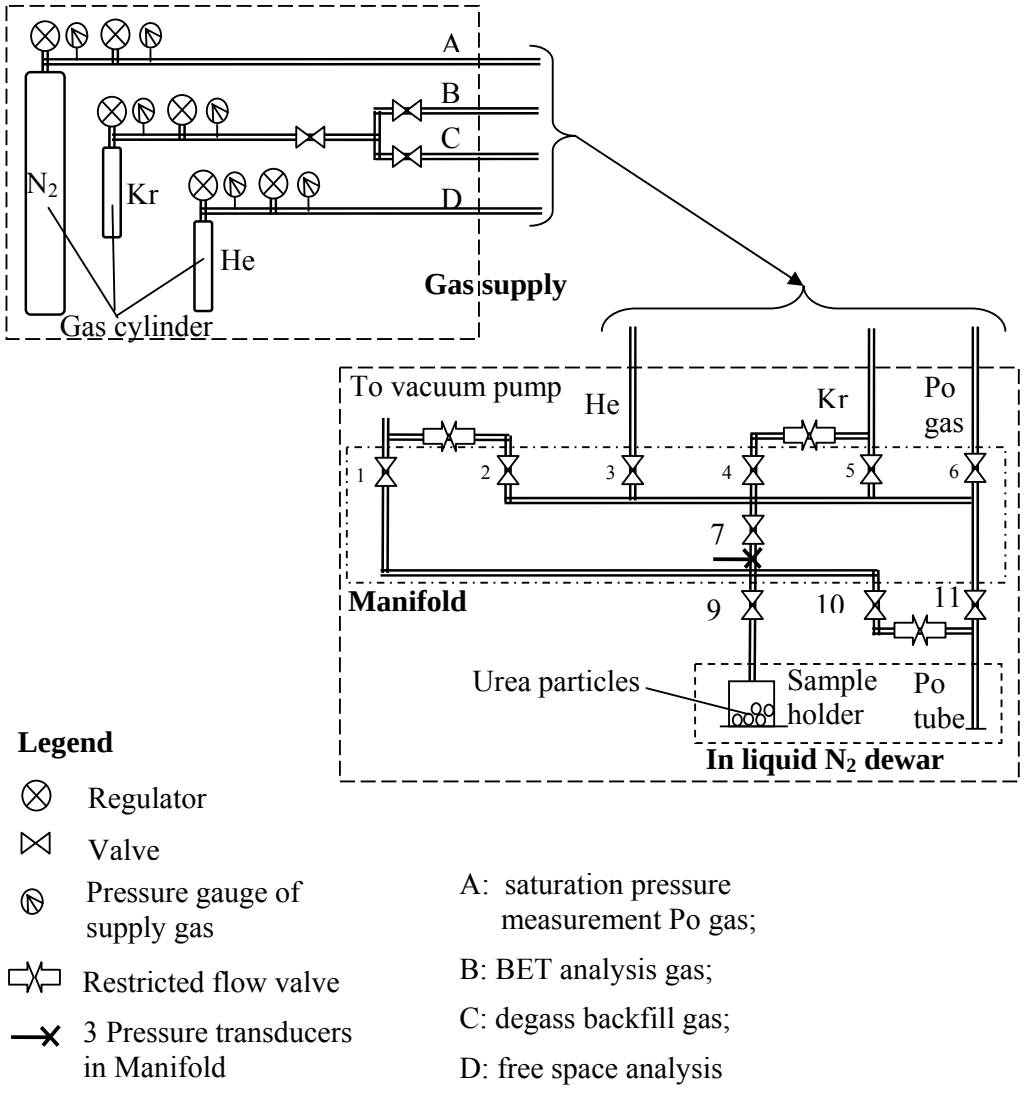

Figure C.4 Schematic diagram of manual control

1) Close the regulator of N_2 and K_r supply.
2) Open valves 1/2/7/4/5 to evacuate the manifold till pressure drops below 4 μm Hg.
3) Close valves 1/2/7/4/5 to finish the evacuation of the manifold.
4) Open valves 1/ 2/ 7/ 10/ 11 to evacuate P_o tube till pressure drops below 4 μm Hg.
5) Close valves 1/ 2 to finish the P_o tube evacuation.
6) Open valves 4/ 5 to store the K_r gas in P_o tube till the pressure reaches 200 mmHg
7) Close valves 4/ 5 to finish storing the Kr gas in the Po tube.
8) Repeat step 2 to 5 many times.
9) Open valves 1/2/4/5/7/10/11 for evacuation for a few hours.

C.3.3 Degassing the test samples

Degassing is to remove previously adsorbed molecules from surfaces and pores. Before degassing, weigh the empty sample holder and record the weight, then add 0.2 g urea sample, i.e., 25 Terico urea particles or 45 Georgia urea particles into the holder, and reweigh the total mass of sample holder together with urea samples before degassing.

Install the sample holder to the degassing port at the left of Micromeritics instrument (i.e. sample station in Figure C.3). Attach the heating mantle to the sample holder. Load the sample and start Auto Degas setting after setting heating temperature at 50^oC and vacuum at 200 μm Hg.

When the green light appears, unload sample and manually remove the sample tube, measure the total weight of urea particles together with the sample holder after degassing. Calculate net weight of the urea sample based on weight after degassing.

C.3.4 Gas sorption and BET analysis

1) Recheck the He, N_2 and Kr gas pressure and valve on the back side of instrument. And recheck whether the saturation pressure P_o tube is properly fixed. Turn on the molecular pump special for Kr analysis.

2) Fill the Dewar flask with liquid nitrogen and place it on the elevator bench.
3) Attach the sample holder to analysis port at the right of the front side of Micromeritics instrument.

4) Go to the main menu and do some pre-setting including sample information (sample weight) and analysis choice, such as sample weight, number of surface area points, number of micro pore points, number of adsorption points, number of desorption points, whether total pore volume measured.

5) Set experimental parameters of choice.

6) Start and perform an analysis till the analysis ends and the report is printed.

C.4 Results and discussion

C.4.1 BET analysis report

BET analysis and experimental results are based on two types of urea particles, Terico and Georgia. Only one detailed report will be presented as an example for terico urea particles using the Kr gas analysis. The isothermal gas adsorption volume, V_a, is plotted versus relative pressure, P/P_o, at the temperature 77K in Figure C.5.

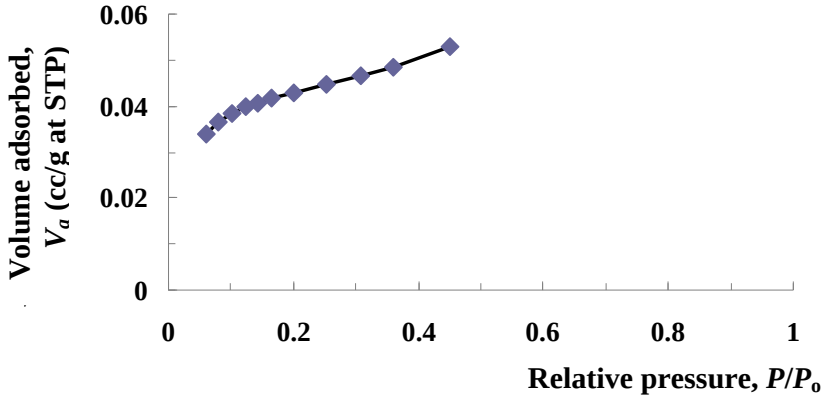

Figure C.5 Isotherm adsorption

BET Transformation on the left side of the gas state equation (C-1), $1/[V_a \cdot (P_o / P - 1)]$, is plotted with respect to the relative pressure P / P_o in Figure C.6. Data in the figure shows that

the BET transformation linearly increases with an increase in relative pressure as equation (C-1) indicated, therefore linear regression line is used to fit the data as followed.

$$\frac{1}{V_a \cdot (P_o / P - 1)} = k \times \frac{P}{P_o} + b \tag{C-5}$$

where $k = (C-1)/(V_m \cdot C)$ and $b = 1/(V_m \cdot C)$. Therefore, the quantity of gas adsorbed when the entire surface is covered with a monomolecular layer, V_m, and the constant BET-C value, C, can be determined from the BET transformation.

$$V_m = \frac{1}{k+b} \tag{C-5a}$$

$$C = \frac{k+b}{b} \tag{C-5b}$$

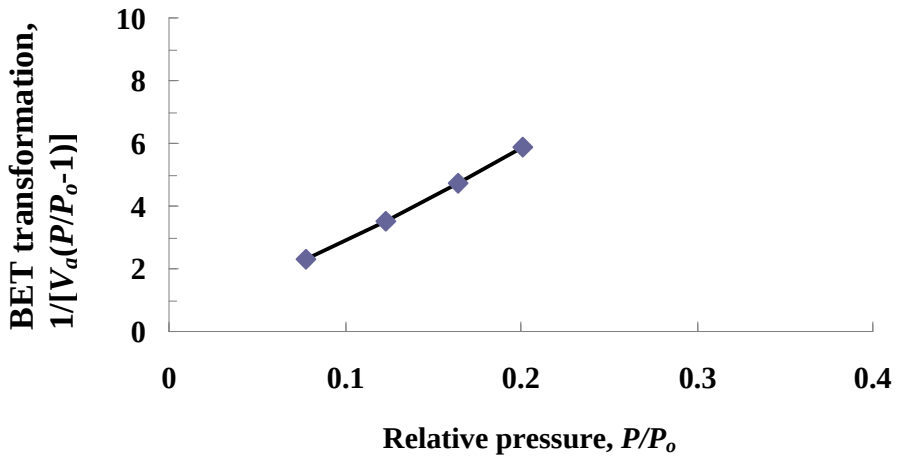

Figure C.6 BET transformation

To describe the thickness of adsorbed molecules, Harkins and Jura (1944) proposed an empirical equation.

$$log\left(\frac{P}{P_o}\right) = B - \frac{A}{V_a^2} \tag{C-6}$$

where the volume of gas adsorbed V_a was proportional to the statistical thickness, t, of the adsorbed film. Inversely, equation (C-6) can be modified to calculate the thickness, t, as following.

$$t = \left\{ 13.99 \Big/ \left[0.034 - log_{10}\left(\frac{P}{P_o} \right) \right] \right\}^{1/2} \qquad \text{(C-7)}$$

Here, the empirical values are substituted, i.e., the slope A=13.99 and the intercept B=0.034 respectively. Figure C.7 is a plot of volume of adsorbed gas by solid surface versus the thickness at different relative pressure.

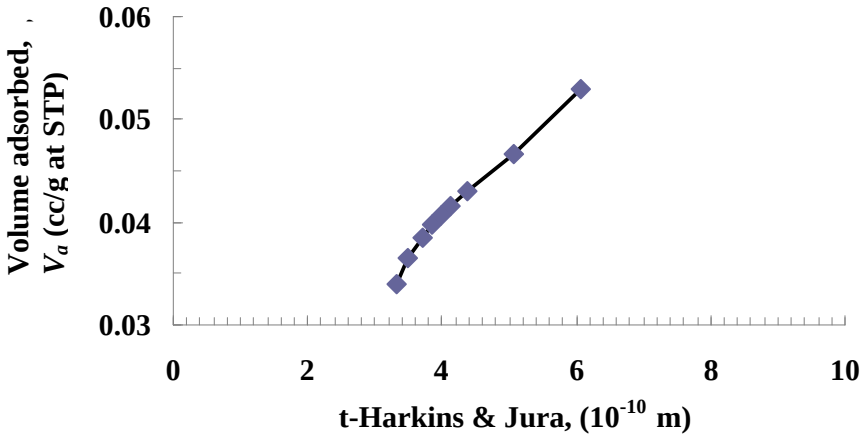

Figure C.7 Thickness plot

C.4.2 Calibration of BET equipment

Calibration is important to know the accuracy of the instrument. A simple test of the system function is to analyze an empty sample tube which should produce a value of zero quantity adsorbed. A more complete test includes data for standard reference materials.

Here a series of calibrations with Kr analysis using low surface area reference materials and an empty sample are used to establish the calibration curves. Table C.2 shows the comparison between measured results and standard test material values.

Table C.2 Calibration results of specific surface area (m^2/g)

Sample	Measured Results	Standard values	Calibration curve
empty	0	0	Y=1.0232x+0.0010
Micromeritics Aluminia	0.4468 ± 0.0053	0.46 ± 0.03	
BCR 170	1.0260 ± 0.0107	1.05 ± 0.05	
BCR 173	8.9577 ± 0.1634	8.23 ± 0.21	Y=0.9203x+0.0497
BCR 173	8.8266 ± 0.1359		

Figure C.8 shows the calibration curves and the uncertainty limits. Figure C.8(b) shows the calibration curve of 4 different standard reference materials (empty, Micromeritics Aluminia, BCR 170, BCR 173) with specific surface area ranging from 0 to 8.5 m^2/g, while Figure C.8 (a) shows the calibration curve of 3 different standard reference materials (empty, Micromeritics Aluminia, BCR 170) that narrows the range of specific surface area less than 1.1 m^2/g. Comparison of R-square of two calibration curve in different ranges shows that the linear regression curve has high R-square and a narrow range of uncertainty. Measurement results of urea particles' specific surface area are less than 1 m^2/g, therefore, the calibration curve in Figure C.8 (a) is better for the calibration of urea particles' specific surface area than that in Figure C.8 (b).

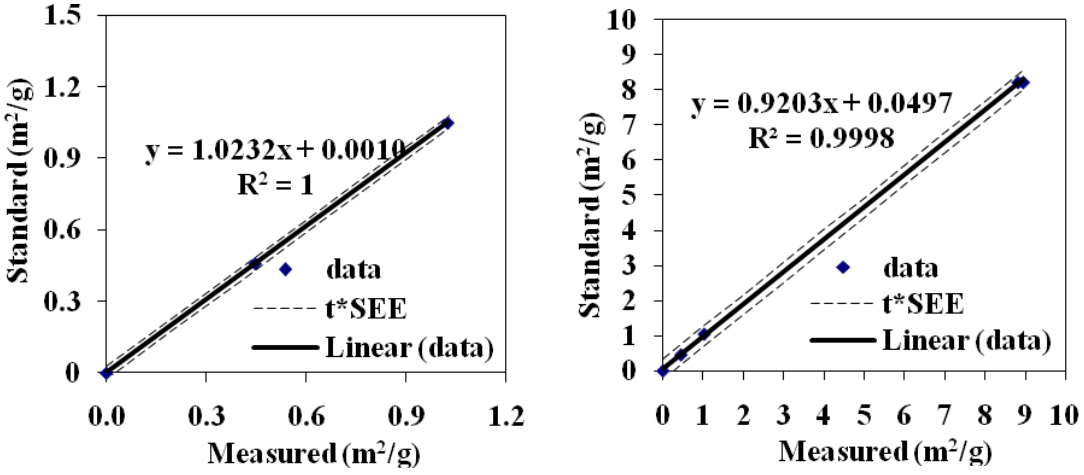

(a) **(b)**

Figure C.8 Calibration curves

C.4.3 Internal properties inside urea particles

C.4.3.1 Specific surface area

After calibration, two different types of dry and wet urea samples were measured with Kr gas. Table C.3 shows the BET analysis results for several samples of total specific surface area for Georgia urea and Terico urea.

Table C.3 Total specific surface area for dry/wet Georgia/Terico urea

Urea Sample		Specific surface area A_m (m^2/g)	Average/uncertainty (m^2/g)
Dry	Georgia 1	0.0705 ± 0.0014	0.072 ± 0.044
	Georgia 2	0.0671 ± 0.0015	
	Georgia 3	0.0415 ± 0.0050	
	Georgia 4	0.1085 ± 0.0421	
Dry	Terico 1	0.1996 ± 0.0039	0.192 ± 0.016
	Terico 2	0.1870 ± 0.0037	
	Terico 3	0.1899 ± 0.0047	
Wet	Georgia 1	0.0581 ± 0.0145	0.072 ± 0.171
	Georgia 2	0.0850 ± 0.0324	
Wet	Terico 1	0.1818 ± 0.0595	0.177 ± 0.056
	Terico 2	0.1730 ± 0.0059	

As SEM pictures indicated in Figure 1.3, both Terico and Georgia urea particles have rough surfaces. Table C.4 shows the allocation of internal and external specific surface area within urea particles. The Carmen equation is used as the best correlation to calculate the specific surface area of a packed bed of smooth particles especially for materials with smooth and nearly spherical particle shapes. It is shown (section B.3 in Appendix B) that the external specific surface area increases with the decrease in porosity of the bed for the same type of urea particles (the shaken bed has a bigger surface area than unshaken beds); as well smaller urea particle bed has bigger external specific surface area (Georgia urea bed has a bigger

surface area than Terico urea bed). The BET reports give the total specific surface. If rough external surface outside of urea particles are taken into consideration, external specific surface area will greatly increase while the internal specific surface area will decrease to some extent. With known external porosity and smooth external specific surface area based on Carman equation, together with BET results, assume that there exist about 2 layers of rough urea crystals for the Terico urea particles and about 4 layers for the Georgia urea, i.e. n=2 or 4 (see section B.3 in Appendix B), internal properties such as porosity and specific surface area are calculated as follows in Table C.4.

Table C.4 Internal and external specific surface area

Specific surface area for shaken beds			Terico	Georgia
External and smooth one per unit bed volume, $A_{v,e}$ (m^2/m^3)			1204	1992
External and smooth one per unit solid volume, $A_{vs,e}$ (m^2/m^3)			1881	3113
External and smooth one per unit mass, $A_{m,e}$ (m^2/g)			0.0014	0.0024
Total one per unit mass		A_m (m^2/g)	0.1922	0.0719
Suppose 2 layers crystal cubes	External specific surface area	$(A_{m,e})_{rough}$ (m^2/g)	0.0156	0.0259
	Internal specific surface area	$A_{m,i}$ (m^2/g)	0.1766	0.0460
	Internal surface ratio	$A_{m,i} / A_m$	0.92	0.64
Suppose 4 layer crystal cubes	External specific surface area	$(A_{m,e})_{rough}$ (m^2/g)	0.0327	0.0541
	Internal specific surface area	$A_{m,i}$ (m^2/g)	0.1595	0.0178
	Internal surface ratio	$A_{m,i} / A_m$	0.83	0.25

The results show that for Terico urea, internal specific surface area dominates the total specific surface area, or the external specific surface area is smaller than the internal one. However for Georgia urea with smaller particle diameter, the roughness of the external surface has an important effect on the allocation of surface area.

C.4.3.2 Internal porosity

Results of specific surface area are based on krypton gas analysis. But krypton gas analysis failed to give information about internal pore volume and size distribution. Table C.5 shows internal pore volume and pore diameter using nitrogen analysis as well as the calculated internal porosity using equation (C-4) for two Terico urea samples. Same BET analysis using Nitrogen gas for Georgia urea particles failed.

Table C.5 Average internal porosity and pore diameter of Terico urea samples

Terico urea sample		1	2
Total adsorption pore volume V_{M_pore} (cc/g)		0.000876	0.000951
Internal porosity, ε_i		0.00116	0.00126
Internal pore diameter or internal hydraulic diameter $d_{h,i}$, $\overset{o}{A}$ (10^{-10} m) without distinguishing internal and external surface area		102.27	108.15
If internal and external surface area are distinguished	$A_{m,i} / A_m$	0.9	0.9
	$d_{h,i}$, ($\overset{o}{A}$ or 10^{-10} m)	116.75	123.46
If internal and external surface area are distinguished	$A_{m,i} / A_m$	0.6	0.6
	$d_{h,i}$, ($\overset{o}{A}$ or 10^{-10} m)	170.45	180.25

C.4.3.3 Internal diffusion

The calculated internal porosity shows that a tiny pore volume fraction exists inside the urea particles and these pores inside are mesopores which is defined as pores between $20\,\overset{o}{A}$ and $500\,\overset{o}{A}$. For water vapor molecules, the mean free path is calculated as

$$\lambda = \frac{k_B T}{2^{5/2} \pi R_m^2 P} \tag{C-8}$$

where k_B is Boltzman constant, $k_B = 1.381 \times 10^{-23}$ J/K ; T is temperature, (K); R_m is collision radius of the molecule, $R_m = 1.8\,\text{Å}$ for air molecules and $R_m = 2.3\,\text{Å}$ for water vapor molecules; P is pressure (P_a). For water vapor at room temperature (295 K) and 1 atm, the mean free path of water vapor molecules $\lambda \approx 400\,\text{Å}$ which is greater than the average pore diameter $d_{h,i} \approx 100 - 200\,\text{Å}$. Since the ratio of mean free path to the estimated average pore size lies in range of 1~10, both Knudsen diffusion and Fick diffusion are important for the transient process during water adsorption within urea particles. It is those tiny mesopores inside that make the internal specific surface area dominate the total specific surface area.

Surface diffusion of adsorbed water may be more important for transient process. How the water diffuses inside each urea particle depends on the structure of internal pores and their distribution inside, however, results of the BET test give only the average information about specific surface area and pore volume of urea samples. Although the BET tests cannot show how the internal cracks are interconnected, the SEM photos in Figure 1.3 imply small external surface area pores connected to larger internal pores. The experimental data and numerical simulation shows that the apparent internal diffusion coefficient increases with the mass of water adsorbed in the urea particles, i.e. internal diffusion coefficient is a function of moisture content and exponentially increases with moisture content. This can be explained by the hypothetical structure of pores inside urea particles shown in Figure C.9.

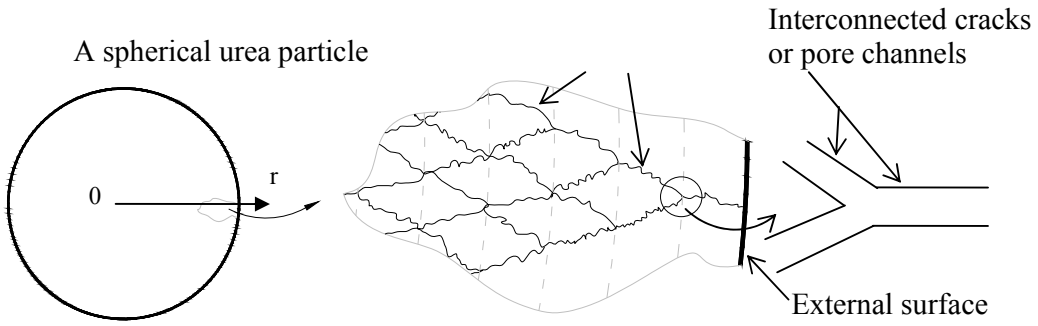

Figure C.9 Hypothetical 2-D network of interconnected crack structures inside a urea particle

Usually pores inside solid particles are taken as lots of cylindrical channels or cracks. When water vapor penetrate into the internal and external surfaces of dry urea particles, one layer of water molecules is firstly adsorbed on the urea surface due to the electrostatic force between urea molecules and water molecules. Then water molecules continue to accumulate on the first layer of water molecules to form a multilayer of molecules of liquid water which can diffuse due to vapor pressure differences or flow through the cracks due to pressure differences. For Georgia urea the penetration of cracks inside urea particles (opposite to r direction), may grow exponentially in number from the external particle surface toward the center because this type of urea is formed by solidifying the liquid urea droplet from the outer surface towards the center where there is more phase change shrinkage. Figure C.9 shows a hypothetical 2-D network structure with exponentially increasing number of cracks or pore channels with distance from the external surface toward the center.

APPENDIX D

A NEW METHOD TO DETERMINE THE HEAT AND MASS CONVECTION COEFFICIENTS IN SPHERICAL PARTICLE BEDS

D.1 Background

Porous beds of particles with a temperature difference between the particles and the interstitial fluid flow are widely used in industry. The determination of the convective heat transfer coefficient, obtained by direct transient measurements or indirectly using simulations, has not lead to a single correlation with a small uncertainty bound. Many correlations of Nusselt number versus Reynolds number have been proposed to predict the convective heat transfer during fluid flow through porous beds. For the same Reynolds number, these correlations differ by more than an order of magnitude. Travkin and Catton (2001) reviewed a series of research studies that used direct measurement and indirect volume averaging analysis technique to find the internal heat or mass transfer coefficients between interstitial fluid flow and a bed of particles for different types of porous media. They found that there are large discrepancies between the predictions from various research groups who used the volume average technique (VAT).

Nie et al. (2008 a & b, 2009 a) presented two different methods to determine the internal heat or mass convection coefficients within a urea particle bed. Nie et al. (2008 a & b) proposed an inverse mathematical method in which numerical simulation results were compared with experimental data of moisture uptake in urea beds. Nie et al. (2009a) used a series of rapid step temperature change experiments to obtain the outlet air temperature responses. A justified theoretical method was presented to derive a relationship between outlet air temperature response and heat convection coefficients. Comparison between theoretical solution and experimental data gave the convective heat transfer coefficient. However the discrepancy up to two orders of magnitude existed between correlations deduced from above two different methods.

Kar and Dybbs (1982) presented the existence of discrepancies among correlations using same methods for different materials or same materials by different researchers but did not explore further causes and reasons. From a theoretical point of view, the Nusselt number should only depend on the geometry of the air flow passages in the bed, Reynolds number and Prandtl number (Shah & London, 1978). That is, changes in the size or type of particle should not be independent variables but changes in the shape of particles and changes in arrangement of particles will be independent factors. Discrepancies in the correlations and deficiencies in the uncertainty analysis imply that there is a need to develop a simple test method to improve the correlation between Nusselt number and Reynolds number and to include a complete uncertainty analysis.

D.2 Experimental method

D.2.1 Experimental test rig

The same experimental test rig and air conditioning system as shown in Figure 2.1 and 2.2 in Chapter 2 are used. But in this appendix, only heat transfer, i.e., the temperature step change at the inlet is considered. A series of tests are performed at several different air flow rates (i.e., 20, 30, 50, 80, 100, 120, 160 and 180 Lpm, the corresponding Darcy velocity are 0.164, 0.247, 0.411, 0.658, 0.822, 0.987, 1.316, 1.480 m/s) for three different types of spherical particles (i.e., lead, steel and glass). These particle properties/particle bed properties and air flow are shown in Table D.1.

Table D.1 Properties of the particles/particle beds and air flow

Properties	Materials					
	Glass		Lead		Steel	
Solid density, ρ_s (kg/m^3)	2300		11300		7800	
Solid specific heat capacity, Cp_s (J/(kg.K))	746.2		130		465	
Solid conductivity, K_s (W/(m.K))	20.2		1.35		54	
Particle size, d_p (mm)	1.0±0.05	3.0±0.05	2.0±0.05	2.5±0.05	3.2±0.05	2.5±0.05
Bed length L (mm)	89.53 ±0.05	91.29 ±0.05	89.96 ±0.05	90.65 ±0.05	90.93 ±0.05	91.68 ±0.05
Solid mass M_s (kg)	0.29629	0.29736	1.22361	1.20784	0.90374	0.8904
Solid fraction, ε_s	0.673	0.655	0.594	0.582	0.628	0.614
Number of particles, N_s	246031	9145	25851	13065	6753	13953
Specific surface area, A_m (m^2/kg)	2.6087	0.8696	0.26549	0.21239	0.24038	0.30769
Specific surface area, A_v (m^2/m^3)	4259.5	1397.5	1781.6	1396.2	1178.8	1474.4
Re_{d_h} at 180 Lpm	90.4	275.6	216.2	259.1	325.5	207.6
Re_{d_h} at 160 Lpm	80.4	2445.0	192.2	230.3	289.3	184.5
Re_{d_h} at 120 Lpm	60.3	183.7	144.1	172.8	217.0	138.4
Re_{d_h} at 100 Lpm	50.2	153.1	120.1	143.9	180.8	115.3
Re_{d_h} at 80 Lpm	40.2	122.5	96.1	115.2	144.7	92.3
Re_{d_h} at 50 Lpm	25.1	76.6	60.1	72.0	90.4	57.7
Re_{d_h} at 30 Lpm	15.1	45.9	36.0	43.2	54.3	34.6
Re_{d_h} at 20 Lpm	10.0	30.6	24.0	28.8	36.2	23.1

D.2.2 Data

Figure D.1 shows typical transient air temperature at the inlet and outlet, and the solid particle bed temperature at three axial positions in the steel bed when the air flow rate was 180 Lpm. The outlet air temperature shows a delayed response because the particle bed temperature increases gradually from the inlet to the outlet due to the thermal energy storage in the bed. Figure D.2 shows the solid particle bed temperature distribution along the bed length at different times. Generally the particle temperature distribution within the bed is not linear at any time. However, near one specific time or over a finite time period, the solid particle temperature distribution is almost spatially linear. For example, the solid particle temperature spatial distribution at 41.85 s is essentially linear but is non-linear at 19.78 s and 60.46 s. The linearity of the bed temperature distribution was determined by a correlation fit of the data.

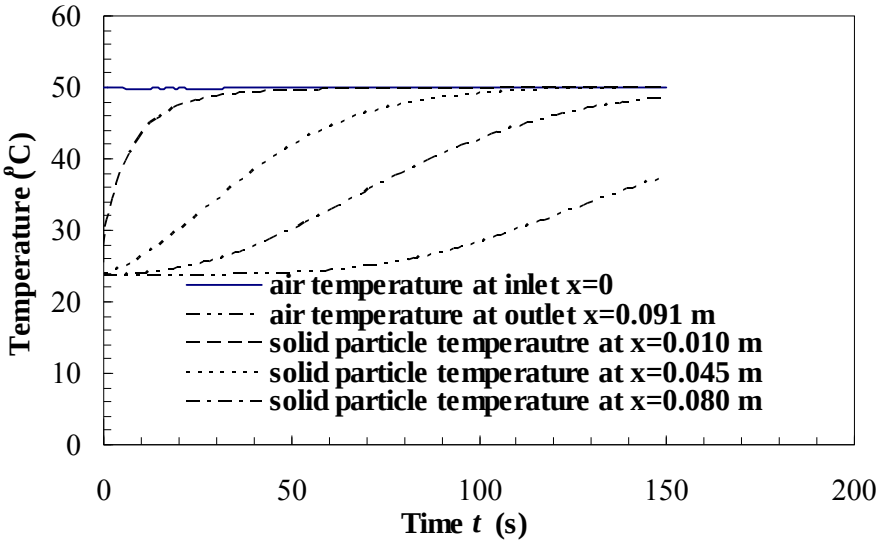

Figure D.1 Transient air temperature at the inlet and outlet, and the solid steel particle bed (d_p=2.5 mm) temperature at three axial positions of the bed subject to 1.48 m/s air flow speed at the inlet.

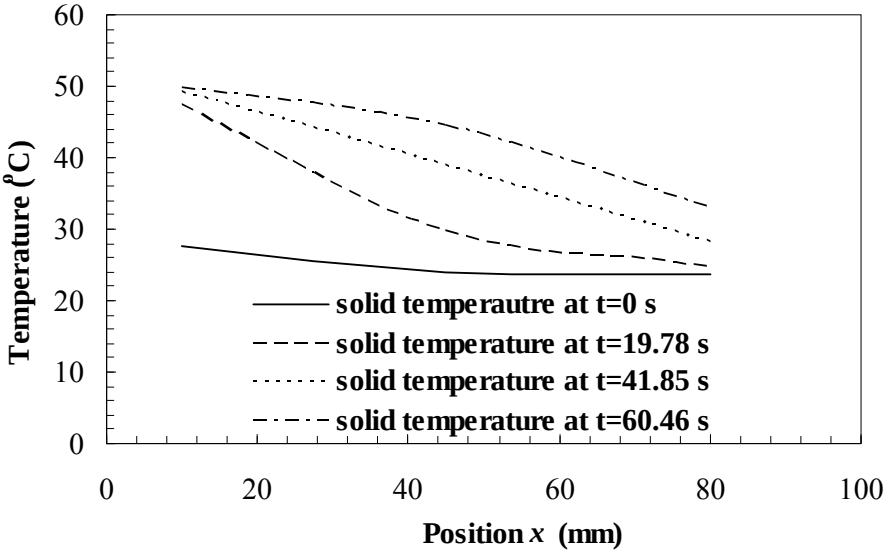

Figure D.2 Solid steel particle bed (d_p=2.5 mm) temperature distribution at different times along the axial position of particle bed subject to 1.48 m/s air flow speed at the inlet.

D.3 Theoretical analysis

When the inlet hot air passes through the particle bed that is initially at room temperature, the particles at different axial positions gain thermal energy by heat convection between air and particles and heat conduction between particles in a layer-wise fashion. As presented by Nie et al. (2008a & b) the temperature gradient inside each solid particle is negligible since the Biot number for each particle is very low. Therefore, at any time the governing equation per unit volume is

$$\rho_s Cp_s \varepsilon_s \frac{\partial T_s}{\partial t} = K_{s,eff} \frac{\partial^2 T_s}{\partial x^2} + \sigma \cdot e \cdot A_v \left(T_{s'}^4 - T_s^4\right) + A_v h_t \left(T_a - T_s\right) \quad \text{(D-1)}$$

where ρ_s is the density of solid particles, Cp_s is the heat capacity of solid particles, ε_s is the volume fraction of solid particles within the bed, $K_{s,eff}$ is the effective thermal conductivity of solid particles, σ=5.6703 10^{-8} (W/m^{2}K^4) is the Stefan-Boltzmann Constant, e is the surface emissivity, A_v is the specific air-particle surface area based on the bed volume, and h_t is the local convective heat transfer coefficient within the particle bed. As the solid temperature and

air temperature are both functions of time and axial position, integration of equation (D-1) along the bed length, L, and over time period t_1 to t_2 gives

$$\rho_s Cp\ \varepsilon_s\left(\int_0^L T_s\big|_{t=t_2}dx-\int_0^L T_s\big|_{t=t_1}dx\right)=K_{s,eff}\int_{t_1}^{t_2}\left(\left.\frac{\partial T_s}{\partial x}\right|_{x=L}-\left.\frac{\partial T_s}{\partial x}\right|_{x=0}\right)dt$$
$$+\sigma\cdot e\cdot A_v\int_{t_1}^{t_2}\int_0^L\left(T_{s'}^4-T_s^4\right)dxdt+A_v\bar{h}_t\left(\int_0^L\int_{t_1}^{t_2}T_a\,dtdx-\int_0^L\int_{t_1}^{t_2}T_s\,dtdx\right) \tag{D-2}$$

The volume average convective heat transfer coefficient between solid particle and air flow $\bar{h}_t$ within the bed can be obtained using equation (D-3).

$$\bar{h}_t=\frac{(1-f_c-f_r)\rho_s Cp_s\varepsilon_s\left(\int_0^L T_s\big|_{t=t_2}dx-\int_0^L T_s\big|_{t=t_1}dx\right)}{A_v\left(\int_0^L\int_{t_1}^{t_2}T_a\,dtdx-\int_0^L\int_{t_1}^{t_2}T_s\,dtdx\right)} \tag{D-3}$$

where f_c and f_r

$$f_c=\frac{K_{s,eff}\int_{t_1}^{t_2}\left(\left.\frac{\partial T_s}{\partial x}\right|_{x=L}-\left.\frac{\partial T_s}{\partial x}\right|_{x=0}\right)dt}{\rho_s Cp_s\varepsilon_s\left(\int_0^L T_s\big|_{t=t_2}dx-\int_0^L T_s\big|_{t=t_1}dx\right)} \tag{D-4a}$$

$$f_r=\frac{\sigma\cdot e\cdot A_v\int_{t_1}^{t_2}\int_0^L\left(T_{s'}^4-T_s^4\right)dxdt}{\rho_s Cp_s\varepsilon_s\left(\int_0^L T_s\big|_{t=t_2}dx-\int_0^L T_s\big|_{t=t_1}dx\right)} \tag{D-4b}$$

are defined as the ratio of the conduction and radiation energy to the total heat energy storage within the solid particle bed over the time interval $t_1<t<t_2$.

In a modeling study on moisture uptake and transport in beds of urea particles, Nie et al. (2008b) assumed that there was no heat flux through the particles at both inlet and outlet of the urea particle bed which implied that f_c was zero at all times. However, this assumption deserves further verification. Since the air temperature at the inlet and outlet, and the solid particle temperature at three axial positions are measured and recorded approximately every 1.5 seconds, it is possible to determine the period of time, from t_1 to t_2, when the solid particle temperature distributions are almost spatially linear. In this work, the criteria for this time period when the temperature distribution of particles in the bed is linear is chosen by performing a linear curve fit on the data and stating a minimum coefficient of determination

during this period for the linear distribution. At times t_1 and t_2, which corresponds to the start and end of the linear distribution period, the required minimum coefficient of determination was set at 0.995, while at the midway time the coefficient of determination is at least 0.999. Since at any time during this linear period, the value of $\int_{t_1}^{t_2}\left(\left(\partial T_s/\partial x\right)\big|_{x=L}-\left(\partial T_s/\partial x\right)\big|_{x=0}\right)dt$ can be considered to be close to zero, and $\int_0^L T_s\big|_{t=t_2}dx-\int_0^L T_s\big|_{t=t_1}dx=\left(T_s\big|_{t=t_2,x=L/2}-T_s\big|_{t=t_1,x=L/2}\right)L$. During this time period, the solid particle bed gains energy from the hot air, implying $T_s\big|_{t=t_2,x=L/2}-T_s\big|_{t=t_1,x=L/2}\neq 0$.

Kaviany (1995) indicated that the effective thermal conductivity of beds K_{eff} was dependent on the thermal conductivity of each phase or the relative magnitude of them, the structure of the solid matrix, the contact resistance between non-consolidated particles and the comparison between the mean free path and the pore size. Kaviany also summarized the effective thermal conductivity of beds of spherical particles predicted by various analysis and compared with experimental data. It was stated that $K_{s,eff}/K_a < K_{eff}/K_a = 8\sim 20$ when $K_s/K_a = 50\sim 2000$. Thus the parameter, f_c, which is the ratio of conduction energy to thermal energy stored in the particles can be determined knowing $K_{s,eff}$, the particle properties listed in Table 1 and the bed length. For these particle beds, f_c was found to be much less than one, e.g., $f_c \sim O(10^{-7})$ for the steel beads in Figure D.4.

Since $\sigma\cdot e\cdot A_v\int_{t_1}^{t_2}\int_0^L\left(T_{s'}^4-T_s^4\right)dxdt=\sigma\cdot e\cdot A_v\Delta t\cdot d_p\sum_{i=1}^{N_l}\left[(T_{s,i+1}^4+T_{s,i-1}^4)/2-T_{s,i}^4\right]_{t=(t_1+t_2)/2}$ in equation (D-4b), the ratio of radiation energy to thermal energy stored in the particles, f_r, was estimated to be also much less than 1, e.g., $f_r \sim O(10^{-4})$ for the steel beads in Figure D.4. This has been verified by Kar and Dybbs (1982). Therefore, the volume average convective heat transfer coefficient, $\overline{h}_t$, can now be calculated via equation (D-3) if the air and solid particle temperatures, $\hat{T}_a$ and $\hat{T}_s$, can be estimated.

Both the solid and air temperature will be spatially and temporally linear over this time interval. The linearity of temporal temperature distribution was verified by the curve fit of the experimental data in which the determination of coefficients was close to 1.0. Therefore, the double integrations, in equation (D-3) can be expressed as

$$\int_0^L\int_{t_1}^{t_2}T_a\,dtdx=\Delta t\int_0^L\overline{T}_a\,dx \qquad \text{(D-5)}$$

$$\int_0^L \int_{t_1}^{t_2} T_s dt dx = \Delta t \int_0^L \overline{T}_s dx \tag{D-6}$$

where $\overline{T}_s = T_s\big|_{t=(t_1+t_2)/2}$ and $\overline{T}_a = T_a\big|_{t=(t_1+t_2)/2}$

The solid particle temperature and air temperature distribution at times, t_1, $(t_1+t_2)/2$, and t_2 are estimated to follow the linear equations. Also the linearity of spatial temperature distribution at times, t_1, $(t_1+t_2)/2$, and t_2 was also verified by the curve fit of experimental data in which the determination of coefficients was close to 1.0.

$$\hat{T}_s\Big|_{t=t_1} = a_1 + b_1 x \tag{D-7a}$$

$$\hat{T}_s\Big|_{t=(t_1+t_2)/2} = a_0 + b_0 x \tag{D-7b}$$

$$\hat{T}_s\Big|_{t=t_2} = a_2 + b_2 x \tag{D-7c}$$

$$\hat{T}_a\Big|_{t=(t_1+t_2)/2} = c_0 + d_0 x \tag{D-8}$$

then $\overline{h}_t$ can be simply determined by equation (D-3) rewritten in the form

$$\overline{h}_t \approx \frac{\rho_s Cp_s \varepsilon_s \left[(a_2 - a_1) - (b_2 - b_1)L/2\right]}{A_v \Delta t \left[(c_0 - a_0) - (d_0 - b_0)L/2\right]} \tag{D-9}$$

The ratio of Rayleigh number to Peclet number, Ra/Pe, is much less than 0.1 for all the tests, where $\mathrm{Ra}_{d_p} = g\beta K d_p (T_h - T_c)/(\upsilon\alpha_m)$ and $\mathrm{Pe}_{d_p} = u_p d_p/\alpha_m$ (Nield and Bejan, 1992). This implies that the buoyancy-induced natural convection effects are negligible compared to the forced convection effects in the energy equation (D-1) such that the calculated volume average convective heat transfer coefficient $\overline{h}_t$ is the forced convective heat transfer coefficient.

D.4 Comparison of methodologies

A simplified transient theoretical analysis method, based on the assumption that the air temperature was linearly distributed along the bed length, was described in Chapter 2 to derive the time constant for a typical exponential growth of the outlet air temperature. This time constant was a function of Reynolds number and heat convection coefficient. Theoretical results were in good agreement with the experimental data implying that this linear assumption could be proper for the urea particle bed. However, for spherical particle beds of glass, lead or steel, the outlet air temperature after the bed was not in exponential form as shown in figure D.1.

In section D.3, a new theoretical analysis of the solid particle phase energy change was developed during a specific time period when the measured bed temperature was almost linearly distributed to deduce the new heat convection coefficient. For glass bead beds, if we substitute the heat convection coefficient from equation (D-9) into equation (3-18), the time constant for the outlet air temperature can be obtained and compared with the approximate time when the measured experimental data of normalized outlet air temperature is 0.632. The comparison presented in Table D.2 shows a small discrepancy between these two time constants. Figure D.3 shows the comparison between the prediction of the outlet air temperature, using the assumption of the linear temperature distribution along the bed all the time, and the experimental data for a bed of glass beads with a diameter of 1 mm at air flow rate of 180 Lpm. The discrepancy, especially for the first 125 seconds, verifies that the linear air temperature distribution along the bed length at any time is invalid for the beds of glass beads. A similar comment can be made for lead or steel particle beds. That is reason why the research work in this appendix D are required to justify the assumption of linear spacial distribution and develop a new method to derive the correlation of Nusselt number and Reynold number.

Table D.2 Comparison of experimental and predicted time constants for a bed of glass beads with two different diameters

Glass beads size (mm)	Air flow rate (Lpm)	Time when normalized experimental outlet air temperature is 0.632 (s)	Time constant predicted using equation (3-18) (s)
1mm	180	125	108
	160	126	122
	120	162	163
	100	190	195
	80	233	244
	50	390	391
	30	665	686
	20	927	961
3mm	180	101	106
	160	115	121
	120	150	159
	100	178	190
	80	219	238
	50	357	379
	30	644	624
	20	953	944

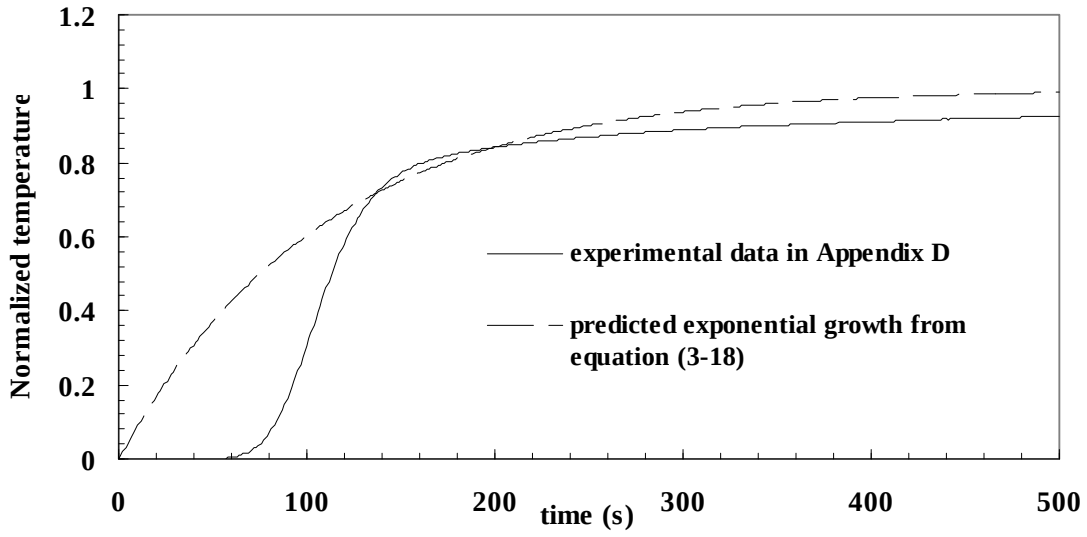

Figure D.3 Comparison between experimental data in appendix D and predicted exponential growth from equation (3-18) for the outlet air temperature after a bed of 1 mm glass beads subject to 1.48 m/s air flow speed at the inlet.

D.5 Results and discussion

There have been several research studies about the determination of the convective heat transfer coefficient between a gas or liquid and a porous particle bed. Since spherical particle beds are considered, the following literature is selected based on the spherical (or cylindrical if aspect ratio of cylinder length to diameter is 1) particle beds or porous media with same range of Reynolds number or porosity. Kar and Dybbs (1982) developed a correlation for sintered powder metal (stainless steel, nickel and copper) specimens with a porosity range from 0.26 to 0.653 for Darcian type laminar flow with Reynolds number range from 0.5 to 10 which were based on mean pore diameter (equivalent to the hydraulic diameter).

$$\mathrm{Nu}_{d_h} = 0.004 \times \mathrm{Re}_{d_h}^{1.35\pm0.14}\,\mathrm{Pr}^{1/3} \quad , 0.5 < \mathrm{Re}_{d_h} < 10 \qquad \text{(D-10a)}$$

where $\mathrm{Nu}_{d_h} = h_t \times d_h / k_a$, $\mathrm{Pr} = \upsilon/\alpha$ and $\mathrm{Re}_{d_h} = u_p d_h / \nu_a$.

For rigid-mesh materials with a porosity of 0.054 the convective heat transfer correlation for Reynolds number range from 20 to 200 was given by

$$\mathrm{Nu}_{d_h} = 0.025 \times \mathrm{Re}_{d_h}^{0.97}\ \mathrm{Pr}^{1/3}, 20 < \mathrm{Re}_{d_h} < 200 \quad \text{(D-10b)}$$

Kays and London (1984) presented experimental data and an empirical correlation for gas flow through a randomly packed spherical particle bed with a porosity range of 0.37 to 0.39 and a Reynolds number range of $10 \le \mathrm{Re}_{d_h} \le 5000$ given by equation (D-11a).

$$\mathrm{Jh} = \mathrm{St} \cdot \mathrm{Pr}^{2/3} = 0.23\,\mathrm{Re}_{d_h}^{-0.3} \quad \text{(D-11a)}$$

where $\mathrm{St} = h_t / (\rho c_p)_a u_p$. This can be transformed to

$$\mathrm{Nu}_{d_h} = 0.23\,\mathrm{Re}_{d_h}^{0.7}\ \mathrm{Pr}^{1/3} \quad \text{(D-11b)}$$

Peng et al. (2000) indirectly developed the correlation, shown in equation (D-12a), to obtain convective heat and mass transfer coefficients and to simulate the non-equilibrium heat and mass transfer process within a packed potash bed for a Reynolds number range of 20 - 100.

$$\mathrm{Jh} = \mathrm{St}\,\mathrm{Pr}^{2/3} = 0.048 \times \mathrm{Re}_{d_h}^{-0.3} \quad \text{(D-12a)}$$

which can be transformed to

$$\mathrm{Nu}_{d_h} = 0.048\,\mathrm{Re}_{d_h}^{0.7}\ \mathrm{Pr}^{1/3} \quad \text{(D-12b)}$$

Potash particles which contain crystalline salt particles, have a complex shape that is difficult to characterize.

Nsofor and Adebiyi (2001) developed a correlation for the gas-pellet heat transfer using cylindrical pellets with an aspect ratio of 1 with a Reynolds number range of 50-170 based on particle diameter.

$$\mathrm{Nu}_{d_p} = 8.74 + 9.34[6(1-\varepsilon)]^{0.2}\ \mathrm{Re}_{d_p}^{0.2}\ \mathrm{Pr}^{1/3} \quad \text{(D-13a)}$$

where d_p was the equivalent diameter of spherical particles for this cylindrical pellet bed. Using the relationship between particle diameter and hydraulic diameter, $d_h / d_p = 2\varepsilon / [3(1-\varepsilon)]$, the correlation (D-13a), for a single bed of metal particles with known porosity 0.32, can be rewritten based on hydraulic diameter, giving

$$\mathrm{Nu}_{d_h} = 2.74 + 3.08\,\mathrm{Re}_{d_h}^{\ 0.2}\,\mathrm{Pr}^{1/3} \qquad \text{(D-13b)}$$

where Reynolds number based on hydraulic diameter ranges from 17 to 57.

Nie et al. (2008 a & b) measured and simulated the uptake of moisture within a urea particle bed subject to humid air flow through the bed. Using an inverse technique to determine the convective heat and mass transfer coefficient within the bed for a Darcy or nearly Darcy flow where $0.2 < \mathrm{Re}_{d_h} < 10$, the correlation equation (D-14a) was developed.

$$\mathrm{Jh} = \mathrm{St}\,\mathrm{Pr}^{2/3} = 0.023 \times \mathrm{Re}_{d_h}^{\ -0.3} \qquad \text{(D-14a)}$$

which can be transformed to

$$\mathrm{Nu}_{d_h} = 0.023\,\mathrm{Re}_{d_h}^{\ 0.7}\,\mathrm{Pr}^{1/3} \qquad \text{(D-14b)}$$

Urea particles are spherical in shape with a small internal porosity in each particle.

The transient energy balance is integrated over both a time period and over bed length, in order to determine the convective heat transfer coefficients for non-Darcy flow over a Reynolds number range of $5 < \mathrm{Re}_{d_h} < 280$. Spherical glass, lead and steel particles each with two diameters were used as the bed materials and the beds were subjected to several step changes in air temperature for each flow entering the bed.

Figure D.4 is a plot of Nusselt number versus Reynolds number for both the curve fits and data of the convective heat transfer coefficients calculated using equation (D-15).

$$\mathrm{Nu}_{d_h} \Big/ \mathrm{Pr}^{1/3} = C \times \mathrm{Re}_{d_h}^{\ n} \qquad \text{(D-15)}$$

The effect of Prandtl number variation was not investigated in this study; however, we expect it to have a similar form as presented by others. For glass beads with diameters of 1.0 mm and 3.0 mm, the correlation (D-15) gives $C = 0.0416 \pm 0.0280$, $n = 0.8883 \pm 0.1285$, $R^2 = 0.9628$, and the correlation uncertainty is $t \times SEE = 0.7902$ at the 95% confidence level. For steel beads with diameters of 2.5 mm and 3.2 mm, $C = 0.0265 \pm 0.0354$, $n = 0.9912 \pm 0.2674$, $R^2 = 0.9308$, and the correlation uncertainty is $t \times SEE = 1.0598$ at the 95% confidence level. For lead beads with diameters of 2.5 mm and 3.0 mm, $C = 0.0863 \pm 0.1041$,

$n = 0.7410 \pm 0.2069$, $R^2 = 0.9065$, and the correlation uncertainty is $t \times SEE = 1.2974$ at the 95% confidence level. Figure D.5 also shows the uncertainty bounds of correlations for glass, lead and steel beads overlapping between $5 < \mathrm{Re}_{d_h} < 280$, verifying that the Nusselt number only depends on the dimensional geometry of the air flow passages in the bed (i.e. spherical particles with a measured porosity), Reynolds number and Prandtl number, and is independent of the type of particle and their size.

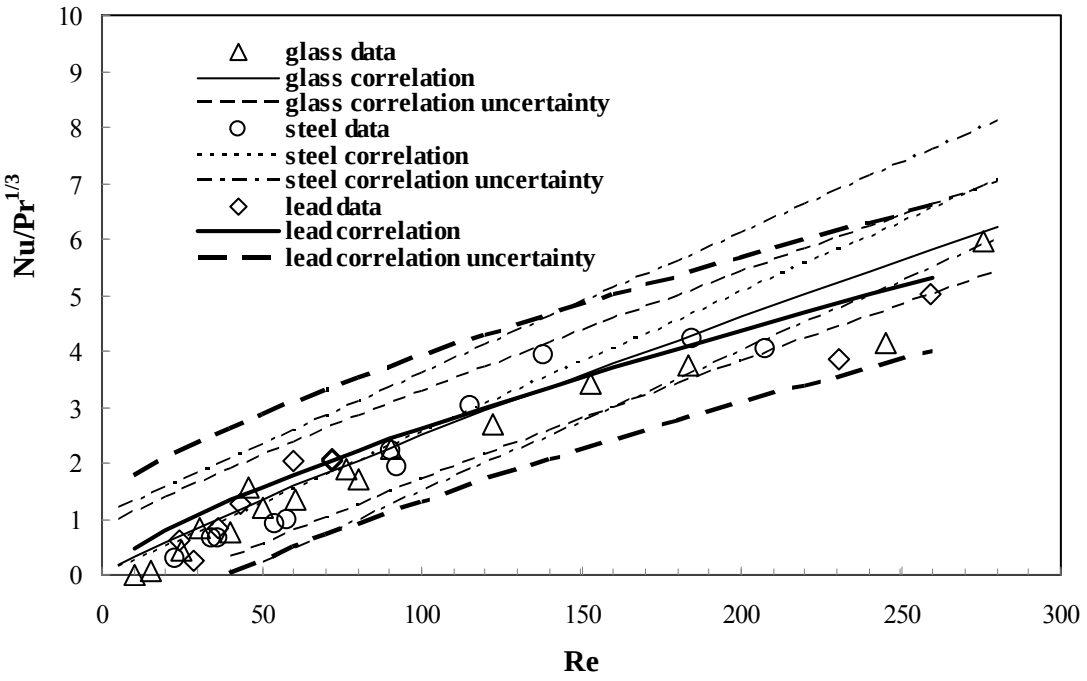

Figure D.4 Experimental data and correlation of Nusselt number versus Reynolds number for beds of spherical glass, steel or lead particles.

To obtain a universal empirical correlation that is independent of the particle material, all of the experimental data for three materials tested were combined together. This yielded the following correlation for the range of $5 < \mathrm{Re}_{d_h} < 280$.

$$\mathrm{Nu}_{d_h} / \mathrm{Pr}^{1/3} = (0.0491 \pm 0.0236) \times \mathrm{Re}_{d_h}^{(0.8572 \pm 0.0937)} \qquad \text{(D-16)}$$

For these combined data, the coefficient of determination is 0.9378, with an uncertainty bound of ± 0.8747 for Nu_{d_h} at the 95% confidence level.

Figure D.5 compares the new correlation, given as equation (D-16), with a series of correlations due to other researchers over the same range of Reynolds number presented using a log-log plot. Both Nusselts number and Reynolds number are based on hydraulic diameter. Differences exist between the various correlations by different researchers. Except for the cylindrical particle bed by Nsofor and Adebiyi (2001), other correlations for particle beds, e.g., spherical particle beds by Kays and London (1984), potash particle beds by Peng (2000), bed of rigid-mesh materials with a low porosity by Kar and Dybbs (1982), lie within or are close to the uncertainty bounds of the present correlation of spherical particle beds for $5 < \mathrm{Re}_{d_h} < 280$, indicating that this new correlation obtained using data from a transient step change method, works well. Nsofor and Adebiyi (2001) focused on the cylindrical pellets, not spherical particles and their experiments were at very high temperature while both radiation and free convection were ignored. The convection heat transfer coefficient correlation of Nie et al. (2008a & b) using an inverse simulation method for a urea particle bed at low Reynolds number $0.2 < \mathrm{Re}_{d_h} < 10$ is lower than the extension of the current correlation curve but still lies within the uncertainty bounds. The correlation of Kar & Dybbs (1982), for sintered powder metal beds, shows a similar trend in Darcy flow regime to that of Nie et al. (2008b). This implies that using these correlations at low Reynolds numbers, $\mathrm{Re}_{d_h} < 10$, will result in relatively large uncertainties compared to $\mathrm{Re}_{d_h} > 100$.

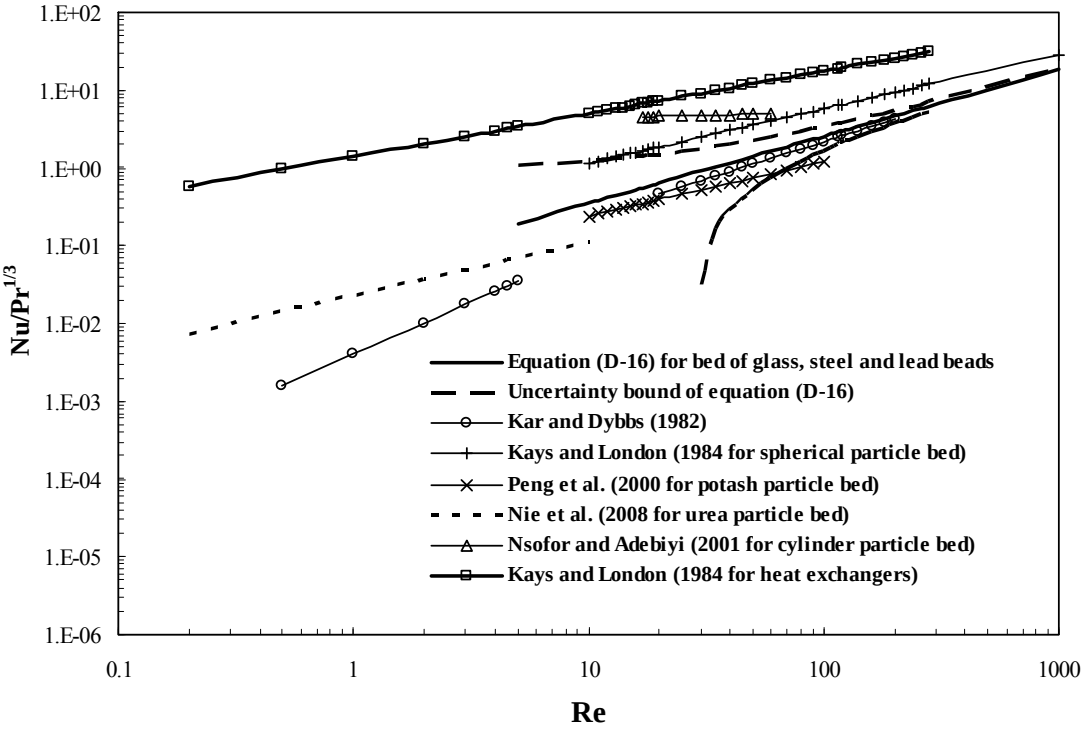

Figure D.5 Comparison of the correlations

D.6 Conclusions

A new test method was presented to determine the convection coefficients in particle beds. A series of experiments on the transient temperature response of particle beds were carried out while the bed was subject to a temperature step change at the inlet. A new method of analysis was presented, for the time interval when the bed temperature distribution were essentially linear, to determine the effective heat transfer coefficient in the bed.

Several types of spherical particles of different sizes were used in a series of experiments that showed that the new correlation for Nusselt number only depends on the Reynolds number. A new correlation with an uncertainty limit at the 95% level for the range $5 < \mathrm{Re}_{d_h} < 280$ was $\mathrm{Nu}_{d_h} \big/ \mathrm{Pr}^{1/3} = (0.0491 \pm 0.0236) \times \mathrm{Re}_{d_h}^{(0.8572 \pm 0.0937)}$ with uncertainty bound of 0.8747 at 95% confidence level.

This new correlation was different than the other correlations for spherical particles presented in the literature. However, most directly determined previous correlations lied within or were close to the uncertainty bounds of the new correlation. Some correlations, indirectly determined using bed simulations and some correlations directly determined from measured data for low Reynolds number less than 10, appeared to have larger uncertainties than those implied by the new correlation.

APPENDIX E

DISCRETIZATION OF GOVERNING EQUATIONS AND BOUNDARY CONDITIONS

E.1 Control volumes and interfaces

The finite volume method (FVM) (Patankar, 1980) is used to discretize governing equations. Two different but coupled solution domains and their control volumes are shown in Figure E.1, E.2, E.3 and E.4 in which grid point are uniformly spaced.

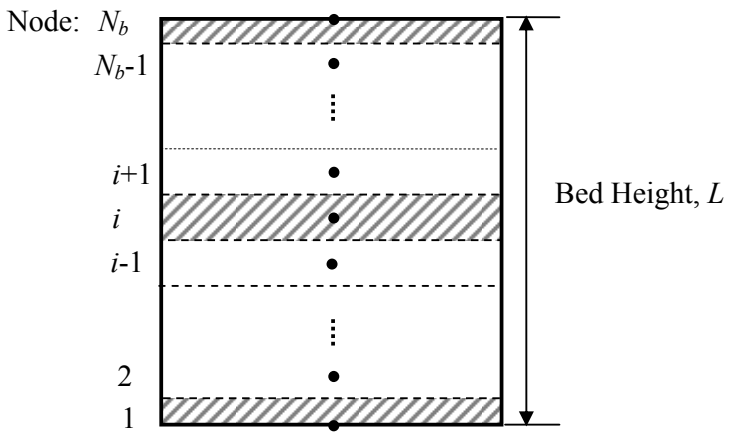

Figure E.1 Schematic diagram of nodes distribution in the external domain of the urea particle bed

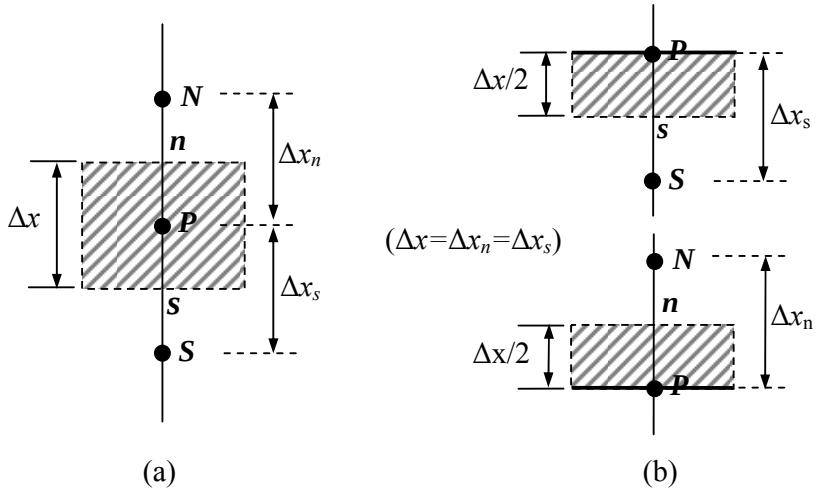

Figure E.2 Geometric schematic diagram of a typical (a) internal control volume at node *P*, and (b) boundary control volume at node 1 and N_b.

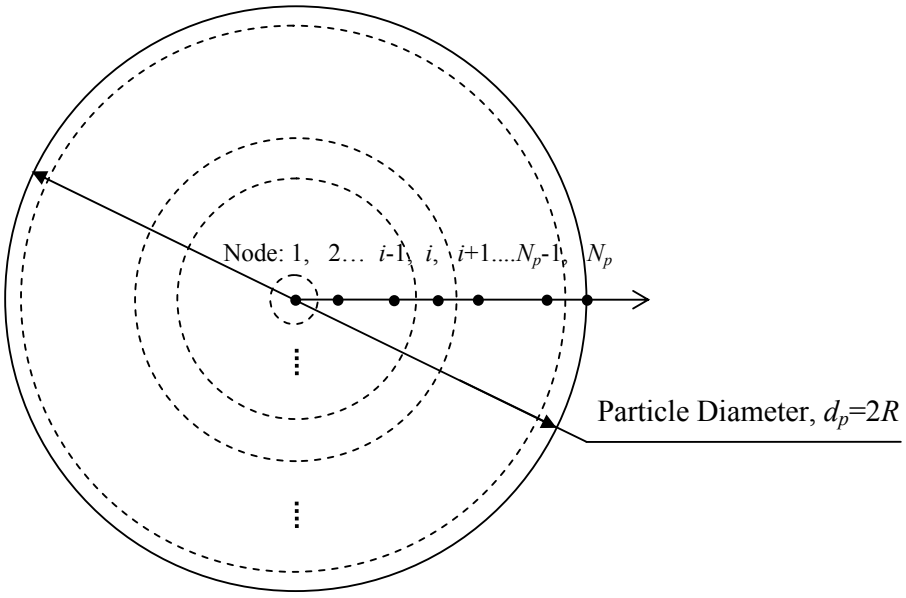

Figure E.3 Schematic diagram of nodes distribution in the internal domain of a urea particle

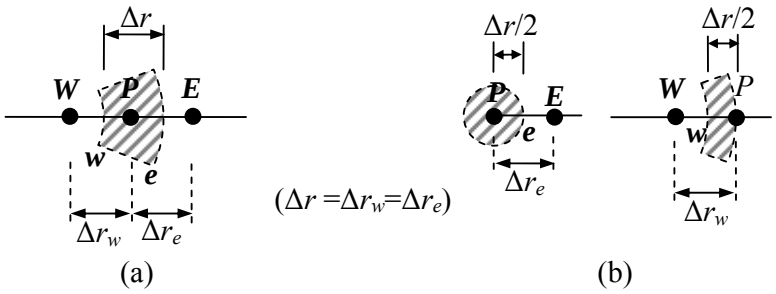

Figure E.4 Geometric schematic diagram of a typical (a) internal control volume at node *P*, and (b) boundary control volume at node 1 and N_p.

Discretized equations can be obtained by integrating governing equations over the control volume space (for example, from *s* face to *n* face, or from *w* face to *e* face for internal control volumes; for boundary control volumes, it will be from node *P* to *e* face, or from *w* face to node *P* as shown in Figure E.2 and E.4) and over the time period *t* to $t+\Delta t$ (i.e. from 0 to 1) to describe how the property of node *P* is calculated from those of its neighbour nodes (*W* and *E*, or *S* and *N*).

Interpolation of some properties at the face between two nodes needs to be defined while integrating governing equations over the control volume. Arithmetic mean is a simple way to evaluate the properties at the face, but harmonic mean takes into account mass or energy continuity, i.e., the heat flux or mass flux through the face. In Cartesian coordinate, heat rate at quasi-steady through n face in Figure E.2 can be expressed as

$$\dot{q}_n = \frac{T_P - T_N}{\frac{1}{K_n}\cdot\frac{1}{\Delta x_n}} = \frac{T_P - T_N}{\frac{1}{K_P}\cdot\frac{1}{\Delta x/2} + \frac{1}{K_E}\cdot\frac{1}{\Delta x/2}} \qquad \text{(E-1)}$$

Therefore, heat conductivity at face *n* can be expressed as

$$K_n = \frac{2K_P K_N}{K_P + K_N} \tag{E-2}$$

Similarly, mass diffusion coefficient at face *n* can be expressed as

$$D_n = \frac{2D_P D_N}{D_P + D_N}. \tag{E-3}$$

In a spherical coordinate, heat rate at quasi-steady state through *e* face in Figure E.4 can be expressed as

$$\dot{q}_e = \frac{T_P - T_E}{\frac{1}{4\pi \cdot K_e} \cdot \left(\frac{1}{r_P} - \frac{1}{r_E}\right)} = \frac{T_P - T_E}{\frac{1}{4\pi \cdot K_P} \cdot \left(\frac{1}{r_P} - \frac{1}{r_e}\right) + \frac{1}{4\pi \cdot K_E} \cdot \left(\frac{1}{r_e} - \frac{1}{r_P}\right)} \tag{E-4}$$

Therefore, heat conductivity at face *e* can be expressed as

$$K_e = \frac{2K_P K_E r_e}{K_P r_P + K_E r_E} \tag{E-5}$$

Similarly, mass diffusion coefficient at face *e* can be expressed as

$$D_e = \frac{2D_P D_E r_e}{D_P r_P + D_E r_E} \tag{E-6}$$

For convection term, $\varphi_e = \frac{1+\alpha_e}{2}\varphi_P + \frac{1-\alpha_e}{2}\varphi_E$, we can take $\alpha_e = 1$ to capture the upwind behaviour which is called upwind differential scheme (UDS). For diffusion term, $\left(\frac{\partial \varphi}{\partial r}\right)_e = \beta_e \frac{\varphi_E - \varphi_P}{\Delta r}$, we tried $\beta_e = 1$ because it is a pure diffusion problem at very low Pe number.

While integrating over the time step, implicit, explicit, Crank-Nicolson scheme can be used as shown in Figure E.5.

$$\int_t^{t+\Delta t} \varphi(t) \cdot dt = \int_0^1 \varphi \cdot dt = \left[(1-f)\varphi^0 + f\varphi^1\right] \cdot \Delta t \tag{E-7}$$

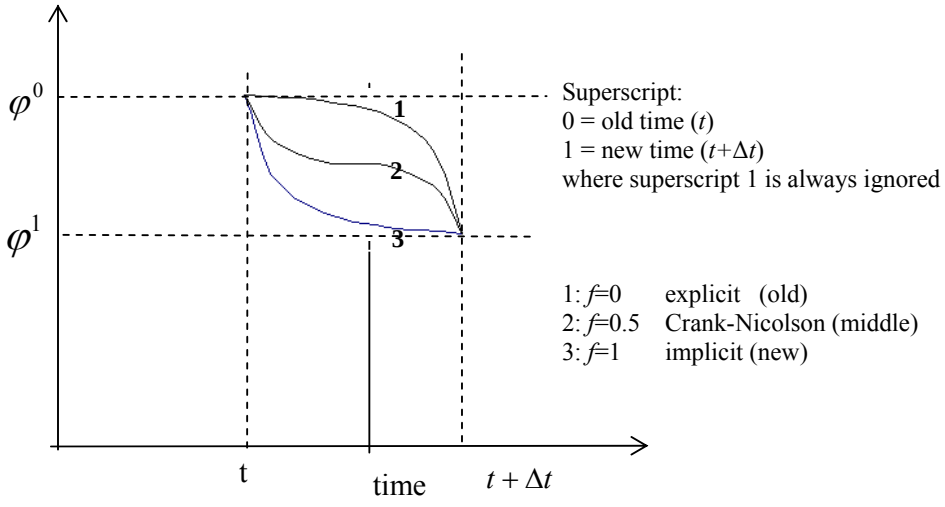

Figure E.5 Implicit, explicit, Crank-Nicolson system

Only the implicit (f=1) method is shown during the following discretization of governing equations.

E.2 Discretization of governing equations

E.2.1 Water vapor transfer in the external domain *e*

$$\frac{\partial\left(\varepsilon_{ge}\rho_{ve}\right)}{\partial t}+\frac{\partial}{\partial x}\left(u_D\rho_{ve}\right)=\frac{\partial}{\partial x}\left(D^t_{e,eff}\frac{\partial\rho_{ve}}{\partial x}\right)-\dot{m}_e+\dot{m}_{ie} \tag{E-8}$$

For an arbitrary internal node *P*, the equation is integrated over the control volume space (from *s* face to *n* face) and over the time period *t* to Δt (i.e. from 0 to 1).

$$\begin{aligned}&\int_s^n\int_0^1\frac{\partial\left(\varepsilon_{ge}\rho_{ve}\right)}{\partial t}dtdx+\int_0^1\int_s^n\frac{\partial}{\partial x}\left(u_D\rho_{ve}\right)dxdt\\&=\int_0^1\int_s^n\frac{\partial}{\partial x}\left(D^t_{e,eff}\frac{\partial\rho_{ve}}{\partial x}\right)dxdt-\int_0^1\int_s^n\dot{m}_e dxdt+\int_0^1\int_s^n\dot{m}_{ie}dxdt\end{aligned} \tag{E-9}$$

After integration with the methods mentioned above, one get that

$$\left(\varepsilon_{ge}\rho_{ve}-\varepsilon_{ge}^{0}\rho_{ve}^{0}\right)_P\Delta x+u_D\left(\rho_{ve,P}-\rho_{ve,S}\right)\Delta t=D_{e,eff,n}\left(\frac{\rho_{ve,N}-\rho_{ve,P}}{\Delta x}\right)\Delta t$$
$$-D_{e,eff,s}^{t}\left(\frac{\rho_{ve,P}-\rho_{ve,S}}{\Delta x}\right)\Delta t-\dot{m}_e\Delta x\Delta t+\dot{m}_{ie}\Delta x\Delta t \tag{E-10}$$

where the source term is

$$-\dot{m}_e=S_{eC}+S_{eP}\rho_{ve,P} \tag{E-11}$$

$$\dot{m}_{ie}=S_{ieC}+S_{ieP}\rho_{ve,P} \tag{E-12}$$

Rearrange this equation in the form of $a_P\rho_{ve,P}=a_N\rho_{ve,N}+a_S\rho_{ve,S}+b$, where

$$a_S=\frac{D_{e,eff,s}^{t}\Delta t}{\Delta x^2}+\frac{u_D\Delta t}{\Delta x} \tag{E-13}$$

$$a_N=\frac{D_{e,eff,n}^{t}\Delta t}{\Delta x^2} \tag{E-14}$$

$$a_P=\varepsilon_{ge,P}+a_S+a_N-S_{eP}\Delta t-S_{ieP}\Delta t \tag{E-15}$$

$$b=\varepsilon_{ge,P}^{0}\rho_{ve,P}^{0}+S_{eC}\Delta t+S_{ieC}\Delta t \tag{E-16}$$

E.2.2 Water vapor diffusion in the internal domain *i*

$$\frac{\partial\left(\varepsilon_{gi}\cdot\rho_{vi}\right)}{\partial t}=\frac{1}{r^2}\cdot\frac{\partial}{\partial r}\left(r^2\cdot D_{i,eff}\cdot\frac{\partial\rho_{vi}}{\partial r}\right)-\dot{m}_i \tag{E-17}$$

For the internal nodes, this equation is integrated over the control volume space and over the time period *t* to Δt

$$\int_w^e\int_0^1\frac{\partial\left(\varepsilon_{gi}\rho_{vi}\right)}{\partial t}dt\cdot 4\pi r^2dr$$
$$=\int_0^1\int_w^e\frac{\partial}{\partial r}\left(r^2\cdot D_{i,eff}\cdot\frac{\partial\rho_{vi}}{\partial r}\right)4\pi dr\cdot dt-\int_0^1\int_w^e\dot{m}_i\,4\pi r^2drdt \tag{E-18}$$

$$\left(\varepsilon_{gi}\rho_{vi}-\varepsilon_{gi}^{0}\rho_{vi}^{0}\right)_P r_P^2\Delta r = \left[\left(r^2 D_{i,eff}\frac{\partial\rho_{vi}}{\partial r}\right)_e-\left(r^2 D_{i,eff}\frac{\partial\rho_{vi}}{\partial x}\right)_w\right]\Delta t-\dot{m}_i r_P^2\Delta r\Delta t \tag{E-19}$$

$$\left(\varepsilon_{gi}\rho_{vi}-\varepsilon_{gi}^{0}\rho_{vi}^{0}\right)_P r_P^2\Delta r=\left(r_e^2 D_{i,e}\frac{\rho_{vi,E}-\rho_{vi,P}}{\Delta r}-r_w^2 D_{i,w}\frac{\rho_{vi,P}-\rho_{vi,W}}{\Delta r}\right)\Delta t - \dot{m}_i r_P^2\Delta r\Delta t \tag{E-20}$$

where the source term is

$$-\dot{m}_i = S_{iC}+S_{iP}\rho_{viP} \tag{E-21}$$

Arrange this equation in the form of $a_P\rho_{viP}=a_W\rho_{viW}+a_E\rho_{viE}+b$, where

$$a_W=\frac{D_{i,eff,w}\Delta t}{\Delta r^2}\cdot\left(\frac{r_P+r_W}{2r_P}\right)^2 \tag{E-22}$$

$$a_E=\frac{D_{i,eff,e}\Delta t}{\Delta r^2}\cdot\left(\frac{r_E+r_P}{2r_P}\right)^2 \tag{E-23}$$

$$a_P=\varepsilon_{gi}+a_W+a_E-S_{iP}\Delta t \tag{E-24}$$

$$b=\varepsilon_{gi,P}^{0}\rho_{viP}^{0}+S_{iC}\Delta t \tag{E-25}$$

E.2.3 Energy transport of humid air (water vapor and dry air) in the domain *e* along the bed

$$\frac{\partial\left[\varepsilon_{ge}\left(\rho Cp\right)_g T_{ge}\right]}{\partial t}+\frac{\partial}{\partial x}\left[u_D\left(\rho Cp\right)_g T_{ge}\right]=\frac{\partial}{\partial x}\left(K^t{}_{e,eff}\frac{\partial T_{ge}}{\partial x}\right)+\dot{h}_{pe} \tag{E-26}$$

$$\int_s^n\int_0^1\frac{\partial\left[\varepsilon_{ge}\left(\rho Cp\right)_g T_{ge}\right]}{\partial t}dtdx+\int_0^1\int_s^n\frac{\partial}{\partial x}\left[u_D\left(\rho Cp\right)_g T_{ge}\right]dxdt = \int_0^1\int_s^n\frac{\partial}{\partial x}\left(K^t{}_{e,eff}\frac{\partial T_{ge}}{\partial x}\right)dtdx+\int_s^n\int_0^1\dot{h}_{pe}dtdx \tag{E-27}$$

$$\left\{\left[\varepsilon_{ge}(\rho Cp)_g T_{ge}\right]_P - \left[\varepsilon_{ge}(\rho Cp)_g T_{ge}\right]_P^0\right\}\Delta x + u_D\left\{\left[(\rho c_p)_g T_{ge}\right]_n - \left[(\rho Cp)_g T_{ge}\right]_s\right\}\Delta t$$
$$= \left[\left(K^t{}_{e,eff}\frac{\partial T_{ge}}{\partial x}\right)_n - \left(K^t{}_{e,eff}\frac{\partial T_{ge}}{\partial x}\right)_s\right]\Delta t + \dot{h}_{pe}\Delta t\Delta x \tag{E-28}$$

$$\left\{\left[\varepsilon_{ge}(\rho Cp)_g T_{ge}\right]_P - \left[\varepsilon_{ge}(\rho Cp)_g T_{ge}\right]_P^0\right\}\Delta x + u_D\left\{\left[(\rho Cp)_g T_{ge}\right]_P - \left[(\rho Cp)_g T_{ge}\right]_S\right\}\Delta t$$
$$= \left[\left(K^t{}_{e,eff}\right)_n\frac{T_{geN}-T_{geP}}{\Delta x} - \left(K^t{}_{e,eff}\right)_s\frac{T_{geP}-T_{geS}}{\Delta x}\right]\Delta t + \dot{h}_{pe}\Delta t\Delta x \tag{E-29}$$

where the source term is

$$\dot{h}_{pe} = S^T_{peC} + S^T_{peP}T_{geP} \tag{E-30}$$

Arrange this equation in the form of $a_P T_{geP} = a_S T_{geS} + a_N T_{geN} + b$, where

$$a_S = \frac{\left(K^t{}_{e,eff}\right)_s}{\Delta x^2} + \frac{u_D(\rho Cp)_{gS}}{\Delta x} \tag{E-31}$$

$$a_N = \frac{\left(K^t{}_{e,eff}\right)_n}{\Delta x^2} \tag{E-32}$$

$$a_P = \frac{\left[\varepsilon_{ge}(\rho Cp)_g\right]_P}{\Delta t} + a_S + a_N - S^T_{peP} \tag{E-33}$$

$$b = \frac{\left[\varepsilon_{ge}(\rho Cp)_g T_{ge}\right]_P^0}{\Delta t} + S^T_{peC} \tag{E-34}$$

E.2.4 Energy transport of urea particles (water vapor and dry air) along the bed

$$\frac{\partial\left\{\left[\varepsilon_p\cdot(\rho Cp)_p + (\varepsilon_{le}+\varepsilon_p\varepsilon_{li})\cdot(\rho Cp)_l\right]T_p\right\}}{\partial t} = \frac{\partial}{\partial x}\left(K_{p,eff}\frac{\partial T_p}{\partial x}\right) - \dot{h}_{pe} + \dot{h}_i \tag{E-35}$$

$$\int_s^n\int_0^1\frac{\partial\left\{\left[\varepsilon_p(\rho Cp)_p + (\varepsilon_{le}+\varepsilon_p\varepsilon_{li})(\rho Cp)_l\right]T_p\right\}}{\partial t}dtdx$$
$$= \int_0^1\int_s^n\frac{\partial}{\partial x}\left(K_{p,eff}\frac{\partial T_p}{\partial x}\right)dxdt - \int_0^1\int_s^n\dot{h}_{pe}dxdt + \int_0^1\int_s^n\dot{h}_i dxdt \tag{E-36}$$

$$\left\{\left[\left(\varepsilon_p \rho_p Cp_p + \left(\varepsilon_{le} + \varepsilon_p \varepsilon_{li}\right)\rho_l Cp_l\right)T_p\right]_P - \left[\left(\varepsilon_p \rho_p Cp_p + \left(\varepsilon_{le} + \varepsilon_p \varepsilon_{li}\right)\rho_l Cp_l\right)T_p\right]_P^0\right\}\Delta x$$
$$= \left[\left(K_{p,eff}\frac{\partial T_p}{\partial t}\right)_n - \left(K_{p,eff}\frac{\partial T_p}{\partial t}\right)_s\right]\Delta t - \dot{h}_{pe}\Delta x\Delta t + \dot{h}_i \Delta t\Delta x \tag{E-37}$$

$$\left\{\left[\left(\varepsilon_p \rho_p Cp_p + \left(\varepsilon_{le} + \varepsilon_p \varepsilon_{li}\right)\rho_l Cp_l\right)T_p\right]_P - \left[\left(\varepsilon_p \rho_p Cp_p + \left(\varepsilon_{le} + \varepsilon_p \varepsilon_{li}\right)\rho_l Cp_l\right)T_p\right]_P^0\right\}\Delta x$$
$$= \left[\left(K_{p,eff}\frac{\partial T_p}{\partial t}\right)_n - \left(K_{p,eff}\frac{\partial T_p}{\partial t}\right)_s\right]\Delta t - \dot{h}_{pe}\Delta x\Delta t + \dot{h}_i \Delta t\Delta x \tag{E-38}$$

where $\dot{h}_i = \overline{\dot{m}}_p \cdot \left[H_{fg} + Cp_v (T_{ge} - T_p)^0 + \beta_s \cdot H_s\right]$.

Arrange this equation in the form of $a_P T_{pP} = a_S T_{iS} + a_N T_{iN} + b$, where

$$a_S = \frac{\left(K_{p,eff}\right)_s}{\Delta x^2} \tag{E-39}$$

$$a_N = \frac{\left(K_{p,eff}\right)_n}{\Delta x^2} \tag{E-40}$$

$$a_P = \frac{\left[\varepsilon_p \rho_p Cp_p + \left(\varepsilon_{le} + \varepsilon_p \varepsilon_{li}\right)\rho_l Cp_l\right]_P}{\Delta t} + a_S + a_N + S_{peP}^T \tag{E-41}$$

$$b = \frac{\left[\varepsilon_p \rho_p Cp_p + \left(\varepsilon_{le} + \varepsilon_p \varepsilon_{li}\right)\rho_l Cp_l\right]_P^0}{\Delta t} - S_{peC}^T + \dot{h}_i \tag{E-42}$$

E.2.5 Aqueous phase continuity equations

$$\dot{m}_i = \rho_l \frac{\partial \varepsilon_{li}}{\partial t} \tag{E-43}$$

$$\dot{m}_e = \rho_l \frac{\partial \varepsilon_{le}}{\partial t} \tag{E-44}$$

Integrating for one corresponding internal control volume from t to $t + \Delta t$ gives

$$\dot{m}_i = \rho_l \frac{\varepsilon_{li} - \varepsilon_{li}^0}{\Delta t} \tag{E-45}$$

$$\dot{m}_e = \rho_l \frac{\varepsilon_{le} - \varepsilon_{le}^0}{\Delta t} \tag{E-46}$$

E.2.6 Source-term linearization for determination of a series of S_C and S_P

The quantities of the coefficients in the source-term linearization forms, shown in equation (E-11), (E-12), (E-21), (E-30), are respectively from their definitions or relationships between source terms and independent variables.

$$-\dot{m}_e = S_{eC} + S_{eP}\rho_{ve,P} \tag{E-11}$$

$$\dot{m}_{ie} = S_{ieC} + S_{ieP}\rho_{ve,P} \tag{E-12}$$

$$-\dot{m}_i = S_{iC} + S_{iP}\rho_{viP} \tag{E-21}$$

$$\dot{h}_{pe} = S_{peC}^T + S_{peP}^T T_{geP} \tag{E-30}$$

For example, in equation (E-11), one have that $-\dot{m}_e = -\rho_l \frac{\partial \varepsilon_{le}}{\partial t}$, $X_e = \frac{\rho_l \varepsilon_{le}}{\rho_p \varepsilon_p}$, $X_e = g(\phi_e)$, $\phi_e = \frac{\rho_{ve}}{\rho_{vs,e}}$, therefore,

$$\begin{aligned} -\dot{m}_e &= -\rho_l \frac{\partial \varepsilon_{le}}{\partial t} = -\rho_p \varepsilon_p \frac{\partial X_e}{\partial t} \\ &= -\rho_u \varepsilon_u \frac{\partial X_e}{\partial \phi_e}\frac{\partial \phi_e}{\partial t} = -\frac{\rho_p \varepsilon_p}{\rho_{vs,e}}\frac{\partial X_e}{\partial \phi_e}\frac{\rho_{ve} - \rho_{ve}^0}{\Delta t} \end{aligned} \tag{E-47}$$

$$-\dot{m}_e = \frac{\rho_p \varepsilon_p}{\rho_{vs,e}}\frac{\partial X_e}{\partial \phi_e}\frac{1}{\Delta t}\rho_{ve}^0 - \frac{\rho_u \varepsilon_u}{\rho_{vs,e}}\frac{\partial X_e}{\partial \phi_e}\frac{1}{\Delta t}\rho_{ve} \tag{E-48}$$

Compared with equation (E-11), two coefficients are

$$S_{eC} = \frac{\rho_p \varepsilon_p}{\rho_{vs,e}}\frac{\partial X_e}{\partial \phi_e}\frac{1}{\Delta t}\rho_{ve}^0 \tag{E-49}$$

$$S_{eP} = -\frac{\rho_p \varepsilon_p}{\rho_{vs,e}} \frac{\partial X_e}{\partial \phi_e} \frac{1}{\Delta t} \tag{E-50}$$

Similarly, in equation (E-21), two coefficients are

$$S_{iC} = \frac{\rho_p \varepsilon_p}{\rho_{vs,i}} \frac{\partial X_i}{\partial \phi_i} \frac{1}{\Delta t} \rho_{vi}^0 \tag{E-51}$$

$$S_{iP} = -\frac{\rho_p \varepsilon_p}{\rho_{vs,i}} \frac{\partial X_i}{\partial \phi_i} \frac{1}{\Delta t} \tag{E-52}$$

Due to $\dot{m}_{ie} = h_m A_{ve} \left(\rho_{vi}\big|_{r=R} - \rho_{ve,P} \right)$, then two coefficients in equation (E-12) are

$$S_{ieC} = h_m A_{ve} \rho_{vi}\big|_{r=R} \tag{E-53}$$

$$S_{ieP} = -h_m A_{ve} \tag{E-54}$$

Due to $\dot{h}_{pe} = h_t A_{ve} \left(T_p - T_{geP} \right)$, then two coefficients in equation (E-30) are

$$S_{peC}^T = h_t A_{ve} T_i \tag{E-55}$$

$$S_{peP}^T = -h_t A_{ve} \tag{E-56}$$

E.3 Discretization of boundary conditions

Boundary conditions for each governing equation are shown in the Table E.1.

For the boundary condition $\rho_{ve}(x=0,t) = \rho_{ve,I}$, it can be easily written in the form of $a_P \rho_{ve,P} = a_N \rho_{ve,N} + a_S \rho_{ve,S} + b$, where

$$a_S = 0 \tag{E-13a}$$

$$a_N = 0 \tag{E-14a}$$

$$a_P = 1 \tag{E-15a}$$

$$b = \rho_{ve,I} \tag{E-16a}$$

Table E.1 Boundary conditions

Governing equations	Boundary conditions	
(E-8)	$\rho_{ve}(x=0,t)=\rho_{ve,I}$	$\frac{\partial \rho_{ve}}{\partial x}(x=L,t)=0$
(E-17)	$\frac{\partial \rho_{vi}}{\partial r}(x,t,r=0)=0$	$-D_{i,eff}\frac{\partial \rho_{vi}}{\partial r}\Big\|_{x,t,r=R} = h_m\left(\rho_{vi}\Big\|_{x,t,r=R}-\rho_{ve}\right)$
(E-26)	$T_{ge}(x=0,t)=T_{ge,I}$	$\frac{\partial T_{ge}}{\partial x}(x=L,t)=0$
(E-35)	$\frac{\partial T_p}{\partial x}(x=0,t)=0$	$\frac{\partial T_p}{\partial x}(x=L,t)=0$

For the boundary condition $\frac{\partial \rho_{ve}}{\partial x}(x=L,t)=0$, the governing equation (E-8) is integrated over the boundary control volume space (from *s* face to *P* node) and over the time period *t* to Δt (i.e. from 0 to 1).

$$\int_s^P \int_0^1 \frac{\partial\left(\varepsilon_{ge}\rho_{ve}\right)}{\partial t} dt dx + \int_0^1 \int_s^P \frac{\partial}{\partial x}\left(u_D \rho_{ve}\right) dx dt$$
$$= \int_0^1 \int_s^P \frac{\partial}{\partial x}\left(D_{e,eff} \frac{\partial \rho_{ve}}{\partial x} \right) dx dt - \int_0^1 \int_s^P \dot{m}_e dx dt + \int_0^1 \int_s^P \dot{m}_{ie} dx dt \tag{E-9b}$$

$$\left(\varepsilon_{ge}\rho_{ve}-\varepsilon_{ge}^{0}\rho_{ve}^{0}\right)_P\frac{\Delta x}{2}+u_D\left(\rho_{ve,P}-\rho_{ve,S}\right)\Delta t$$
$$=D_{e,eff,n}\left(\frac{\partial\rho_{ve}}{\partial x}\right)_P\Delta t-D_{e,eff,s}\left(\frac{\rho_{ve,P}-\rho_{ve,S}}{\Delta x}\right)\Delta t-\dot{m}_e\frac{\Delta x}{2}\Delta t+\dot{m}_{ie}\frac{\Delta x}{2}\Delta t \tag{E-10b}$$

Which can be easily written in the form of $a_P\rho_{ve,P}=a_N\rho_{ve,N}+a_S\rho_{ve,S}+b$, where

$$a_S=\frac{D_{e,eff,s}\Delta t}{\Delta x^2}+\frac{u_D\Delta t}{\Delta x} \tag{E-13b}$$

$$a_N=0 \tag{E-14b}$$

$$a_P=\frac{\varepsilon_{ge,P}}{2}+a_S+a_N-\frac{S_{eP}\Delta t}{2}-\frac{S_{ieP}\Delta t}{2} \tag{E-15b}$$

$$b=\frac{\varepsilon_{ge,P}^{0}\rho_{ve,P}^{0}}{2}+\frac{S_{eC}\Delta t}{2}+\frac{S_{ieC}\Delta t}{2} \tag{E-16b}$$

For the boundary condition, $\frac{\partial\rho_{vi}}{\partial r}(x,t,r=0)=0$, the governing equation (E-17) is integrated over the boundary control volume space (from *P* node to *e* face) and over the time period *t* to Δt (i.e. from 0 to 1).

$$\int_P^e\int_0^1\frac{\partial\left(\varepsilon_{gi}\rho_{vi}\right)}{\partial t}dt\cdot 4\pi r^2dr$$
$$=\int_0^1\int_P^e\frac{\partial}{\partial r}\left(r^2\cdot D_{i,eff}^{t}\cdot\frac{\partial\rho_{vi}}{\partial r}\right)4\pi dr\cdot dt-\int_0^1\int_P^e\dot{m}_i4\pi r^2drdt \tag{E-18a}$$

$$\left(\varepsilon_{gi}\rho_{vi}-\varepsilon_{gi}^{0}\rho_{vi}^{0}\right)_P r_e^2\frac{\Delta r}{2}$$
$$=\left[\left(r^2D_{i,eff}^{t}\frac{\partial\rho_{vi}}{\partial r}\right)_e-\left(r^2D_{i,eff}\frac{\partial\rho_{vi}}{\partial x}\right)_P\right]\Delta t-\dot{m}_ir_e^2\frac{\Delta r}{2}\Delta t \tag{E-19a}$$

$$\left(\varepsilon_{gi}\rho_{vi}-\varepsilon_{gi}^{0}\rho_{vi}^{0}\right)_P r_e^2\frac{\Delta r}{2}=\left(r_e^2D_{i,eff}\frac{\rho_{vi,E}-\rho_{vi,P}}{\Delta r}\right)\Delta t-\dot{m}_ir_e^2\frac{\Delta r}{2}\Delta t \tag{E-20a}$$

Arranging this equation in the form of $a_P \rho_{viP} = a_W \rho_{viW} + a_E \rho_{viE} + b$, where

$$a_W = 0 \tag{E-22a}$$

$$a_E = \frac{D_{i,eff,e}\Delta t}{\Delta r^2} \tag{E-23a}$$

$$a_P = \frac{\varepsilon_{gi}}{2} + a_W + a_E - \frac{S_{iP}\Delta t}{2} \tag{E-24a}$$

$$b = \frac{\varepsilon^0_{gi,P}\rho^0_{viP}}{2} + \frac{S_{iC}\Delta t}{2} \tag{E-25a}$$

For the boundary condition, $-D_{i,eff}\left.\frac{\partial \rho_{vi}}{\partial r}\right|_{x,t,r=R} = h_m\left(\rho_{vi}\big|_{x,t,r=R} - \rho_{ve}\right)$, the governing equation (E-17) is integrated over the boundary control volume space (from *w* face to *P* node) and over the time period *t* to *t*+Δ*t* (i.e. from 0 to 1).

$$\begin{aligned}&\int_w^P\int_0^1 \frac{\partial\left(\varepsilon_{gi}\rho_{vi}\right)}{\partial t}dt \cdot 4\pi r^2 dr \\ &= \int_0^1\int_w^P \frac{\partial}{\partial r}\left(r^2 \cdot D_{i,eff} \cdot \frac{\partial \rho_{vi}}{\partial r}\right)4\pi dr \cdot dt - \int_0^1\int_w^P \dot{m}_i 4\pi r^2 dr dt\end{aligned} \tag{E-18b}$$

$$\begin{aligned}&\left(\varepsilon_{gi}\rho_{vi} - \varepsilon^0_{gi}\rho^0_{vi}\right)_P r_P^2 \frac{\Delta r}{2} \\ &= \left[\left(r^2 D_{i,eff}\frac{\partial \rho_{vi}}{\partial r}\right)_P - \left(r^2 D_{i,eff}\frac{\partial \rho_{vi}}{\partial x}\right)_w\right]\Delta t - \dot{m}_i r_P^2 \frac{\Delta r}{2}\Delta t\end{aligned} \tag{E-19b}$$

$$\begin{aligned}&\left(\varepsilon_{gi}\rho_{vi} - \varepsilon^0_{gi}\rho^0_{vi}\right)_P r_p^2 \frac{\Delta r}{2} = h_m\left(\rho_{ve} - \rho_{vi,P}\right)r_P^2\Delta t \\ &-\left(r_w^2 D_{i,eff,w}\frac{\rho_{vi,P} - \rho_{vi,W}}{\Delta r}\right)\Delta t - \dot{m}_i r_P^2 \frac{\Delta r}{2}\Delta t\end{aligned} \tag{E-20b}$$

Arrange this equation in the form of $a_P \rho_{viP} = a_W \rho_{viW} + a_E \rho_{viE} + b$, where

$$a_W = \frac{D_{i,eff,e}\Delta t}{\Delta r^2} \tag{E-22b}$$

$$a_E = 0 \tag{E-23b}$$

$$a_P = \frac{\varepsilon_{gi}}{2} + a_W + a_E - \frac{S_{iP}\Delta t}{2} + \frac{h_m \Delta t}{\Delta r} \tag{E-24b}$$

$$b = \frac{\varepsilon^0_{gi,P}\rho^0_{viP}}{2} + \frac{S_{iC}\Delta t}{2} + \frac{h_m \rho_{ve}\Delta t}{\Delta r} \tag{E-25b}$$

For the boundary condition, $T_{ge}(x=0,t) = T_{ge,I}$, it can be easily written in the form of $a_P T_{geP} = a_S T_{geS} + a_N T_{geN} + b$, where

$$a_S = 0 \tag{E-31a}$$

$$a_N = 0 \tag{E-32a}$$

$$a_P = 1 \tag{E-33a}$$

$$b = T_{ge,I} \tag{E-34a}$$

For the boundary condition, $\frac{\partial T_{ge}}{\partial x}(x=L,t) = 0$, the governing equation (E-26) is integrated over the boundary control volume (from *s* face to *P* node) and over time period *t* to $t+\Delta t$ as follows,

$$\begin{aligned} &\int_s^P \int_0^1 \frac{\partial \left[\varepsilon_{ge}(\rho Cp)_g T_{ge}\right]}{\partial t} dtdx + \int_0^1 \int_s^P \frac{\partial}{\partial x}\left[u_D (\rho Cp)_g T_{ge}\right] dxdt \\ &= \int_0^1 \int_s^P \frac{\partial}{\partial x}\left(K_{e,eff}\frac{\partial T_{ge}}{\partial x}\right) dtdx + \int_s^P \int_0^1 \dot{h}_{pe} dtdx \end{aligned} \tag{E-27b}$$

$$\begin{aligned} &\left\{\left[\varepsilon_{ge}(\rho Cp)_g T_{ge}\right]_P - \left[\varepsilon_{ge}(\rho Cp)_g T_{ge}\right]_P^0\right\}\frac{\Delta x}{2} + u_D\left\{\left[(\rho Cp)_g T_{ge}\right]_P - \left[(\rho Cp)_g T_{ge}\right]_s\right\}\Delta t \\ &= \left[\left(K_{e,eff}\frac{\partial T_{ge}}{\partial x}\right)_P - \left(K_{e,eff}\frac{\partial T_{ge}}{\partial x}\right)_s\right]\Delta t + \dot{h}_{pe}\Delta t\frac{\Delta x}{2} \end{aligned} \tag{E-28b}$$

$$\left\{\left[\varepsilon_{ge}(\rho Cp)_g T_{ge}\right]_P - \left[\varepsilon_{ge}(\rho Cp)_g T_{ge}\right]_P^0\right\}\frac{\Delta x}{2} + u_D\left\{\left[(\rho Cp)_g T_{ge}\right]_P - \left[(\rho Cp)_g T_{ge}\right]_S\right\}\Delta t$$
$$= -\left(K_{e,eff}\right)_s \frac{T_{geP} - T_{geS}}{\Delta x}\Delta t + \dot{h}_{pe}\Delta t\frac{\Delta x}{2} \qquad \text{(E-29b)}$$

Arrange this equation in the form of $a_P T_{geP} = a_S T_{geS} + a_N T_{geN} + b$, where

$$a_S = \frac{\left(K_{e,eff}\right)_s}{\Delta x^2} + \frac{u_D(\rho Cp)_{gS}}{\Delta x} \qquad \text{(E-31b)}$$

$$a_N = 0 \qquad \text{(E-32b)}$$

$$a_P = \frac{\left[\varepsilon_{ge}(\rho Cp)_g\right]_P}{2\Delta t} + a_S + a_N - \frac{S_{peP}^T}{2} \qquad \text{(E-33b)}$$

$$b = \frac{\left[\varepsilon_{ge}(\rho Cp)_g T_{ge}\right]_P^0}{2\Delta t} + \frac{S_{peC}^T}{2} \qquad \text{(E-34b)}$$

For the boundary condition, $\frac{\partial T_p}{\partial x}(x=0,t)=0$, the governing equation (E-35) is integrated over the boundary control volume (from node *P* to *n* face) and over time period *t* to $t+\Delta t$ as followed,

$$\int_P^n\int_0^1 \frac{\partial\left\{\left[\varepsilon_p(\rho Cp)_p + (\varepsilon_{le} + \varepsilon_p\varepsilon_{li})(\rho Cp)_l\right]T_p\right\}}{\partial t}dtdx$$
$$= \int_0^1\int_P^n \frac{\partial}{\partial x}\left(K_{p,eff}\frac{\partial T_p}{\partial x}\right)dxdt - \int_0^1\int_P^n \dot{h}_{pe}dxdt + \int_0^1\int_P^n \dot{h}_i dxdt \qquad \text{(E-36a)}$$

$$\left\{\left[(\varepsilon_p\rho_p Cp_p + (\varepsilon_{le} + \varepsilon_p\varepsilon_{li})\rho_l Cp_l)T_p\right]_P - \left[(\varepsilon_p\rho_p Cp_p + (\varepsilon_{le} + \varepsilon_p\varepsilon_{li})\rho_l Cp_l)T_p\right]_P^0\right\}\frac{\Delta x}{2}$$
$$= \left[\left(K_{p,eff}\frac{\partial T_p}{\partial t}\right)_n - \left(K_{p,eff}\frac{\partial T_p}{\partial t}\right)_P\right]\Delta t - \dot{h}_{pe}\frac{\Delta x}{2}\Delta t + \dot{h}_i\Delta t\frac{\Delta x}{2}$$

(E-37a)

$$\left\{\left[\left(\varepsilon_p \rho_p Cp_p + \left(\varepsilon_{le} + \varepsilon_p \varepsilon_{li}\right)\rho_l Cp_l\right)T_p\right]_P - \left[\left(\varepsilon_p \rho_p Cp_p + \left(\varepsilon_{le} + \varepsilon_p \varepsilon_{li}\right)\rho_l Cp_l\right)T_p\right]_P^0\right\}\frac{\Delta x}{2}$$
$$= \left(K_{p,eff}\right)_n \frac{T_{p,N} - T_{p,P}}{\Delta x}\Delta t - \dot{h}_{pe}\frac{\Delta x}{2}\Delta t + \dot{h}_i \Delta t \frac{\Delta x}{2}$$

(E-38a)

Arrange this equation in the form of $a_P T_{pP} = a_S T_{pS} + a_N T_{pN} + b$, where

$$a_S = 0 \tag{E-39a}$$

$$a_N = \frac{\left(K_{p,eff}\right)_n}{\Delta x^2} \tag{E-40a}$$

$$a_P = \frac{\left(\varepsilon_p \rho_p Cp_p + \left(\varepsilon_{le} + \varepsilon_p \varepsilon_{li}\right)\rho_l Cp_l\right)_P}{2\Delta t} + a_S + a_N + \frac{S_{peP}^T}{2} \tag{E-41a}$$

$$b = \frac{\left[\left(\varepsilon_p \rho_p Cp_p + \left(\varepsilon_{le} + \varepsilon_p \varepsilon_{li}\right)\rho_l Cp_l\right)T_p\right]_P^0}{2\Delta t} - \frac{S_{peC}^T}{2} + \frac{\dot{h}_i}{2} \tag{E-42a}$$

For the boundary condition, $\frac{\partial T_p}{\partial x}(x = L, t) = 0$, the governing equation (E-35) is integrated over the boundary control volume (from *s* face to node *P*) and over time period *t* to $t + \Delta t$ as followed,

$$\int_s^P \int_0^1 \frac{\partial\left\{\left[\varepsilon_p (\rho Cp)_p + \left(\varepsilon_{le} + \varepsilon_p \varepsilon_{li}\right)(\rho Cp)_l\right]T_p\right\}}{\partial t} dt dx$$
$$= \int_0^1 \int_s^P \frac{\partial}{\partial x}\left(K_{p,eff}\frac{\partial T_p}{\partial x}\right) dx dt - \int_0^1 \int_s^P \dot{h}_{pe} dx dt + \int_0^1 \int_s^P \dot{h}_i dx dt \tag{E-36b}$$

$$\left\{\left[\left(\varepsilon_p \rho_p Cp_p + \left(\varepsilon_{le} + \varepsilon_p \varepsilon_{li}\right)\rho_l Cp_l\right)T_p\right]_P - \left[\left(\varepsilon_p \rho_p Cp_p + \left(\varepsilon_{le} + \varepsilon_p \varepsilon_{li}\right)\rho_l Cp_l\right)T_p\right]_P^0\right\}\frac{\Delta x}{2}$$
$$= \left[\left(K_{p,eff}\frac{\partial T_p}{\partial t}\right)_P - \left(K_{p,eff}\frac{\partial T_p}{\partial t}\right)_s\right]\Delta t - \dot{h}_{pe}\frac{\Delta x}{2}\Delta t + \dot{h}_i \Delta t \frac{\Delta x}{2} \tag{E-37b}$$

$$\left\{\left[\left(\varepsilon_p \rho_p Cp_p + \left(\varepsilon_{le} + \varepsilon_p \varepsilon_{li}\right)\rho_l Cp_l\right)T_p\right]_P - \left[\left(\varepsilon_p \rho_p Cp_p + \left(\varepsilon_{le} + \varepsilon_p \varepsilon_{li}\right)\rho_l Cp_l\right)T_p\right]_P^0\right\}\frac{\Delta x}{2}$$
$$= -\left(K_{p,eff}\right)_s \frac{T_{p,P} - T_{p,S}}{\Delta x}\Delta t - \dot{h}_{pe}\frac{\Delta x}{2}\Delta t + \dot{h}_i \Delta t \frac{\Delta x}{2} \qquad \text{(E-38b)}$$

Arrange this equation in the form of $a_P T_{pP} = a_S T_{pS} + a_N T_{pN} + b$, where

$$a_S = \frac{\left(K_{p,eff}\right)_s}{\Delta x^2} \qquad \text{(E-39b)}$$

$$a_N = 0 \qquad \text{(E-40b)}$$

$$a_P = \frac{\left(\varepsilon_p \rho_p Cp_p + \left(\varepsilon_{le} + \varepsilon_p \varepsilon_{li}\right)\rho_l Cp_l\right)_P}{2\Delta t} + a_S + a_N + \frac{S_{peP}^T}{2} \qquad \text{(E-41b)}$$

$$b = \frac{\left[\left(\varepsilon_p \rho_p Cp_p + \left(\varepsilon_{le} + \varepsilon_p \varepsilon_{li}\right)\rho_l Cp_l\right)T_p\right]_P^0}{2\Delta t} - \frac{S_{peC}^T}{2} + \frac{\dot{h}_i}{2} \qquad \text{(E-42b)}$$

APPENDIX F

SENSIVITY STUDY

The sensitivities of grid size and time steps used in numerical models are studied respectively. Since moisture sorption happens simultaneously in both the internal domain and the external domain, two time steps and two size steps are required in numerical simulations. They are carefully chosen until the simulation results do not have significant change (less than 1%).

F.1 Sensitivity study of size steps

The model of coupled heat and moisture migration within a urea particle includes a model that covers the heat and moisture transfer along the bed length in air flow direction in external domain and a subroutine that presents the internal moisture diffusion process inside a particle (internal domain). To simplify sensitivity study in two coupled domains, the size step in the internal domain, dr, was determined by means of developing this subroutine program for internal moisture diffusion inside a particle to be an independent program. The convective boundary condition on the external surface of a particle was unchangeable. Internal size step, $dr = d_p / 80$, i.e. 40 control volumes, was determined until there was negligible change ($\leq 1\%$) in simulated water vapor distributions inside a particle, water vapor density gradient on the particle surface and the volume average moisture content.

In Figure F.1, a sensitivity study of grid size step in the external domain showed that simulated average moisture uptake of a urea particle bed was insensitive to changes in dx from $0.5d_p$ to d_p. However, the thermal conductivity due to contacts points between particles was very sensitive to the particle size, therefore dx was taken equal to d_p in this study.

F.2 Sensitivity study of time steps

Two different time steps in both external domain and internal domain were taken the same, i.e., $dt_e = dt_i$, because the coupled non-linear heat and mass transport process between

internal diffusion process and the external at the same time need the latest properties to update the coupled source/sink term or boundary condition for the current time step. The time step $dt_e = dt_i = 1$ s was selected after the simulation did not has significant change (1%) in simulated results as shown in Figure F.2.

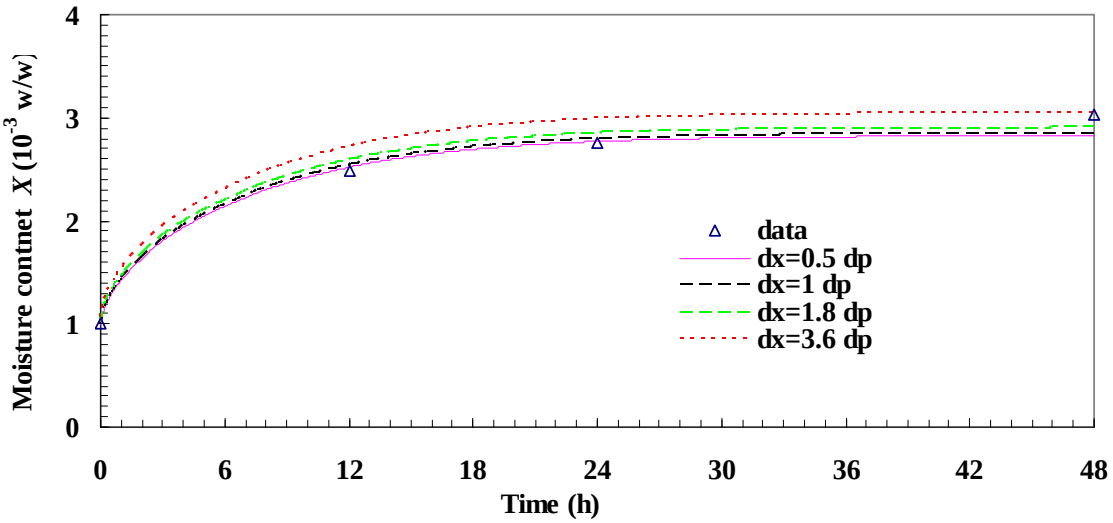

Figure F.1 Moisture sorption process of a Terico urea particle bed subject to an air flow of $\phi = 0.6 \sim 0.7$ and $\mathrm{Re}_{d_h} = 1.5$ ($dt_e = dt_i = 1$ s, $dr = d_p / 80$).

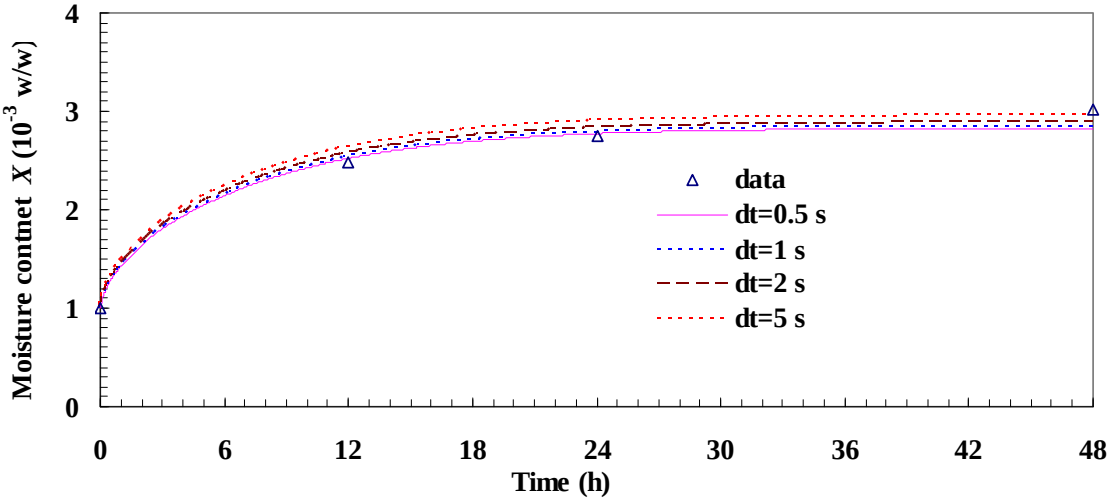

Figure F.2 Moisture sorption process of Terico urea particle bed subject to an air flow of $\phi = 0.6 \sim 0.7$ and $\mathrm{Re}_{d_h} = 1.5$. ($dr = d_p / 80$, $dx = d_p$).

APPENDIX G

PROPERTIES USED IN THE NUMERICAL SIMULATIONS

Some properties used in the numerical simulation in Chapter 5 are listed as follows.

Density, ρ_u=ρ_s=1323 kg/m^3 for urea, ρ_l=1000 kg/m^3 for water, ρ_a=1.19 kg/m^3 for air;

Heat capacity, Cp_s=80.7 J/(mol.K) for urea, Cp_l =4179 J/(kg.K) for water, Cp_a =1007 J/(kg.K) for air, Cp_v =1872 J/(kg.K) for vapor;

Thermal conductivity, K_a=0.0263 W/(m.K) for air, K_v =0.0196 W/(m.K) for vapor;

Effective thermal conductivity, $K_{b,eff}$=0.2110 W/(m.K) for dry Terico urea beds; $K_{b,eff}$ =0.1761 W/(m.K) for dry Georgia urea particle beds;

Gas constant, R_a = 287 J/(Kg·K) for air, R_v = 462 J/(Kg·K) for vapor;

Air properties, υ=15.4×10^{-6} m^2/s for viscosity, α=22.5 ×10^{-6} m^2/s for thermal diffusion, $D_{a,v}$= 2.52×10^{-5} m^2/s for air-vapor mass molecular diffusivity, Pr=0.707 for Prandtl number;

External porosity, ε_e= 0.36 for both Terico and Georgia particle beds;

Internal porosity, ε_i= 0.004 for Terico, ε_i= 0.0035 Georgia;

External tortuosity, τ_e= 1.5 for Terico, τ_e= 1.7 for Georgia;

External surface area if smooth, A_{ve}=1204 m^2/m^3 for Terico, A_{ve}=1992 m^2/m^3 for Georgia;

Internal moisture diffusivity is a function of moisture content during moisture sorption process, but is a constant during moisture desorption process.

APPENDIX H

EXPERIMENTAL DATA NOT LISTED IN CHAPTERS

Due to the limited moisture sorption capacity of urea particles in the air environments with relative humidity less than 60%, which was comparable to the measurement uncertainty of moisture content using Karl Fischer titrator, humid air with relative humidity of 65% was preferred in the adsorption process. But it changed with time because it was not easy to be kept constant. Usually inlet air relative humidity varied in the range of 60%~70% for adsorption process but 4~10% for desorption process. Table H.1 and H.2 showed some experimental data not listed in Chapter 4 and 5 for moisture adsorption and desorption processes in Terico and Georgia urea particle beds.

Table H.1 Measured average moisture content of Terico urea particle beds at different times while subject to humid air (ϕ = 60~70%) or dry air (ϕ = 4~10%) with different air flow rates at room temperature (T = 23°C), X (10^{-3} g/g or w/w).

air flow rate 200±2 Lpm				
Time t (h) / Process	0	3.5	11.3	24
Adsorption	0	1.11	1.33	1.60
Time t (h) / Process	0	2.8	11.8	24
Desorption	1.60	1.16	1.01	0.89

air flow rate 160±2 Lpm (initial moisture content 0.193)					
Time t (h) / Process	0	2	5	12	24
Adsorption	0	1.111	1.873	2.216	2.212
Time t (h) / Process	0	2	6		24
Desorption	2.212	1.683	1.411		1.292

Table H.1 (continued)

air flow rate 100±2 Lpm (initial moisture content 0.230)					
Time *t* (h) / Process	0	2.2	6.6	12	24
Adsorption	0	1.448	1.730	1.841	2.000
Time *t* (h) / Process	0	2.1	12.7	24	
Desorption	2.000	1.456	1.137	0.982	
air flow rate 75±1 Lpm					
Time *t* (h) / Process	0	10	22	46	
Adsorption	1.268±0.507	1.755±0.228	2.021±0.667	2.342±0.143	
Time *t* (h) / Process	0	12	24	48	
Desorption	2.342±0.143	2.042±0.765	1.627 ±0.089	1.592 ±0.334	
air flow rate 50±1 Lpm					
Time *t* (h) / Process	0	12	24	48	
Adsorption	2.377±0.643	2.489±0.712	2.289±0.375	2.338±0.843	
Desorption	2.338±0.843	1.907±0.391	2.004±0.835	1.777±0.411	
air flow rate 25±1 Lpm					
Time *t* (h) / Process	0	12	24	48	
Adsorption	0.913±0.369	2.247±0.163	2.608±0.480	3.035±0.348	
Desorption	3.035±0.348	2.501±0.427	2.058±0.562	1.871±0.253	
air flow rate 17.5±0.5 Lpm					
Time *t* (h) / Process	0	12	24	48	
Adsorption	0.999	2.48±0.12	2.75±0.21	3.02±0.25	
Desorption	3.02±0.25	2.11±0.30	1.94±0.73	1.68±0.22	
air flow rate 10±0.5 Lpm					
Time *t* (h) / Process	0	24	48	72	
Adsorption	0.128	1.377±0.246	1.940±0.233	2.405±0.646	
Desorption	2.405±0.646	1.629±0.135	1.556±0.100	1.633±0.541	

Table H.1 (continued)

air flow rate 10±0.5 Lpm				
Time *t* (h) / Process	0	24	48	72
Adsorption	0.189	1.065±0.412	1.117±0.395	1.419±0.271
Desorption	1.419±0.271	1.080±0.107	0.943±0.598	0.839±0.303

Table H.2 Measured average moisture content of Georgia urea particle beds at different times while subject to humid air (ϕ = 60~70%) or dry air (ϕ = 4~10%) with different air flow rates at room temperature (T = 23°C), X (10^{-3} g/g or w/w).

air flow rate 75±1 Lpm (initial moisture content of dry urea: 1.268)				
Time *t* (h) / Process	0	10	22	46
Adsorption	0	1.087	1.939	2.226
Time *t* (h) / Process	0	12	24	48
Desorption	2.226	1.185	0.961	0.667
air flow rate 50±1 Lpm (initial moisture content of dry urea: 2.377)				
Time *t* (h) / Process	0	12	24	48
Adsorption	0	0.915	1.048	1.134
Desorption	1.134	0.499	0.365	0.149
air flow rate 25±1 Lpm (initial moisture content of dry urea: 0.913)				
Time *t* (h) / Process	0	12	24	48
Adsorption	0	1.035	1.321	1.775
Desorption	1.775	1.125	0.855	0.645

Numerical simulations and comparisons with experimental data of both adsorption and desorption process within a Terico urea particle bed subject to an inlet air flow of 17.5 Lpm

were shown in Figure H.1 ~ Figure H.8. Constant boundary conditions for both air temperature and relative humidity at the inlet were used in the simulation.

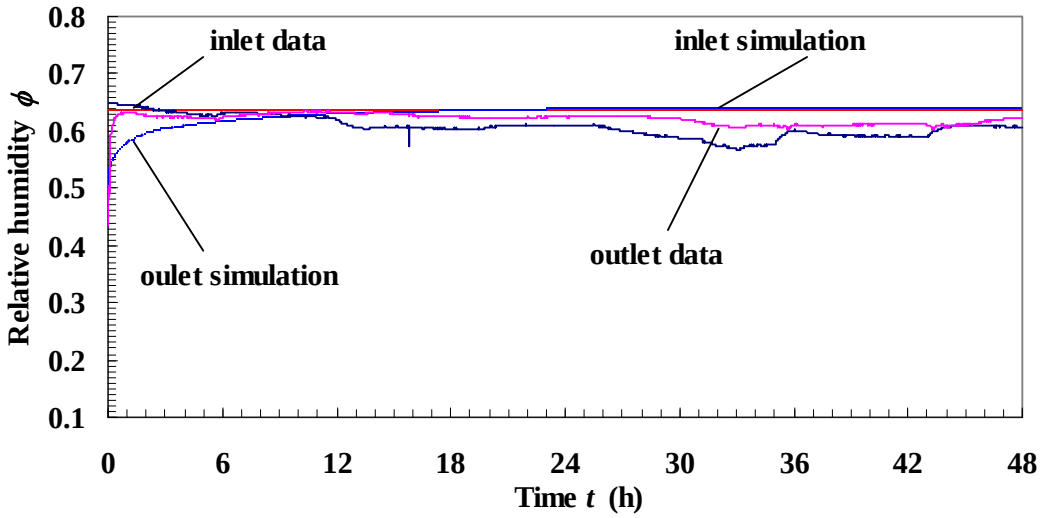

Figure H.1 Comparison of simulations and data of relative humidity for an adsorption process within a Terico urea particle bed, $T_0 = 23^{\circ}\mathrm{C}$, $\mathrm{Re}_{d_h} = 1.5$.

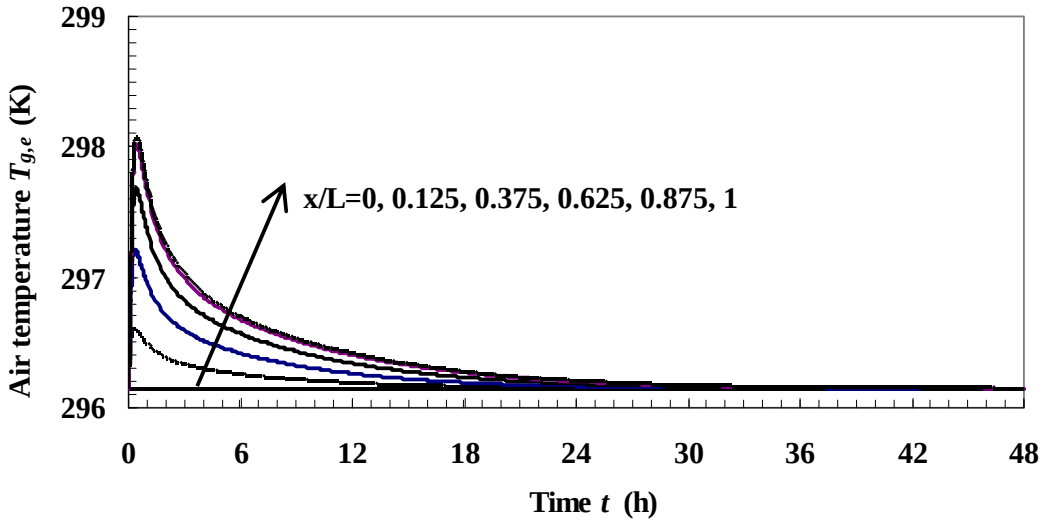

Figure H.2 Simulated air temperature versus time for an adsorption process at different depths of the Terico urea particle bed, $T_0 = 23^{\circ}\mathrm{C}$, $\mathrm{Re}_{d_h} = 1.5$.

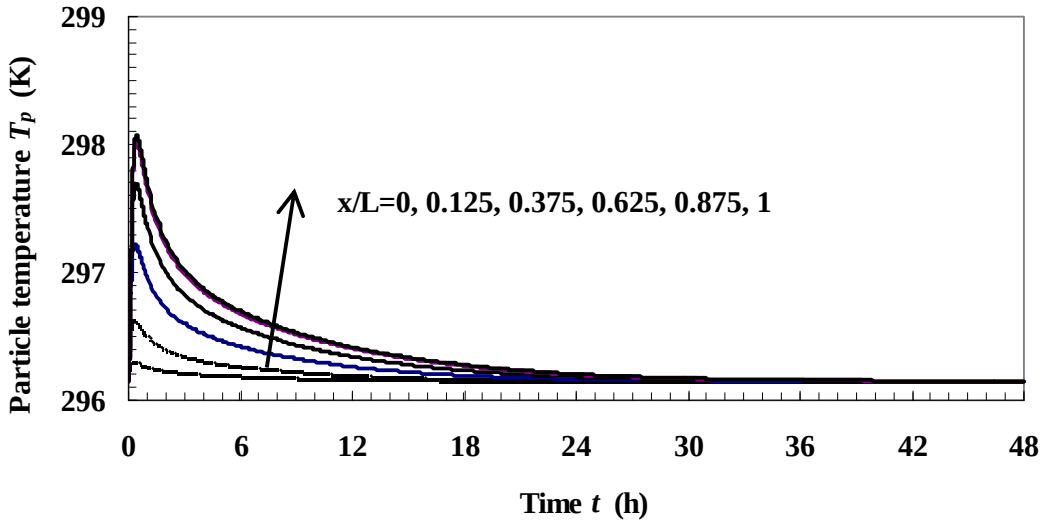

Figure H.3 Simulated transient particle temperature versus time for an adsorption process at different depths of Terico urea particle bed, $T_0 = 23^{\circ}\mathrm{C}$, $\mathrm{Re}_{d_h} = 1.5$.

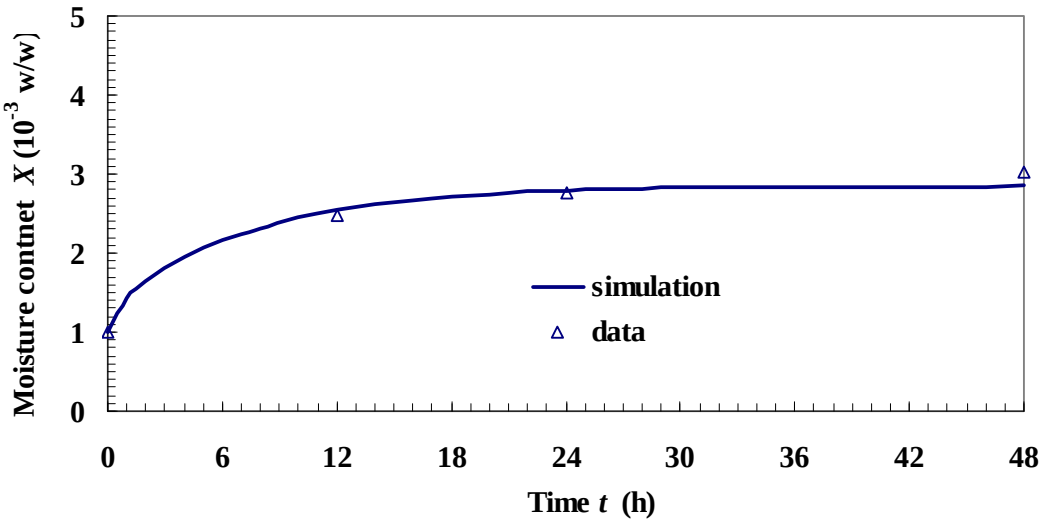

Figure H.4 A comparison of predicted and experimental data of the transient average moisture content of the Terico urea particle bed during an adsorption process, $T_0 = 23^{\circ}\mathrm{C}$, $\mathrm{Re}_{d_h} = 1.5$.

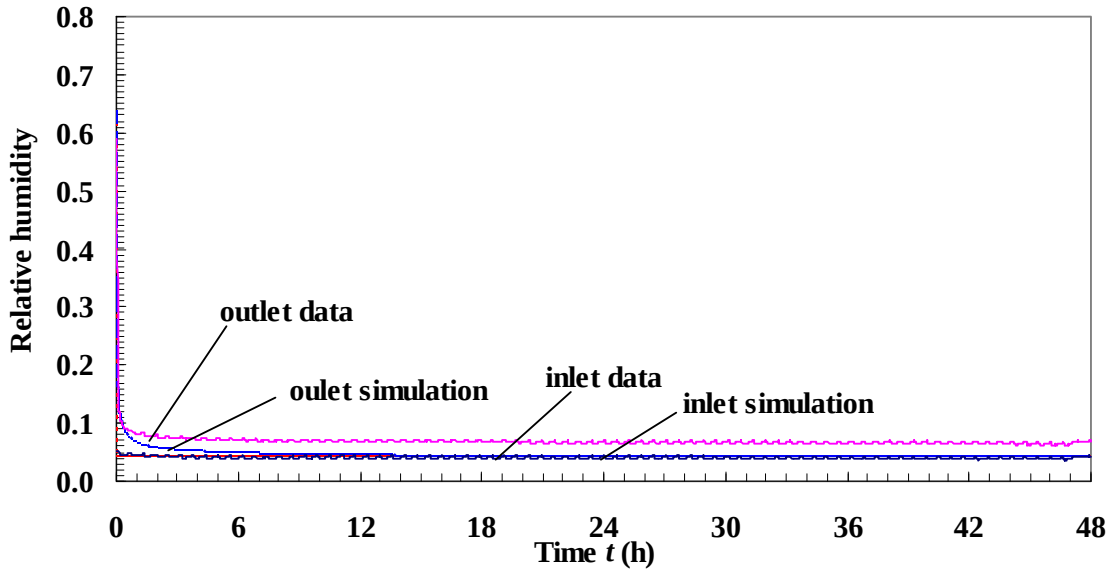

Figure H.5 Comparison of simulations and data of relative humidity for a desorption process within a Terico urea particle bed, $T_0 = 23^{\circ}\mathrm{C}$, $\mathrm{Re}_{d_h} = 1.5$.

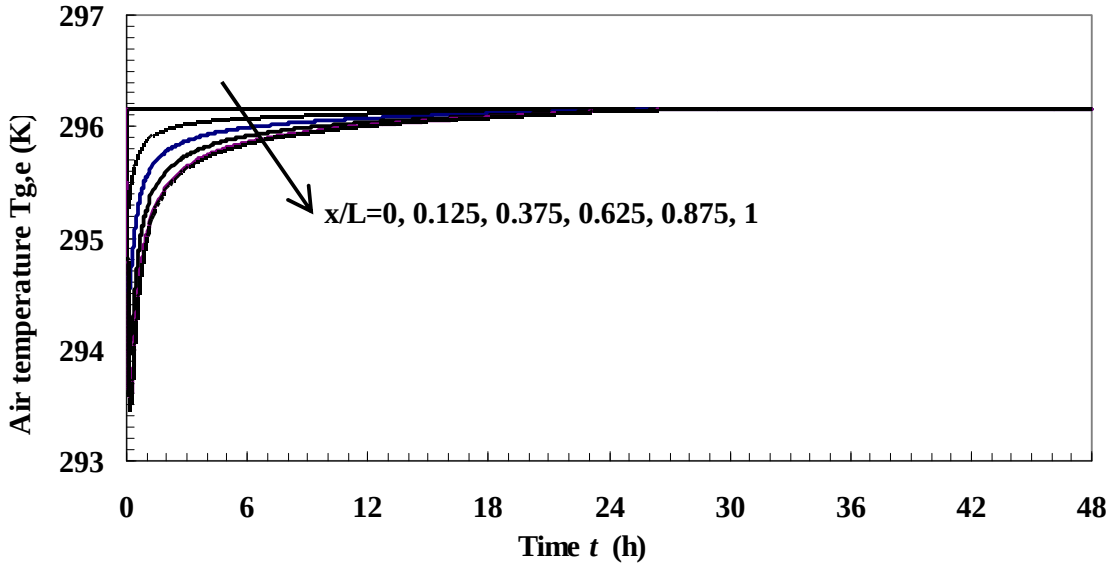

Figure H.6 Simulated air temperature versus time for a desorption process at different depths of the Terico urea particle bed, $T_0 = 23^{\circ}\mathrm{C}$, $\mathrm{Re}_{d_h} = 1.5$.

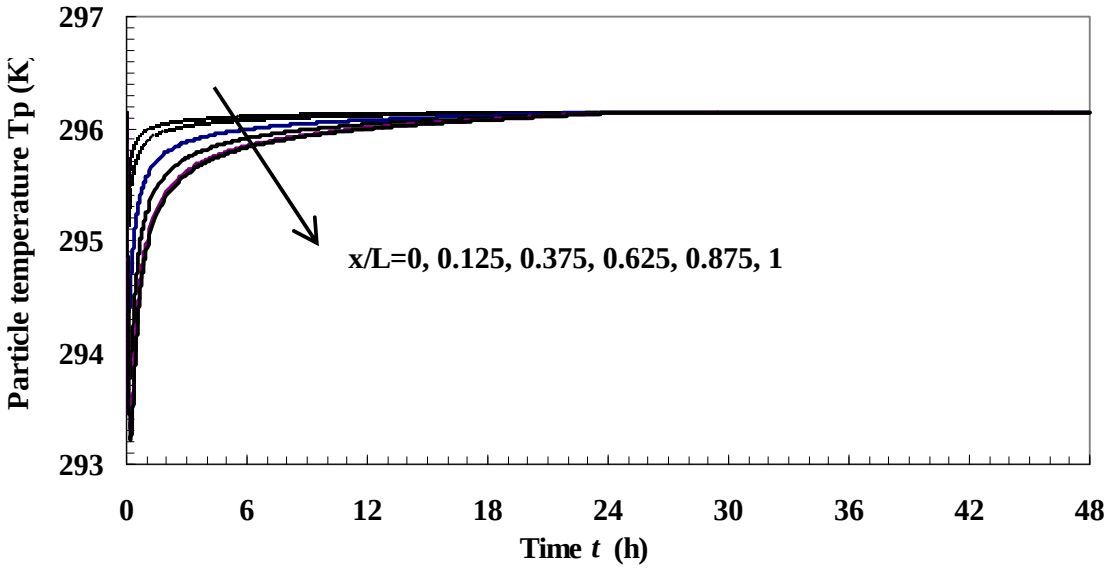

Figure H.7 Simulated transient particle temperature versus time for a desorption process at different depths of the Terico urea particle bed, $T_0 = 23^{\circ}\mathrm{C}$, $\mathrm{Re}_{d_h} = 1.5$.

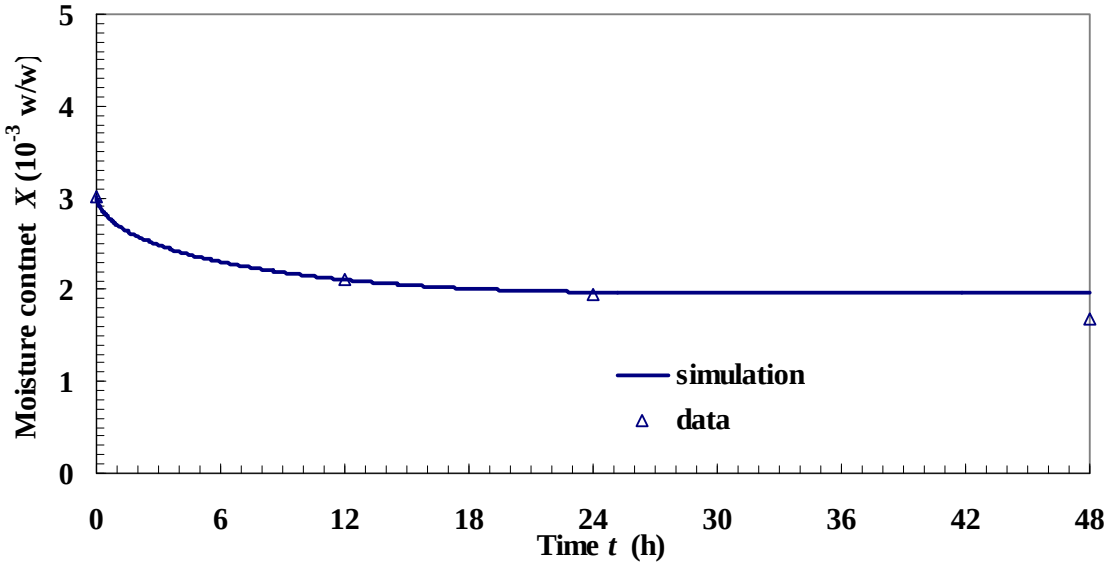

Figure H.8 A comparison of predicted and experimental data of the transient average moisture content of the Terico urea particle bed during a desorption process, $T_0 = 23^{\circ}\mathrm{C}$, $\mathrm{Re}_{d_h} = 1.5$.